



**HAL**  
open science

# Genetic engineering of organoids using nanoblades and probing the role of UBTD1 as a modulator of cell adhesion strength in prostate organoids

Victor Tiroille

## ► To cite this version:

Victor Tiroille. Genetic engineering of organoids using nanoblades and probing the role of UBTD1 as a modulator of cell adhesion strength in prostate organoids. Cellular Biology. Université Côte d'Azur, 2021. English. NNT: 2021COAZ6039 . tel-04349530

**HAL Id: tel-04349530**

**<https://theses.hal.science/tel-04349530>**

Submitted on 18 Dec 2023

**HAL** is a multi-disciplinary open access archive for the deposit and dissemination of scientific research documents, whether they are published or not. The documents may come from teaching and research institutions in France or abroad, or from public or private research centers.

L'archive ouverte pluridisciplinaire **HAL**, est destinée au dépôt et à la diffusion de documents scientifiques de niveau recherche, publiés ou non, émanant des établissements d'enseignement et de recherche français ou étrangers, des laboratoires publics ou privés.



# THÈSE DE DOCTORAT

Ingénierie génétique d'organoïdes à l'aide de nanoblades et étude du rôle d'UBTD1 comme modulateur de la force d'adhésion cellulaire dans les organoïdes de prostate

--

Genetic engineering of organoids using nanoblades and probing the role of UBTD1 as a modulator of cell adhesion strength in prostate organoids

## Victor TIROILLE

Centre Méditerranéen de Médecine Moléculaire - INSERM U1065  
Équipe 5 : Targeting prostate cancer cell metabolism

**Présentée en vue de l'obtention  
du grade de docteur en Sciences de la Vie  
et de la Santé d'Université Côte d'Azur**

**Dirigée par :** Dr Frédéric Bost

**Soutenue le :** 17 Décembre 2021

**Devant le jury, composé de :**

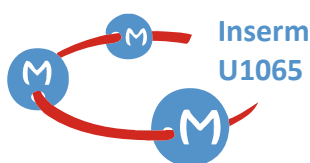
**Dr. Vincent GOFFIN**, Rapporteur

**Dr. Rik GIJSBERS**, Rapporteur

**Dr. Kai KRETZSCHMAR**, Examineur

**Dr. Els VERHOEYEN**, Présidente du jury

**Dr. Frédéric BOST**, Directeur de Thèse



Ingénierie génétique d'organoïdes à l'aide de nanoblades et étude du  
rôle d'UBTD1 comme modulateur de la force d'adhésion cellulaire  
dans les organoïdes de prostate

--

Genetic engineering of organoids using nanoblades and probing the role of  
UBTD1 as a modulator of cell adhesion strength in prostate organoids

Jury :

Présidente du jury

Dr. Els VERHOEYEN, Université Côte d'Azur, INSERM U1065, Nice, France

Rapporteur

Dr. Vincent GOFFIN, Université Paris Descartes, INSERM U1151, INEM, Paris

Dr. Rik GIJSBERS, Katholieke Universiteit Leuven, Belgique

Examineur

Dr. Kai KRETZSCHMAR, University Hospital Würzburg, Allemagne

Directeur de Thèse

Dr. Frédéric BOST, Université Côte d'Azur, INSERM U1065, Nice, France

**Titre :** Ingénierie génétique d'organoïdes à l'aide de nanoblades et étude du rôle d'UBTD1 comme modulateur de la force d'adhésion cellulaire dans les organoïdes de prostate

**Résumé :** Au cours de ma thèse, j'ai travaillé sur le modèle d'organoïde 3D en suivant deux objectifs principaux : i) développer des outils génétiques pour modifier le génome des organoïdes et ii) déchiffrer le rôle de la ubiquitin domain-containing protein 1 (UBTD1) dans le développement des organoïdes de la prostate.

L'ingénierie du génome est devenue ces dernières années plus accessible grâce aux endonucléases programmables par ARN telles que le système CRISPR-Cas9. Cependant, l'utilisation de cette technologie d'édition dans des organes synthétiques appelés "organoïdes" reste très inefficace. Ceci est principalement dû aux méthodes de livraison utilisées pour la machinerie CRISPR-Cas9, qui sont principalement réalisées par électroporation de RNP contenant le complexe CAS9-gRNA, une procédure toxique pour les organoïdes. Nous décrivons ici l'utilisation de la technologie "Nanoblade" pour réaliser l'édition du génome dans les organoïdes. Les nanoblades ont dépassé de loin les niveaux de knock-out (KO) obtenus avec d'autres techniques utilisées jusqu'à présent pour la livraison de la machinerie d'édition de gènes. Nous avons atteint jusqu'à 80 % de knockout génétique dans les organoïdes après traitement avec les nanoblades. Nous avons atteint un niveau élevé de KO médié par les nanoblades pour le gène codant le récepteur des androgènes (AR) et le gène du cystic fibrosis transmembrane conductance regulator (CFTR) avec des nanoblades contenant un seul ARNg ou un double ARNg. Plus important encore, contrairement à d'autres méthodes d'édition de gènes, ce résultat a été obtenu sans toxicité pour les organoïdes. En outre, il ne faut que quatre semaines pour obtenir des lignées stables KO pour un gène dans les organoïdes et aucun INDELS indésirable évident dans un site hors cible du génome n'a été détecté. En conclusion, les nanoblades simplifient et permettent une édition rapide du génome dans les organoïdes avec peu ou pas d'effets secondaires. La morphogenèse et le remodelage des tissus sont des processus finement régulés, régis par les adhésions entre cellules. Cependant, le contrôle spatial et temporel des molécules d'adhésion reste partiellement inexploré. Nous avons étudié ici le rôle d'UBTD1 comme modulateur de la force des adhésions dans l'épithélium de la prostate. Nous avons montré que la régulation négative d'UBTD1 perturbe l'auto-organisation des cellules en trois dimensions. Inversement, nous avons démontré que la surexpression d'UBTD1 induit des monocouches épithéliales plus régulières et augmente la tension de la surface cellulaire. Les analyses transcriptomiques ont révélé un profil d'expression génique des protéines impliquées dans les jonctions cellulaires affectées par la modulation d'UBTD1. En utilisant le modèle d'organoïde de prostate, nous avons montré que l'expression d'UBTD1 dans les cellules luminales perturbe la formation de lumen dans les organoïdes de prostate de souris. Enfin, en utilisant une approche de co-immunoprécipitation couplée à la spectrométrie de masse, nous avons montré que UBTD1 interagit avec des partenaires impliqués dans les jonctions cellule-cellule et que ces interactants voient leur expression modulée par la dérégulation de UBTD1. Nos résultats montrent qu'une protéine impliquée dans les processus de dégradation des protéines régule la force des jonctions d'adhérence.

**Mots clés :** Organoïde, CRISPR, Jonctions cellulaire, UBTD1, Nanoblade, Prostate

**Title :** Genetic engineering of organoids using nanoblades and probing the role of UBTD1 as a modulator of cell adhesion strength in prostate organoids

**Abstract :** During my thesis, I worked on the 3D organoid model following two main objectives: i) developing genetic tools to modify the genome of organoids and ii) deciphering the role of ubiquitin domain-containing protein 1 (UBTD1) in the development of prostate organoids. Genome engineering has become in the last few years more accessible thanks to the RNA programmable endonucleases such as the CRISPR-Cas9 system. However, using this editing technology in synthetic organs called 'organoids' is still very inefficient. This is mainly due to the delivery methods used for the CRISPR-Cas9 machinery, which are predominantly performed by electroporation of RNPs containing the CAS9-gRNA complex, a procedure toxic for the organoids. Here we describe the use of the 'Nanoblade' technology to accomplish genome editing in organoids. Nanoblades outperformed by far knockout (KO) levels achieved with other techniques used to date for delivery of the gene editing machinery. We reached up to 80% of gene knockout in organoids after treatment with nanoblades. We achieved high-level nanoblade-mediated KO for the androgen receptor (AR) encoding gene and the cystic fibrosis transmembrane conductance regulator (CFTR) gene with single gRNA or dual gRNA containing nanoblades. Most importantly, in contrast to other gene editing methods, this was obtained without toxicity for the organoids. Moreover, it requires only four weeks to obtain stable lines KO for a gene in organoids and no obvious unwanted INDELS in off-target site in the genome were detected. In conclusion, nanoblades simplify and allow rapid genome editing in organoids with little to no side-effects.

Morphogenesis and tissue remodeling are finely regulated processes governed by cell-cell adhesions. However, the spatial and temporal control of adhesion molecules remains partially unexplored. Here we studied the role of UBTD1 as a modulator of the strength of adherens in the prostate epithelium. We showed that down-regulation of UBTD1 disrupted the self-organization of cells in three dimensions. Conversely, we demonstrated that overexpression of UBTD1 induced more regular epithelial monolayers and increased cell surface tension. Transcriptomic analyses revealed a gene expression profile of proteins involved in cell junctions affected by UBTD1 modulation. Using the prostate organoid model, we showed that UBTD1 expression in luminal cells disrupted cyst formation in mouse prostate organoids. Finally using a co-immunoprecipitation approach coupled to mass spectrometry, we showed that UBTD1 interacts with partners involved in cell-cell junctions and that these interactants have their expression modulated by UBTD1 deregulation. Our results show that a protein involved in protein degradation processes regulates the strength of adherens junctions.

**Keywords :** Organoid, CRISPR, cell junction, UBTD1, Nanoblade, prostate

# TABLE OF CONTENTS

<b>Table of Contents .....</b>	<b>3</b>
<b>Acknowledgement.....</b>	<b>5</b>
<b>Abbreviations list.....</b>	<b>9</b>
<b>List of Figures.....</b>	<b>12</b>
<b>List of tables .....</b>	<b>12</b>
<b>Introduction .....</b>	<b>13</b>
<b>Prostate.....</b>	<b>15</b>
I. Prostate development.....	15
A. Prostate induction .....	16
B. Budding of the UGE in the UGM.....	17
C. Morphogenesis of the epithelial branching duct network .....	18
D. Differentiation and functionalization of the prostate epithelium .....	18
II. Prostate Cancer .....	20
A. Risk factors for cancer .....	21
B. Prostatic Intraepithelial Neoplasia (PIN) and Cancer .....	21
<b>Cell Junction .....</b>	<b>23</b>
I. Composition of the adherens junction complex .....	24
A. E-cadherin.....	24
B. Catenins.....	25
1. p120-catenin .....	25
2. $\beta$ -catenin.....	26
3. $\alpha$ -catenin.....	26
C. Vinculin.....	27
D. Arp2/3.....	27
E. Rho GTPase family .....	28
1. Rac1 & Cdc42 .....	28
2. RhoA .....	28
F. Myosin II .....	29
G. $\alpha$ -actinin .....	29
II. Adherens junction formation process.....	30
A. Formation of Initial Cell–Cell Contacts .....	30
B. Junction maturation - actin reorganization .....	31
C. Stable junctions .....	32
III. Epithelial Cell Adhesion Molecule – EpCAM .....	32
<b>Ubiquitination and Ubiquitin-Like Proteins .....</b>	<b>35</b>
I. Ubiquitylation process .....	35
A. Ubiquitin .....	35
B. E1 ubiquitin-activating enzyme .....	35
C. E2 ubiquitin-conjugating enzymes.....	36
D. E3 ubiquitin ligases .....	36
II. Ubiquitin partners .....	37
A. Ubiquitin-binding domains .....	37
B. Ubiquitin-like proteins.....	37
III. Ubiquitin domain-containing protein 1.....	37
<b>Organoid.....</b>	<b>39</b>

I.	History of organoid culture .....	39
II.	Organoids to study human biology and diseases .....	40
A.	Spectrum of organism models.....	40
B.	ASCs-derived human organoids.....	40
1.	Establishment of organoids <i>in vitro</i> .....	40
2.	Physiological relevance .....	41
3.	Organoids to study infectious diseases .....	42
4.	Organoids to model genetic pathologies.....	43
5.	Organoid to model cancer .....	44
6.	Genetic repair in organoids .....	45
III.	Engineering organoid and next generation organoids .....	45
A.	Limitations of organoids .....	45
B.	Organoid system engineering.....	46
1.	Matrix compositions .....	46
2.	Geometrical parameter .....	47
IV.	Prostate Organoid .....	48
	<b>Gene editing .....</b>	<b>50</b>
I.	Nucleases .....	50
A.	ZFN-Fok1.....	51
B.	TALENs.....	52
C.	CRISPR.....	52
1.	Origin of CRISPR system.....	52
2.	How does the CRISPR Cas9 system function.....	53
3.	Cas9 off-targets.....	54
II.	Delivery of Cas9 and sgRNA .....	55
A.	Non-viral vehicle.....	58
1.	Microinjection.....	58
2.	Electroporation .....	58
3.	Liposome transfection .....	59
B.	Viral Vectors .....	60
1.	AAV .....	60
2.	Retroviral vectors.....	61
3.	Virus-like particles for introduction of the gene editing machinery .....	63
4.	Pseudotyping of viral vectors or virus-like particles .....	63
	<b>Scientific background and objectives .....</b>	<b>65</b>
	<b>Results.....</b>	<b>69</b>
	<b>Manuscript 1.....</b>	<b>71</b>
	<b>Manuscript 2.....</b>	<b>107</b>
	<b>Discussion and perspectives .....</b>	<b>163</b>
	<b>REFERENCES .....</b>	<b>175</b>
	<b>Annexes.....</b>	<b>187</b>
	<b>Article 1 .....</b>	<b>189</b>
	<b>Article 2.....</b>	<b>215</b>
	<b>Curriculum Vitae.....</b>	<b>227</b>
	<b>List of publications .....</b>	<b>231</b>
	<b>Résumé .....</b>	<b>235</b>

## ACKNOWLEDGEMENT

I would like to thank Dr. Vincent Goffin and Dr. Gijssbers Rik for agreeing to be rapporteurs in my this thesis jury and for taking the time to read this manuscript and evaluate my thesis work.

I would like to thank Dr. Kai Kretzschmar for accepting to attend my thesis defense as an examiner. I want to thank him for following me during these three years. I also want to thank him for the inspiration he gave me at the beginning of my thesis, and for some valuable advice to keep in mind when you do scientific research. One of them is "Don't reinvent the wheel".

Je tiens à remercier la présidente de mon jury, Dr. Els Verhoeyen. Je tiens à te remercier pour tout ce que tu as fait pour moi. S'il reste encore quelques braises de la jeune flamme scientifique qui brûlait en moi, c'est en grande partie grâce à toi. Merci pour tout Els.

Je tiens à remercier mon directeur de thèse, le Dr. Frédéric Bost pour m'avoir donné l'opportunité de réaliser ma thèse dans son équipe. Merci pour le temps que tu m'as accordé. Merci de m'avoir permis de réaliser ma thèse avec autant d'indépendance. Merci pour ton soutien face aux épreuves que l'on peut rencontrer dans la thèse. Tout n'aura pas été rose, mais on a réussi à s'en sortir.

Thank you to Pr. Hans Clevers for allowing me to do an internship in his laboratory. I guess you will never read this, but thank you for all the exciting articles you have published.

Thank you Else, Joep and Maarten. Thank you Else for allowing me to learn so much in such a short time. Thanks to Joep for giving me some tips and tricks. Thanks to Maarten for teaching me how to pick organoids. I hope to meet you again one day.

Merci à toi Nathalie pour ton soutien scientifique et humain. Merci pour tes conseils précieux. Merci pour les clés que tu m'as données pour évoluer dans des environnements « fluctuants ». Le tamis a beaucoup aidé.

Merci à Mounia pour tes conseils et ton soutien.

Merci Michel et Yingbo pour votre énergie. C'était un plaisir de pouvoir vous transmettre quelques trucs. J'espère que vos thèses se passeront bien pour tous les deux. Vous avez tous les deux appris très vite le CRISPR ! Bien joué ;) N'hésitez pas à monter des projets sous-marins (comme les appelle Fred), ce seront les plus funs ! 待来日, 江湖再见! أراك لاحقاً يا ميشيل

Merci à toi Abigaïl, c'était vraiment chouette de travailler avec toi ! Merci pour ta bonne humeur et ton sourire quotidien, ils n'ont pas de prix ! J'espère qu'on pourra se recroiser après la thèse ;)

Je tiens à remercier certaines personnes de passages dans l'équipe 5, en particulier Marc et Carlier #l'onco\_et\_l'uro. C'était vraiment sympa de vous avoir tous les deux au labo. « Un excellent investissement » comme diraient certains. Un conseil, s'il vous venait à l'idée de vouloir faire une thèse de science : ne travaillez pas pour la gloire, ce n'est pas rentable ;p

Merci à Lucilla et Monique. C'était vraiment génial d'avoir pu travailler avec vous ! Et tout le reste était encore plus fou !! J'ai vraiment hâte de vous revoir ! Lucilla, je viendrais te voir à Paris pour sûr ! Et Monique, dès que je peux m'acheter un billet d'avion pour le Brésil, c'est avec grand plaisir que je viendrais visiter Curitiba :D

Merci à Julie pour ces trois ans de thèses passés avec toi (ou plutôt un an et demi comme tu le dis XD). Cependant, je n'ai toujours pas pu voir ton fameux tatouage XD Plus sérieusement, merci à toi. Merci pour le soutien que tu m'as apporté. Merci pour m'avoir appris à relativiser sur certaines choses. Merci pour ton sourire, et ton énergie. Tu me manqueras, c'était vraiment chouette ! Envoie des photos quand tu seras en Guadeloupe ! ;D

Sa..lut 🙌 t'aurais de la T4 ? Merci Adrien. Je ne sais pas si j'aurais pu finir sans toi... J'espère quand même que tout ce qui s'est passé ne t'empêchera pas de t'épanouir à fond dans la thèse. Je sais ce que tu me dis à propos de la médecine. Je suis persuadé que tu serais excellent dans ce domaine, mais je pense qu'en science aussi. Les mois de janvier et février 2020 ont été parmi les plus cools de la thèse. Si tu hésites où aller en post-doc, essayes de voir du côté de chez Lancaster ;) Tu me manqueras vieux Krugos.

Ana, thank you for everything! Thank you for the lovely brunches ! Thank you for your positivity and for your many advices ! I'm really looking forward to visiting London with you ;) I also really want to discover South Africa ! We have to plan to go to festivals for 2022, as you said, it's the year of music ! See you soon

Merci à toi Marie pour ton énergie de tous les jours ! Merci pour toutes ces heures de microscopie gratuite ;) J'essayerais bien de faire de la boxe moi aussi, ça a l'air cool ! À bientôt.

Merci à Dominique pour avoir toujours gardé son calme malgré toutes mes bêtises dans les commandes ! « Encore des oligos » ;)

Sofiaaaa ! Merci pour tout ! C'était vraiment génial quand tu étais à Nice ! J'ai hâte de pouvoir te rendre visite à Paris ! Sto imparando l'italiano, mais il me reste encore un peu à apprendre ;p on se voit vite

Serana ! Merci à toi pour tout !! Hâte de te voir à Lyon !!

Duuude !! Chuck thank you for teaching me to speak American! Thank you for everything we've experienced together so far! Thank you for so many things! See you soon! Now that I have finished the thesis, we have to hang out!

Congratulations Dr. Marissa! We did it! My American big sister!! I can't wait to drink mojitos with you again! Thanks for everything! See you soon !

Thank you for everything Nikooos ! Looking forward to party with you! "Guys, I know a place"

Juan, merci pour tout ! Merci pour tout le soutien que tu m'as apporté quand j'en avais besoin. Merci mon ami, j'espère qu'on pourra se revoir dans un environnement plus 'relaxé'. Looking forward to party with you! Je sais pas pourquoi je parle anglaise XD j'ai pas bu cette fois ! See you soon

Thank you Adrianna and Manuel! Good luck Adrianna for the end of the thesis! It's almost done!

Merci à Serge aussi!

Merci à Océane. C'était cool l'escalade ! Dommage que le COVID nous ait stoppé ! Bon courage pour la suite

Merci à Philippe Gual pour son soutien et son expérience dans le monde scientifique. Tes conseils ont été très précieux.

Merci à Émilie, merci pour ton sourire chaque jour.

Merci à Rodolphe et Stoyan.

Merci à mon boulanger qui me réservait une baguette chaude même à 22h quand je revenais tard du labo ! Ça n'a pas de prix !

Ghania, je ne t'ai pas oublié ;p Je n'arrive pas à croire que ça fait déjà 8 ans qu'on se connaît ! Mon dieu, le temps passe trop vite !! Tu le sais déjà, mais merci pour tout Ghania. Tu es ma meilleure amie depuis tant d'années, merci. Je t'avoue que j'écris ces remerciements, alors qu'il est 2h54 du matin XD Ce n'est certainement pas la bonne heure pour faire ça xdx. À très vite

Emma, t'avoir comme élève était l'une des choses les plus fantastique de la thèse. Tu sais déjà tout Emma. Je suis ravie que tu sois chez Clevers et Anne Rios of course. Ces quatre années se passeront très bien, j'en suis persuadé. Je ne m'étalerai pas plus. Je t'embrasse. Victor  
Ps : merci pour le burp de bienvenue

Merci à Paquebottte et Twinkos.

Poutoux à Sanjay ;)

Énormes poutoux les padres, A et Lu !!! Oune bisoute

## ABBREVIATIONS LIST

A1AT	Alpha-1-Antitrypsine
AAV	Adeno-Associated Viruses
ACE2	Angiotensin-Converting Enzyme 2
ADP	Adenosine-Diphosphate
AMACR	Alpha-Methylacyl-Coa Racemase
AMP	Adenosine Monophosphate
APC	Adenomatous Polyposis Coli
AR	Androgen Receptor
ARP	Actin-Related Protein
ASAH1	N-Acylsphingosine Amidohydrolase 1
ASC	Adult Stem Cell
ATP	Adenosine Triphosphate
BaEV	Baboon Endogenous Retrovirus
BAP1	BRCA1 Associated Protein-1
BMP	Bone Morphogenetic Protein
BMP	Bone Morphogenetic Protein
CBD	Catenin Binding Domain
CDC42	Cell Division Cycle 42
CFTR	Cystic Fibrosis Transmembrane Conductance Regulator
CHGA	Chromogranin A
CIP	Contact Inhibition Of Proliferation
CK	Cytokeratin
CRISPR	Clustered Regularly Interspaced Palindromic Repeats
crRNA	Crispr Rna
DECODR	Deconvolution Of Complex DNA Repair
DHT	Dihydrotestosterone
DNA	Deoxyribonucleic Acid
DSB	Double Strand Break
DUB	Deubiquitinase
EC	Extracellular Cadherin
ECM	Extracellular Matrix
EDC	Endocrine Disruptor
EGF	Epidermal Growth Factor
EGFR	Epidermal Growth Factor Receptor
EMT	Epithelial-Mesenchymal Transition
EpCAM	Epithelial Cell Adhesion Molecule
ESC	Embryonic Stem Cell
ETS	E26 Transformation-Specific
FGF	Fibroblast Growth Factor
GDP	Guanosine Diphosphate
GFP	Green Fluorescent Protein

GTP	Guanosine Triphosphate
HDR	Homology Directed Repair
HECT	Homologous To The E6-AP Carboxyl Terminus
HEK	Human Embryonic Kidney
HGF	Hepatocyte Growth Factor
HIV	Human Immunodeficiency Virus
IDLV	Integrase-Deficient Lentivirus
IGF	Insulin-Like Growth Factor
INDEL	Insertion/Deletion
IQGAP1	Ras Gtpase-Activating-Like Protein
JMD	Juxtamembrane Domain
KI	Knock-In
KO	Knockout
LDL	Low Density Lipoprotein
LDLR	Low Density Lipoprotein Receptor
LV	Lentivirus
MDM2	Murine Double Minute 2
MET	Mesenchymal-Epithelial Transition
MLV	Murine Leukemia Virus
MSI	Microsatellites Instability
NF1	Neurofibromatose 1
NHEJ	Non-Homologous End-Joining
NK	Natural Killer
NLS	Nuclear Localization Sequence
NMT	N-Myristoyltransferase
NPF	Nucleation Promoting Factors
PAM	Protospacer Adjacent Motif
PEG	Poly(Ethylene Glycol)
PhIP	2-Amino-1-Methyl-6-Phenylimidazo[4,5-B]Pyridine
PIN	Prostatic Intraepithelial Neoplasia
PSC	Pluripotent Stem Cell
PTEN	Phosphatase And TENsin Homolog
RAC1	Ras-Related C3 Botulinum Toxin Substrate 1
RAD23	Rad23 Homolog A
Rho	Rhodopsin
Rho GDI	Rho Protein GDP Dissociation Inhibitor
RhoGEF	Rho Gtpase Guanine Nucleotide Exchange Factors
RhoGEF	Rho Gtpase-Activating Proteins
RING	Really Interesting New Gene
RNA	Ribonucleic Acid
RNF26	Ring Finger Protein 26
RNP	Ribonucleoprotein
ROCK	Rho-Associated Coiled-Coil Kinase

ROS	Reactive Oxygen Species
RPS27A	Ribosomal Protein S27a
RSV	Rous Sarcoma Virus
RVD	Repeat-Variable Diresidues
SARS	Severe Acute Respiratory Syndrome
sgRNA	Single Guide RNA
SHH	Sonic Hedgehog
SMAD	Acronym From The Fusion Of Caenorhabditis Elegans Sma Genes And The Drosophila Mad, Mothers Against Decapentaplegic
SMTNL	Smoothelin Like
SNV	Spleen Necrosis Virus
SQSTM1	Sequestosome 1
tacrRNA	Trans-Activating Crrna
TALENs	Transcription Activator-Like Effector Nucleases
TCF	T Cell Factor
TGF	Transforming Growth Factor
TM	Transmembrane Domain
TMPRSS2	Trans-Membrane Protease Serine 2
TP53	Tumor Protein 53
UBA1	Ubiquitin Like Modifier Activating Enzyme 1
UBA52	Ubiquitin A-52 Residue Ribosomal Protein Fusion Product 1
UBB	Ubiquitin B
UBC	Ubiquitin C
UBD	Ubiquitin-Binding Domain
UBL	Ubiquitin Like Proteins
UBTD1	Ubiquitin Domain-Containing Protein 1
UGE	Urogenital Sinus Epithelium
UGM	Urogenital Sinus Mesenchyme
VEGF	Vascular Endothelial Growth Factor
VH	Vinculin Homology
VLP	Virus-Like Particles
VSVG	Vesicular Stomatitis Virus G Protein
WASP	Wiskott- Aldrich Syndrome Protein
WT	Wild Type
YAP	Yes-Associated Protein
ZFNs	Zinc Finger Nucleases

## LIST OF FIGURES

Figure 1. Scheme of the anatomy of an adult human prostate.....	15
Figure 2. Simplified representation of the stages of prostate organogenesis.....	16
Figure 3. Differentiated adult human prostate epithelium. ....	19
Figure 4. Cell progenitors and the different cell types derived from them present during prostate organogenesis.....	20
Figure 5. Representative stages of adenocarcinoma progression in the prostate gland..	22
Figure 6. The junctional complexes and adhesion molecules of a polarized epithelial cell are distributed at the cell-matrix interface and at cell-cell contacts. ....	23
Figure 7. Adhesion junctions are composed of clusters of the transmembrane protein E-cadherin. ....	24
Figure 8. Scheme representing a model for the formation of adherens junctions in migrating cells. ....	30
Figure 9. Scheme representing a model of the maturation of adherens junctions in migrating cells. ....	31
Figure 10. Schema representing a model of stable epithelial junctions mediated by E-cadherin. ....	32
Figure 11. Schema representing a model of E-cadherin inhibition by EpCAM. ....	33
Figure 12. Process and partner involved in ubiquitination.....	36
Figure 13. Establishment of organoids derived from ASCs.....	41
Figure 14. Applications of the organoid model. Organoids can be used to model disease. ....	43
Figure 15. Engineering strategy for organoids.....	47
Figure 16. Simplified model of prostate organoid growth.. ....	49
Figure 17. Overview of the possible repair and recombination reactions performed by the cellular machinery after a nuclease-induced DSB.....	50
Figure 18. Simplified representation of the structure of zinc finger nuclease (ZFN) and transcription activator-like effector nuclease (TALEN). ....	51
Figure 19. Type II CRISPR-Cas system.. ....	53
Figure 20. RNA guided DNA cleavage of genomic DNA.....	54
Figure 21. Delivery strategies for gene-editing studies.....	56
Figure 22. Non-viral methods for delivery of CRISPR-Cas9 components in organoids.	57
Figure 23. Lentiviral production process and transduction of a targeted cell. ....	62
Figure 24. Knock-in of a reporter gene to reveal nanoblade induced-KO in organoids. ....	169
Figure 25. Simplified representation of the anchoring of UBTD1 to the cytoplasmic membrane. ....	170

## LIST OF TABLES

Table 1. CRISPR delivery system: common feature, advantages and limitations. ....	50
Table 2. Gene editing efficiency in organoids. ....	115

## **INTRODUCTION**



# Prostate

The prostate is a walnut-sized organ located just below the bladder and surrounding the urethra (**Figure 1**). It consists of a network of ducts composed of a pseudostratified epithelium surrounded by a contractile stroma<sup>1</sup>. The prostate is an accessory male sex gland that secretes prostatic fluid which contributes to ejaculate, and therefore contributes to male fertility. The development of the prostate takes place before birth. Its maturation and functionalization occurs during puberty under the influence of androgen. Interestingly, this organ is highly susceptible to oncogenic transformations in older men. Here, we describe the mechanisms involved in the development of the prostate and the cells that compose the epithelium. The oncogenic processes will also be discussed.

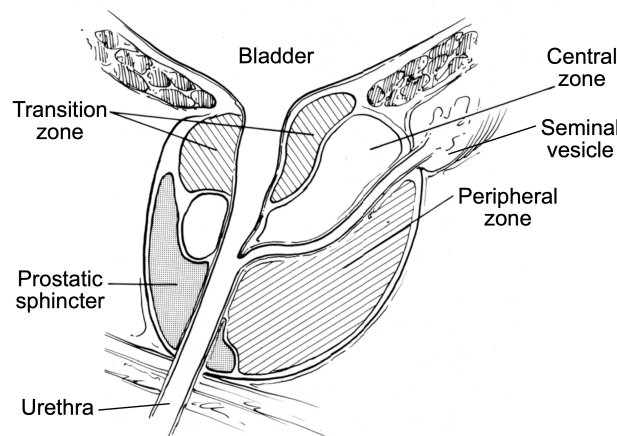


*Figure 1. Scheme of the anatomy of an adult human prostate. Modified from McNeal, J.E. 1969, and Toivanen et al., 2017.*

## I. Prostate development

The prostate development takes place during embryogenesis. It can be described in four phases (**Figure 2**). The first phase corresponds to the induction of the prostate under the direct and indirect influence of androgens. The second androgen-dependent stage corresponds to the budding of the urogenital sinus epithelium (UGE) into the urogenital sinus mesenchyme (UGM). This corresponds to the emergence of the epithelial ducts. The third phase is the development of the branched network of ducts. The fourth and final phase, which takes place at puberty, corresponds to the differentiation and functionalization of the epithelium under the dependence of androgens<sup>1</sup>.

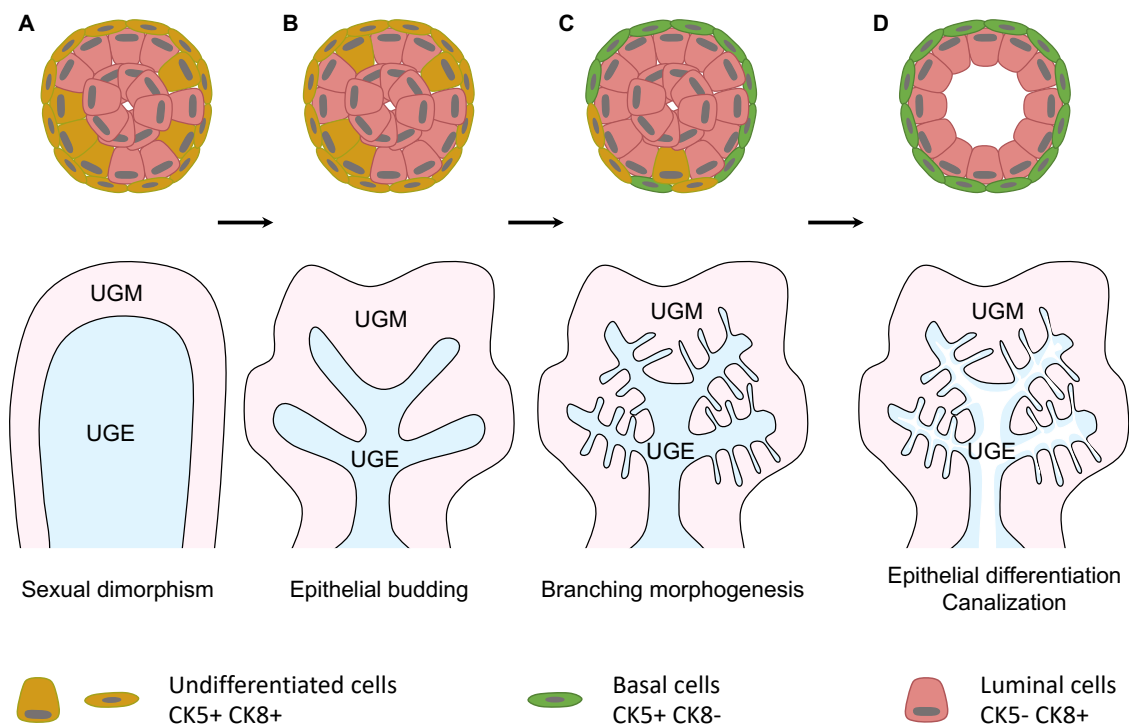


**Figure 2. Simplified representation of the stages of prostate organogenesis.** The prostate organogenesis is divided into four stages: (A) sexual dimorphism, (B) epithelial budding, (C) branching morphogenesis and (D) epithelial differentiation. The upper part represents the epithelial tissue and its composition during the four stages of differentiation. It must be noted that the UGE is not clearly defined in the first stage (A); however, cells positive for the CK5 and CK8 markers are present. The lower part represents in a simplified way the general evolution of the UGE, UGE and UGM during the four developmental stages. Scheme inspired by Toivanen et al., 2017.

### A. Prostate induction

Sexual dimorphism of the urogenital sinus (UGE) results in the formation of the prostate at the expense of a portion of the vagina in women. The transformation of the UGE into the prostate is under the influence of circulating androgens. These are secreted by the Leydig cells in the testis, about 9 weeks after the beginning of pregnancy. Testosterone is then converted in the UGE into dihydrotestosterone (DHT) by the enzyme  $5\alpha$ -reductase. DHT binds to the androgen receptor (AR) which then acts as a transcription factor. Interestingly, the formation of the prostate from the UGE is independent of genetic sex. Indeed, XX mouse embryos develop a prostate if sufficient levels of androgens are administered<sup>2</sup>. Importantly, paracrine signals from the UGM to the urogenital sinus epithelium (UGE) are also essential for prostate formation. It was shown that combination of a bladder epithelium with UGM induced prostate tissue formation<sup>3</sup>.

AR is essential in UGM to promote UGE induction. It was shown by tissue recombination that UGMs mutant null for AR did not induce the formation of wild-type UGE<sup>4</sup>. Conversely, AR is also required in UGE to induce differentiation of mesenchyme into smooth muscle<sup>5</sup>. Furthermore, AR expression in the UGE is essential for the subsequent differentiation of the prostatic epithelium.

AR-mediated hormonal pathways appear to be essential for prostate induction. Its expression in the mesenchyme is required for prostate induction and in the epithelium AR is required for differentiation of the epithelium and mesenchyme.

## **B. Budding of the UGE in the UGM**

The second phase characterized by the budding of the UGE in the UGM is androgen dependent. However, the mechanism of dialogue between the UGM and the UGE remains unclear. In particular the molecular signaling resulting from AR activation in the UGM. As recapitulated in a review published in 2017, there are two models to explain budding induction<sup>1</sup>.

The first model relies on andromedins. Andromedins are growth or signaling factors that are supposed to be upregulated upon AR activation in the UGM. These andromedins would be expressed in the UGM under the influence of androgens and then act in the UGE, where they would induce epithelial budding. Fibroblast growth factor 10 (*FGF10*) can induce epithelial budding in the presence of DHT<sup>6</sup>. However, *FGF10* is not really up-regulated by androgens. Nevertheless, the deletion of *FGF10* prevents epithelial budding. This suggests that this factor participates in the budding process without being the initiator.

Some studies have looked at the involvement of ligands involved in the Wnt signaling pathway, however, none of them seem to fit the model mentioned above.

The second model suggests that UGE budding is constitutive and independent of androgens. In this model the mesenchyme would control the budding by acting as a barrier. Upon differentiation of the mesenchyme into smooth muscle cells under the influence of androgens, budding would be stopped. Epithelial buds could no longer grow in these differentiated regions of the UGM.

These two models are not exclusive. Indeed, the epithelium can grow and be stimulated by paracrine signaling factors emitted by the UGM. In parallel, androgens can induce the differentiation of the UGM, which acts as a final brake on the growth of the epithelium. The emergence of differentiated smooth muscle cells could act as a feedback loop.

Beyond the general mechanisms inducing the budding of epithelial cords in the UGM, the specification of the epithelium is also finely regulated during this phase. Several studies focused on the role of the winged-helix transcription factor *FOXAI*. Using a model of transplantation of prostate rudiments KO for *FOXAI* into WT mice, the phenotypic consequences could be analyzed. *FOXAI* deletion in the prostate leads to basal cell hyperplasia with the absence of luminal cells and consequently to the absence of lumen formation in the epithelial cords. An increase in the number of cells co-expressing basal and luminal markers simultaneously was observed. *FOXAI*-mediated chromatin opening in luminal prostate cells is essential for binding of the transcription factor AR to its targeted promoters and induce cell differentiation<sup>7-9</sup>.

Downstream in the *FOXAI* signaling pathway is the transcriptional regulator *HOXB13*. Deletion of this regulator in mice only minimally affects the development of the anterior and dorsolateral lobes but disrupts their function. As described in a study published in 2003, *HOXB13* KO disrupts the final differentiation and thus functionality of prostate luminal cells. In this case, prostate luminal cells still express AR in the nucleus but display a loss of polarity<sup>10</sup>.

### **C. Morphogenesis of the epithelial branching duct network**

The budding stage, which comprises the development of epithelial ducts in the prostatic mesenchyme, is followed by the morphogenesis of a branched network of epithelial ducts with distal outgrowth. This stage results in the formation of the characteristic zones of the prostate, i.e. transition zone, central zone and peripheral zone.

The development of this network of branched epithelial ducts was shown to be partly controlled by the protein Sonic hedgehog (SHH). Studies showed that UGE budding in the mesenchyme was not affected by SHH deletion. However, channel branching required the presence of SHH<sup>11</sup>.

Other studies have focused on the bone morphogenetic protein (BMP) pathway in the control of channel network branching. One study showed that addition of BMP4 decreases the number of channels, conversely partial deletion of BMP4 increases branching morphogenesis<sup>12</sup>.

The formation of branched networks of epithelial channels is thus coordinated by several signaling pathways. However, the coordination of the BMP and sonic hedgehog pathways remains unsolved. It should also be noted that this branching phase seems to be independent of androgens<sup>13-15</sup>.

It was indeed shown that androgen deletion did not prevent channel growth at this stage<sup>13</sup>. Moreover, the administration of androgens did not promote either the growth of these branched ducts<sup>1</sup>.

### **D. Differentiation and functionalization of the prostate epithelium**

As mentioned above, the maturation of the prostate takes place during puberty, under the dependence of androgens. The epithelial cords that compose the prostate will undergo the canalization mechanism. The basal and epithelial cells will differentiate and form a mature and functional gland.

The mechanisms of canalization that take place in the prostate epithelial cords are not yet totally understood. As observed in the mammary glands, where channeling occurs partly by apoptosis, studies have observed apoptotic phenomena in the center of the epithelial cords in rats during the canalization phase. However, the signaling pathways involved are not clear. Future studies will be necessary to elucidate which actors are involved in this process.

Apart from the canalization phenomenon, the cell types involved and their appearance during this phase require more study (**Figure 3**).

The epithelial cords are composed of undifferentiated multipotent cells co-expressing markers of basal and luminal cells. This cell population was positive for cytokeratins 19 and 8<sup>16</sup>.

After induction of differentiation by androgens, we find three main cell types in the prostate epithelium: luminal cells (AR, CK8), basal cells (P63, CK5, CK14), and neuroendocrine cells (CHGA).

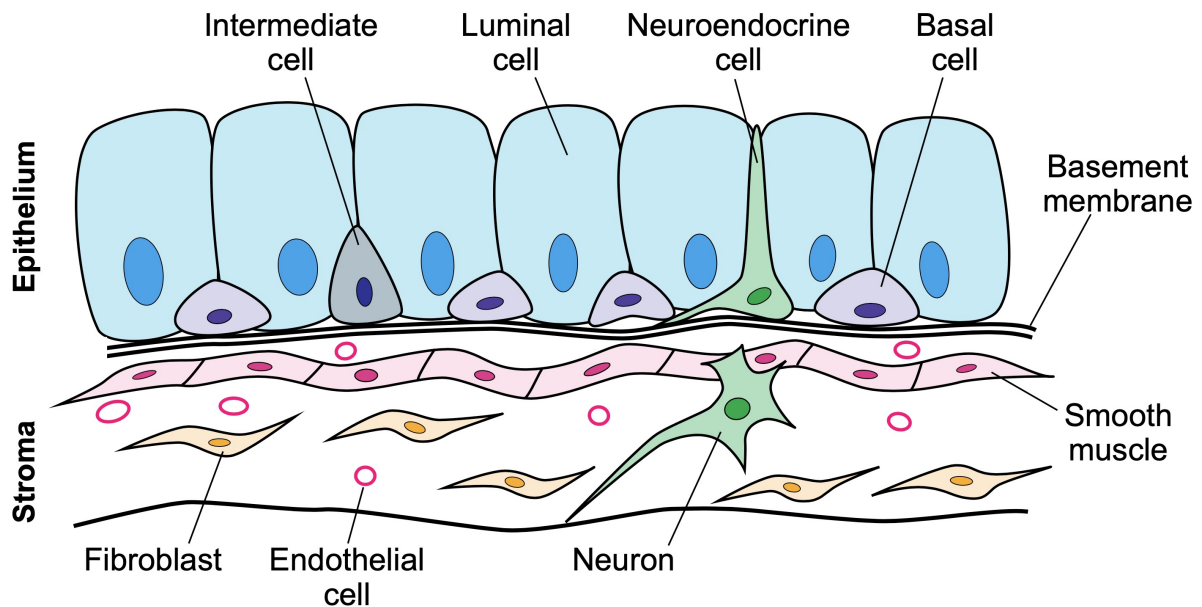


**Figure 3. Differentiated adult human prostate epithelium.** The prostate epithelium is composed of luminal secretory columnar cells and basal cells. Rare neuroendocrine cells are found in the basal cell layer. The epithelium is surrounded by a stroma composed of smooth muscle cells, fibroblasts, neurons, and endothelial cells forming blood vessels. Modified from Toivanen 2017.

As shown in studies published by Blanpain's group<sup>17</sup>, postnatal prostate development is ensured by basal multipotent cells capable of giving rise to basal, luminal and neuroendocrine cells and also unipotent basal and luminal progenitors. They identified bipotent and unipotent basal progenitors and also basal cells committed to luminal differentiation. The model of cell lineage that occurs after birth consists of a bipotent basal progenitor giving 50% of bipotent basal progenitors and 50% of progenitors committed to luminal differentiation. These luminal progenitors subsequently have the ability to proliferate and to regenerate the luminal cell pool. During homeostasis, in adulthood, basal cells will self-renew like luminal cells.

Studies based on single-cell transcriptomic analyses showed the existence of a termed type C luminal cell population (Luminal-C) with a high regenerative capacity<sup>18</sup>. In addition, a study published in 2020 reported a regenerative potential of all luminal cell type. They showed that both differentiated luminal cells and stem-like luminal cells were able to regenerate the prostate after androgen ablation<sup>19</sup>.

Recent studies have shown that CD49<sup>+</sup> basal cells cultured *ex vivo* can yield both basal and luminal cells. Similarly, CD26<sup>+</sup> luminal cells can give basal and luminal cells. Nevertheless, the proportion of basal and luminal cells varied depending on the cell type of origin<sup>20</sup>.

Considering these recent studies, the models proposed so far do not take into account all cell types present in the prostate epithelium, and their regenerative capacity (**Figure 4**). Future studies will be needed to fully elucidate and understand the significance of these different cell lineages.

As described above, many studies have focused on luminal and basal epithelial cells, nevertheless some studies have focused on neuroendocrine cells and their origin. Some studies showed that enteroendocrine cells could have an epithelial origin, others showed a possible caudal neural crest origin<sup>1</sup>. Indeed, neuroendocrine cells express chromogranin A, which is found in neural crest ectoderm<sup>1</sup>. Furthermore, cell lineage analyses published in 2017 reveal that neuroendocrine cells are derived from the neural crest<sup>21</sup>.

Overall, the cell types composing the 'static' prostate are now fairly well characterized; nevertheless, studies on cell lineage are still needed to fully understand prostate homeostasis.

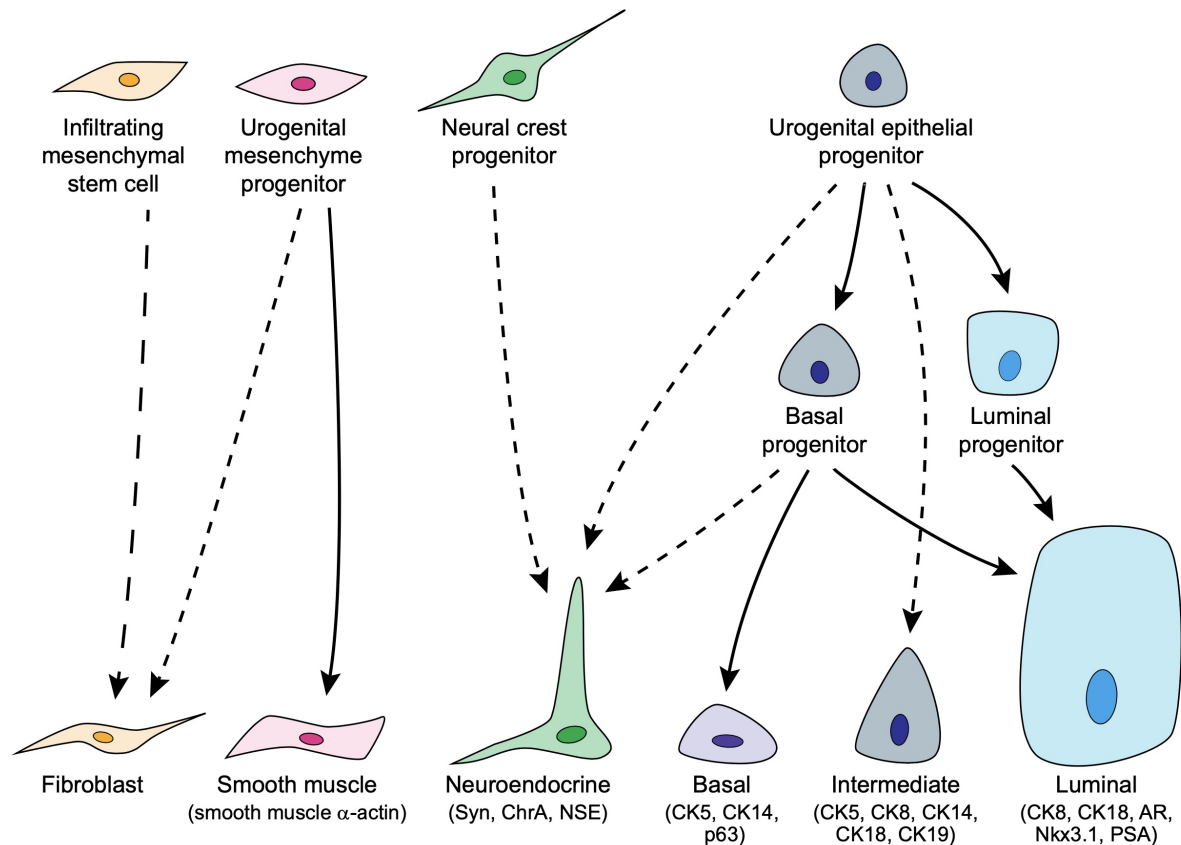


**Figure 4. Cell progenitors and the different cell types derived from them present during prostate organogenesis.** Mesenchymal stem cells differentiate upon the action of androgens. The undifferentiated epithelial progenitors give basal progenitors and luminal progenitors that ensure the renewal and homeostasis of the prostate gland. Neuroendocrine cells originate from neural crest progenitors. Modified from Toivanen 2017.

## II. Prostate Cancer

Prostate cancer is an age-related disease. A man under 40 has a one in 10,000 chance of developing cancer; a man over 60 has a one in seven chance (American Cancer Society). However, age is not the only factor in the development of prostate cancer. Environment, lifestyle and diet can also have an influence. Here we briefly detail some of the risk factors that can promote the development of cancer. We also explain the different forms of prostate degeneration, more or less linked to the appearance of cancer.

## **A. Risk factors for cancer**

The incidence of prostate cancer increases with age. As mentioned in previous studies, the incidence of prostate cancer increases from 60 cases per 100,000 men under the age of 55 to 900 cases per 100,000 men aged 65 to 74.

Some studies showed that heredity could be a risk factor for prostate cancer. Indeed, the risk of developing prostate cancer is 2.5 to 3 times higher in men whose father or brother had prostate cancer.

Epidemiological studies have looked at diet and lifestyle as risk factors for prostate cancer. Indeed, one study showed a 10-fold difference in the onset of cancer between Western and Asian men. This study reported that the gap disappeared when Asian populations migrated to Western countries. Diet and lifestyle could therefore play a role in the incidence of this cancer. More precisely, some studies have looked at inflammation as a risk factor for cancer. One study showed that chronic administration of potent heterocyclic amine PhIP in rodents induced inflammation and led to prostate hyperplasia<sup>22</sup>.

Endocrine disruptors (EDCs) have also been identified as increasing the chances of developing prostate cancer. As mentioned in several studies, chlordecone significantly increases the risk of prostate cancer<sup>23</sup>.

Other studies focused on oxidative stress and its influence on DNA damage. Indeed, oxidative stress results from an imbalance of reactive oxygen species (ROS) in the cell and can lead to DNA damage<sup>24</sup>. As mentioned in studies, the prostate is sensitive to oxidative stress, which is probably a consequence of inflammation.

## **B. Prostatic Intraepithelial Neoplasia (PIN) and Cancer**

As mentioned earlier, men tend to develop more prostate cancer with age. Nevertheless, older men can develop prostatic intraepithelial neoplasia, which is considered a precursor to cancer. Prostatic intraepithelial neoplasia (PIN) is characterized by hyperplasia of the luminal. An increased level of luminal cell proliferation is usually observed in advanced PINs<sup>1</sup> (**Figure 5**).

Prostate cancer is a cancer displaying great phenotypic heterogeneity, however, more than 95% of prostate cancers are adenocarcinomas. Prostate adenocarcinoma is also characterized by hyperproliferation of luminal cells and disappearance of basal cells.

From a clinical point of view, the different grades of prostate adenocarcinoma are classified according to the Gleason score. The Gleason score is a prognostic system based on the architecture of the gland. Cancers with a high Gleason score are more aggressive. In advanced adenocarcinomas, basal markers (P63, CK5) are not found, while luminal markers (AMACR) are overexpressed.

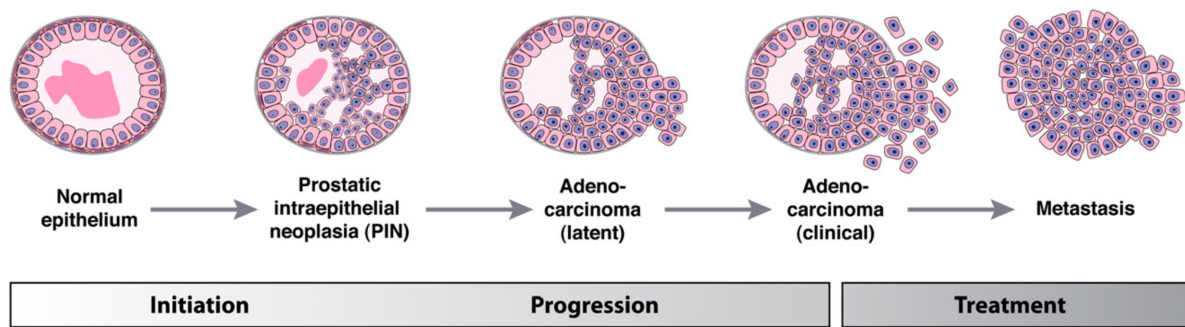


**Figure 5. Representative stages of adenocarcinoma progression in the prostate gland.** Modified from Shen *et Abate-Shen* 2010.

## Cell Junction

In a multicellular organism, epithelial tissues act as barriers that separate either the organism from the outside world or different compartments of the body. Two types of epithelium can be distinguished: the simple epithelium and the stratified epithelium. The simple epithelium is composed of a monolayer of joined and polarized cells. They are found in organs prone to absorption, secretion and filtration such as the intestine or the kidneys. Stratified epithelia are composed of multiple layers of cells, such as the skin and cornea. The epithelium regulates the movement of fluid, molecules and immune cells that pass between the joined cells. The characteristics of a simple epithelium include the presence of cilia on the apical pole of the cells and the numerous junctions located laterally at the cell-cell contact and at the basal membrane with the extracellular matrix (**Figure 6**). The lateral junctional complexes present at the apical pole of the epithelial cells include the adhesion junctions and the tight junctions which play respectively a major role in the cell-cell adhesion, and the maintenance of the impermeability of the epithelium. These two types of junctions are connected to the actin cytoskeleton coupled to myosin.

Here we describe the processes of adhesion junction formation, as well as the composition and connections of these junctions to the actin cytoskeleton.

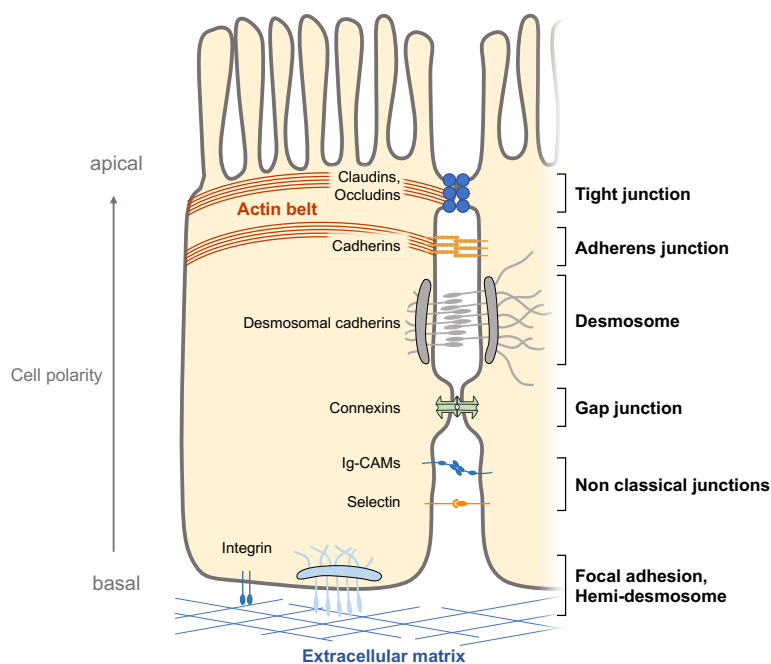


**Figure 6.** The junctional complexes and adhesion molecules of a polarized epithelial cell are distributed at the cell-matrix interface and at cell-cell contacts. Tight junctions control the permeability of cell-cell junctions, and the integrity of the epithelial barrier. Tight junctions, like adherens junctions, are connected to the contractile actomyosin belt. Adhesion junctions supported by E-cadherins coupled to the cytoskeleton ensure the strength of cell-cell adhesion. Desmosomes are composed of desmosomal cadherins associated with intermediate filaments. Gap junctions connect the cytoplasmic compartments of two adherent cells. Non classical junctions group different adhesion molecules performing homophilic or heterophilic interactions. Focal adhesion and hemidesmosomes connect and anchor the epithelial cell to the extracellular matrix.

## I. Composition of the adherens junction complex

E-cadherin-dependent adherens junctions associate with numerous proteins that finely regulate their formation, maturation and stability. The core of proteins forming adherens junctions consists of cell adhesion molecules such as E-cadherin, catenins (e.g. p120,  $\beta$ -catenin,  $\alpha$ -catenin), and proteins associated with the regulation of the actin cytoskeleton<sup>25</sup>.

### A. E-cadherin

The cadherin family is composed of different transmembrane proteins associated or not with glycoproteins. These cadherins act on cell-cell junctions in a  $\text{Ca}^{2+}$  dependent manner. The cadherin family includes four categories: (1) the classical cadherins (E-, N- and P-cadherin), (2) the desmosomal ones (desmoglein and desmocollin), (3) the protocadherins and (4) other unconventional cadherins. Here we focus on E-cadherin, important for cell-cell junctions in epithelial tissues<sup>25</sup>.

E-cadherin was first discovered in 1977 by Takeichi's group<sup>26</sup>, where he established that V79 Chinese hamster lung cell agglutination depends on calcium-dependent cell-cell adhesion. In subsequent studies, antibodies targeting E-cadherin were shown to interfere with cell-cell adhesion.

The expression of E-cadherin is finely regulated and involved in processes of embryonic development, tissue remodeling and some pathologies such as cancer.

E-cadherin is expressed starting from the two-cell stage in a mouse embryo<sup>27</sup>. More recently, E-cadherin was shown to have a determining role in lumen formation in mouse blastocysts<sup>28</sup>. A major role of E-cadherin is its involvement in the contact inhibition of proliferation (CIP). The loss of cell junctions is part of the epithelial-mesenchymal transition (EMT). When E-cadherin is mutated or lost, cells continue to proliferate and begin to grow on top of each other as is often found in cancers. Subsequently, this allows the cell to acquire migratory capacity<sup>29</sup>.

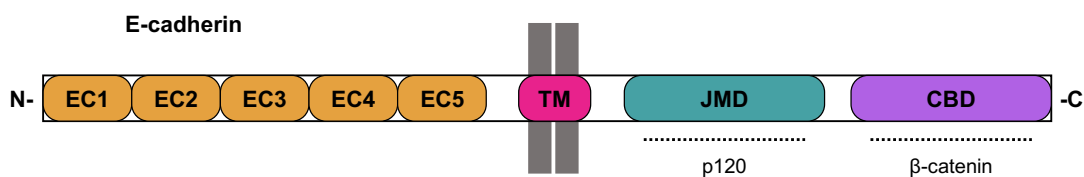


**Figure 7.** Adhesion junctions are composed of clusters of the transmembrane protein E-cadherin. The five N-terminal extracellular cadherin repeat domains (EC) form homophilic interactions with other E-cadherins in trans (with neighboring cells) or cis (in E-cadherin clusters). The cytoplasmic C-terminal domain includes two partner protein binding domains, i.e. the juxtamembrane domain (JMD) and catenin binding domain (CBD). The p120 and  $\beta$ -catenin proteins bind to domains contained in the JMD and CBD, respectively. The dots represent the binding sites of the proteins.

E-cadherin is composed of an extracellular N-terminal domain, a transmembrane domain (TM) and a cytoplasmic C-terminal domain (**Figure 7**).

The N-terminal extracellular domain is composed of five extracellular cadherin (EC) repeat domains. These EC domains can associate to form trans-cadherin interactions with neighboring cells<sup>30</sup> and associate in cis along the cell membrane to form E-cadherin clusters<sup>31</sup>. The association of these extracellular domains in cis or trans depends on conformational change mediated by Ca<sup>2+</sup> binding on each of the EC domains<sup>32</sup>. Studies showed that deletions of the EC1 domain disrupted trans binding between cadherins and prevented junction formation<sup>33</sup>. Other studies using antibodies neutralizing the EC4 and EC5 domains reported the absence of cell-cell junction formation<sup>34</sup>.

The cytoplasmic C-terminal domain is also essential for the functionality of E-cadherin. This cytoplasmic domain is composed of a juxtamembrane domain (JMD) and a catenin binding domain (CBD). These two domains alone are responsible for E-cadherin trafficking, intracellular signaling and control of the underlying actin cytoskeleton. The JMD domain contains a binding domain (CH2) to catenin p120 that disrupts cell junction formation if deleted<sup>35</sup>. The CBD contains the CH3 domain to which  $\beta$ -catenin binds.

## **B. Catenins**

The connection of E-cadherin with the actin cytoskeleton and signaling pathways is mediated by a family of proteins called catenins. This family includes p120,  $\beta$ -catenin and  $\alpha$ -catenin.

### **1. p120-catenin**

The p120 protein was discovered in 1977 as a substrate for Src tyrosine kinase<sup>36</sup>. p120 is a protein encoded by a gene with four alternatively spiced exons. In addition, there are four transcription start sites, resulting in many possible isoforms. However, the function of these isoforms of p120 remain largely unexplored. Interestingly, not all isoforms of p120 are expressed in the same proportion in attached epithelial cells compared to mesenchymal cells<sup>37,38</sup>.

Functionality studies have established that p120 binds to the cytoplasmic JMD domain of E-cadherin and participates in the stabilization of E-cadherin at the cytoplasmic membrane<sup>39</sup>. It was shown that p120 was responsible for the formation of E-cadherin clusters in nascent adhesion junctions by homodimerizing while remaining bound to E-cadherin. This homodimerization was shown to be promoted by the dephosphorylation of residues located at the N-terminus of the protein<sup>40,41</sup>. Interestingly, it was reported that binding of p120 to the JMD domain of E-cadherin prevented the binding of E3 ligase, and thus prevented the degradation of E-cadherin<sup>40</sup>.

Another important role of p120 catenin is its interaction with members of the actin cytoskeleton regulator family, the Rho GTPases. It was indeed shown that the cytosolic free form of p120 could bind directly to RhoA and inhibit its activation<sup>42</sup>. It was also shown that p120 catenin interacted with regulators of Rho GTPases, guanine nucleotide exchange factors (RhoGEFs) and GTPase-activating proteins (RhoGAPs). At the formation of adherens junctions, cytosolic p120 interacts with RhoGEF, Vav2, which has the role of activating Rac1 and Cdc42 GTPases and inducing remodeling of the actin cytoskeleton<sup>43</sup>.

Catenin p120 thus has a primary and versatile role in the regulation of E-cadherin. For this reason, studies have investigated the role of p120 in pathologies involving changes in cell junctions, for example cancer<sup>44</sup>. Indeed, deletion of p120 *in vivo* in the oral cavity, esophagus, and forestomach results in invasive squamous cell cancer, desmoplasia, and inflammation indicating that p120 might be a tumor suppressor gene.

## 2. $\beta$ -catenin

$\beta$ -catenin is a central component of the E-cadherin-associated core complex. This 92 kDa protein was identified as being tightly associated with E-cadherin<sup>45</sup>. Today the interaction of  $\beta$ -catenin with the cytoplasmic CBD-CH3 domain of E-cadherin is known to be regulated by phosphorylation. It was reported that casein kinase II and glycogen synthase kinase 3  $\beta$  were responsible for phosphorylating the CBD domain of E-cadherin at serines 684, 686, and 692 which increased  $\beta$ -catenin/E-cadherin interactions<sup>46,47</sup>. On the other hand, phosphorylation of  $\beta$ -catenin tyrosines 489 and 654 disrupted the interaction with E-cadherin<sup>48</sup>. In the same study, it was also shown that phosphorylation of  $\beta$ -catenin tyrosine 142 decreased its interaction with  $\alpha$ -catenin.

Functionally, the binding of  $\beta$ -catenin to E-cadherin, which takes place in the endoplasmic reticulum, results in the transport of the complex via secretory pathways to the cytoplasmic membrane<sup>49,50</sup>. When associated with E-cadherin, at the cytoplasmic membrane,  $\beta$ -catenin interacts with  $\alpha$ -catenin. Nevertheless, this interaction can be decreased upon Ras GTPase-activating-like protein (IQGAP) binding to the  $\beta$ -catenin. At the initiation of adherens junctions the scaffold protein IQGAP can be activated to interact with the Rho GTPases Rac1 and Cdc42 by detaching from the  $\beta$ -catenin. This dissociation of IQGAP from the  $\beta$ -catenin then allows the re-association of  $\alpha$ -catenin with the  $\beta$ -catenin and thus the formation of the E-cadherin core complex necessary for the maturation of junctions<sup>51</sup>.

Beyond its role at the membrane,  $\beta$ -catenin acts as a transcription factor in the Wnt/  $\beta$ -catenin signaling pathway. When  $\beta$ -catenin is phosphorylated on its tyrosines, mentioned above, by BCL9-2, its affinity for E-cadherin and  $\alpha$ -catenin is decreased<sup>48</sup>. In this case, it is imported into the nucleus, and binds to the T cell factor (TCF) to promote transcription of Wnt target genes. This role of  $\beta$ -catenin is finely regulated by its ligation with proteins of the canonical Wnt pathway<sup>52</sup>. Interestingly, this pathway also controls the degradation of  $\beta$ -catenin. Indeed, the binding of  $\beta$ -catenin to the APC protein, participates in its degradation mediated by  $\beta$ -TrCP protein, upon binding with other partners<sup>52</sup>.

Additionally,  $\beta$ -catenin mutations or its overexpression played a role in several types of cancer, i.e. colorectal carcinoma, lung cancer or malignant breast tumors<sup>53</sup>.

## 3. $\alpha$ -catenin

$\alpha$ -catenin is a 102-kDa protein that has been identified as the link between  $\beta$ -catenin and the actin cytoskeleton<sup>32</sup>. The ability of  $\alpha$ -catenin to bind  $\beta$ -catenin<sup>25</sup> and actin filaments<sup>54</sup> suggested that a complex associating  $\alpha$ -catenin,  $\beta$ -catenin and actin filaments existed. Nevertheless, no such complex was identified *in vitro*<sup>55</sup>.

A study published in 2005 highlighted the role of  $\alpha$ -catenin as a molecular switch that binds the E-cadherin/ $\beta$ -catenin complex and regulates actin-filament assembly<sup>56</sup>. This study reported that  $\alpha$ -catenin can be in monomeric and homodimeric forms, and that these forms influence its

binding properties. When  $\alpha$ -catenin is in monomeric form, it binds more strongly to the E-cadherin/ $\beta$ -catenin complex, whereas in dimeric form, it will preferentially bind to actin filaments. The ability to change its binding properties by conformational change makes  $\alpha$ -catenin an allosteric protein. Furthermore,  $\alpha$ -catenin directly regulates the nature of the actin cytoskeleton by competing with the Arp2/3 complex, and thus preventing the branched polymerization of actin.

Even today, what controls the switch between monomeric and dimeric forms is not fully understood. It was reported that  $\alpha$ -catenin binds spontaneously to  $\beta$ -catenin and a 10-fold increased concentration of cytosolic  $\alpha$ -catenin was required to form homodimers and bind to actin. Nevertheless, it is likely that mechanisms such as phosphorylation are involved in this hetero - homo dimer switch<sup>57</sup>.

A study reported a role for  $\alpha$ -catenin in colon cancer<sup>58</sup>. They presented a model in which  $\alpha$ -catenin interacted with APC to regulate  $\beta$ -catenin degradation and repress Wnt targeted genes.

### **C. Vinculin**

Discovered in 1979<sup>59,60</sup>, vinculin is a 117 kDa cytoskeletal protein associated with cell-cell and cell-matrix junctions. It has 20-30% sequence homology with  $\alpha$ -catenin, which performs a similar function<sup>61</sup>. Vinculin is structured with helical bundles organized with a globular head at its N terminal part comprising four vinculin homology (VH) domains. The VH1 domain allows binding to  $\beta$ -catenin. Note that the VH1 domain overlaps with the domain allowing vinculin to homodimerize. The VH2 domain allows binding with  $\alpha$ -catenin or  $\alpha$ -actinin, and also allows vinculin to homodimerize. The VH3 domain allows it to bind to F-actin<sup>62</sup>.

Identified as a major protein for focal adhesion<sup>63</sup>, vinculin also plays a role in cell-cell contact. Although vinculin is not essential for the formation of adherens, downregulation or loss of vinculin reduces the strength of cell-cell junctions<sup>61</sup>. In addition, vinculin was found in the pool of proteins involved in the first step of junction formation<sup>64</sup>. Vinculin was also shown to be essential for the formation of adherens junctions in a model not expressing  $\alpha$ -catenin<sup>65</sup>.

A recent study showed the mechanical roles of vinculin/ $\beta$ -catenin interaction in adherens junction<sup>66</sup>. They showed that  $\alpha$ -catenin served as an initial activator of vinculin, which allowed vinculin to form a direct link between the E-cadherin/ $\beta$ -catenin complex and the actin cytoskeleton.

### **D. Arp2/3**

The Actin-related protein 2/3 (Arp2/3) complex is the main actor of the branching polymerization of the actin cytoskeleton. Arp2/3 is a complex formed by seven subunits ARP2, ARP3, ARPC1 to 5. The Arp2/3 complex binds to a parent actin filament and induces the nucleation of a new filament branched at an angle of 70° to the parent filament. The Arp2/3 complex is activated under the dependence of Nucleation promoting factors (NPFs), such as the Wiskott- Aldrich syndrome protein (WASP). WASP has a domain that allows it to bind to several Arp2/3 subunits and stabilize the whole complex in a so-called "close conformation".

Actin monomers bind to the domain of the WASP protein, and to the ARP2 and ARP3 subunits to begin nucleation of the new filament<sup>67</sup>.

In the context of cell junction formation, the Arp2/3 complex is responsible for branching the actin network contained in lamellipodia, responsible for establishing cell-cell contacts. When cell-cell junctions are initiated,  $\alpha$ -catenin homodimers prevent branching polymerization by competing with the Arp2/3 complex for binding to actin filaments.

Arp2/3 has been reported to be involved in several pathologies, such as idiopathic pulmonary fibrosis, where it represses human lung myofibroblast differentiation<sup>68</sup>.

## **E. Rho GTPase family**

Rho GTPases are a conserved family of signaling G proteins. Rho GTPases have been identified as actively regulating the actin cytoskeleton in many contexts, such as cell migration, or cell-cell junction establishment. Among this family, three members have been widely studied: RhoA, Rac1 and Cdc42. These G proteins are considered as molecular switches that oscillate between a GDP bound - inactive - and a GTP bound - active - form. When they are in their GTP bound form, they can bind to the membrane and perform their role by interacting with other cytoskeleton proteins<sup>69,70</sup>. The switch between the active and inactive form of Rho GTPases is regulated by a very complex system. This system contains at least 145 multidomain guanine nucleotide exchange factors (RhoGEFs) and GTPase-activating proteins (RhoGAPs). Rho GTPases are activated by RhoGEFs and inactivated by RhoGAPs<sup>71</sup>. When Rho GTPases are in GDP form, they can also be sequestered and inhibited by a Rho protein GDP dissociation inhibitor (Rho GDI)<sup>71</sup>.

### **1. Rac1 & Cdc42**

Ras-related C3 botulinum toxin substrate 1 (Rac1) and Cell division control protein 42 homolog (Cdc42) are proteins of the Rho GTPase family.

Their activities are finely regulated by GEFs and GAPs that switch them from GDP to GTP binding and vice versa. They are also regulated by scaffold proteins that control their activation locally. When p120 is in cytosolic form, it binds to Vav2 (GEF) which activates Rac1<sup>71</sup>.

Rac1-GTP and Cdc42-GTP are found in the initiation phase of cell-cell contact<sup>72</sup>. In combination, Cdc42 and Rac1 will promote Arp2/3 mediated branched actin polymerization via their respective effectors WAVE and N-WASP. Cdc42 also allows the generation of protrusive filopodia responsible for the formation of cell-cell contacts.

Cdc42 and Rac1 were shown to be overexpressed in several types of cancer, such as lung cancer or colorectal carcinoma. In order to grow and invade other sites, cancer cells must be able to migrate. This is one of the hallmarks of cancer. Experiments overexpressing Rac1 or using constitutively active forms showed an increase in cell migration<sup>73</sup>.

### **2. RhoA**

RhoA, also known as Ras homolog family member A, is a GTPase responsible for the assembly of actin filaments in the cell. As mentioned above, it oscillates between an inactive GDP and an active GTP form under the control of GEFs and GAPs. RhoA was reported to be involved

in the regulation of cell shape, polarity, or migration via the control of actin polymerization and myosin-associated contractility<sup>72</sup>.

Specifically, RhoA promotes actin polymerization, and contractile network formation via effector proteins. For example, formin nucleates unbranched linear actin filaments. RhoA was also shown to interact with Rho-associated coiled-coil kinase (ROCK), which participates in the phosphorylation of Myosin II, and thus increases contractility<sup>72</sup>.

It was shown that RhoA could bind the protein p120 in its cytosolic form. Binding with p120 inhibits RhoA activity<sup>72</sup>.

In other studies, RhoA was shown to be hyperactive in gastric cancer cells. Its downregulation partially decreased cell proliferation<sup>74</sup>.

## **F. Myosin II**

Myosins are a family of motor proteins involved in dynamic cellular processes, such as protein translocation or cell contraction<sup>75</sup>. In association with actin, myosins are the major contractile proteins of muscle cells. Myosins are composed of two heavy chains, two regulatory light chains and two light chains that stabilize the heavy chain structure. In epithelial cells, type II myosin makes actin filaments, connected to adherens junctions, slide over each other to generate tension. These tensions participate in the establishment and maintenance of the adherens junctions. At the cell or tissue level, these contractions of the myosin II-dependent actin cytoskeleton lead to changes in cell shape and participate in the remodeling of a tissue<sup>72</sup>. As shown in one study, deletion of myosin IIA in intestinal epithelial cells resulted in altered adherens junctions leading to an impaired intestinal barrier<sup>76</sup>. In another study, an epithelial to mesenchymal transition was induced by overexpression of the transcription factor Snail. Interestingly, myosin II-dependent contraction prevented the disassembly of adherens junctions induced by Snail overexpression<sup>77</sup>.

The role of myosin goes beyond the simple contraction of the actin cytoskeleton. Indeed, the previously mentioned studies show a role for myosin II-dependent contraction to stabilize junctions. Moreover, one study showed that under the effect of myosin II-induced tension, the  $\alpha$ -catenin protein recruits vinculin to adherens junctions. Vinculin subsequently recruits partner proteins to induce actin polymerization and strengthen adherens junctions<sup>72,78,79</sup>.

## **G. $\alpha$ -actinin**

The  $\alpha$ -actinin is a spectrin family protein that binds to the actin cytoskeleton. It is structured as an anti-parallel rod-shaped dimer with actin-binding domains at each end<sup>80</sup>. In association with myosin II,  $\alpha$ -actinin forms the contractile actin belt. With its two actin-binding domains, it can bundle actin filaments at adherens junctions<sup>81</sup>. In addition to binding to F-actin,  $\alpha$ -actinin associates with other proteins involved in the regulation of the actin cytoskeleton such as vinculin<sup>82</sup>.

Besides the classical junctional adhesion complex,  $\alpha$ -actinin was shown to be essential for the localization of epithelial cell adhesion molecule (EpCAM) at the cell-cell contact zone<sup>83</sup>.

## II. Adherens junction formation process

The formation of adherens occurs in two types of context. In embryos, polarity signals lead to the establishment of junctions between cells where contact is pre-existent. In contrast, migrating cells will undergo a mesenchymal-epithelial transition (MET). In this case, the junctions formed define the polarity of the cells. We develop here the different steps responsible for the establishment of E-cadherin dependent adherens junctions in the latter case.

### A. Formation of Initial Cell-Cell Contacts

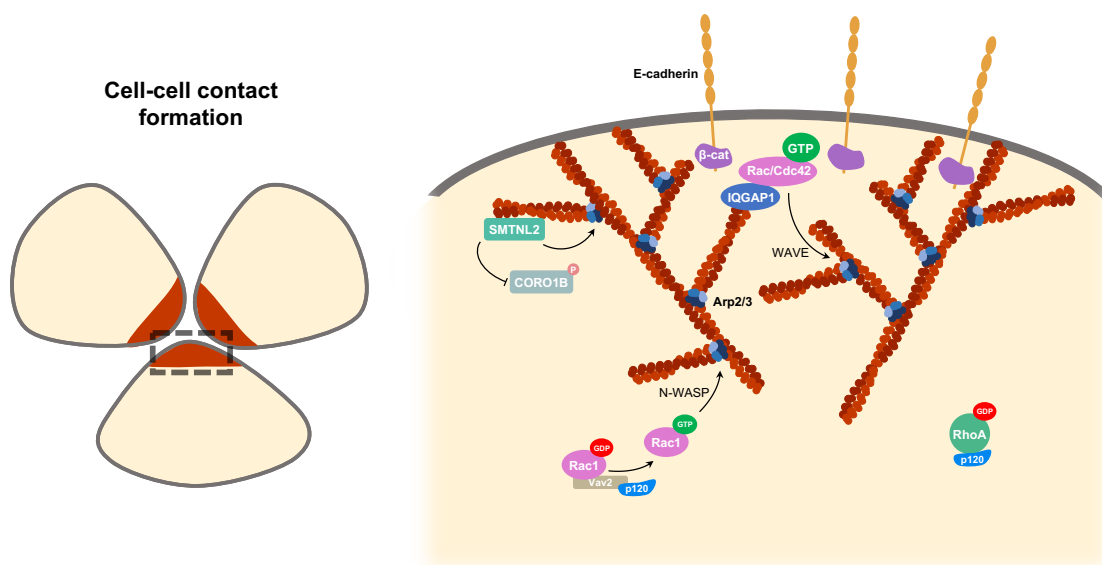


**Figure 8.** Scheme representing a model for the formation of adherens junctions in migrating cells (left). The proteins depicted in the diagram represent key players in the establishment of cell-cell contact (right). The cells are pushed toward each other by a dynamic branched cytoskeleton promoted by Rac1, Cdc42 and Arp2/3.

To initiate cell-cell contacts, cells organize a branched actin network, via Arp2/3, to push the membranes of two neighboring cells toward each other. At the initiation phase of junctions, the branched network organization is activated by the Rho GTPases Rac1 and Cdc42. As mentioned earlier, Rac1-GDP is activated by the GEF Vav2 associated with cytosolic p120. Rac1-GTP and Cdc-42-GTP activate Arp2/3 via WAVE and N-WASP proteins, respectively. Note that the cytosolic form of p120 also acts as a GDI-like by binding with cytosolic RhoA. In parallel the IQGAP1 protein binds to actin and Rac1 and/or Cdc42. The binding of IQGAP1 to Rho GTPases prevents their inhibition by RhoGDI. Cdc-42-GTP is also responsible for the formation of protrusive filopodia important for cell-cell contact formation. In parallel, a protein called SMTNL stimulates branched polymerization via Arp2/3 and inhibits coronin B by

phosphorylation. Also during the initiation phase of adherens junctions,  $\beta$ -catenin binds to the C-terminal part of E-cadherin and induces its transport to the cytoplasmic membrane.

## B. Junction maturation - actin reorganization

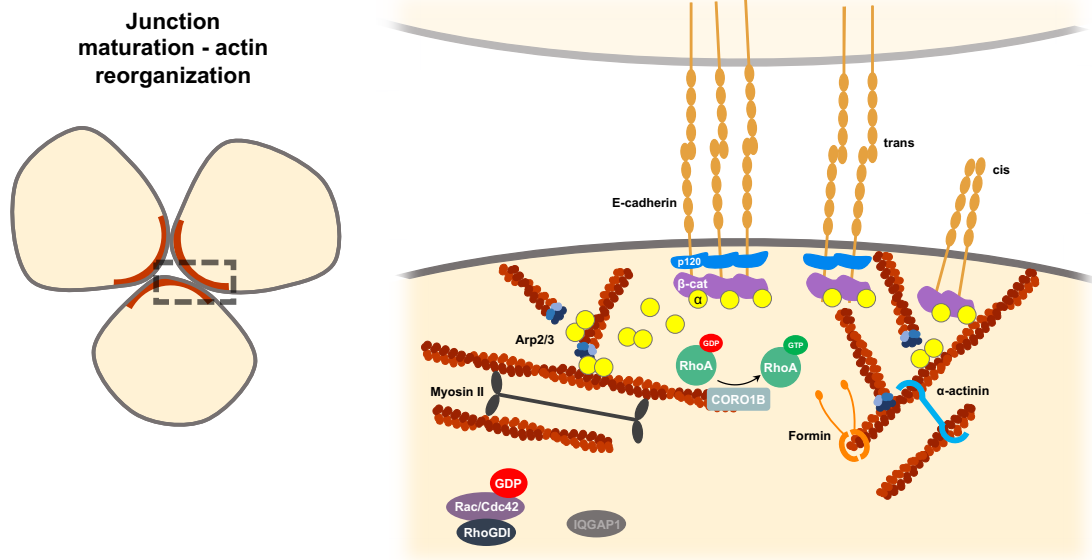


**Figure 9.** Scheme representing a model of the maturation of adherens junctions in migrating cells (left). The proteins represented in the schematic represent key players in the remodeling of the actin cytoskeleton (right). Cell-cell contacts are extended by RhoA-activated cytoskeleton remodeling. The branched cytoskeleton is converted into linear actin fibers bundled by  $\alpha$ -actinin. Yellow circles:  $\alpha$ -catenin.

During the maturation phase, the branched actin cytoskeleton is converted into a contractile cytoskeleton composed of linear actin filaments associated with myosin.

When Coronin 1B is no longer inhibited by SMTNL, it activates RhoA. Arp2/3 is then no longer activated. RhoA-GTP activates another protein responsible for actin nucleation, formin, and activates via a protein called ROCK the myosins II responsible for the contraction of the cytoskeleton.

The IQGAP1 protein is inactivated in a calcium-dependent manner. Rac1 and Cdc42 are then inactivated by binding with RhoGDIs.

In parallel, catenin p120 binds to the CH2 domain of E-cadherin. Its ability to homodimerize induces the formation of E-cadherin clusters on the cell surface. The  $\alpha$ -catenin binds to the  $\beta$ -catenin associated with E-cadherin. Furthermore, when  $\alpha$ -catenin is in homodimer form, it can bind to actin and competes with Arp2/3, and thus allows for decreased branching of the cytoskeleton.

## C. Stable junctions

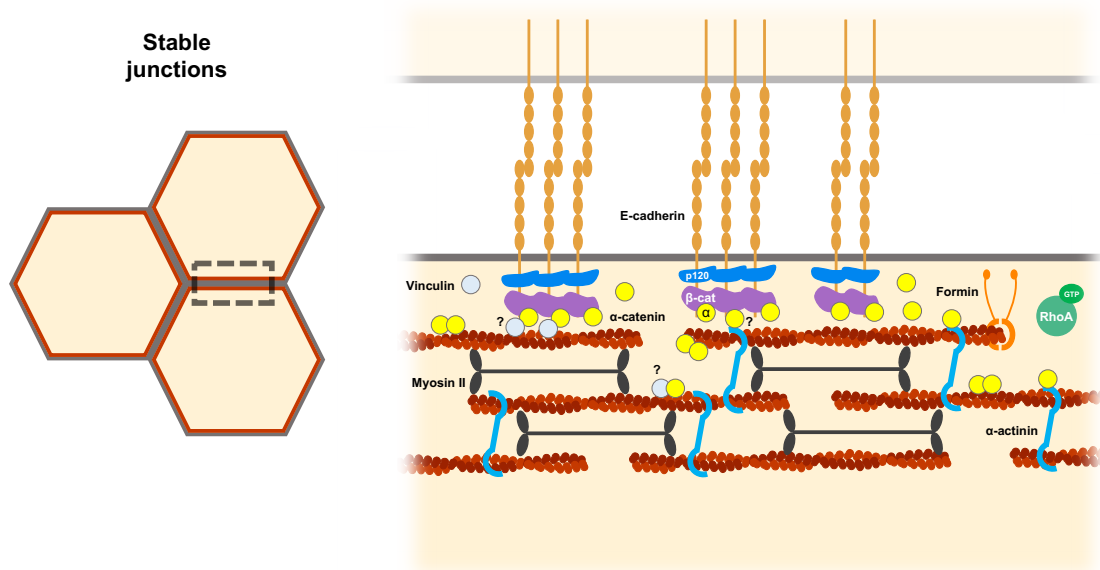


**Figure 10.** Schema representing a model of stable epithelial junctions mediated by E-cadherin. The proteins represented in the diagram represent the key players involved in the maintenance of junctions. Stable junctions are mediated by a linear F-actin cytoskeleton coupled to contractile Myosin II. Filament turnover is mediated by RhoA-mediated formin. Myosin II is activated by RhoA via ROCK.

Stable junctions are maintained by an actin cytoskeleton that is organized as a contractile actomyosin belt. The actin cytoskeleton is maintained as long linear filaments via RhoA which stimulates actin nucleation by formin and Myosin II activity.

E-cadherin clusters are maintained by catenin p120. The  $\alpha$ -catenin, coupled to vinculin regulates the tension applied by actin on the junctions. It should be noted that the interaction of  $\alpha$ -catenin with actin is still debated.

### III. Epithelial Cell Adhesion Molecule – EpCAM

The integrity of an epithelial tissue is ensured by its junctions. Cell-cell adhesions regulate the polarity, proliferation and differentiation of epithelial cells. Contact inhibitions mediated by cell-cell adhesion are crucial for organogenesis and tissue homeostasis. As previously described, cell-cell adhesions are mediated by transmembrane cell adhesion molecules, including cadherins, integrins, selectins and Ig-like.

Discovered in 1970, the epithelial cell adhesion molecule EpCAM, is a homophilic adhesion molecule that does not fit in any of the families mentioned<sup>83</sup>. This 40 kDa molecule was frequently found over-expressed in highly proliferative cancer cells. For these reasons EpCAM has long been used as a biomarker of cancer cells. Beyond its high expression in cancer cells, EpCAM also plays roles in morphogenesis processes in epithelial tissues.

A study published in 1997 showed that EpCAM could promote  $\text{Ca}^{2+}$ -independent homophilic cell-cell adhesion in normally non-joining cells<sup>84</sup>. Indeed, the expression of EpCAM in non-joining cells not normally expressing EpCAM resulted in cell aggregation and cell-cell contact

formation. This study highlighted the adhesive role of EpCAM. Another study demonstrated its ability to form homophilic adhesions by deleting a portion of the extracellular domain of EpCAM. Deletion of this domain also disrupted its accumulation at cell-cell contacts.

Unlike E-cadherin which induces strong cell-cell adhesion, EpCAM-mediated adhesions are relatively weak. In contrast to highly jointed cells that express only E-cadherin, cells co-expressing EpCAM have weaker junctions. Strikingly, when EpCAM is brought into cells that expressed only E-cadherin, this results in a strong decrease in E-cadherin-mediated cell-cell adhesion. It was shown that this weakening of cell-cell junctions was not due to a decrease or delocalization of E-cadherin, but to a disruption of its association with the actin cytoskeleton<sup>83</sup>. Indeed EpCAM has a cytoplasmic domain of 26 amino acids capable of binding  $\alpha$ -actinin. It was shown that cleavage of the cytoplasmic part of EpCAM was sufficient to lose the effects on junctions mediated by E-cadherins.

On the other hand, while cellular levels of  $\beta$ -catenin remain constant when EpCAM is overexpressed; the cellular content of  $\alpha$ -catenin decreases<sup>83</sup>.

As widely described previously, E-cadherin is essential for the maintenance of epithelial architecture. Loss of E-cadherin has been shown to be associated with a loss of contact inhibition, increased proliferation and migratory capacity.

In many epithelia, such as in the prostate gland, E-cadherin and EpCAM are co-expressed, thus regulating the strength of cell junctions. However, increased expression of EpCAM leads to an imbalance and is associated with tumor transformation.

Overall, EpCAM is able to promote cell-cell adhesions through homophilic interactions. However, its antagonistic role on E-cadherin-mediated adhesion junctions suggests that it acts as a modulator of cell-cell adhesion rather than as a promoter. These data suggest that EpCAM must be finely regulated during morphogenesis processes. Nevertheless, its deregulation seems to be involved in the initiation of neoplastic processes.

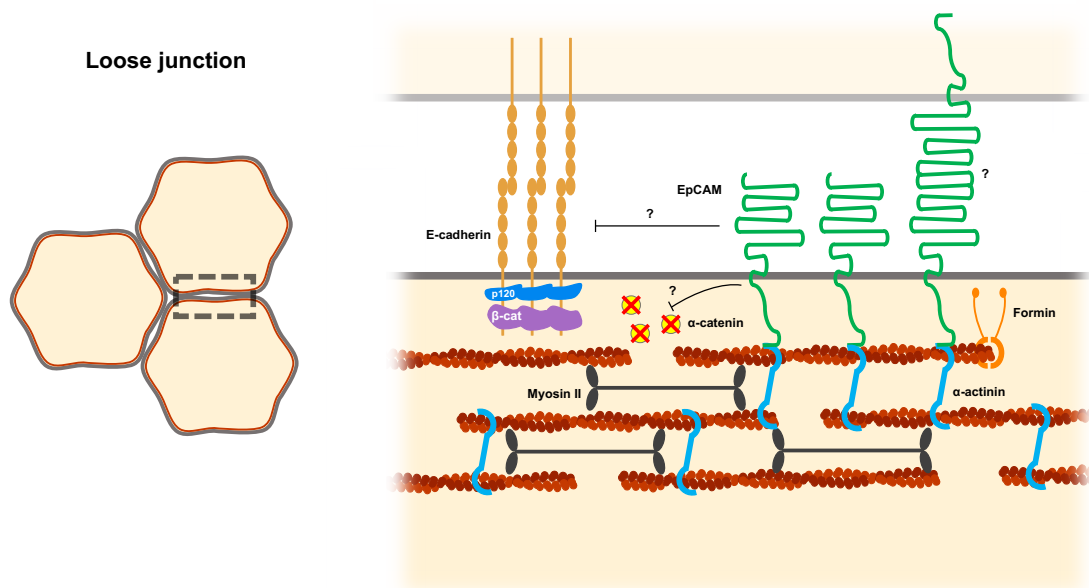


**Figure 11.** Schema representing a model of E-cadherin inhibition by EpCAM. EpCAM may weaken E-cadherin-mediated adherens junctions by disrupting its connection to the actin cytoskeleton. EpCAM is associated with a decrease in the cellular pool of  $\alpha$ -catenin and localizes to the cytoplasmic membrane

*through interaction with  $\alpha$ -actinin via its cytoplasmic domain. EpCAM performs homophilic interactions; the exact domain of interaction is still debated.*

# Ubiquitination and Ubiquitin-Like Proteins

Ubiquitination (or ubiquitylation) is a post-translational modification of proteins highly conserved in evolution<sup>85</sup>. Ubiquitylation consists of the attachment of one or more ubiquitin molecules to a protein. The number and conformation of these ubiquitins will induce different outcomes, such as increasing protein-protein interaction or promoting protein degradation<sup>85</sup>. These ubiquitination processes are regulated by a machinery comprising numerous enzymes. Here we describe the key molecules of the ubiquitination machinery. We also describe some of the partner proteins of this system, as well as the progress on the characterization of Ubiquitin domain-containing protein 1 (UBTD1).

## I. Ubiquitylation process

Ubiquitylation is a finely regulated process involving mainly three types of enzymes: Ubiquitin-activating enzyme also known as E1 enzymes, Ubiquitin-conjugating enzyme also called E2 enzymes, and a ubiquitin ligase also known as E3 ubiquitin ligase. These enzymes control the addition of the small molecule ubiquitin to proteins. The different topologies of ubiquitin conjugated to substrates define the cellular outcome<sup>85,86</sup>.

### A. Ubiquitin

Discovered in 1975, the ubiquitin molecule is a small protein (76 aa) of 8.6 kDa found in many eukaryotic cells<sup>86</sup>. In the human genome, four genes encode ubiquitin: *UBA52*, *RPS27A*, *UBB* and *UBC*. The *UBA52* and *RPS27A* genes encode ubiquitin fused to ribosomal proteins L40 and S27a respectively. The *UBB* and *UBC* genes encode polyubiquitin precursor proteins that form polyubiquitin cassettes. Deubiquitinases (DUBs) cleave from these proteins to monomeric modifiers (**Figure 12**).

Under basal conditions, without stress or stimuli, ubiquitin production is ensured by ribosomal fusions encoded by the *UBA52* and *RPS27A* genes. Under stressful conditions, or for dynamic processes, large amounts of ubiquitin are rapidly encoded by the *UBB* and *UBC* genes. This kind of variation can be determinant in developmental processes. Indeed, one study showed that a deletion of the *UBB* and *UBC* genes disrupted neural differentiation<sup>85,87</sup>.

Once ubiquitins are produced, they are assembled into different types of conjugates that have different functions. For example, monoubiquitylation of a substrate modulates the affinity of protein-protein interactions. The assembly of ubiquitin chains in particular conformations can participate in cell division regulation, or simply in protein degradation.

### B. E1 ubiquitin-activating enzyme

The human genome has only two E1 enzymes encoded by the *UBA1* and *UBA6* genes<sup>88</sup>. The first step of the ubiquitination mechanism is catalyzed by the E1 enzymes in an ATP-dependent manner. The first step of ubiquitin activation is characterized by the binding of an ATP-Mg<sup>2+</sup> to the E1 enzyme. This allows the binding of ubiquitin to the E1 enzyme which catalyzes C-

terminal acyl adenylation of ubiquitin. The second step shows a transfer of ubiquitin to an active cysteine residue with release of an AMP. This second step is characterized by a thioester linkage between C-terminal carboxyl group of ubiquitin and the E1 cysteine sulfhydryl group.

### C. E2 ubiquitin-conjugating enzymes

The human genome encodes 35 different E2 enzymes<sup>89</sup>. The conjugation step is characterized by a transfer of ubiquitin from E1 to E2 by a trans-esterification reaction.

### D. E3 ubiquitin ligases

There are several hundred different E3 ubiquitin ligases, with greater selectivity for their substrates than the E1s and E2s<sup>85</sup>. These catalyze the final step of ubiquitination. E3s are able to recognize a specific substrate and simultaneously interact with E2 enzymes. It was also reported that E3s could activate certain E2s.

There are two types of E3s, the E3s that contain the homologous to the E6-AP carboxyl terminus (HECT) domain and the E3s with the really interesting new gene (RING) domain. The HECT domain allows the transient binding to ubiquitin and its transfer to the substrate while the RING domain catalyzes the transfer of ubiquitin directly from the E2 to the substrate.

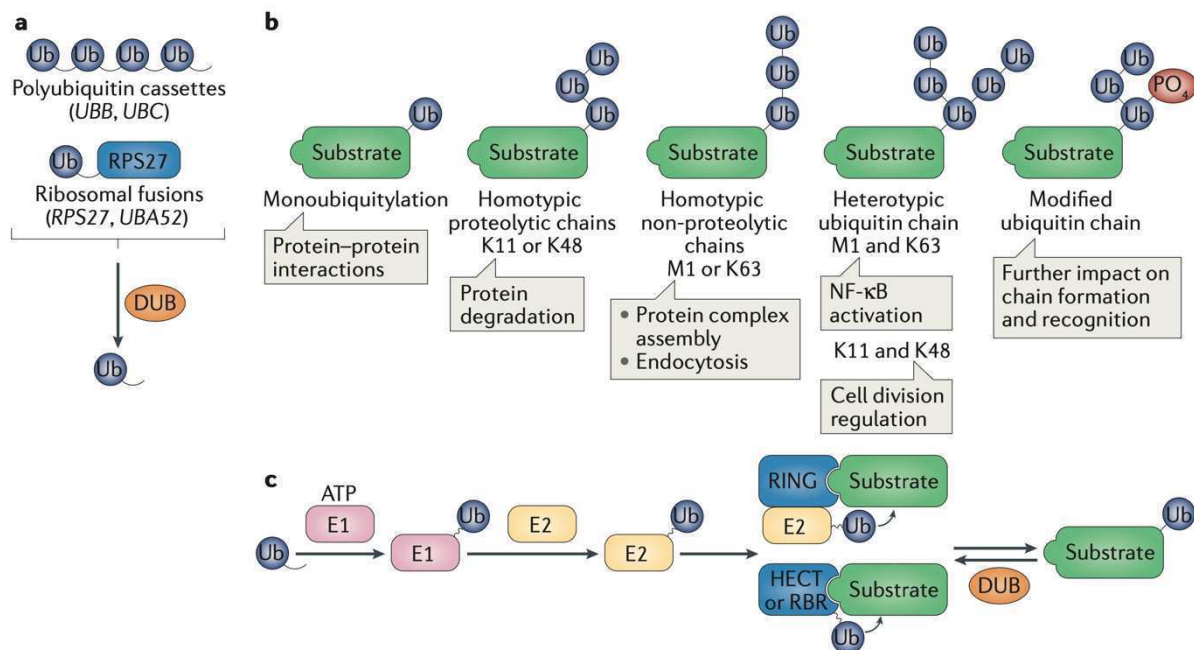


**Figure 12. Process and partner involved in ubiquitination.** (A) Types of ubiquitin produced in eukaryotic cells. (B) Different types of ubiquitin conjugation to substrate molecules. The conformations and number of ubiquitins define the cellular outcome. (C) Process of ubiquitination of a substrate molecule. Modified from Rape 2018.

## **II. Ubiquitin partners**

### **A. Ubiquitin-binding domains**

The ubiquitin-binding domain (UBD) is found on proteins that interact with monoubiquitin and/or polyubiquitin chains<sup>85</sup>. This type of domain is found on proteins that participate in ubiquitination or deubiquitination. As mentioned in the review published by Hicke et al, the presence of a UBD domain in a protein suggests that it interacts with a ubiquitin or ubiquitinated protein<sup>90</sup>.

It was shown that proteins containing a membrane-associated UBD only target monoubiquitins. Indeed, the majority of proteins involved in endocytosis are monoubiquitinated. A membrane-associated protein is likely to be exposed only to monoubiquitylated substrates.

Previous studies have looked at the affinity level of UBD domains for ubiquitinated molecules. It was shown that UBDs have a relatively low affinity for monoubiquitin. Weak UBD interactions with monoubiquitins are probably not a coincidence. For example, the assembly of the protein network that promotes budding of plasma membrane relies on numerous weak interactions. This type of network is therefore dynamic, with easily reversible protein-protein interactions.

It is interesting to note that the accessibility of these UBD domains can be controlled by steric conformation changes. It was shown that the binding of ubiquitin to the ubiquitin receptor RAD23 was dependent on the interaction between its UBD domain and its other domain called UBL<sup>91</sup>.

### **B. Ubiquitin-like proteins**

Ubiquitin like proteins (UBLs) are small non-enzymatic proteins that share a structure similar to ubiquitin<sup>91</sup>. There are two main categories of UBLs. They are classified according to their ability to covalently conjugate to other molecules. The first category contains a particular sequence containing two C-terminal glycine residues. These two residues allow covalent binding to other molecules after activation by proteolysis. This proteolysis reaction makes the glycine residues accessible. The second family of UBLs does not show covalent binding to other molecules. Nevertheless, the way in which these UBLs function remains debated and still partially unclear. However, it is proposed that these UBLs may participate in the regulation of protein-protein interactions.

## **III. Ubiquitin domain-containing protein 1**

Ubiquitin domain-containing protein 1 (UBTD1) belongs to a small protein family containing UBTD1 and UBTD2. This 25,9kDa protein contains a ubiquitin-like domain (UBL)<sup>92</sup> and an ubiquitin binding domain (UBD). In previous studies it was demonstrated that UBTD1 interacts with the UBE2D family of E2 ubiquitin conjugating enzymes. Additionally, UBTD1 stabilized P53 by ubiquitinating MDM2, the E3 enzyme responsible for its degradation<sup>93</sup>. Similarly, our laboratory recently confirmed that UBTD1 participated in the degradation of the transcriptional regulator yes-associated protein (YAP) by modifying its ubiquitination level<sup>94</sup>.

Finally, we showed the involvement of UBTD1 in coordinating EGFR signaling by controlling the cellular level of ceramide through the ubiquitination of several proteins involved in this process. ASAH1 and the ubiquitination of SQSTM1 by RNF26<sup>95</sup> (see article in Appendix). UBTD1 was found to be associated with the level of cancer aggressiveness, and survival of patients with prostate, liver and lung cancer<sup>92,94,96</sup>.

# Organoid

Organoids are a self-organizing three-dimensional (3D) culture system derived from pluripotent stem cells<sup>97,98</sup>. They recapitulate the architecture, composition and functionality of their epithelial tissues of origin better than the traditionally used two-dimensional immortalized cell lines. This model can be used to study the processes of differentiation and spatial organization of stem cells. Thus, organoid technology is ideal for deciphering the role of genes involved in human organogenesis or pathologies<sup>99</sup>.

## I. History of organoid culture

The first cell models used *in vitro* were derived from cancer cells<sup>100</sup>. These were easily cultured because of their immortal properties. The molecular and cellular characteristics of cancer cells differ from their tissue of origin. This is what enables the cancer cell to survive in different environments. The central signaling pathways, growth factors and receptors are deregulated, which prevents the study of cellular mechanisms. In addition, the changes associated with a cancer cell line will only reflect the cell from which it originated since not all cancer cells can be cultured *ex vivo*<sup>101</sup>. Immortalized cell lines cultivated *in vitro* do not recapitulate all the features of healthy cells nor the different cell types present *in vivo*. 2D cell culture on rigid supports, does not recapitulate the mechanisms of spatial cell organization. To overcome these limitations, *ex vivo* explant were developed, recapitulating more faithfully the original tissue<sup>102</sup>. However, these cultures had limited lifetimes due to the lack of self-renewal capacity of the tissue.

In 1975, a study reported the long-term culture of non-transformed and non-cancerous human cells<sup>103</sup>. This work by James Rheinwald and Howard Green consisted of co-cultivating human keratinocytes with mouse fibroblasts. They recapitulated a stratified squamous epithelium similar to the stratification found in the skin. A study published in 1987 by Mina Bissel's group reported the *in vitro* formation of alveolar-type structures that partially recapitulated the functional characteristics of a mammary epithelium<sup>104</sup>. This type of culture was performed in a synthetic 3D extracellular matrix. It allowed for the first time to study the processes of morphogenesis *in vitro*.

In 2009, a study published by the laboratory of Hans Clevers showed 3D organized structures containing stem cells and differentiated cells<sup>105</sup>. These authors reported the first organoid cultures. *In vivo*, adult stem cells (ASCs) are able to proliferate and participate in the renewal of the organ in which they are localized. To obtain organoids, they isolated intestinal stem cells and seeded them in an extracellular matrix with factors acting as a niche surrogate. These organoids derived from ASCs, allowed to obtain models partially recapitulating the architecture and the differentiation into different cell types of several tissues, such as intestines, colon, prostate or breast. These organoids allow to maintain *in vitro* an untransformed cell population. However, concerns about uncomplete differentiation remained.

A study published in 2011 by Yoshiki Sasai's group, reported the culture of pluripotent stem cells (PSCs) to form three-dimensional structures reproducing optical cups<sup>106</sup>.

Together, organoids derived from ASCs and PSCs pave the way for the *in vitro* study of physiological processes and the study of human pathologies in a complementary way to animal models.

## **II. Organoids to study human biology and diseases**

### **A. Spectrum of organism models**

The idea that many mechanisms are conserved during evolution led scientists to develop mirror models of human physiology. These models have been widely developed during the last century. Models such as yeast, drosophila, or mice have been used for a long time, and are still used today by many scientists. Easily accessible, low-cost models such as the *Caenorhabditis elegans* worm allowed the study of many genes involved in differentiation and cell fate decision<sup>107</sup>. However, each model has limitation. As described in several studies, about 70% of the genes in *C. elegans* have orthologous genes in humans, and 42% of the genes involved in human pathologies are found in *C. elegans*, which makes it a very interesting model<sup>108,109</sup>. Nevertheless, other aspects such as the immune system or metabolism are very different from human physiology.

In mammalian model systems, mice occupy a very important place today. Molecular biology techniques allowing the generation of genetically modified mice have made this model very versatile and useful to study many pathologies. Nevertheless, the cost of this model remains very high. In addition, many human physiological processes are not faithfully reproduced in animal models<sup>110</sup>. The striking example of ibuprofen illustrates this difference. Indeed, ibuprofen is prescribed as an anti-inflammatory in humans, while it is toxic in rodents<sup>111</sup>. This type of difference limits the use of animal models to find new therapeutic drugs that can be administered to humans. The development of new models more faithful to human physiology is therefore necessary.

### **B. ASCs-derived human organoids**

Organoids derived from ASCs have emerged as an alternative or at least a complementary model to those used till now<sup>112</sup>. These organoids partially recapitulate the structure and composition of the epithelium from which they originate (**Figure 13**). Organoids can be generated using ASCs isolated from biopsies of healthy or diseased organs<sup>113</sup>. However, ASCs can be grown *in vitro* to form organoids only if the culture conditions are well defined meaning that they include the necessary factors characteristic of the niche in sufficient quantities.

#### **1. Establishment of organoids *in vitro***

To establish a new organoid model the limitations are the identification of ASCs and the factors allowing them to proliferate and differentiate<sup>114</sup>. The first studies that established the organoid model focused on the identification of factors stimulating self-renewal, assimilated as proliferation, and factors controlling differentiation<sup>105</sup>. The first model established by Clevers' group relied on a medium composed of mitogen factors such as EGF and Noggin to control and block the activity of bone morphogenetic protein (BMP). In addition, R-spondin was added to

stimulate the activity of the Wnt pathway, which is necessary for ASC renewal. However, niche-specific factors that can be produced by 'neighboring' cells should also be added. For example, Paneth cells, which are not fully functional in intestinal organoids and are responsible for Wnt production *in vivo*, require the addition of Wnt3a to the medium. In addition, inhibition of TGF $\beta$  or p38 pathways was necessary for the maintenance of the cultures after several passages<sup>112</sup>. All these parameters must be adjusted for each type of organoid culture (**Figure 13**).

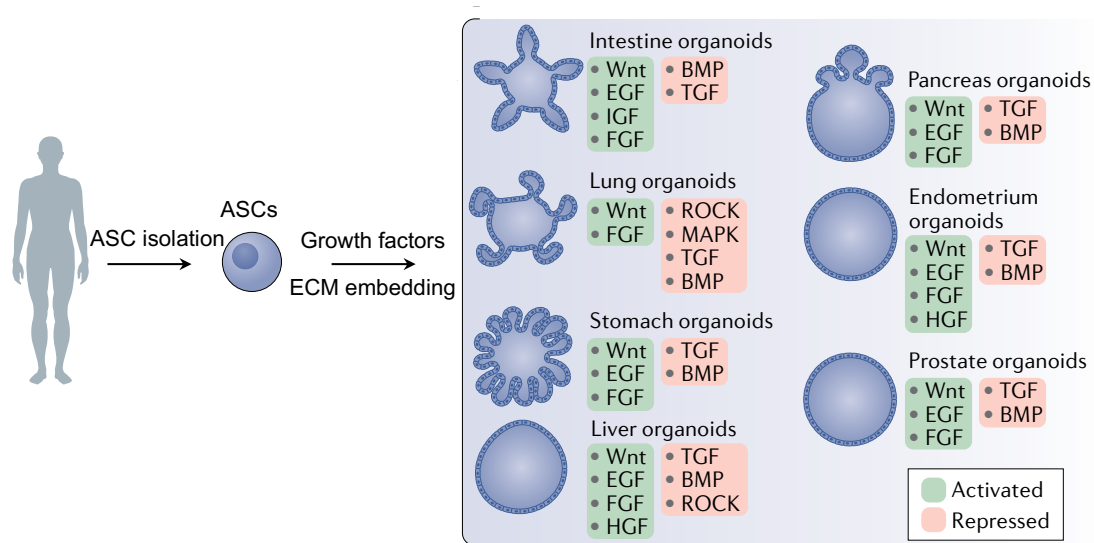


**Figure 13. Establishment of organoids derived from ASCs.** Adult stem cells are isolated from human tissue. ASCs are seeded in an extracellular matrix (ECM) with a medium reproducing the niche factors. The physical environment and chemical signals are important to induce self-renewal and differentiation of the stem cells. On the diagram, the activated (green) and inhibited (red) signaling pathways are shown. BMP, bone morphogenetic protein; EGF, epidermal growth factor; FGF, fibroblast growth factors; HGF, hepatocyte growth factor; IGF, insulin-like growth factor; ROCK, RHO-associated protein kinase; TGF, transforming growth factor; VEGF, vascular endothelial growth factor. Schema from Kim 2020.

## 2. Physiological relevance

During the last decade, the establishment of organoids for many organs has made it possible to grow cell types that were previously impossible to grow<sup>115</sup>. For example, long-term culture of human hepatocytes was impossible. Based on the conditions for culturing bipotent biliary tree-derived progenitor organoids, a protocol for culturing hepatocyte organoids was developed<sup>116,117</sup>. Allowing the cultivation of hepatocytes up to 20 passages *in vitro*. In these models, they were able to form hepatocytes expressing albumin and cytochrome P450 enzyme, demonstrating the maturity of these hepatocytes *in vitro*.

The study of the effect of growth factors on cell differentiation in the intestinal crypt is an example of a physiological phenomenon that could be achieved with the organoid model. In a first study, Clevers' group established the culture conditions to obtain enteroendocrine cells<sup>118</sup>. A study published the following year used this organoid model to study the expression of hormones by endocrine cells under the influence of growth factors<sup>119</sup>. They showed that the presence of BMP4 influenced hormone expression and confirmed these findings in mice. These studies showed the existence of a BMP gradient along the intestinal crypt that influences hormone expression by enteroendocrine cells.

In the stomach, proliferating Lgr5 stem cells are located at the base of the pyloric gland<sup>120</sup>. Based on intestinal organoid cultures, one group showed long-term organoid cultures that reproduced mature pyloric epithelium<sup>121</sup>. Cells called Chief cells are able to dedifferentiate in the gastric corpus gland to regenerate the epithelium in case of damage. The culture of these cells *in vitro* led to the generation of long-term gastric organoids<sup>122</sup>.

### 3. Organoids to study infectious diseases

Organoids have now been used to model bacterial and viral infections (**Figure 14**). Organoids allow to recapitulate and study *in vitro* characteristics of infections, and also of the immune system.

A study published in 2020 reported the co-culture of intestinal organoids with genotoxic *E. coli* pks+ bacteria to study the occurrence of oncogenic mutations<sup>123</sup>. Indeed, *E. coli* bacteria can carry the pathogenic island pks which encodes for enzymes, such as colibactin, that induces double stranded cuts in DNA. By performing repeated injections of these bacteria into the lumen of intestinal organoids, whole-genome sequencing analysis revealed a distinct mutational signature that was absent from organoids injected with pks- bacteria.

Another study looked at the role of *Helicobacter pylori* in chronic gastritis, peptic ulcers, and stomach cancer<sup>124</sup>. Here they injected *H. pylori* into the lumen of stomach organoids. Injection of the bacteria into the lumen of the stomach organoids triggered an NF- $\kappa$ B-mediated inflammatory response<sup>122</sup>.

Organoids can also be infected by viruses. One study reported the possibility of using intestinal organoid monolayers to allow replication of human norovirus *in vitro*<sup>125</sup>. Previously, replication of these viruses was not possible in classical 2D cultures. Interestingly, the addition of bile to the culture medium was necessary for some strains to infect and replicate in the intestinal organoids<sup>126</sup>. The cell type and the environment, which compose the niche, are therefore both equally important.

In 2019, a new strain of coronavirus responsible for severe acute respiratory syndrome (SARS-CoV-2) appeared. It was observed that this influenza-like disease was localized in the lungs. However, evidence suggested that the intestines could also be infected by the virus. A study published in 2020 reported evidence that SARS-CoV-2 infects human gut enterocytes<sup>127</sup>. Considering that the receptor angiotensin-converting enzyme 2 (ACE2) is highly expressed in differentiated enterocytes, the enterocytes present in the organoids were infected when they were in the presence of the virus. In this study, they were able to produce virus particles. The organoid model can therefore be used to study viral infectious mechanisms and to identify and test therapeutic anti-viral treatments.

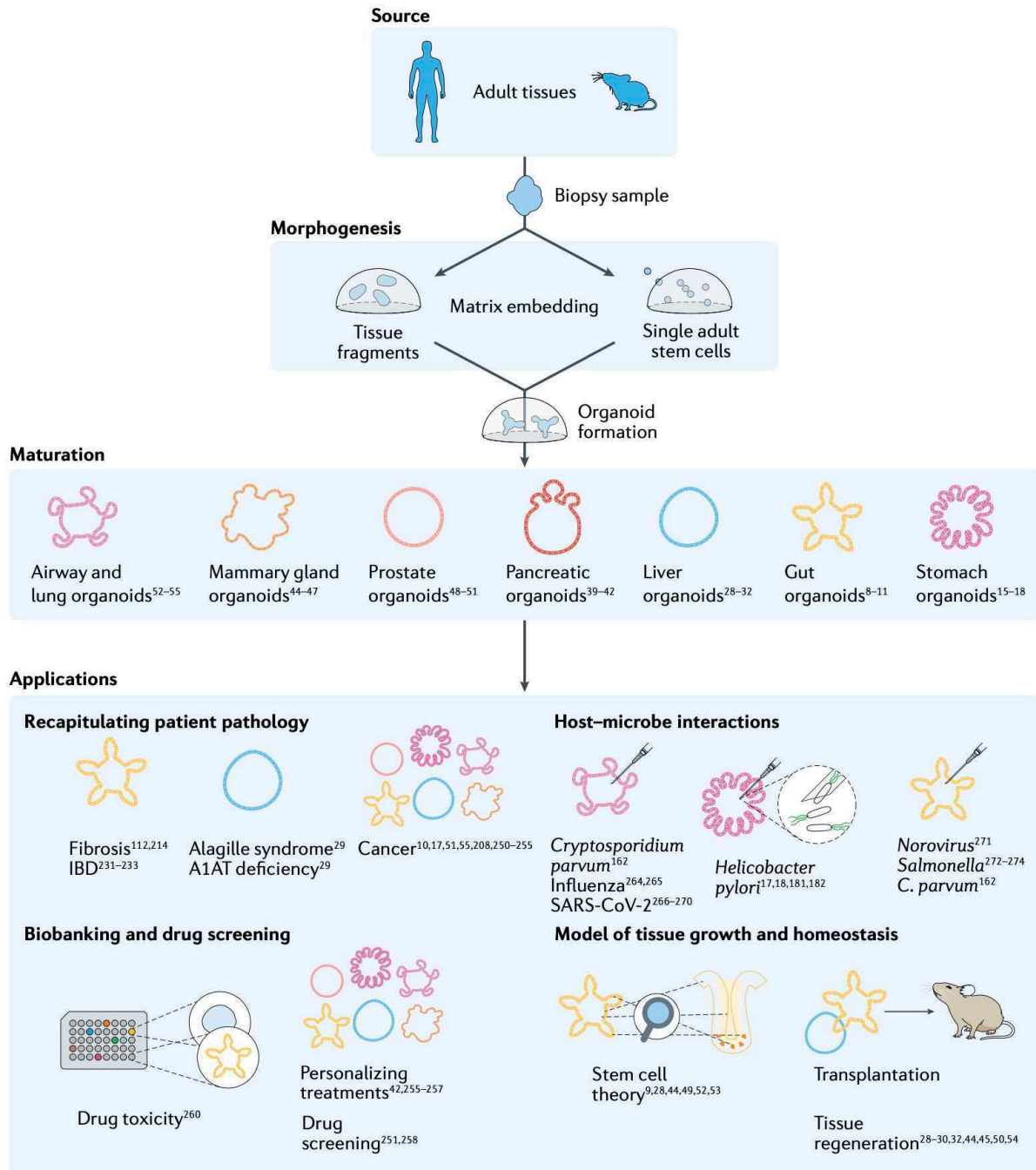


**Figure 14. Applications of the organoid model.** Organoids can be used to model disease. They allow to understand genetic disease mechanisms, and to study genes involved in cancer. Organoids can be used to study host-pathogen interactions with co-culture with bacteria or viruses. Biobanks of organoids from patient samples can be used for drug screening. They can be stored for future studies. Organoids can be used to study developmental processes, stem cell homeostasis, and its response to physical and chemical stimuli. Schema from Hofer 2021.

#### 4. Organoids to model genetic pathologies

The genetic stability of organoids made it possible to consider growing samples of patients with genetic diseases as organoids<sup>128</sup>. The organoids derived from these patients showed recapitulation of the phenotypes associated with the disease (**Figure 14**).

Insufficient production of  $\alpha$ 1-antitrypsin by the liver results in insufficient protection of the lung against neutrophil elastase leading to destruction of lung parenchyma. This genetic pathology is associated with a deficiency of the A1AT gene responsible for the production of this enzyme. In 2015, a study showed the establishment of stable genome culture of liver organoid derived from patient with this mutation. The organoids with A1AT deficiency reflected the pathology *in vivo*<sup>128</sup>.

Organoids can be used for the evaluation of personalized medicines. Organoids can be used as an avatar of patients with genetic pathology to test drugs *in vitro*.

Cystic fibrosis is a monogenic channelopathy caused by a mutation leading to the inactivation of the cystic fibrosis transmembrane conductance regulator (CFTR). As a result, mutation of this channel leads to a decrease in chloride transport from the cytoplasmic compartment to the extracellular medium in the lung and pancreas, resulting in a decrease in water flux by osmosis, which leads to an increase in mucus viscosity. It should be noted that the loss of function of this channel is not due to a single mutation, in fact more than 2000 different mutations have been identified in patients with this disease<sup>129</sup>. There are drugs that act as potentiators that increase the activity of the CFTR channel. However, these drugs work in combination with specific mutations. It is therefore important to test the best mix of drugs for each patient. In 2013, a Forskolin-based assay was used to test the functionality of the CFTR channel in intestinal organoids<sup>130</sup>. The assay was based on the swelling of organoids induced by forskolin-induced cAMP signaling. Using organoids derived from small endoscopic biopsies of patients, this assay was shown to predict the response of patients to drugs tested individually or in combination.

## 5. Organoid to model cancer

As seen in many studies, there are now two different ways to use organoids to study cancer (**Figure 14**). Either, as shown in 2011, by generating organoids derived from patients' tumors<sup>131</sup> or by using normal organoids and applying genome engineering techniques to study the role of genes involved in tumorigenesis<sup>132</sup>.

The culture conditions developed for organoids allow to grow cancer cells very easily. Tumor organoids could be generated from primary or metastatic tumors of colon<sup>133,134</sup>, brain<sup>135</sup>, prostate<sup>113</sup>, breast<sup>136</sup> and many other organs. The same cell heterogeneity was found in tumor organoids compared to the tumor from which they were derived. In 2019, a team established that an ovarian cancer organoid platform could recapitulate intra and inter patient tumor heterogeneity<sup>137</sup>.

According to a study published in 2018, the response to treatment of the tumor organoid matched the response of the patient<sup>138</sup>. When the drug has no effect on the tumor organoid, the drug has no effect on the patient and vice versa. Nevertheless, the representativeness compared to the evolution of the patient's tumor remained limited. We can nevertheless imagine that with the increase in the number of tumor organoids established, the techniques will become more routine and reliable to predict the best response to therapy for each patient.

Organoids can be genetically edited with CRISPR-Cas9. This technique has been used in organoids to recreate oncogenic mutations.

In colorectal cancer, mutation of the MutL homolog 1 gene, a DNA mismatch repair enzyme, is responsible for the accumulation of mutations in tumors. Loss of this enzyme leads to instability of microsatellites (MSI), repeated sequences in the genomes, which results in a change in copy number. In a 2017 publication, they knocked out the MLH1 gene in colon organoids with the CRISPR-Cas9 technique. After 2 months of *in vitro* culture, gDNA analyses revealed an increase in the number of mutations compared to the control. Moreover, the acquired mutational profile obtained was similar to that found in patients with MSI<sup>139</sup>.

A fusion between the androgen receptor (AR)-responsive trans-membrane protease serine 2 (TMPRSS2) gene and E26 transformation-specific (ETS) gene family members is found in 80% of prostate cancers<sup>140</sup>. Using CRISPR-Cas9, a fusion between TMPRSS2 and one of the ETS gene, i.e. ERG, was induced in mouse prostate organoids. This induction of ERG by AR could be reversed using androgen inhibiting agents<sup>141</sup>.

The deubiquitinating enzyme BAP1, considered a tumor suppressor in humans, has a homolog in mice known to deubiquitinate histone H2AK119. A group of researchers dissected its role by introducing a CRISPR-Cas9 mediated knockout of BAP1 in a normal human cholangiocyte organoid model. This BAP1 knockout induced a phenotype associated with cell-cell junctions and the cytoskeleton. Using a combination of knockouts with TP53, PTEN, SMAD4, and NF1, they observed that BAP1 knockout induced the acquisition of malignant features upon xenotransplantation<sup>132</sup>.

These different examples illustrate that the organoid technology brings the possibility to study and identify genes involved in cancer in a human context.

## **6. Genetic repair in organoids**

As a proof of principle to show that it is feasible to repair DNA in organoid derived from patients with a pathogenic mutation, Clevers' group published a study in 2013 showing functional repair of the CFTR channel in intestinal organoids<sup>142</sup>. The intestinal organoids were derived from patients with a homozygous F508 deletion. After repair using CRISPR-Cas9, the functionality of the channel was restored and tested with the forskolin-induced swelling assay<sup>130</sup>.

With the improvement of genome editing techniques, and the evidence that 'classical' Cas9 can cause chromosomal rearrangements. The same team used prime editing technique to correct and repair CFTR in organoids<sup>143</sup>.

These proofs of principle suggest that it may be possible in the future to transplant repaired organoids into patients. Nevertheless, the precision of the editing technique and the quantity and sites of transplantation of the organoids are still a limitation today.

# **III. Engineering organoid and next generation organoids**

## **A. Limitations of organoids**

Organoids have achieved a degree of fidelity and maturity in cell type composition that surpasses many other *in vitro* models<sup>105</sup>. However, despite these advances, no organoid completely reproduces the spectrum of cell types present in the organ of origin. In fact, organoids do not reproduce fully functional cell types. Moreover, organoids only reproduce the

epithelial gland, the interactions with the mesenchymal, vascular and immune compartments are not reproduced. Some models have been established to reconstitute these interactions but they remain difficult to establish and they only partially reproduce the interactions between these different compartments<sup>144</sup>.

Another limitation that might play a role in the differentiation of cells in organoids is the culture time. Indeed, organoids are usually grown for 7 to 10 days before being dissociated and reseeded. This short life span of the organoid can be an additional barrier to the complete maturity of some cell types present in the organoid. Furthermore, in cystic organoids, such as prostate organoids, if the organoids are attempted to be cultured longer than one week, they will begin to fill their lumen with dead cells.

Organoids are also very heterogeneous regarding formation efficiency, morphology, and 'functionality'. The end-point heterogeneity may be due to the number of initial cells that form an organoid. Indeed, an aggregate of cells will give a mature organoid faster than a single cell. This variability is a limitation for using organoids for drug screening, especially when the read-out is based on the morphology.

Commonly used read-outs are often based on imaging and image analysis techniques. However, these read-outs provide only a limited amount of information on the level of differentiation of the cells. To fully dissect the level of cell maturity single cell transcriptomic analyses are necessary. Also, if we are interested in cell junctions and epithelial integrity, transepithelial electrical resistance measurements, classically used in 2D, are technically challenging or even not applicable in organoids<sup>145</sup>.

## **B. Organoid system engineering**

### **1. Matrix compositions**

Many parameters play a role in the development of organoids. Since the first intestinal organoids were developed, niche factors have been considered as determinant<sup>105</sup>. Nevertheless, the physical environment in which ASCs evolve is also important for the development of organoids (**Figure 15**).

The extracellular matrix (ECM) is an important parameter for the differentiation and organization of cells in the organ and logically in the organoids<sup>105,146</sup>. Today a large majority of organoid cultures are performed in an extracellular matrix called Matrigel. This matrix extracted from Engelbreth-Holm-Swarm mouse sarcoma provides the mechanical conditions and ECM-like signals necessary for organoid development. However, the matrigel is not precisely defined, and its composition can vary from batch to batch, which brings additional variability to the model. Furthermore, the fact that this matrix is animal derived hinders its use for clinical purposes. This is why more standardized hydrogels are being developed today<sup>147</sup>.

There are indeed two types of matrices currently developed: matrices developed from 'natural' material such as fibrin or collagen or from synthetic hydrogels. In the latter case, some synthetic hydrogel matrices have been developed from poly(ethylene glycol) (PEG)<sup>148</sup>. To mimic and 'functionalize' this synthetic matrix, molecules found in the extracellular matrix can be added, such as membrane protein laminin. This type of controlled matrix has the advantage of generating matrices with specific compositions, which can perhaps influence the differentiation

of some cell types. Synthetic matrices also bring the possibility to modulate the rigidity of the ECM.

This type of improvements opened new research directions trying to modulate the physical and chemical input received by the ASCs.

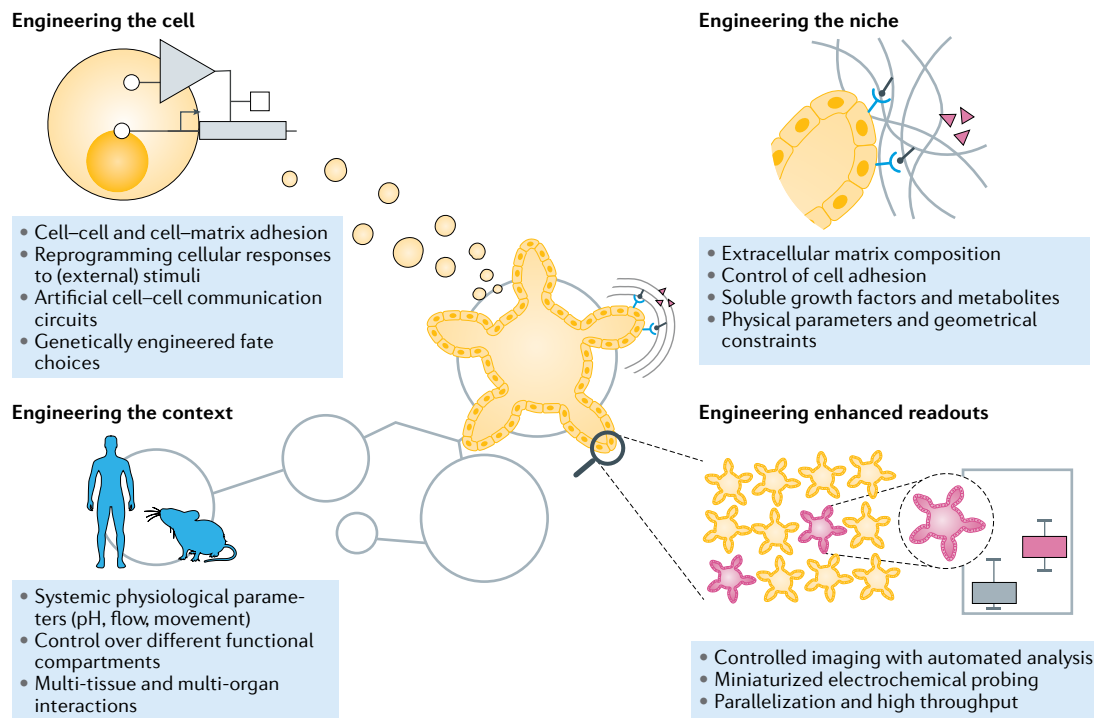


**Figure 15. Engineering strategy for organoids.** The engineering of organoids can be performed at different levels. At the cell level with gene editing approaches. It can be at the matrix level, to control the adhesion of cells to the matrix or to induce physical constraints by playing on the ECM rigidity. By using organ on chip technology, context and interactions with other compartments can be introduced. Finally, the automation or the increase of the sensitivity of the read-out can also be improved by of imaging process for example. Schema from Hofer 2021.

## 2. Geometrical parameter

Physical constraints play an equally important role as chemical signals in developmental processes (**Figure 15**). With the emergence of artificial matrices, shape-guided morphogenesis technologies have been developed. Lutolf's group has been developing micromanufacturing, 3D printing and laser cutting technologies for the cultivation of ASCs *in vitro*<sup>148,149</sup>.

Crypt formation in the intestine is a random process that is uncontrolled. By using micro-engineered scaffolds, they predefined the shape that the intestinal organoids could take. This type of organoid culture allowed a long-term homeostasis, and permitted easier access to the apical and basal poles of the cells. The tubular shape of these organoids allowed to 'clean' the lumen of the organoids by removing the dead cells that usually accumulate in a classical organoid. The longevity of these organoids allowed to obtain cell types that are not found in

classical short term organoids. Interestingly, without any growth factor gradient, the different cell types were organized in a pattern similar to that of a classical crypt<sup>150</sup>. The geometry of the environment seems to guide morphogenesis processes.

Organoid models can be established from many organs to reconstitute at a smaller scale characteristic of the original tissue. However, relying on the self-organizing properties of the cells in organoid cultures leads to variability and prevents precise control of certain physical and chemical parameters. Moreover, the lack of interaction with other organs, or interaction with components of the immune system limits the use of the model.

To overcome these limitations, today an explosion of technologies gravitating around organoids are developed. The organ on chip technology, the vascularization of organoids, or the addition of components of the immune system open the way to new fields of research.

#### **IV. Prostate Organoid**

As described previously, the prostate gland is composed of a pseudostratified epithelium containing basal and luminal cells. Prior to the establishment of organoid models, the study of the prostate *in vitro* was limited to immortalized cell lines.

In 2014, a study published by the Clevers' group reported the development of human prostate organoids<sup>20</sup>. Using the basal CD49+ and luminal CD26+ surface markers, they isolated basal and luminal cells. These fractions contain stem/progenitor cells. It must be noted that it is currently not possible to isolate/enrich stem cells by FACS because no marker has been identified. They described a protocol to obtain prostate organoids composed of basal and luminal cells expressing the markers cytokeratin 5 (CK5) and cytokeratin 8 (CK8) respectively (**Figure 16**). Interestingly, when CD26+ luminal cell-derived organoids were treated with or without dihydrotestosterone (DHT), this resulted in cystic or compact organoids respectively. The level of differentiation of the secretory luminal cells was likely affected. A study published in 2017 reported the identification of enriched luminal progenitors in pten-null prostate tumors<sup>151</sup>. This cell population corresponded to proliferative and undifferentiated luminal cells capable of giving back organoids if isolated and seeded *in vitro*. These cells were characterized by the expression of cytokeratin 4 (CK4). It would be interesting to evaluate the expression of this marker with the maturation stages of DHT-dependent prostate organoids.

A study published in 2020 revealed the regenerative potential of prostate luminal cells by single cell analysis<sup>19</sup>. By castrating mice, they induced a 90% decrease in prostate size due to loss of luminal cells. When stimulation with androgens was restored, the prostate regenerated. They identified a population of luminal cells expressing stemlike genes and a population of differentiated luminal cells. They showed that in organoids, these two populations contributed equally to prostate regeneration. Thus, they proposed that all luminal cell types participate in the regeneration of the prostate gland.

Prostate adenocarcinoma is the major form of prostate cancer found in men. It is initiated by a hyper proliferation of luminal cells in the lumen of the gland<sup>140</sup>. In 2016, Drost and colleagues published a standardized protocol for establishing prostate organoid cultures from healthy prostate tissue, prostate cancer metastasis biopsies or circulating prostate tumor cells<sup>101</sup>. It appeared that the establishment of organoid lines from primary prostate tumor was not successful. As mentioned in several studies, organoids generated from healthy cells tend to overgrow, resulting in the loss of cancerous organoids<sup>113,152,153</sup>. The lack of a marker to isolate cancer cells remains a barrier for the establishment of organoid cultures from primary prostate tumors. Beyond this limitation, several studies reported the establishment of organoids derived from patients with advanced prostate cancer. The organoids in these studies were generated from metastatic tumors.

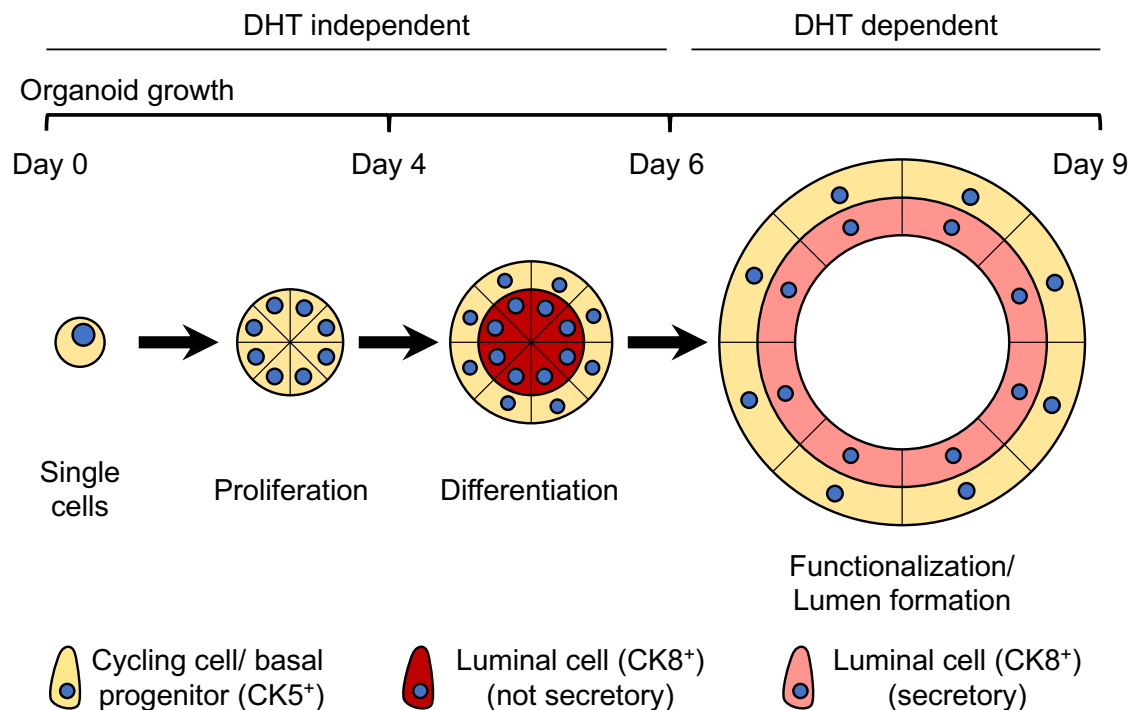


**Figure 16. Simplified model of prostate organoid growth.** Adult CK5<sup>+</sup> stem cells are embedded in the ECM with adapted medium at day 0. CK5<sup>+</sup> cells proliferate until day 4 when CK8<sup>+</sup> luminal cells start to appear in the center of the organoid. Under the influence of dihydrotestosterone (DHT), luminal cells will start to secrete fluid. The microlumen present between the luminal cells join by hydraulic fracturing of the cell junctions to form a mature lumen at day 9.

## Gene editing

Gene editing consists in modifying with precision the genome of a targeted cell. It consists in inactivating a gene, introducing a precise mutation, correcting a mutation or inserting a gene at a specific genomic site. Contrary to classical lentiviral vectors, which introduce genetic information randomly into the host cell genome, gene editing ensures a more physiological gene expression through precise modification of the gDNA thereby avoiding insertional mutagenesis and gene silencing. Gene editing relies on enzymes called nucleases that induce double strand breaks in the DNA (DSB). The cell repairs this DSB by two possible mechanisms, non-homologous end-joining or by homology directed repair when a DNA template with homologous sequences is present or delivered in the cell<sup>154</sup> (**Figure 17**).

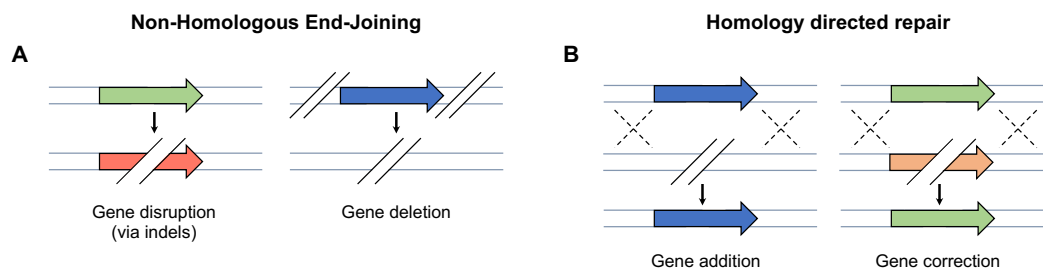


**Figure 17.** Overview of the possible repair and recombination reactions performed by the cellular machinery after a nuclease-induced DSB. DSBs induced by endonucleases can be repaired either by Non-Homologous End-Joining (NHEJ) or by Homology directed repair (HDR). (A) In the absence of a donor DNA template, the cell will repair the nuclease-induced double-strand break by making small nucleotide insertions or deletions called indels. These indels can lead to a frame shift which mostly causes a disruption of the targeted gene. If nucleases are guided by 2 or more gRNA to different positions in a gene simultaneously, this can result in large deletions. (B) In the presence of a donor DNA template with arms homologous to the sequence on either side of the nuclease-targeted locus, transgene insertion or correction or an endogenous gene is possible.

### I. Nucleases

Nucleases used for gene editing are chimeric enzymes composed of a non-specific DNA cleaving enzyme linked to a programmable DNA binding module. These enzymes generate DSBs in specific locations of the genome.

Historically, there are zinc finger nucleases and Transcription activator-like effector nucleases (TALENs). In the last decade, the Clustered Regularly Interspaced Palindromic Repeats, CRISPR-Cas9 technology has emerged. Many derivatives of the latter method have recently emerged<sup>155</sup>.

## A. ZFN-FokI

Zinc finger nucleases (ZFNs) are enzymes that consist of a DNA recognition domain called a "zinc finger" and a nuclease that non-specifically cuts the DNA<sup>154</sup> (**Figure 18A**).

Zinc fingers are originally present in many transcription factors. The zinc ion in the protein will play an important role in the three-dimensional conformation of the protein<sup>156</sup>. In transcription factors, these domains surrounding the zinc ion stabilize the interaction zone of the protein with the DNA. This part of the protein determines the selectivity of the protein to a specific DNA sequence.

More precisely, these zinc fingers are composed of about 30 amino acids. They are organized in two beta sheets and an alpha helix. Some amino acids, located at the C-terminal part of the protein, at the alpha helix, will be in contact with the double strand DNA. A classical alpha helix will be specifically linked to 3 nucleotides.

The modular structure of these zinc fingers has made them attractive to molecular biologists. It is indeed possible to design zinc fingers that bind specifically to a DNA sequence. Subsequently, 'synthetic' zinc fingers have been designed to recognize DNA sequences ranging from 9 to 18 bp. The enzyme usually coupled to these zinc fingers is the FokI endonuclease. This enzyme works when it is dimerized. Once dimerized, it will generate a DSB in the double strand DNA. In order to recognize non-palindromic DNA sequences, it was therefore necessary to synthesize two different zinc fingers coupled to FokI nucleases.

The zinc finger nuclease technology has been used for many years. It has now been largely replaced by other less expensive, laborious and time consuming approaches.

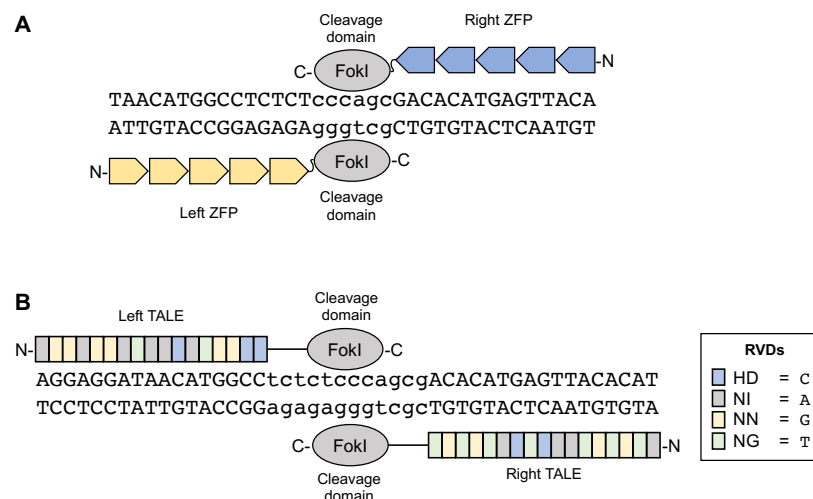


**Figure 18.** Simplified representation of the structure of zinc finger nuclease (ZFN) and transcription activator-like effector nuclease (TALEN). (A) Scheme representing a zinc finger dimer bound to a DNA sequence. Each zinc finger recognizes 9 to 18 bp of DNA. The two zinc finger binding sites are separated by 5 to 7 nucleotides. This sequence is cleaved by FokI. (B) Scheme representing a dimer of TALEN bound to DNA. The two TALE binding sites are separated by 12 to 20 bp. This sequence is cleaved by FokI. Each individual TALE recognizes via its variable amino acids a specific nucleotide. They are called Repeat-variable diresidues (RVD).

## B. TALENs

Transcription activator-like effector nuclease, also called TALENs, are proteins composed of a DNA recognition domain and a restriction endonuclease that cuts DNA in an unspecific manner<sup>154,156,157</sup>.

TALENs which come from the plant pathogenic bacteria genus *Xanthomonas* are proteins composed of series of 33 to 35 identical amino acids (**Figure 18B**). Only two highly variable amino acids located generally at position 12 and 13 will specifically recognize a nucleotide. Like zinc fingers, TALENs can be assembled to form proteins that will specifically recognize longer DNA sequences.

Thus, TALENs are composed of an N-terminal nuclear localization signal (NLS), a series of 10 to 30 TALE domains, and a C-terminal FokI restriction endonuclease.

As for zinc fingers, since FokI operates as a dimer, it was necessary to generate two locus-specific TALEs. The restriction enzymes FokI dimerize and induce DSBs.

This method has also been used extensively, despite some limitations. Indeed, the TALENs were sensitive to the methylation of the targeted DNA. The fact that the sequence encoding the TALENs are highly repeated did not favor an ideal packaging in viral vectors since these repeat can induce recombination during vector production.

## C. CRISPR

### 1. Origin of CRISPR system

Research conducted in the 2000s showed the existence of short interspersed repeats in the genome of *Escherichia coli*<sup>158,159</sup>. They were named clustered regularly interspaced palindromic repeats (CRISPR). Subsequent studies showed that the short sequences contained in the CRISPR locus were derived from viral or plasmid sequences<sup>159,160</sup>. With the discovery that the gene located in the CRISPR locus, called cas (CRISPR-associated) encodes a protein with a helicase domain and a nuclease domain, the CRISPR-Cas system was proposed as a bacterial defense system against phages<sup>159-161</sup>.

This immune system works in three phases. We first see an insertion of a viral DNA fragment between the repeated sequences of the CRISPR locus, then we have the transcription of a precursor CRISPR RNA. This one is cut into individual crRNAs (**Figure 19A**). It is composed of a repeated segment and a viral DNA fragment. Finally, the Cas protein coupled to the crRNA cuts the viral DNA complementary to the crRNA<sup>159</sup>.

Three systems have been identified (type I, II and III). The type II system uses a single Cas protein for RNA-guided DNA cleavage (**Figure 19B**). This system is the most versatile and useful for genome engineering applications<sup>159</sup>.

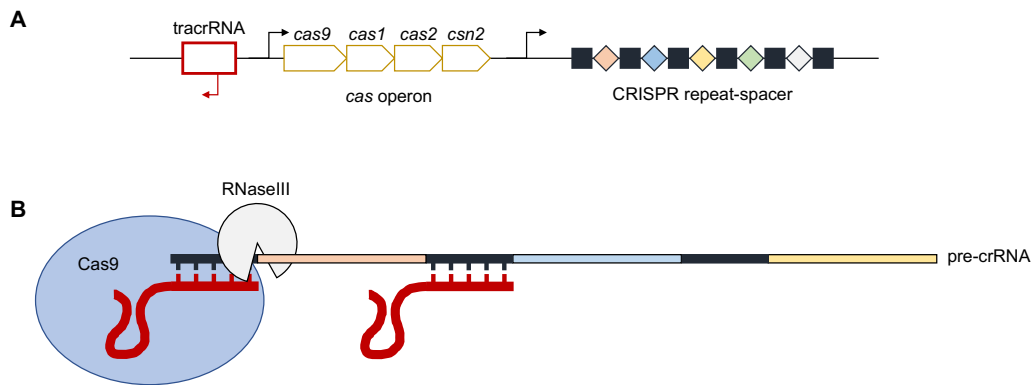


**Figure 19.** Type II CRISPR-Cas system. (A) Genomic CRISPR locus. The operon coding for Cas proteins, the repeated sequence interspaced with viral DNA fragment and the tracrRNA sequence. (B) Maturation of the tracrRNA with the crRNA and complex formation with the Cas9. The ribonuclease III (Rnase III) processes the pre-crRNA by cutting it into individual crRNA (modified from <sup>159</sup>).

## 2. How does the CRISPR Cas9 system function

In the CRISPR-Cas9 system, the nuclease is coupled to a crRNA. It is composed of 42 nucleotides, 20 compose the protospacer sequence, and the 22 are the repeat sequence. The trans-activating crRNA (tracrRNA) is necessary for the maturation of pre-crRNA by RNase III. The crRNA coupled with tracrRNA guides Cas9 to the target DNA. If there is an adjacent sequence called protospacer adjacent motif (PAM), NGG for Cas9, the Cas9 creates 3 bp upstream of the PAM sequence a DSB (**Figure 20**).

It has been reported that Cas9 is composed of two nuclease domains. These two sites are responsible for Cas9-induced DSBs. Cas9 uses a domain called HNH to cleave the DNA strand complementary to the crRNA sequence. The RuvC-like domain cleaves the opposite strand of DNA (**Figure 20**). If one of these sites is mutated, this produces a Cas9 that generates single-stranded DNA cleavage (nickase).

The tracrRNA coupled to crRNA was then engineered and simplified to form a single guide RNA (sgRNA). The 3' double stranded portion is required to bind to Cas9.

Only the last 20 nucleotides of the sgRNA are needed to program Cas9 to cleave DNA at a specific locus as long as it is adjacent to a PAM sequence.

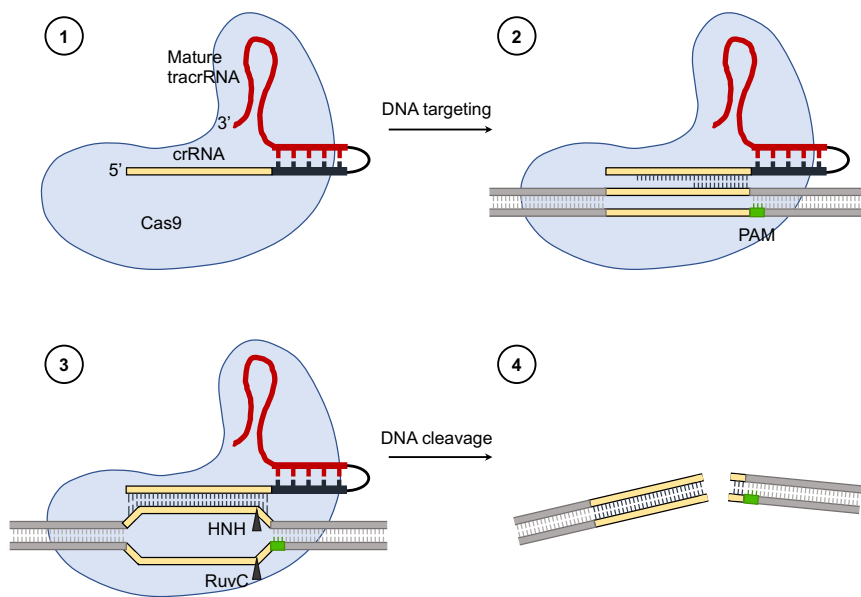


**Figure 20.** RNA guided DNA cleavage of genomic DNA. A single guide RNA (sgRNA) is represented in the scheme. (1) Cas9-sgRNA complex. (2) The Cas9-sgRNA complexes links to the target gDNA. (3) Formation of the R-loop. (4) Cleavage by the two nuclease domains HNH and RuvC of the double-stranded DNA target 3 bp upstream of the PAM sequence.

### 3. Cas9 off-targets

It has been reported that the CRISPR-Cas9 system has more off-target effects than other specific nucleases<sup>154</sup>. The majority of the off-target effects of the CRISPR-Cas9 system is conditioned by the specificity of the sgRNA. It has been shown, using catalytically inactive Cas9, that it binds to sites other than the one targeted by the sgRNA. However, active Cas9 though rarely can cut into off-target sites and therefore this needs to be carefully evaluated especially in the case of therapeutic gene editing applications. Indeed, if the crRNA is not perfectly complementary with the DNA strand, Cas9 will cut with much lower efficiency.

Unpredicted off-target effects raise concerns if this technology is used in gene therapy. Scientists need to know if the guide RNAs they use can create unwanted off-target DSBs. To answer this question, bioinformaticians have developed tools that can predict whether a guide RNA will be likely to cleave at off-target sites. Tools like TagScan<sup>162</sup>, Bowtie<sup>163</sup> can be used but they are limited by the number of mismatches and the PAM sequence used. Indeed, potential off-target sites will be classified according to the number of mismatches detected. The mismatches correspond to the number of base pairs that change compared to the correct target sequence. An off-target site with three mismatches means that 3 base pairs are different. A site with 4 or 5 mismatches will be less prone to be cleaved than a site with 1 or 2 mismatches<sup>164</sup>. The main tool I used here is CasOFFinder<sup>165</sup>. The advantage of CasOFFinder over the others is that it is not limited by the number of mismatches and can search for off-target sites with PAM sites of different Cas9. For example, 5'-NGG-3' for SpCas9, 5'-NNGRRT-3' (R=A or G) for a Cas9 from *Staphylococcus aureus*.

Once translated, these sites are experimentally amplified and analyzed by Sanger sequencing. To visualize and quantify the percentage of indels on or off target, there are open access sites like DECODR or ICE. Deconvolution of Complex DNA Repair (DECODR) is a deconvolution algorithm that can detect Cas9-induced indels from clonal or bulk cell genome sequencing. It can detect deletions of several hundred bp and identify the bases inserted in the DSBs<sup>166</sup>. Whole genome sequencing is also used to detect off-target effects as a more unbiased method. Indeed, it allows the detection of off-targets, or chromosomal rearrangements<sup>167</sup>. The prediction and analysis of off-targets is greatly facilitated by the open access availability of all these tools. Without having to change techniques, this kind of preliminary study allows to minimize the undesirable effects, and thus to optimize the experimental procedures.

## II. Delivery of Cas9 and sgRNA

To efficiently edit a cell, the delivery system of the editing machinery must be adapted to the cell model used. Here I present the characteristics, advantages and disadvantages of the different types of delivery systems used in cells, with a focus on organoids (**Table 1**).

A first distinction is to be made when talking about delivery methods. We can either talk about the cargo or the vehicle.

Cargo : DNA plasmids, single strand DNA, mRNAs, or RNPs

There are four main methods to bring the Cas9-sgRNA machinery into a cell: (1) plasmids encoding the Cas9 endonuclease and sgRNA; single strand DNA (2) and mRNAs (3) that code for Cas9. In that case, the sgRNA is co-delivered; and finally ribonucleoproteins (RNPs) for which the Cas9 is delivered as a protein complexed with the sgRNA.

If we do not consider yet the type of vehicle used, the major difference between these types of cargos is on the off-target effects. Indeed, single-stranded DNA sequences can easily be integrated into the genome of the targeted cell. This can lead to gene disruption, and more importantly, if the Cas9 coding sequence is integrated, it will be constitutively expressed in the cell. This increases considerably the off-target effects such as cellular toxicity or cell cycle arrest induced by Cas9.

For the mRNA approach, the advantage is that when introduced into the cytoplasm of a cell Cas9 is directly translated and associated with sgRNA. Providing the machinery as mRNA ensures a time-limited presence of the endonuclease, which may help to reduce off-target effects.

Providing Cas9 as a protein will still reduce its presence in the cell. Compared to plasmids that will express Cas9 for a relatively long time, RNPs will be rapidly degraded in the cell. The use of RNPs has been shown to decrease the off-target effects.<sup>154</sup>

Delivery vehicle

To deliver the cargo into the cells, there are two major class of vehicles: non-viral vehicles and viral vehicles. Microinjection, electroporation are the most used non-viral techniques. The most used viral vectors for delivery of the gene editing system are adenovirus, retrovirus and lentivirus<sup>154</sup> (**Figure 21**).

Each of these delivery techniques will be more or less adapted to the targeted model, such as *in vivo*, or *in vitro*. Also, the vehicles are only adapted to certain types of cargo, which also confers advantages or limitations. Both, viral and non-viral techniques have been used successfully to edit cells *in vitro*. However, for some applications, the main limitation is the manipulation of the target cell. As with *ex vivo* cell manipulations, some *in vitro* models, such as organoids, are sensitive to manipulation and culture conditions. These drawbacks limit the types of vehicles that can be used. In general, for *in vivo* studies, viral vectors will be more suitable due to their higher efficiency compared to non-viral systems. However, viral vectors are limited by their packaging capacity, but also by their production costs (adeno-associated virus).

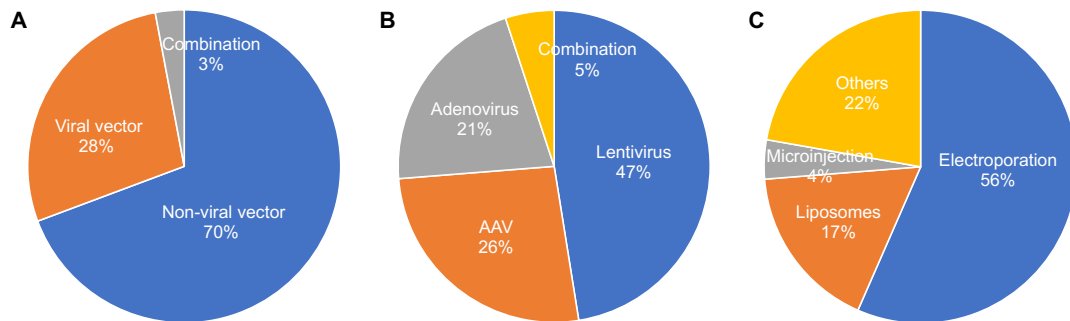


**Figure 21.** Delivery strategies for gene-editing studies. Percentage of therapeutic gene editing of non-clinical development based on (A) delivery system, (B) viral vector type, (C) non-viral type. Figure modified from Shim 2017. These figures, representing the percentage of use of each system for therapeutic gene editing and gives a general idea of the state of the art regarding the most used techniques. Modified from <sup>168</sup>.

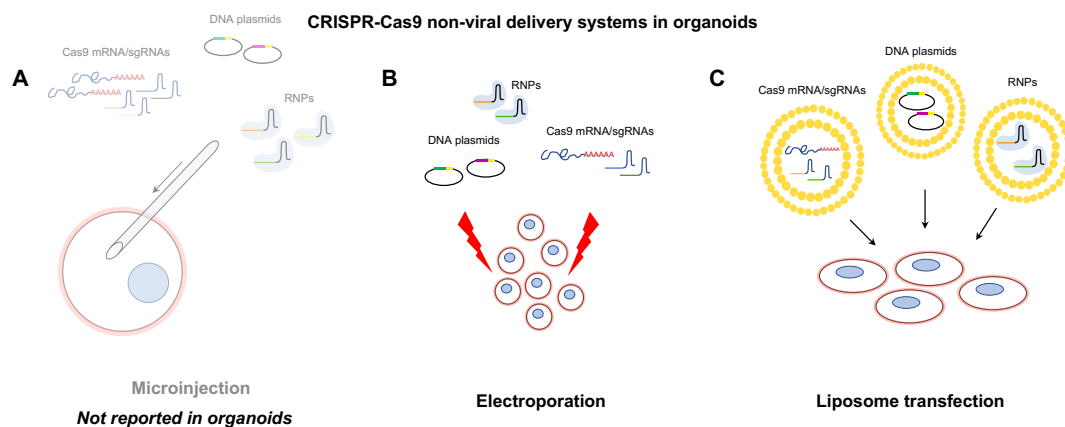


**Figure 22.** Non-viral methods for delivery of CRISPR-Cas9 components in organoids. (A) Microinjection allows integration of plasmids, mRNAs coding for Cas9 and sgRNAs or RNPs. Despite its great efficiency for mice embryos gene editing, microinjection has never been used to edit organoids. (B) Electroporation of plasmids encoding for the Cas9 and sgRNAs is today the most used technique in organoids. (C) Liposome transfection of plasmids coding for the Cas9 and sgRNAs has been used at the very beginning for organoid gene editing. This last approach has been largely replaced by other more efficient techniques.

**Table 1.** CRISPR delivery system: common feature, advantages and limitations. Table modified from Lino 2018.

Delivery vehicle	Composition	Cargo	Capacity	Advantages	Limitations	Used in organoids	Organoid text refs
Microinjection	Needle	DNA plasmid ; mRNA ; RNPs	nMs of Cas9 sgRNA	Guaranteed delivery on cell of interest	Time consuming Difficult	not reported	
Electroporation	Electric current	DNA plasmid ; mRNA ; RNPs	nMs of Cas9 sgRNA	Delivery to cell population	Harsh for cells Low efficiency	+++	Beumer <i>et al.</i> 2021 Sun <i>et al.</i> 2021, Geurts <i>et al.</i> 2021, Artegiani <i>et al.</i> 2020, Artegiani <i>et al.</i> 2019, Fujii <i>et al.</i> 2015, etc.
Liposome transfection	Natural or synthetic lipids	DNA plasmid ; mRNA ; RNPs	nMs of Cas9 sgRNA	Simple manipulation; Low cost	Low efficiency	++	Fujii <i>et al.</i> 2015, Drost <i>et al.</i> 2015, Schwank <i>et al.</i> 2013
Adeno-associated virus (AAV)	Non-enveloped, ssDNA	DNA plasmid	<5kb nucleic acid	High efficiency delivery Minimal immunogenicity	Low capacity	+	Garita-Hernandez <i>et al.</i> 2020
Lentivirus (LV)	Enveloped, RNA	DNA plasmid	10kb nucleic acid	High efficiency delivery Persistent gene transfer	Prone to insertional mutagenesis; High off-target with stable Cas9 expression	+	Sun <i>et al.</i> 2021
Virus-like particule (VLP)	Enveloped or non-enveloped, protein	RNPs	nMs of Cas9 sgRNA	High efficiency delivery Transitional transfer	Specific cell tropism	In progress	Tiroille <i>et al.</i> submitted

## A. Non-viral vehicle

### 1. Microinjection

Microinjection is one of the most efficient techniques to insert CRISPR machinery inside cells. In 2013, the study published by Yang et al showed editing levels close to 100% using CRISPR-Cas9<sup>169</sup>. They developed a technique to easily create mice with fluorescent tag reporters in endogenous genes. With microinjection, plasmids encoding Cas9 and sgRNAs, mRNAs encoding Cas9, or Cas9 protein with sgRNA can be used to be inserted inside cells<sup>170</sup>.

Technically, it uses fine needles that will pass through the cytoplasmic and/or nuclear membranes to deliver the CRISPR components inside the targeted cellular compartment. Studies have compared several possible injection methods: plasmid injection into the nucleus, RNA injection into the nucleus or into the cytoplasm<sup>170</sup>. Here, RNA injection into the cytoplasm is the most efficient technique for generating blastocyst stage embryos and full-term pups<sup>171</sup>. Microinjection also allows the injection of RNPs into cells<sup>172</sup>.

The versatility of this technique allows the injection of almost any type of cargo. In addition, microinjection has no real limitation in the size of the cargo to be injected; unlike viral vectors. Controlling the nature and quantity of the cargo injected into the cells allows to avoid off-target effects as much as possible. Indeed, mRNAs and RNPs have a limited life span in the cell<sup>173</sup>, which reduces off-target effects. Moreover, the toxicity for the cells is low when a single injection is performed<sup>169</sup>.

Thus this technique offers a versatility of approach and a low toxicity for the cells. However, this technique is limited to *in vitro* or *ex vivo* approaches, as a microscope is required to do so. Surprisingly, despite these advantages, no studies using the organoid model have used this technique.

### 2. Electroporation

Electroporation is a physical method to deliver the CRISPR-Cas9 machinery inside a cell. During electroporation, cells are resuspended in an appropriate buffer. The cells are subjected to a pulsed high-voltage electric current to create nanometer-sized pores in the cell membrane, which allows the DNA or RNA to enter the cell. Electroporation is an effective method in many cell models. However, like microinjection, electroporation is not suitable for *in vivo* models<sup>154</sup>. There are many protocols for electroporation in eukaryotic cells. Nucleofection is a type of electroporation where the CRISPR package is delivered directly into the nucleus of the cell. The advantage of nucleofection is that it allows the delivery of DNA encoding Cas9 or RNPs directly into the nucleus without breaking the membrane of the nucleus, which is very useful for quiescent cells. A study not yet published, done by the group of Emma L. Rawlins reported the use of nucleofection for organoid CRISPR engineering<sup>174</sup> (**Figure 22**).

Electroporation for delivery of Cas9 encoding plasmid to human colon organoid has been reported<sup>175</sup>. The use of electroporation in the organoid model was shown to be more effective than other delivery methods, such as liposomal transfection. They optimized the electroporation protocol by modifying electroporation buffer, and adjusting the cell manipulation procedure. They reached 30% of transduction efficiency of the piggyBac vector. Nonetheless, only 0.04 % of electroporated organoids were puromycin resistant.

To counteract this low level of knock-out obtained in the organoid model, several studies have developed knock-in systems to visualize the edited cells. Despite the ease with which this type of system can be used, the level of gene editing is still very low, i.e. it never exceeds 5 to 10%<sup>174,176</sup>.

Another study published in 2014, reported the use of electroporation to deliver RNPs into primary human cells. Compared to electroporation of plasmid, the RNPs were less cytotoxic for the cells. They were reaching a twofold increase of embryonic stem cell (ESC) colony formation with the electroporation of RNPs compared to plasmid electroporation<sup>177</sup>.

Regarding the toxicity of the methods, if the buffer and the voltage are not adjusted to the used cell, the technique can be harsh for the cell, and even though it is well adjusted, the level of cell death remains quite high.

Overall, electroporation remains a major technique to efficiently deliver CRISPR-Cas9 components *in vitro*.

### **3. Liposome transfection**

Liposome transfection combines cargos and a lipid solution<sup>154</sup>. The positive charges provided by the lipid will surround the negative charges carried by the DNA. Once the DNA is encapsulated, the lipid particle can fuse to the cytoplasmic membrane. By fusing to the membrane of the targeted cell, the liposomes will release and introduce into the cytoplasmic compartment the genetic material. The plasmid DNA will then be imported into the nucleus, where the transcription of the Cas9 encoding gene will take place.

Lipid nanoparticles have been used for a long time for the transfection of many molecules in a wide variety of *in vitro* models.

From a safety point, liposomes do not contain any viral material, which minimizes the risks compared to viral vehicles.

A study published in 2016 reported the use of lipid nanoparticles to transfect negatively supercharged Cre or Cas9/sgRNA complex. Because Cas9 coupled with sgRNA is negatively charged, the lipofectamine reagent is perfectly suited to deliver this cargo inside a cell<sup>150,178</sup>.

Some of the first genetic manipulation of organoid with CRISPR-Cas9 method were performed using lipofectamine transfection. In a study published by Clevers' group in 2013, they used Lipofectamine-mediated transfection to integrate a Cas9 expressing plasmids and sgRNAs<sup>142</sup>. With this technique they were successfully repairing a CFTR mutation in intestinal stem cell organoids of cystic fibrosis patients. In a latter paper, published by the same group, thanks to CRISPR-Cas9 approach using lipofectamine transfection, they induced sequential cancer mutations in cultured human intestinal stem cells<sup>139</sup>. Despite these studies, a paper published by Sato's team in 2015, assessed that using the best suitable Lipofectamine reagent for organoids, they did not exceed 0.02% of transduced organoid<sup>175</sup>.

As for viruses, lipid nanoparticles are limited in the size of the cargo they can carry. Also, it appears that once internalized, some of the lipid nanoparticles are degraded via the lysosomal pathways<sup>154</sup>.

Different studies compared the efficiency of lipofectamine transfection with electroporation<sup>175,179</sup>. It appears that both of these studies concluded that electroporation was more efficient than lipofectamine to introduce Cas9 and sgRNA components inside cells.

Overall, lipid nanoparticles have been useful for many applications. However, for some models, like with organoids, they reached some limits and tend to be abandoned for more efficient techniques, such as electroporation or viral vectors.

## **B. Viral Vectors**

Viruses have evolved to deliver their genomes inside a cell efficiently. This is essential for their replication. Scientists have taken advantage of these aspects, and have modified them into non-replicating particles so that they can deliver genes of interest into cells. This process is called transduction.

Viruses have long been used for genetic manipulation of cells. The efficiency of the best viral vectors can reach 100% transduction of the targeted cells. Of course, this depends on the type of vector used and the cell transduced<sup>180</sup>.

### **1. AAV**

Adeno-associated viruses (AAV) are viruses capable of infecting humans and other animal species but are not currently known to cause disease. They are of the Dependovirus genus and of the family Parvoviridae. They are small, non-replicating, non-enveloped viruses. Their genome is composed of single-stranded linear DNA, and measures approximately 4.5 to 5 kb<sup>181,182</sup>.

Because of the small packaging capacities of AAVs, encapsidation of a 4.2kb plasmid encoding for both Cas9 and the sgRNA has been challenging and remains up to now inefficient. Even if the packaging of the vector genome encoding for the gene editing tools is successful, it remains limiting if one wants to introduce additionally a donor DNA template to perform a knock-in. For example, a commonly used fluorescent tag protein like mNeonGreen measures 0.7kb. Its addition into an AAV vector resulting in more than 4 kb is not very efficient. To overcome these limitations, some approaches use AAVs to just deliver sgRNAs into cells already expressing Cas9<sup>183</sup>.

In another approach, they chose to use a dual-vector system where Cas9 and sgRNAs were packaged in two separate vectors<sup>184</sup>. This type of approach allows to bring other genetic material than only Cas9 and sgRNA. An advantageous of using AAV as a delivery system for the gene editing machinery is that it is not integrating its vector genome into the target cell but remains as episomal only transiently in the cell limiting Cas9 induced toxicity.

A study published in 2015 showed the use of a Cas9 from *Staphylococcus aureus* to do genome editing *in vivo*<sup>185</sup>. The Cas9 from *Staphylococcus aureus* is 30% smaller than the Cas9 classically used (which comes from *Streptococcus pyogenes*). This allows the use of a single vector encoding to deliver the Cas9 and the sgRNAs. However, this type of Cas9 uses a different PAM sequence, which may become a limitation in the target cell of interest.

In the organoid model, AAVs have been used for gene delivery into retinal organoids derived from Human Induced Pluripotent<sup>186</sup>. Other than that example, no studies have been reported.

## 2. Retroviral vectors

Retroviruses are viruses with an RNA genome. These viruses have the necessary machinery to reverse transcribe their genome into double-stranded DNA when they infect a cell. The viral genome in the form of dsDNA is inserted into the host cell genome through integrases encoded by the virus. The host cell transcribes and translates the viral genome as its own gDNA. This allows the virus to be replicated.

This type of virus began to be used 40 years ago when it was shown that the delivery of genetic information by retroviruses was more efficient than DNA transfection. This type of study opened the way to developments in the field of gene therapy<sup>187</sup>. Since then, viral vectors have been engineered based on different members of the Retroviridae family. They have been derived from Human Immunodeficiency Virus (HIV-1)<sup>188,189</sup>, Murine Leukemia Virus (MLV), Bovine Leukemia Virus<sup>190</sup>, Rous Sarcoma Virus (RSV)<sup>191</sup>, Spleen Necrosis Virus (SNV)<sup>192</sup>, and Mouse Mammary Tumor Virus<sup>193</sup>.

The most commonly used viral vector is derived from the Murine Leukemia Virus, since they can transduce and integrate into many cell types in the human body. However, these MLV vectors are not capable of transducing quiescent, non-proliferative cells. In contrast, lentiviral vectors, based on HIV, are capable of transducing non-proliferative cells. These capabilities have made these lentiviral vectors useful for many research and clinical applications.

Lentiviruses (LV) derive their names from their long incubation period in human or animal cells. The most characterized lentivirus is the human immunodeficiency virus (HIV). As mentioned earlier, they are able to infect non-dividing cells. This characteristic makes these viruses extremely effective in delivering genetic content into cells. Another advantage of LVs is their much larger size than other viruses such as AAVs, i.e. 80 to 100nm for LVs versus 20nm for AAVs<sup>154</sup>. As a consequence these LV can encode larger expressing cassettes in their genome of up to 10kb.

These viral vector particles are produced by transfections of some of the structural and functional viral components into HEK 293T cells. As detailed in the figure, the viral particles will be assembled in the cytoplasm of the cell and secreted into the supernatant (**Figure 23**).

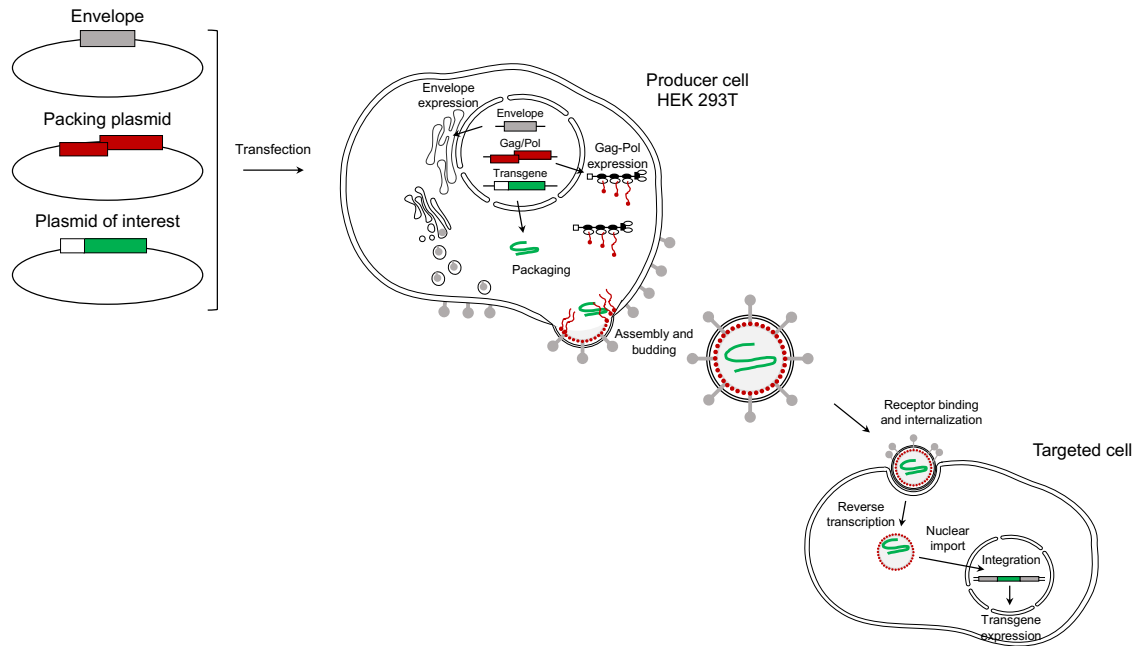


**Figure 23.** Lentiviral production process and transduction of a targeted cell. HEK 293T cells are transfected with the plasmids coding for envelope, gag, pol, and the transgene of interest (Cas9 and sgRNAs for example). Once the viral particle is produced and assembled, the viral suspension is collected, concentrated and used to transduce targeted cells.

From a safety point of view, three generations of packaging systems have been developed. In the first system, all HIV-1 genes except the envelope are encoded by a plasmid. The second generation system (the most commonly used) is deleted from all accessory genes: vpr, vif, vpu, and nef. It consists of three plasmids encoding (1) the transgene, (2) Gag, Pol, Tat, and Rev, and (3) the coat. The most commonly used envelope is the envelope of vesicular stomatitis virus (VSVG) because it allows entry into many different cell types. We are talking about a broad tropism. Finally, the third generation system includes Gag, Pol, Rev and Tat, each encoded by separate plasmids.

These second and third generation systems offer maximum biosafety. The transfection of 3, 4 or 5 plasmids considerably reduces the possibilities of recombination that can generate a replication competent vector.

Many research studies have used LVs as a vehicle to integrate the CRISPR-Cas9 machinery into targeted cells. In this case the lentiviral vector encoded Cas9 and sgRNAs<sup>194</sup>.

Given the high transduction capacity of LVs, research groups have also used them to create libraries of sgRNAs. Indeed, these studies tested tens of thousands of sgRNAs in cells previously modified to express Cas9. This type of genomic screen allows to identify new therapeutic targets in the long term, and in the shorter term to understand certain cellular mechanisms still unknown today.

In the organoid field, only a very recent, not yet published study used LVs to deliver the CRISPR-Cas9 machinery<sup>174</sup>.

Lentiviruses are very efficient tools to edit genome by bringing Cas9 and sgRNAs encoding plasmids into a cell. Despite this high level efficiency, one drawback still remains. Indeed, these vectors mediate stable integration of a gene encoding Cas9 into the host cell, which increases the risk of off-target effects. To counteract these problems, LVs containing a mutated integrase have been developed. In this case the vector genome remains in the cell as episomal DNA circles

### **3. Virus-like particles for introduction of the gene editing machinery**

Virus-like particles are particles devoid of a viral genome, but form virion like particles consisting of viral structural proteins. These vehicles, like liposomes, will deliver the proteins or nucleotide sequence they contain into the cells they target. Since they have no viral genome, VLPs do not conserve a replication capacity.

VLPs were developed when a 1979 study showed the reconstitution of the glycoprotein of VSV in liposomes<sup>195</sup>. Since then studies have shown that VLPs allow for much higher levels of DNA content delivery inside a cell than classical transfection.

Note that there are two main classes of VLPs, i.e. VLPs with a envelope and VLPs without a envelope. If they have a envelope, they will go through a budding step. This step is crucial for the acquisition of an envelope<sup>196</sup>.

Recently, a technology based on a virus-like particle (VLP) derived from a murine leukemia virus (MLV) has been developed<sup>197,198</sup>. This technology consist in using these VLPs to introduce into the cells the Cas9/sgRNA ribonucleoproteins. This system, called nanoblades, carries the Cas9 proteins complexed with the sgRNAs, which allows a very quick and transient delivery of the gene editing machinery into the targeted cells. In this system, the Cas9 protein is fused with the viral structural Gag protein. This, ensures the encapsidation of RNPs.

### **4. Pseudotyping of viral vectors or virus-like particles**

Pseudotyping consists in producing viral vectors with viral glycoproteins from heterologous viruses. This surface modification determines the host range of the viral vectors or VLPs produced. The resulting vector will have the tropism of the virus from which the envelope was employed. Pseudotyping will alter or improve viral titers, packaging efficiency, stability, cell tropism, and transduction efficiency. The production of a viral vector with modified envelope glycoproteins will be performed by providing plasmids coding for different glycoproteins during their production. Among the most widely used pseudotyping envelopes, we find the vesicular stomatitis virus G protein (VSV-G)<sup>199,200</sup>. This envelope is widely used by scientists for pseudotyping of retroviral vectors because of its very broad tropism, high titers, and stability.

## VSV-G

Vesicular stomatitis virus (VSV) is an RNA virus belonging to the Rhabdoviridae family. This virus naturally infects insects and many mammals. Its 11kb genome allows it to code for five major proteins. It encodes for a G surface protein that allows it to infect a wide range of cells. This G protein allows it to anchor to the cell via the LDL receptor (LDL-R) which is expressed by many cell types<sup>201</sup>.

VSVG has been shown to be very stable and effective in transducing many cell types. This envelope also allows for good packaging of the viral material, resulting in high viral titer.

## BaEV

Baboon endogenous retrovirus was isolated from a specimen of baboon placenta cocultivated with other mammalian host cell lines<sup>202</sup>.

Recent studies have shown that pseudotyping of LVs with BaEV envelope outperformed VSVG based lentivirus for gene transfer into cytokine stimulated or resting hematopoietic cells such as B, NK and T cells and hematopoietic stem cells<sup>200</sup>. A study released in 2019 was reporting how baboon envelope glycoprotein pseudotyped lentiviral vectors (BaEV-LVs) were outperforming other LV pseudotypes for transduction of naive adult and fetal interleukin-7–stimulated T cells. Indeed, BaEV-LVs efficiently transduced thymocytes and T-cell progenitors generated by culture of CD34+ cells in the presence of Delta-like ligand 4.<sup>203</sup> It has also been shown that these BaEV-LVs were allowing efficient NK-cell transduction. They reached in that study a transduction rate of 23.0% in freshly-isolated human NK-cells and 83.4% in NK-cells obtained from the NK-cell Activation and Expansion System<sup>204</sup>, where classical VSV-G pseudotyped lentiviral vector only reached 5 %.

Another study described and characterized VLPs to efficiently vectorize the CRISPR-Cas9 system into primary cells, embryos, and animals. Since VLPs are similar to viral vector but they do not carry a viral genome it is also possible to explore diverse pseudotyping options for VLPs. In a recent study they finally used VSVG and the Baboon Envelope in combination, which systematically displayed the best cleavage results in most recipient cells. This system allowed to do genome editing in primary cells and *in vivo*<sup>197</sup>.

A later study showed how baboon envelope pseudotyped nanoblades carrying Cas9/gRNA complexes allowed efficient genome editing in human T, B, and CD34+ cells . A brief incubation of human T and B cells with nanoblades incorporating two gRNAs resulted in 40 and 15% edited deletion in the Wiskott-Aldrich syndrome gene locus, respectively.

Pseudotyping with other envelope gps thus allows to overcome the limits of a classical vectors pseudotyped with VSV-G envelope. It allows to increase its tropism and consequently to increase the transduction efficiency of viral vectors in cell types that are not easily transduced or genetically edited.

## **SCIENTIFIC BACKGROUND AND OBJECTIVES**



## **Scientific background and objectives**

During my thesis, I worked on the prostate organoid model with two main objectives: (1) to develop genome engineering techniques and (2) to study the role of the UBTD1 protein.

(1) to develop genome engineering techniques in organoids

The first objective of my thesis is to develop genome engineering techniques adapted to the organoid model. As mentioned in the introduction, genome editing in organoids using the CRISPR Cas9 technique remains challenging. The low levels of editing efficiency are mainly due to the type of cargo and delivery vehicle used. Here, we develop the use of Nanoblades to edit the genome of organoids.

(2) to study the role of UBTD1 in prostate development in organoids.

The second objective of my thesis is to study the role of Ubiquitin domain-containing protein 1 in the prostate epithelium. My laboratory showed that this protein is involved in the degradation of several proteins in different contexts. For example, it was shown that UBTD1 participated in the degradation of the transcriptional regulator yes-associated protein (YAP) by modifying its ubiquitination level in prostate cancer cells (Torrino et al 2019). Here we decipher the role of the UBTD1 protein in the homeostasis and development of the normal prostate epithelium. UBTD1 has been shown to be localized at cell-cell contacts. We therefore focused on its role in cell-cell junctions in normal prostate epithelium.



## **RESULTS**



**Manuscript 1**



## **Nanoblades allow high-level genome editing in organoids**

Victor Tiroille<sup>1,\*</sup>, Adrien Krug<sup>1,\*</sup>, Emma Bokobza<sup>1</sup>, Frédéric Larbret<sup>1</sup>, Alejandra Gutierrez-Guerrero<sup>2</sup>, Louise Medaer<sup>3</sup>, Philippe Mangeot<sup>2</sup>, Frédéric Bost<sup>1#</sup> and Els Verhoeyen<sup>#1,2</sup>

<sup>1</sup>Université Côte d'Azur, INSERM, C3M, 06204 Nice, France

<sup>2</sup>CIRI – International Center for Infectiology Research, Inserm, U1111, Université Claude Bernard Lyon 1, CNRS, UMR5308, Ecole Normale Supérieure de Lyon, Université Lyon, F-69007, Lyon, France

<sup>3</sup>Laboratory for Viral Vector Technology & Gene Therapy, Department of Pharmaceutical and Pharmacological Sciences, Faculty of Medicine, Katholieke Universiteit Leuven, Leuven, Belgium

\* Equal contribution

# co-senior

Keywords : Genome editing, CRISPR, Nanoblade, organoid, knock-out

Acknowledgement : This work has been supported by the French government, through the UCAJEDI Investments in the Future project managed by the National Research Agency (ANR) with the reference number ANR-15-IDEX-01. V.T. and A.K. are supported by the French Ministry of Research. FB is a CNRS investigator.

# Nanoblades allow high-level genome editing in organoids

## Abstract

Genome engineering has become in the last few years more accessible thanks to the RNA programmable endonucleases such as the CRISPR-Cas9 system. However, using this editing technology in synthetic organs called ‘organoids’ is still very inefficient. This is due to the delivery methods used for the CRISPR-Cas9 machinery, which are mainly performed by electroporation of RNPs containing the CAS9-gRNA complex, a procedure toxic for the organoids. Here we describe the use of the ‘Nanoblade’ technology to accomplish genome editing in organoids. Nanoblades outperformed by far knockout levels achieved with other techniques used to date for delivery of the gene editing machinery. We reached up to 80% of gene knockout in organoids after treatment with nanoblades. We achieved high-level nanoblade-mediated KO for the androgen receptor (*AR*) encoding gene and the cystic fibrosis transmembrane conductance regulator (*CFTR*) gene with single gRNA or dual gRNA containing nanoblades. Most importantly, in contrast to other gene editing methods, this was obtained without toxicity for the organoids. Moreover, it requires only four weeks to obtain stable lines of a gene KO in organoids and no obvious unwanted INDELS in off-target site in the genome were detected. In conclusion, nanoblades simplify and allow rapid genome editing in organoids with little to no side-effects.

## INTRODUCTION

Organoids are a self-organized three-dimensional (3D) culture system derived from adult stem cells (ASCs)<sup>1-3</sup>. They recapitulate architecture, composition and functionality of their original epithelial tissues better than the traditionally used two-dimensional immortalized cell lines<sup>4,5</sup>. This model can be used to study stem cell differentiation and spatial organization processes<sup>6</sup>. Thus, organoid technology is ideal for deciphering the role of genes involved in organogenesis or human pathologies<sup>7,8</sup>. Therefore, engineered mouse tissue-derived organoids and organoids derived from human ASCs require efficient approaches to edit the genome *in vitro*<sup>9-14</sup>.

Gene editing consists in manipulating the genome to induce gene silencing, gene modification or transgene integration at a precise locus<sup>15</sup>. In contrast to ectopic DNA sequence integration using integrative vectors, genome editing allows more physiological gene manipulation. Genome editing also avoids gene silencing and adverse mutagenic effects such as insertional mutagenesis. Gene editing is based on the induction of double strand breaks (DSBs) at a precise locus<sup>16</sup>. It relies on engineered nucleases with a sequence specific genomic DNA-binding domain coupled to a non-specific endonuclease. Several engineered nucleases have been developed, such as zinc finger nucleases (ZFN), transcription activator-like effector nucleases (TALENs)<sup>17</sup>. More recently, clustered regularly interspaced short palindromic repeats (CRISPR)/associated protein 9 (Cas9) has been introduced in the field. The CRISPR-Cas9 technology is based on an endonuclease that uses a single guide RNA sequence (sgRNA) to introduce a site-specific DSB in the targeted DNA. The most common repair that occurs after a DSB is non-homologous end-joining (NHEJ). This consist in the fusion of the two DNA ends and can lead to the insertion or deletion of a few base pairs (indels). The frame shift induced by these indels will block partially or totally gene transcription and translation. Alternatively, homology directed repair (HDR) can occurs when a donor sequence, with locus-specific homologous arms, is brought with the endonuclease. This allows the introduction of a specific DNA mutation, like single-base substitution and also insertion of site-specific ectopic DNA sequences. However, HDR is restricted to the S/G2 phases of the cell cycle, which makes this approach challenging for scientists in some primary cell models.<sup>18</sup>

The CRISPR-Cas9 technology has revolutionized the methodology to induce gene-specific knock-out due to its high specificity, easy design and efficiency in genetic manipulation of cell lines and primary cells. The endonucleases and sgRNAs can be introduced in the cell, by using

CRISPR/Cas9 encoding retroviral vectors<sup>19</sup> or alternatively by electroporation of plasmids and RNA encoding for the Cas9 can also be used<sup>20,21</sup>. Currently, the main approach, used in cell lines, but also in ASC-derived organoids is electroporation of plasmids coding for the Cas9 endonuclease and the sgRNA<sup>10</sup>. Despite the fact that electroporation is widely used today, this technique leads to very low efficiency and induces a high toxicity for the cells which leads to a high level of cell death<sup>10,12</sup>. Nevertheless, a recent study reported that the use of ribonucleoprotein (RNP), made up of Cas9 protein and a synthetic single-strand gRNA (ssRNP), provided higher transfection efficiency<sup>22</sup>.

To compensate for this very low efficiency, knock-in technologies have been developed in the organoid field. This allowed insertion of an expression cassette encoding a fluorescent protein such as GFP flanked by homologous genome sequences through recombination at the DSB induced by Cas-9, which permitted easy identification of knock-out organoids<sup>12</sup>.

Gene editing has already been performed in several types of organoids such colon organoids. Cystic fibrosis transmembrane conductance regulator (*CFTR*) is an integral membrane protein that forms an anion channel activated by cAMP-dependent phosphorylation<sup>23</sup>. A functional *CFTR* assay showed the use of Forskolin to induce fluid secretion into the lumen and swelling of colon organoids<sup>24</sup>. A study published in 2013 by the Clever's group reported the use of the CRISPR/Cas9 genome editing system to correct the *CFTR* gene and thus restoring forskolin-induced swelling in patient-derived intestinal organoids<sup>9</sup>.

Androgenic signals through the *AR* are required for luminal differentiation of some prostate basal stem cells. *AR* deletion in luminal cells has been shown to alter cell morphology and induce transient overproliferation<sup>25</sup>. The first study that established prostate organoid cultures<sup>26</sup>, showed that dihydrotestosterone (DHT) deprivation of CD26 + luminal cell-derived organoids disrupted lumen formation. Therefore, *AR*-KO prostate organoids generated by gene editing are expected to be compact even when stimulated with DHT.

Recently, a technology based on a virus-like particle (VLP) derived from a murine leukemia virus (MLV) has been developed<sup>27,28,28,29</sup>. This technology consists in using these VLPs to introduce into the cells the Cas9/sgRNA ribonucleoproteins. These nanoblades carry the Cas9 proteins complexed with the sgRNAs, and are devoid of a viral genome, which allows a very quick and transient delivery of the gene editing machinery into the targeted cells. Here, we demonstrated that nanoblades allowed a very high knock-out efficiency for *CFTR* and *AR* in

colon and prostate organoids, respectively, with very low to no toxicity and off-target effects. This facilitates the generation of gene KO in organoids without the need to use reporter encoding knock-in cassettes.

## **MATERIALS AND METHODS**

### **Organoid culture**

Mouse prostate organoids were generated as described by Drost *et al.*<sup>4</sup>. Briefly, the prostates of 7-8-week-old mice were isolated, and minced in small fragments. Tissue fragments were digested with type II collagenase at 5mg/ml for 1 hour at 37°C and subsequently incubated with 1X TrypLE (Gibco, Waltham, USA) for 15 minutes at 37°C. Cells were washed between each step with 15 ml of advanced complete DMEM/F12 (adDMEM/F12 containing penicillin/streptomycin, 10 mM HEPES and 2 mM GlutaMAX (100× diluted)) (ThermoFisher, Waltham, USA). Then cells were passed through a 70-µm cell strainer (ThermoFisher, Waltham, USA) to remove excessively large debris. The cells were then labeled with CD49f-APC conjugated antibody or CD24-PE conjugated antibody (ThermoFisher, Waltham, USA) and sorted by flow cytometry (BD FACSAria™ Cell Sorter). The isolated cells were then washed with complete adDMEM/F12 and after centrifugation at 200g for 5 minutes, the cell pellet was re-suspended in growth factor reduced phenol red-free Matrigel (Corning, NY, USA) at a concentration of 200 cells per microliter of Matrigel. Mouse prostate organoids were maintained in complete adDMEM/F12 supplemented with 50 X diluted B27 (Life Technologies Carlsbad, USA), 1,25 mM N-acetyl-l-cysteine (Sigma-Aldrich, Saint-Louis, USA), 50 ng/ml EGF (PeproTech, Cranbury, USA), 200 nM A83-01 (Tocris Bioscience, Bristol, UK), 1% Noggin conditioned medium, 10% R-spondin 1 conditioned medium, 1 nM DiHydro-Testosterone (Sigma-Aldrich, Saint-Louis, USA) and 10 µM Y-27632 dihydrochloride (PeproTech Cranbury, USA). Culture medium was replenished every two days.

Mouse colon organoids were maintained in complete adDMEM/F12 supplemented with 50 X diluted B27 (Life Technologies, Carlsbad, USA), 100 X diluted N2 (Life Technologies Carlsbad, USA), 1 mM N-acetyl-l-cysteine (Sigma-Aldrich, Saint-Louis, USA), 50 ng/ml EGF (PeproTech Cranbury, USA), 1% Noggin conditioned medium, 20% R-spondin 1 conditioned medium, 50% Wnt3a conditioned medium and 10 µM Y-27632 dihydrochloride (PeproTech Cranbury, USA). Culture medium was replenished every two days.

For passage of the organoid cultures, each drop of Matrigel containing the organoids was resuspended in 1 ml of ice cold complete adDMEM/F12, which were centrifuged for 5 minutes at 200g at 4 ° C. Prostate and colon organoids were then incubated in TrypLE for 5 and 3 minutes respectively at 37 ° C and mechanically dissociated by pipetting up and down with a P10 / P1000 pipet tip. Cells were then washed with complete adDMEM/F12 and centrifuged. Cells were seeded back in Matrigel at a concentration of 100 cells/ $\mu$ L. The appropriate medium was added to the cells and replenished every two days.

Organoids were passaged every 7 to 10 days.

### **Plasmids**

All the plasmids (Gagpol MLV, GagMLV-Cas9, VSV-G) and gRNA expressing plasmids to produce the nanoblades are described previously<sup>27,28</sup>. The BaEVRless envelope glycoproteins were previously described<sup>30</sup>. All envelope glycoproteins (VSV-G and BAEV) were expressed in the pCMV-G expression plasmid<sup>31</sup>.

### **sgRNA design**

The sgRNAs of the different targeted genes were cloned into the gRNA expressing plasmid CRIZI using the BsmBI restriction site. The sequences of the sgRNA are as follows:

GFP_B182	5' -CGAGGAGCTGTTACCGGG-3'
Ms_AR_1	5' -ATGTACGCGTCGCTCCTGGG-3'
Ms_AR_2	5' -TTCAAGGGAGGTTACGCCAA-3'
Ms_CFTR_1	5' -GTGGCGATCATGTTGCTGCG-3'
Ms_CFTR_2	5' -AGTTCCGGATTCTGAACAGG-3'
Hu_P53	5' -AACCATTGTTCAATATCGTC-3'
Hu_CFTR	5' -GGAGAACTGGAGCCTTCAGA-3'
mNG238	5' -TGGAAAGGCGACATCCCGTC-3'
mNG46	5' -ATGTGTAACATCATGTGTCGC-3'
mNG126	5' -GGCACCGCAATCCAAATGA-3'
mNG260	5' -GTATCCGGAGCCATCTACCA-3'

### **Production of Nanoblades**

Nanoblades were produced in 293T HEK cells.  $5.10^6$  cells were plated per 10 cm plate 24h prior to transfection. To produce nanoblades, plasmids coding for MLVGagPol (3  $\mu$ g),

GagCas9 (3 µg), BaeVRless (2 µg), VSVG (2 µg) and CRIZI (6 µg) were co-transfected with transfection reagent at a 2.6/1 ratio of Polyethylenimine (PEI; Polysciences, Warrington, USA) (µg)/total DNA (µg). The medium was replaced 24 hours after transfection by 6 ml of OptiMEM (Life Technologies Carlsbad, USA) supplemented with penicillin – streptomycin and HEPES. The next day, Nanoblade-containing medium was clarified by centrifugation (2000 rpm for 5 min) and filtered through a 0.45 µm pore-size filter before centrifugation overnight (3000g for 16h at 4 ° C). Supernatant was carefully removed by aspiration leaving a volume to obtain 100-150x concentration of the nanoblade preparation. Nanoblades can be stored at -80 °C.

### **Nanoblade transduction procedure**

Organoids were resuspended in ice-cold complete adDMEMF/12, then centrifuged at 200g for 5 minutes at 4 °C. Once the supernatant was aspirated, 1X TrypLE was added to the tube and incubated for 5 minutes at 37 ° C while pipetting up and down to dissociate the organoids. After washing the cells with complete adDMEMF/12, 1E4 cells were distributed in a 96-well plate in 100 µl of complete adDMEMF/12 with 10 µM Y-27632 to which nanoblades (4 µmoles of Cas9 protein), were added. The plate was then centrifuged at 200g for 60 min at room temperature. The plate was incubated for 6 hours at 37 °C. The cells were then collected in Falcon15 tube containing 5 ml of complete adDMEMF/12 and centrifuged at 200g for 5 min. The supernatant was removed and the cells were resuspended in 100 µl of Matrigel (356231) and drops of 40 µl were deposited in P24-well plates. After an incubation of 15 minutes at 37 ° C, 500 µl of mouse prostate organoid medium was added to each well as previously described. Alternatively, the 96-well plate can be coated with RetroNectin® (Clontech/Takara; 12µg/ml PBS according to manufacturer's recommendations) overnight at 37 °C before seeding the cells and addition of the nanoblades.

Establishment of organoid lines expressing eGFP: We used a lentiviral vector (plasmid pHIV-SFFV-IRES-GFP) which contains an eGFP under the control of an SFFV promoter. The transduction procedure is the same than the one used for the Nanoblades. We applied a low MOI of 0,3 to ensure that we obtained only one integrated copy of the eGFP expression cassette into the genome of the mouse organoids. We then sorted the cells by flow cytometry (BD FACSAria™ Cell Sorter). We seeded the sorted cells in Matrigel at a concentration of 200 cells/µL. Then the corresponding media was added and replenished every two days.

### **Flow cytometry analysis**

Organoids were harvested with ice cold complete adDMEMF/12. After centrifugation at 250g for 5 min at 4 °C, the supernatant was aspirated and discarded, then 1X TrypLE (Gibco, Waltham, USA) was added to each tube and incubated for 5 minutes at 37 °C. After vortexing the tubes, up and down pipetting was performed to dissociate the organoids into single cell suspension. The cells were washed with complete adDMEMF/12, and then analyzed by flow cytometry for measuring the fluorescence of GFP to determine its expression levels.

### **Immunofluorescent stainings and imaging**

For live imaging, organoids were observed with an Evos optical microscope. For immunofluorescence staining, organoids were harvested and washed once with ice cold complete adDMEMF/12. They were fixed for 1 hour in 4% PFA, permeabilized with 0.5% Triton X-100 for 30 minutes and then blocked with 2% Fetal Bovine Serum (FBS) in PBS for 1 hour at room temperature (RT). Primary antibodies against cytokeratin 8 (Abcam, Cambridge, UK), cytokeratin 5 (AlexaFluor647 coupled antibody, Abcam, Cambridge, UK), and androgen receptor (Abcam, Cambridge, UK) were incubated for 2 hours at RT. After washing with PBS, secondary antibodies coupled to an AlexaFluor 488 and 594 (Life Technologies, Carlsbad, USA) were incubated for 1h30 at RT. DAPI was used to stain nuclear DNA. Organoids were mounted and imaged with a confocal Nikon microscope. Organoids were also cultivated in 96-well flat-bottom plates (Dutscher, Bernolsheim, France). They were then directly fixed and permeabilized with 4% PFA, 0.8% Triton X-100, 5 mM EGTA, 1 mM MgCl<sub>2</sub> in PBS. Antibody staining was performed as described above. Images were processed with ImageJ and Imaris for 3D reconstruction.

### **Determination of nanoblade toxicity on organoid development**

The number of organoids was determined 9 days after incubation with Nanoblades using a counting cell.

### **Detection of single gRNA on-target efficiency**

After incubation with nanoblades, organoids were grown for 9 days. Primers were designed to amplify approximately 400-700 bp of the region targeted by the guide RNAs (**supplementary Table 5**). Genomic DNA (gDNA) was extracted using a genomic DNA extraction kit (Macherey-Nagel). 50 ng of gDNA was used for PCR amplification. The size of the PCR fragments was checked using an agarose gel. PCR fragments were then purified using a gel

extraction kit (New England Biolabs) and sent for sequencing. Sequencing results were analyzed for the percentage of INDEL using ICE (<https://ice.synthego.com/#/>) or DECODR (<https://decodr.org/analyze>).

### **Off-target Detection**

The potential off-target sites for the guide RNAs used in this study were determined using Cas-OFFinder (<http://www.rgenome.net/cas-offinder/>). Some of the off-target sites with 2 or 3 mismatches for each guide RNA were selected for further analysis. Note, only off-target sites with a PAM sequence (NGG) were tested here. PCR primers were designed to amplify a fragment of about 400 to 700 bp around the identified off-target site (**Supplementary table 5**). Genomic DNA was isolated and the PCR and fragment isolation were performed as mentioned above. The PCR fragments were then sequenced by Sanger sequencing. The resulting sequencing was analyzed for the percentage of INDEL using ICE (<https://ice.synthego.com/#/>) and DECODR (<https://decodr.org/analyze>).

### **Statistical Analysis**

We have applied either a Mann-Whitney test or a non-parametric Kruskal-Wallis test when we compared two or three experimental conditions, respectively. Experiments were performed at least three times using for each experiment a different nanoblade preparation.

## RESULTS

### **Nanoblades allow efficient genome editing with low toxicity in organoid cells**

To have an easy read-out for nanoblade gene editing efficiency in organoids we chose initially to knock-out eGFP in prostate organoids expressing eGFP. First, we established a mouse prostate organoid cell line expressing eGFP by transduction of organoid cells with a lentiviral vectors encoding for eGFP driven by the SFFV promoter at low MOI of 0,3 to ensure that we obtained only one integrated copy of the eGFP expression cassette into the genome of the mouse prostate organoids. We sorted the eGFP positive cells.

To assess eGFP KO, we selected a sgRNA targeting eGFP that **showed 75%** of eGFP KO<sup>27</sup> in bone marrow-derived macrophages. The nanoblade treatment is schematically represented in **Figure 1A**. Organoids were dissociated and incubated with the nanoblades for only 6 hours to avoid cell death due to lack of growth factors as we determined previously. Moreover, a brief incubation with nanoblades was expected to be sufficient since receptor mediated entry of the nanoblades is a fast process as show for other primary cells previously<sup>27,28</sup>. The cells were then rinsed to remove the nanoblades and seeded in matrigel. Without any prior selection for gene edited cells, the cells were cultured for 9 days to differentiate into organoids. Fluorescence microscopy revealed a strong reduction of GFP+ organoids (**Figure 1B**). Additionally, the bulk population of dissociated organoids was quantified by fluorescence activated cell sorting analysis (FACS) for nanoblade mediated loss of GFP (**Figure 1C**). We observed that increasing doses of anti-GFP nanoblades permitted to increase gene editing and achieve up to 80% of edited cells (**Figure 1C**).

In order to further improve the efficiency of nanoblades, we compared a constant dose of nanoblades in combination with the two facilitating agents polybrene and/or retronectin (**Figure 1D**). We did not observe a significant increase in gene editing efficiency of the nanoblades in the presence of retronectin or polybrene or both as compared to the control condition in absence of these facilitating agents.

Of high importance, even after treatment of dissociated organoid cells with the maximum dose of nanoblades tested (4  $\mu$ moles of Cas9 protein) no significant toxicity was detected since the number of cells developing into prostate organoids was equivalent in the presence or absence of nanoblade incubation (**Figure 1E**). These data proved that nanoblades can reach high level of gene editing in organoids without side-effects such a cellular toxicity.

### **Nanoblades allow highly efficient gene knock-out in prostate organoids**

As a proof of concept, we chose to knock-out the gene coding for the androgen receptor (*AR*), a key protein in the development of mouse prostate organoids. Therefore, we designed two sgRNAs targeting the *AR* gene (**Exon 1/8**). The lay-out of the entire experimental set-up is shown in **Figure 2A** and **as indicated** can be performed in 4 to 6 weeks. This includes cloning of the gRNA in the expressing plasmid, followed by the nanoblade production carrying the *AR*-targeting sgRNAs. Then the dissociated mouse prostate wild type (WT) organoids were treated either with the nanoblades carrying the AR\_1 sgRNA or the nanoblades carrying the AR\_2 sgRNA. We also treated with a nanoblade that integrated both sgRNAs simultaneously. 9 days after culture of the organoids, we revealed a strong phenotypic change in the organoids KO for *AR* showing very compact round spheric structures without any lumen as compared to controls (**Figure 2B and C**). This is in agreement with the literature<sup>26</sup>, since organoids that are not stimulated for the androgen pathway show a compact phenotype. Indeed, a Cyst organoid phenotype is dependent on the stimulation of prostate luminal cells by dihydrotestosterone (DHT). Confocal microscopic acquisitions of the *AR* KO organoids have shown an absence of lumen in the center of the organoid (**Figure 2C**). Labeling of AR with an anti-AR antibody also confirmed the absence of the AR protein in the compact *AR* KO organoids (**Figure 2C**).

Nine days after the treatment of the organoids with the nanoblades, we isolated genomic DNA (gDNA) of the bulk organoid population and amplified a 557 bp sequence surrounding the genomic loci targeted by gRNA-AR\_1 and gRNA-AR\_2 using the AR\_ctrl\_fw and AR\_ctrl\_rv primers. Then, we sequenced these PCR products. Analysis of the sequences by ICE confirmed that NB incorporating only gRNA-AR\_1 resulted in 12% indels, while gRNA-AR\_2 containing NBs resulted in 27 % indels. When the two gRNAs AR\_1 and AR\_2 were combined in the same nanoblade, we reached 17% indels (**Figure 2D**). We also evaluated here the level of toxicity induced by treatment of the organoids with nanoblades targeting the *AR* gene (**Figure 2E**). We revealed that the number of organoids formed nine days after the treatment with or without nanoblades was equivalent and thus that the nanoblade incubation was not significantly toxic to survival of the cells and their organoid differentiation.

Clonogenicity is a major asset of the organoid model. Indeed, when we pass the organoids, each reseeded cell will reform a complete organoid. The organoid will then have the genetic identity of the original cell. In order to evaluate if the generation of organoid KO line is easily performed, we picked ten organoids per condition. For each of these organoids the genomic locus targeted for gene editing was PCR amplified individually and evaluated for *AR* KO using

DECODR. For the NB containing gRNA AR\_1, three out of ten organoid lines generated were KO for *AR*, which results in a level of 30% of *AR* KO organoids. For the NB containing gRNA AR\_2, two of the ten organoids picked and amplified were KO for *AR*. Thus, we reached 20% *AR* KO for this organoid (**Figure 2F and Supplementary Figure 1**).

### **Nanoblades allow also efficient gene editing in mouse colon organoids**

Colon organoids are one of the first organoid models which have been developed<sup>3</sup>. They are also cultured in matrigel. The culture medium is slightly different in composition compared to that used for culture of mouse prostate organoids as described in material and methods, therefore, the nanoblade mediated editing efficiency and toxicity might be different in this type of organoids.

As described above for prostate organoids, nanoblade gene editing efficiency in colon organoids was initially tested by knocking-out eGFP in colon organoids expressing eGFP. Equivalent to the prostate organoids, we established a mouse colon organoid cell line expressing eGFP (see above and **Figure 3A**). We incubated the dissociated colon organoid cells with anti-GFP nanoblades as described before. The bulk population of dissociated organoids was quantified by FACS for nanoblade mediated loss of GFP (**Figure 3B**). We obtained with the colon organoids similar levels of knock-out as for the prostate organoids. Indeed, with the maximum dose of anti-GFP nanoblades we achieved a gene editing efficiency of 80% for the colon organoid cells (**Figure 3C**). Equivalent to prostate organoids, after treatment of dissociated colon organoid cells with the maximum dose of nanoblades tested (4  $\mu$ moles of Cas9 protein) no significant toxicity was detected since the number of cells developing into organoids was equivalent in the presence or absence of nanoblades (**Figure 3D**).

Overall, this first evaluation of nanoblade mediated gene editing in mouse colon organoids shows a very high efficiency of genome editing with low toxicity, equivalent to what we observed for prostate organoids.

### **Nanoblades allow efficient *CFTR* gene knock-out in colon organoids**

As mentioned previously, *CFTR* is an anion channel activated by cAMP-dependent phosphorylation<sup>23</sup>. Previous studies have shown that *CFTR* is responsible for fluid secretion into the lumen and swelling of organoids, leading in intestinal organoids to a strong morphological phenotype<sup>9,14,24</sup>.

We used the same experimental approach as for *AR* knockout in prostate organoids here for colon organoids (**Figure 2A**). We designed two gRNAs targeting the mouse *CFTR* gene (**Exon 14/27**) and treated the colon organoids for 6 hours with nanoblades carrying either the *CFTR\_1*, *CFTR\_2* or *CFTR\_1* & *CFTR\_2* gRNAs (**Figure 4A**).

Nine days after the treatment of the organoid cells with the nanoblades and their culture in colon organoid differentiation medium, we isolated gDNA of the bulk organoid population (**Figure 4B**). We amplified a 625 bp genomic fragment around the loci targeted by the *CFTR\_1* sgRNAs or *CFTR\_2* sgRNA. The indel analysis performed by ICE software, showed an indel frequency of 28% for *CFTR\_1* sgRNA, 28% for *CFTR\_2* sgRNA. The percentage of indels reached 38% when both guide RNAs were provided by the same nanoblade.

Toxicity was also evaluated by counting the number of organoids formed nine days after treatment with or in the absence of the nanoblades (**Figure 4C**). Here again the nanoblades did not induce a significant level of toxicity compared to the control conditions.

Nanoblade mediated gene editing was thus also highly efficient for mouse colon organoids underlining the ease and versatility of nanoblades for gene editing and KO generation in the organoid model.

### **Nanoblades do not induce off-target genotoxicity in organoids**

Another advantage of the nanoblades is that we provide Cas9 as a protein. The CRISPR-CAS9 gRNA complexes contained in the VLPs are only transiently expressed once delivered into the targeted cell. The fact that Cas9 is present in the cell for a short time should theoretically decrease the number of cuts in off-target sites. Using the Cas-OFFinder open access website, we predicted potential off-target sites for each of our sgRNAs (**Supplementary Tables 1 and 2**). We included in our analysis only the off-target sites containing a protospacer adjacent motif (PAM). Moreover, we chose the most probable off-target sites and therefore kept the off-target sites for the *AR\_1* sgRNA with 3 mismatches (**Figure 5A**). One was located on chromosome 9 and the other one on chromosome 13. We designed PCR primers (see material and methods) to amplify by PCR a 602 bp region around the chromosome 9 off-target site, and a 622 bp fragment around the potential chromosome 13 off-target site. For the *AR\_2* sgRNA we did not detect off-target sequence with 1, 2, or 3 mismatches and only found off-target sites with 4 mismatches compared to the target locus, and randomly choose 2 for analysis (**Supplementary Table 2 and Figure 5A**).

We amplified by PCR the off-target regions in the gDNA isolated from the organoid bulk treated with either AR\_1 or AR\_2 sgRNA and sequenced the PCR products. Analysis for indels by ICE , showed that no gene editing was detected in the off-target sites analyzed (Figure 5B). We also predicted the potential off-target sites for the sgRNAs CFTR\_1 and CFTR\_2 using the open access program Cas-OFFinder (**Supplementary Tables 3 and 4**; no more than 3 mismatches are listed). We proceeded as for AR gRNA off-targets and under these experimental conditions, no off-target gene editing was detected for the 4 different *CFTR* off-target analyzed (**Figure 5C and D**).

## DISCUSSION

Here we have shown that nanoblades facilitate and increase the level of gene editing in organoids. Previous studies showed much lower levels of editing in organoids. Nanoblades, in contrast to other techniques, have two major advantages: cargo and vehicle delivery. Until very recently<sup>22</sup>, most studies performing gene editing in organoids used plasmid DNA as cargo. For example, two studies published in 2013 and 2015 introduced plasmid DNA by liposome transfection into adult stem cells<sup>9,32</sup>. The study published in 2013, which described the use of the CRISPR/Cas9 system to correct the *CFTR* mutation in organoids derived from cystic fibrosis patients, showed low levels of gene editing<sup>9</sup>. The same research team reported the use of CRISPR/Cas9 to induce sequential cancer mutations in cultured human intestinal stem cells and they achieved also in this context low levels of editing. In these two cases, the low levels of gene editing can also come from the delivery vehicle<sup>32</sup>. Indeed, a study published in 2015<sup>10</sup>, showed higher levels of gene editing. The introduction of DNA plasmid into organoid cells was performed by electroporation. This change of vehicle for delivery allowed a fourfold increase in efficiency. However, the levels of gene editing did not exceed 1%.

To counteract these low efficiency levels, which made the use of CRISPR time-consuming and inefficient, several groups developed more efficient reporter gene knock-in techniques<sup>12,22</sup>. The insertion of a fluorescent cassette into the Cas9-induced DSB allows for easier identification of the edited organoids. Despite the advantage of this approach, it should be noted that the addition of a knock-in cassette adds an additional difficulty because a donor template sequence needs to be co-introduced together with the gene editing system into the cell. Furthermore, the knock-in levels achieved by electroporating plasmid DNA remained below 5%<sup>12</sup>.

Viruses have already been used for a long time to genetically manipulate cells. The efficiency of the best performing viral vectors such as lentiviral vectors can reach 100% transduction of the targeted cells<sup>33</sup>. In this study, as proof of principle, we evaluated for the first time VLPs incorporating CRISPR/Cas9 anti-GFP gRNA complexes called ‘nanoblades’ for eGFP KO in GFP expressing organoids. We reached up to 80% of edited cells, underlining that this technique is more efficient than any other methods in inducing a gene knock-out in organoids. A crucial point in Cas9-mediated gene editing is the off-target effect. When Cas9 is introduced into cells by a plasmid, it results in a longer presence of Cas9 protein in the cells and this increased the risk of INDELS at off-target sites. A recent study reported the nucleofection of RNPs to edit organoids<sup>22</sup>. This approach had two advantages. First, in a detailed comparison of the different types of cargo to deliver Cas9, RNPs coupled to single strand gRNAs were more efficient than plasmid DNA encoding Cas9 for editing cells. The second advantage is the reduction of off-target effects. Indeed, by providing Cas9 as a protein, its half-life in the cell is considerably reduced. Therefore, the off-target effects are decreased<sup>34</sup>.

In this study we provided Cas9 as RNPs delivered by nanoblades. We checked the off-target effects of the sgRNAs used, and none of them induced non-specific cleavage when evaluated by detected by sanger sequencing and ICE analysis of the off-target genomic sequences.

Another advantage of the nanoblades is their absence of toxicity for the treated cells. Indeed, electroporation remains harsh for the cells. Mammalian cells are sensitive to the voltage and the time of application of the current<sup>34</sup>.

In this study we reported the generation of an *AR* KO organoid prostate line. As shown previously, luminal cells knocked out for *AR* failed to achieve terminal differentiation<sup>25</sup>. Additionally, it was reported that the swelling of luminal organoids is directly dependent on the stimulation of the androgen pathway<sup>26</sup>. In accordance, the organoids KO for *AR* that we generated here induced a compact phenotype. The lumen formed by fluid secretion from the luminal cells did not occur when the cells were KO for *AR*. It would be interesting to understand whether the absence of lumen is indeed due to impaired terminal differentiation of luminal cells. Further studies, using single-cell RNA sequencing for example, would allow to fully understand this observation.

Overall, nanoblades are a versatile strategy to edit organoids *in vitro*. It allows to obtain fast and efficient knockouts in the organoid model with knock-out levels that outperform other current techniques. Moreover, organoids offer a tool with low toxicity for cells and low off-target effects. Finally, the experimental strategy is fast since it allows to generate organoid

lines in 4 to 6 weeks. Nanoblades offer the possibility to efficiently generate high level editing in organoids without the need to use reporter encoding knock-in cassettes.

## REFERENCES

1. Sato, T. *et al.* Single Lgr5 stem cells build crypt-villus structures in vitro without a mesenchymal niche. *Nature* 459, 262–265 (2009).
2. Sato, T. *et al.* Paneth cells constitute the niche for Lgr5 stem cells in intestinal crypts. *Nature* 469, 415–418 (2011).
3. Sato, T. *et al.* Long-term Expansion of Epithelial Organoids From Human Colon, Adenoma, Adenocarcinoma, and Barrett’s Epithelium. *Gastroenterology* 141, 1762–1772 (2011).
4. Drost, J. *et al.* Organoid culture systems for prostate epithelial and cancer tissue. *Nat Protoc* 11, 347–358 (2016).
5. Clevers, H. Modeling Development and Disease with Organoids. *Cell* 165, 1586–1597 (2016).
6. Matano, M. *et al.* Modeling colorectal cancer using CRISPR-Cas9–mediated engineering of human intestinal organoids. *Nat Med* 21, 256–262 (2015).
7. Dutta, D., Heo, I. & Clevers, H. Disease Modeling in Stem Cell-Derived 3D Organoid Systems. *Trends in Molecular Medicine* 23, 393–410 (2017).
8. Drost, J. *et al.* Use of CRISPR-modified human stem cell organoids to study the origin of mutational signatures in cancer. *Science* 358, 234–238 (2017).
9. Schwank, G. *et al.* Functional Repair of CFTR by CRISPR/Cas9 in Intestinal Stem Cell Organoids of Cystic Fibrosis Patients. *Cell Stem Cell* 13, 653–658 (2013).
10. Fujii, M., Matano, M., Nanki, K. & Sato, T. Efficient genetic engineering of human intestinal organoids using electroporation. *Nat Protoc* 10, 1474–1485 (2015).
11. Artegiani, B. *et al.* Probing the Tumor Suppressor Function of BAP1 in CRISPR-Engineered Human Liver Organoids. *Cell Stem Cell* 24, 927-943.e6 (2019).

12. Artegiani, B. *et al.* Fast and efficient generation of knock-in human organoids using homology-independent CRISPR–Cas9 precision genome editing. *Nat Cell Biol* 22, 321–331 (2020).
13. Hofer, M. & Lutolf, M. P. Engineering organoids. *Nat Rev Mater* 6, 402–420 (2021).
14. Geurts, M. H. *et al.* Evaluating CRISPR-based prime editing for cancer modeling and CFTR repair in organoids. *Life Sci. Alliance* 4, e202000940 (2021).
15. Doudna, J. A. & Charpentier, E. The new frontier of genome engineering with CRISPR–Cas9. *Science* 346, 1258096 (2014).
16. Gaj, T., Gersbach, C. A. & Barbas, C. F. ZFN, TALEN, and CRISPR/Cas-based methods for genome engineering. *Trends in Biotechnology* 31, 397–405 (2013).
17. Gutierrez-Guerrero, A. & Verhoeyen, E. *In Vivo* Hematopoietic Stem Cell Gene Therapy Might Become a Reality. *Human Gene Therapy* 32, 14–16 (2021).
18. Hustedt, N. & Durocher, D. The control of DNA repair by the cell cycle. *Nat Cell Biol* 19, 1–9 (2017).
19. Heckl, D. *et al.* Generation of mouse models of myeloid malignancy with combinatorial genetic lesions using CRISPR–Cas9 genome editing. *Nat Biotechnol* 32, 941–946 (2014).
20. Mandal, P. K. *et al.* Efficient Ablation of Genes in Human Hematopoietic Stem and Effector Cells using CRISPR/Cas9. *Cell Stem Cell* 15, 643–652 (2014).
21. Hendel, A. *et al.* Chemically modified guide RNAs enhance CRISPR–Cas genome editing in human primary cells. *Nat Biotechnol* 33, 985–989 (2015).
22. Dawei, S., LewisD, E. & Emma L., R. *Organoid Easytag: an efficient workflow for gene targeting in human organoids*. <https://prelights.biologists.com?p=20966> (2020)  
doi:10.1242/prelights.20966.
23. Moran, O. Model of the cAMP activation of chloride transport by CFTR channel and the mechanism of potentiators. *Journal of Theoretical Biology* 262, 73–79 (2010).

24. Dekkers, J. F. *et al.* A functional CFTR assay using primary cystic fibrosis intestinal organoids. *Nat Med* 19, 939–945 (2013).
25. Xie, Q. *et al.* Dissecting cell-type-specific roles of androgen receptor in prostate homeostasis and regeneration through lineage tracing. *Nat Commun* 8, 14284 (2017).
26. Karthaus, W. R. *et al.* Identification of Multipotent Luminal Progenitor Cells in Human Prostate Organoid Cultures. *Cell* 159, 163–175 (2014).
27. Mangeot, P. E. *et al.* Genome editing in primary cells and in vivo using viral-derived Nanoblades loaded with Cas9-sgRNA ribonucleoproteins. *Nat Commun* 10, 45 (2019).
28. Gutierrez-Guerrero, A. *et al.* Baboon Envelope Pseudotyped “Nanoblades” Carrying Cas9/gRNA Complexes Allow Efficient Genome Editing in Human T, B, and CD34+ Cells and Knock-in of AAV6-Encoded Donor DNA in CD34+ Cells. *Front. Genome Ed.* 3, 604371 (2021).
29. Bernadin, O. *et al.* Baboon envelope LVs efficiently transduced human adult, fetal, and progenitor T cells and corrected SCID-X1 T-cell deficiency. *Blood Advances* 3, 461–475 (2019).
30. Girard-Gagnepain, A. *et al.* Baboon envelope pseudotyped LVs outperform VSV-G-LVs for gene transfer into early-cytokine-stimulated and resting HSCs. *Blood* 124, 1221–1231 (2014).
31. Maurice, M. *et al.* Efficient gene transfer into human primary blood lymphocytes by surface-engineered lentiviral vectors that display a T cell-activating polypeptide. *Blood* 99, 2342–2350 (2002).
32. Drost, J. *et al.* Sequential cancer mutations in cultured human intestinal stem cells. *Nature* 521, 43–47 (2015).
33. Levine, F. & Friedmann, T. Gene therapy techniques. *Current Opinion in Biotechnology* 2, 840–844 (1991).

34. Lino, C. A., Harper, J. C., Carney, J. P. & Timlin, J. A. Delivering CRISPR: a review of the challenges and approaches. *Drug Delivery* 25, 1234–1257 (2018).

**Figure 1. Strategy and efficiency of nanoblade induced knock-out in mouse prostate organoids.**

- A. Experimental workflow of the use of nanoblades for gene editing of mouse prostate organoids. Organoids are dissociated, treated with the nanoblades, and seeded back into matrigel supplemented with factors inducing organoid generation.
- B. Representative bright-field images of mouse prostate organoids 9 days after treatment or not with nanoblades targeting the GFP-coding sequence. Scale bar, 200  $\mu$ m.
- C. Left panel, flow cytometry analysis of GFP expressing organoids treated or not with nanoblades targeting the GFP-coding sequence. Right panel, flow cytometry analysis of GFP expressing organoids treated with different quantities of nanoblades anti-GFP (means  $\pm$  SD; n = 3; \*p<0.05; \*\*p<0.01, \*\*\*p<0.001).
- D. Flow-cytometry analysis of GFP expressing organoids treated with fixed amounts of nanoblade anti-GFP with or without Polybrene and Retronectin (means  $\pm$  SD; n = 3; ns= not significant).
- E. The toxicity in organoids is evaluated, nine days after incubation of organoid cells with or without nanoblades by counting of the number of organoids (means  $\pm$  SD; n = 3; ns= not significant).

**Figure 2. Nanoblades enable efficient generation of knock-out organoid lines from mouse prostate organoids.**

- A. Stepwise procedure for nanoblade mediated gene knocked-out in organoid cell lines
- B. Representative bright-field images of mouse prostate organoids at 9 days after treatment with nanoblades targeting the Androgen-Receptor (AR). Two different sgRNAs (AR\_1 and AR\_2) were used to knock-out AR, either alone or together. Scale bar, 200  $\mu$ m.
- C. Representative immunofluorescence images of the center of WT and AR-KO mouse prostate organoids. Staining for basal marker CK5 (cyan), luminal marker CK8 (red) and AR (green). Nuclei were stained with DAPI (blue). Scale bar, 50  $\mu$ m.
- D. Bulk gDNA sequencing analysis of organoids treated with nanoblades targeting AR. Sanger sequencing was performed of the 557 bp PCR surrounding the AR target loci and was subjected to ICE analysis which revealed on-target INDEL frequencies at gRNA AR1 or AR2 target loci. Sequence decomposition of INDEL events is shown.

- E. The toxicity in organoids is evaluated nine days after treatment by counting the number of organoids treated or not with nanoblades targeting AR using a counting cell (means  $\pm$  SD; n = 3; ns= not significant).
- F. Single organoids were harvested, gDNA was isolated and sequenced for the loci targeted by the different AR guide RNAs. Sanger sequencing was performed of the 557 bp PCR surrounding the AR target loci and was subjected to ICE analysis which revealed on-target INDEL frequencies at gRNA AR1 or AR2 target loci.

**Figure 3. Efficient nanoblade induced knock-out in mouse colon organoids.**

- A. Representative bright-field images of mouse colon organoids 9 days after treatment or not with nanoblades targeting the GFP-coding sequence. Scale bar, 200  $\mu$ m.
- B. Flow cytometry analysis of GFP expressing organoids treated or not with nanoblades targeting the GFP-coding sequence.
- C. Flow cytometry analysis of GFP expressing organoids treated with different with different quantities of anti-GFP nanoblades (means  $\pm$  SD; n = 3).
- D. Toxicity of nanoblades in organoids is evaluated nine days after treatment by counting the number of organoids treated or not with nanoblades using a counting cell (means  $\pm$  SD; n = 3; ns= not significant).

**Figure 4. Nanoblades enable the efficient generation of knock-out mouse colon organoid cell lines**

- A. Representative bright-field images of mouse colon organoids 9 days after treatment with nanoblades targeting CFTR. Two different sgRNAs were used to knock-out CFTR, which were employed alone or combined.
- B. Bulk gDNA sequencing analysis of organoids treated with nanoblades targeting CFTR. Sanger sequencing was performed of PCR band including the CFTR target loci

and was subjected to ICE analysis which revealed on-target INDEL frequencies at gRNA CFTR\_1 or CFTR\_2 target loci. Sequence decomposition of INDEL events is shown.

- C. Toxicity of nanoblades in organoids is evaluated nine days after treatment by counting the number of organoids treated or not with nanoblades using a counting cell (means  $\pm$  SD; n = 3; ns= not significant).

**Figure 5. Nanoblades do not confer off-target genotoxicity upon KO of genes in organoids.**

- A. Cas-OFFinder algorithm was used to search for potential off-target sites for the sgRNAs AR1 and AR2 (see supplementary Table 1).
- B. Sanger sequencing of sgRNAs AR1 and AR2 potential off-target loci subjected to ICE analysis revealed no off-target DSBs.
- C. Cas-OFFinder algorithm was used to search for potential off-target sites for the sgRNAs CFTR\_1 and CFTR\_2 (see supplementary Table 1).
- D. Sanger sequencing of sgRNAs CFTR\_1 and CFTR\_2 potential off-target loci subjected to ICE analysis revealed no off-target DSBs.

**Supplemental Figure 1.**

Sequencing results of each of the amplified clones of organoids treated with nanoblades containing AR1 and AR2 sgRNAs.

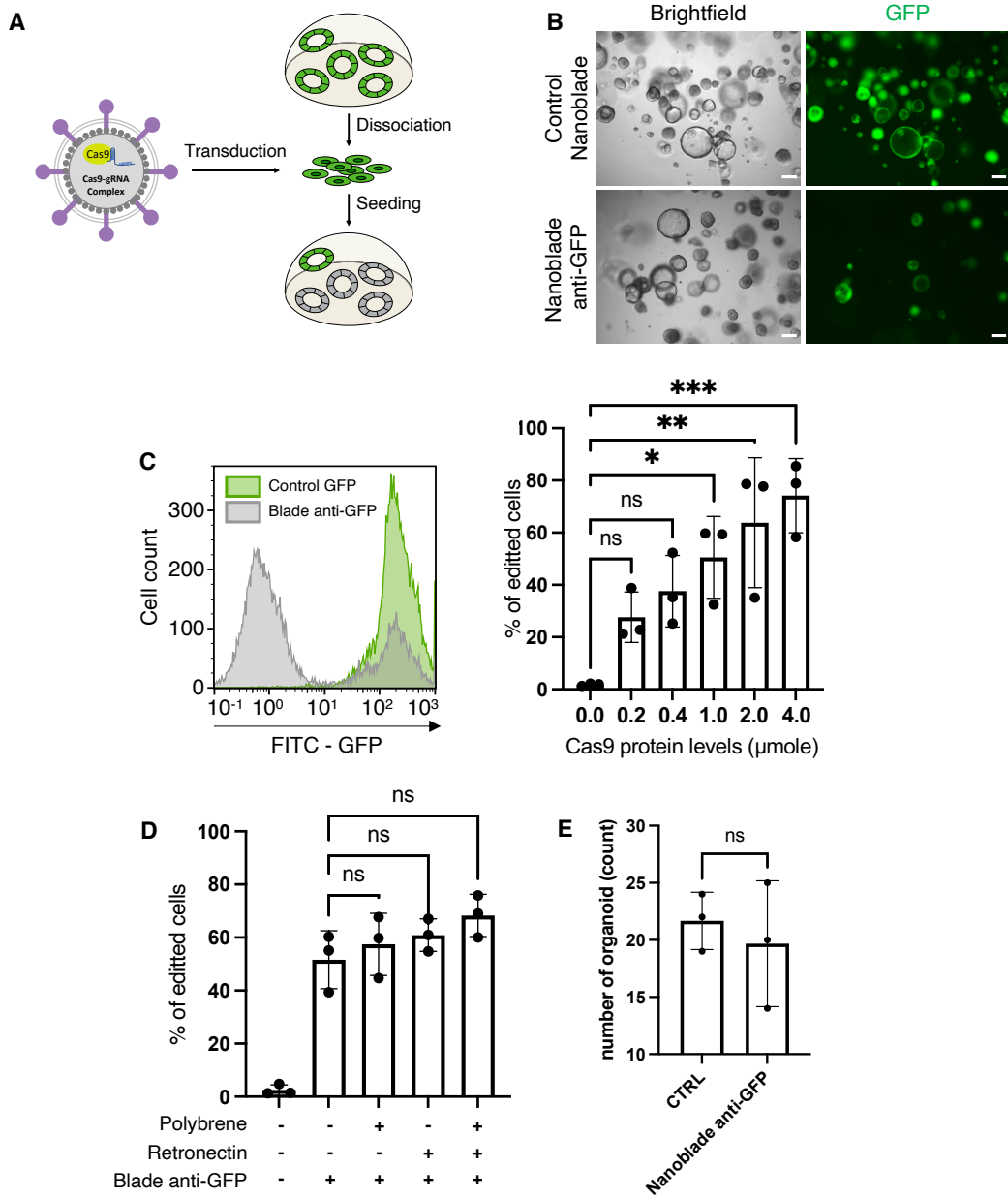


Figure 1

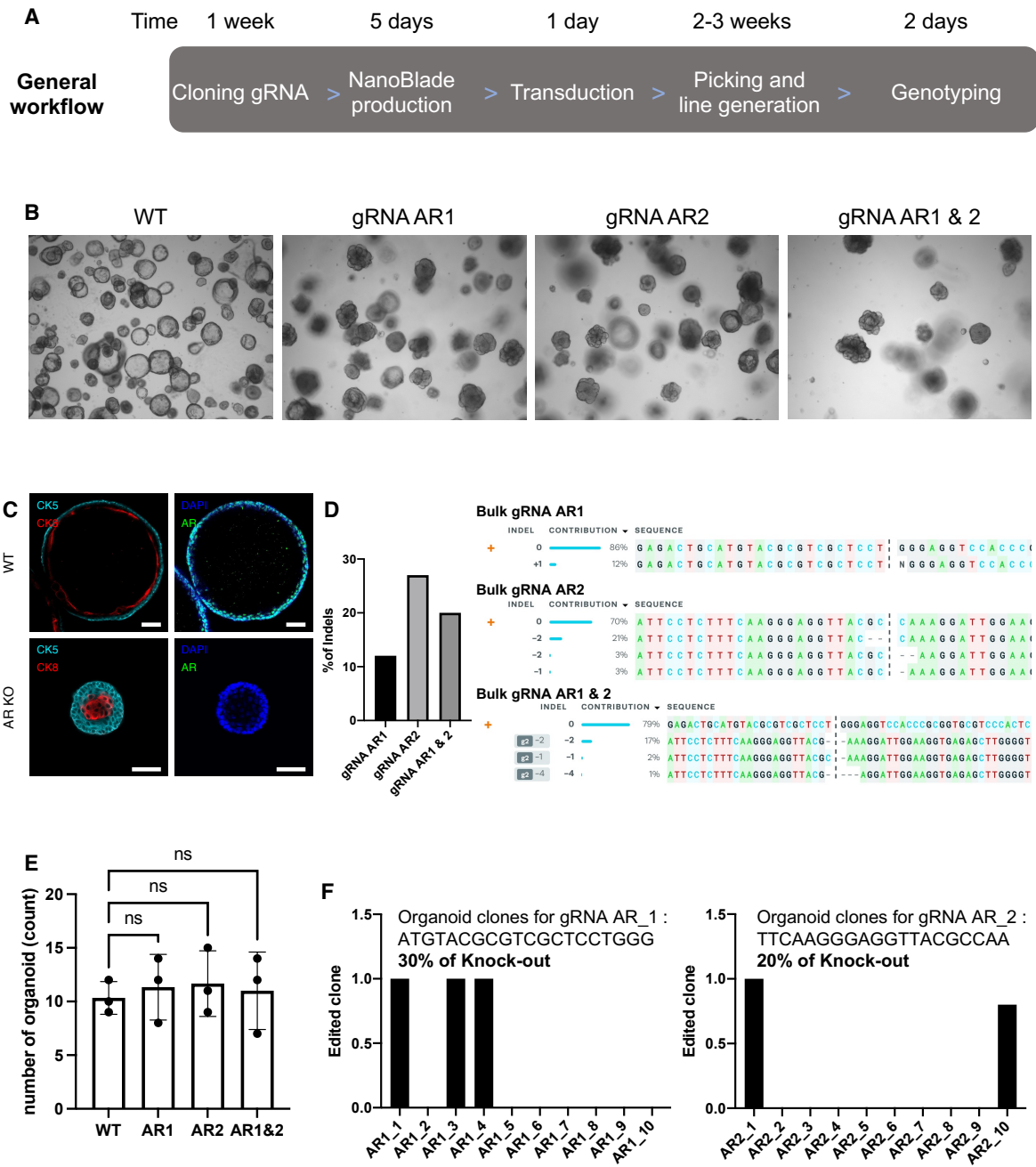


Figure 2

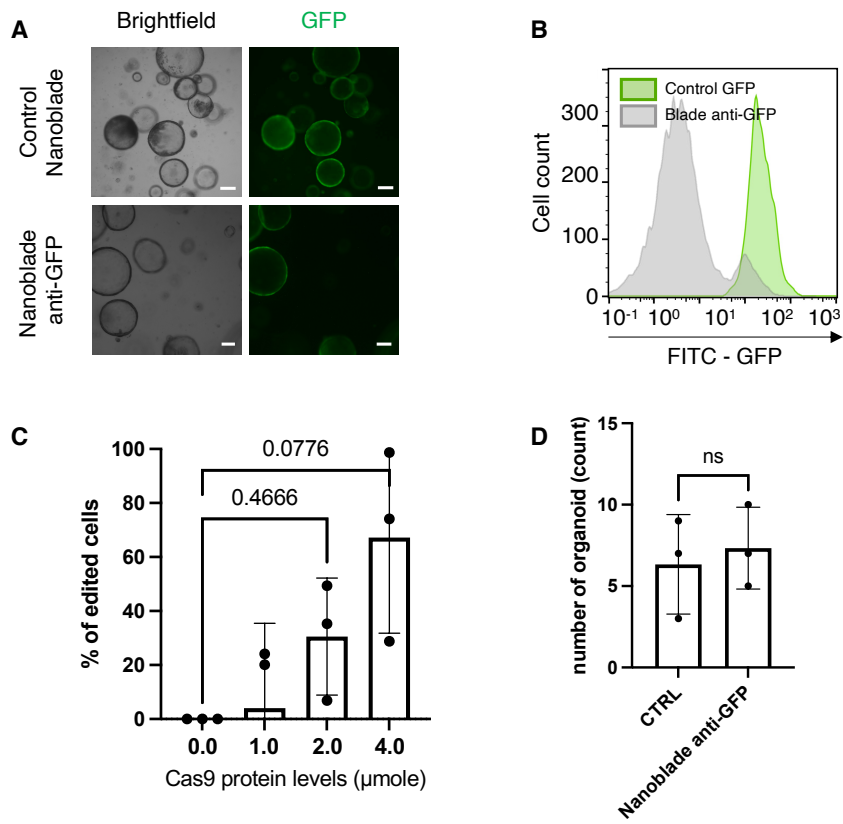
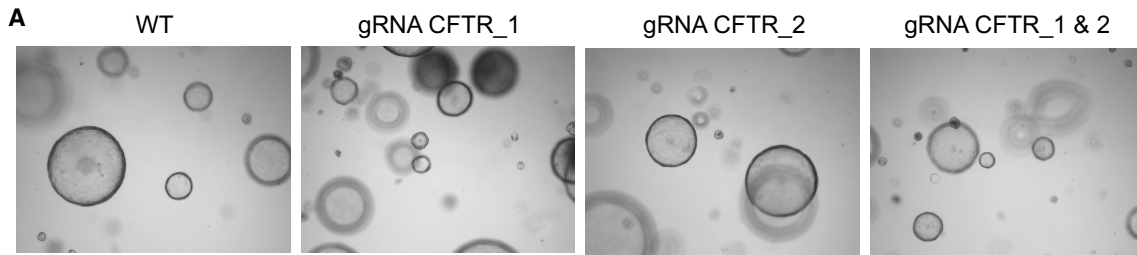


Figure 3



**B**

**Bulk gRNA CFTR\_1**

INDEL	CONTRIBUTION	SEQUENCE
0	32%	ACAGGGGGAGGCTGCTCTGCGCGC   AGCAACATGATCGCCACCGGCCAC
+2	13%	ACAGGGGGAGGCTGCTCTGCGCGC   NNAGCAACATGATCGCCACCGGCCAC
+1	9%	ACAGGGGGAGGCTGCTCTGCGCGC   NNAGCAACATGATCGCCACCGGCCAC
-14	2%	ACAGGGGGAGGC-----   -GCAACATGATCGCCACCGGCCAC
-15	2%	ACAGGGGGAGGCTGCTCTGCGC-----   -----CGCCACCGGCCAC
+7	1%	ACAGGGGGAGGCTGCTCTGCGCGC   NNNNNNAGCAACATGATCGCCACCG
+3	1%	ACAGGGGGAGGCTGCTCTGCGCGC   NNNAGCAACATGATCGCCACCGGCC

**Bulk gRNA CFTR\_2**

INDEL	CONTRIBUTION	SEQUENCE
0	49%	CTGTCCCTAGTTCCGGATTCTGAAC   AGGGGAGGGCTGCTCTGCGCGCAGC
+2	14%	CTGTCCCTAGTTCCGGATTCTGAAC   NNAGGGGAGGGCTGCTCTGCGCGCA
+1	8%	CTGTCCCTAGTTCCGGATTCTGAAC   NNAGGGGAGGGCTGCTCTGCGCGAG
+7	2%	CTGTCCCTAGTTCCGGATTCTGAAC   NNNNNNAGGGGAGGGCTGCTCTGCG
-14	2%	CTGTCCCTAGTTCCGGATTCTGAAC   -----CTGCGCGCAGC
+15	1%	CTGTCCCTAGTTCCGGATTCTGAAC   NNNNNNAGGGGAGGGCTGCTCTGCG
+6	1%	CTGTCCCTAGTTCCGGATTCTGAAC   NNNNNNAGGGGAGGGCTGCTCTGCG

**Bulk gRNA CFTR\_1 & CFTR\_2**

INDEL	CONTRIBUTION	SEQUENCE
0	33%	CTGTCCCTAGTTCCGGATTCTGAAC   AGGGGAGGGCTGCTCTGCGCGCAGCAACATGATCGCCACCGGCCAC
g1 +1	+1	ACAGGGGAGGGCTGCTCTGCGCGC   NAGCAACATGATCGCCACCGGCCACATTTCCAGGCAAGAAAGAC
g1 +2	+2	ACAGGGGAGGGCTGCTCTGCGCGC   NNAGCAACATGATCGCCACCGGCCACATTTCCAGGCAAGAAAGAC
g2 +2	+2	CTGTCCCTAGTTCCGGATTCTGAAC   NNAGGGGAGGGCTGCTCTGCGCGCAGCAACATGATCGCCACCGGCC
g1 +3	+3	ACAGGGGAGGGCTGCTCTGCGCGC   NNNAGCAACATGATCGCCACCGGCCACATTTCCAGGCAAGAAAGAC
g1 -15	-15	ACAGGGGAGGC-----   -CAACATGATCGCCACCGGCCACATTTCCAGGCAAGAAAGAC
g1 -14	-14	ACAGGGGAGGC-----   -GCAACATGATCGCCACCGGCCACATTTCCAGGCAAGAAAGAC
g1 -15	-15	ACAGGGGAGGGCTGCTCTGCC-----   -----CGCCACCGGCCACATTTCCAGGCAAGAAAGAC
g1 +7	+7	ACAGGGGAGGGCTGCTCTGCGCGC   NNNNNNAGCAACATGATCGCCACCGGCCACATTTCCAGGCAAGAA
g1 -29	-29	ACAGGGGAGG-----   -ACCGCCACATTTCCAGGCAAGAAAGAC
g1 -14	-14	ACAGGGGAGGC-----   -CAACATGATCGCCACCGGCCACATTTCCAGGCAAGAAAGAC
g1 -9	-9	ACAGGGGAGGGCTGCT-----   -CAACATGATCGCCACCGGCCACATTTCCAGGCAAGAAAGAC
g2 +7	+7	CTGTCCCTAGTTCCGGATTCTGAAC   NNNNNNAGGGGAGGGCTGCTCTGCGCGCAGCAACATGATCGCCAC

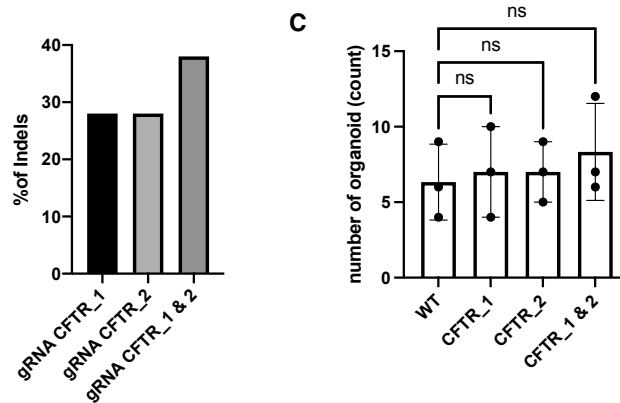


Figure 4

**A**

Selected off-target sites for CRISPR/Cas9_gRNA AR_1 & gRNA AR_2				
crRNA	gDNA	Chromosome	Direction	Mismatches
ATGTACGCGTCGCTCCTGGGNGG	ATGTACaCtTtGCTCCTGGGTGG	chr9	+	3
ATGTACGCGTCGCTCCTGGGNGG	cTtaACGCGTCGCTCCTGGGCGG	chr13	-	3
TTCAAGGGAGGTTACGCCAANGG	TaCAAGGGAGGTTACTCaAcAGG	chr8	+	4
TTCAAGGGAGGTTACGCCAANGG	TTCAAGGaAGGTTcCctCAATGG	chr15	-	4

**B** gRNA AR\_1 Off target Chromosome 9

Status Succeeded

Guide Target ATGTACACTTTGCTCCTGGG

PAM Sequence TGG

Indel % 0

Model Fit (R<sup>2</sup>) 1

INDEL CONTRIBUTION SEQUENCE  
+ 0 100% A C A A A G A A T G T A C A C T T T G C T C C T ; G G G T G G A A T G T T C T G G A A G T G C C A A A T A G T T T A C T T T A G C T G A T A T G T T

gRNA AR\_2 Off target Chromosome 15

Status Succeeded

Guide Target TTCAAGGAAGGTTCCCTCAA

PAM Sequence TGG

Indel % 0

Model Fit (R<sup>2</sup>) 1

INDEL CONTRIBUTION SEQUENCE  
+ 0 100% G C T A G A C T G G C C A A C T C T G C C A T T G ; A G G G A C C T T C T T G A A G A A C A T A G T G G A G A C T A A C C C A G G A A G A C T C T G

**C**

Selected off-target sites for CRISPR/Cas9_gRNA CFTR_1 & gRNA CFTR_2				
crRNA	gDNA	Chromosome	Direction	Mismatches
GTGGCgATCATGTTGCTGCGNNG	GTGGCcATCATGTTGgTGctGGG	chr14	-	3
GTGGCgATCATGTTGCTGCGNNG	GTGGCctTCATGTTGCTGCaCGG	chr13	-	3
AGTTCCGGATTCTGAACAGGNGG	AGTTtCtGtTTCTGAACAGGTGG	chr8	+	3
AGTTCCGGATTCTGAACAGGNGG	AGTTcTGGAcTCTGAgCAGGGGG	chr2	+	3

**D**

gRNA CFTR\_1 Off target Chromosome 14

Status Succeeded

Guide Target GTGGCCATCATGTTGGTGCT

PAM Sequence GGG

Indel % 0

Model Fit (R<sup>2</sup>) 0.99

INDEL CONTRIBUTION SEQUENCE  
+ 0 99% A G A G G A C C T T G G C G C A A T T C C A G C ; A C C A A C A T G A T G C C C A A C C A T C T G A G G C T C C A G T T C C A G A G G A C C T G A

gRNA CFTR\_2 Off target Chromosome 2

Status Succeeded

Guide Target AGTTCTGGACTCTGAGCAGG

PAM Sequence GGG

Indel % 0

Model Fit (R<sup>2</sup>) 1

INDEL CONTRIBUTION SEQUENCE  
+ 0 100% A G A G T A T G A G T T C T G G A C T C T G A G C ; A G G G G G A C G G G G C T G G G G A G C C C T G G T C T G G A T C T G T G G T T C T A C T G T G T

Figure 5

Organoid clones for gRNA AR\_1 : ATGTACGCGTCGCTCCTGGG

30% of Knock-out

FILENAME —	INDEL —	% —	TGCATGTACGCGTCGCTCCT GGGAGGTCACCCCGGGTGCCTCCCACTCCTTGTGCGCCGCTGCCGGAATG
AR1_2_CtrlAR1AR2_3_	1	100.0	TGCATGTACGCGTCGCTCCT GGGAGGTCACCCCGGGTGCCTCCCACTCCTTGTGCGCCGCTGCCGGAATG
AR1_1_CtrlAR1AR2_3_	0	100.0	TGCATGTACGCGTCGCTCCT GGGAGGTCACCCCGGGTGCCTCCCACTCCTTGTGCGCCGCTGCCGGAATG
AR1_3_CtrlAR1AR2_3_	1	100.0	TGCATGTACGCGTCGCTCCT GGGAGGTCACCCCGGGTGCCTCCCACTCCTTGTGCGCCGCTGCCGGAATG
AR1_4_CtrlAR1AR2_3_	-14	100.0	TGCATGTACGC----- -----GTCCACCCCGGGTGCCTCCCACTCCTTGTGCGCCGCTGCCGGAATG
AR1_5_CtrlAR1AR2_3_	0	100.0	TGCATGTACGCGTCGCTCCT GGGAGGTCACCCCGGGTGCCTCCCACTCCTTGTGCGCCGCTGCCGGAATG
AR1_6_CtrlAR1AR2_3_	0	100.0	TGCATGTACGCGTCGCTCCT GGGAGGTCACCCCGGGTGCCTCCCACTCCTTGTGCGCCGCTGCCGGAATG
AR1_7_CtrlAR1AR2_3_	0	100.0	TGCATGTACGCGTCGCTCCT GGGAGGTCACCCCGGGTGCCTCCCACTCCTTGTGCGCCGCTGCCGGAATG
AR1_8_CtrlAR1AR2_3_	0	100.0	TGCATGTACGCGTCGCTCCT GGGAGGTCACCCCGGGTGCCTCCCACTCCTTGTGCGCCGCTGCCGGAATG
AR1_9_CtrlAR1AR2_3_	0	100.0	TGCATGTACGCGTCGCTCCT GGGAGGTCACCCCGGGTGCCTCCCACTCCTTGTGCGCCGCTGCCGGAATG
AR1_10_CtrlAR1AR2_3_	0	100.0	TGCATGTACGCGTCGCTCCT GGGAGGTCACCCCGGGTGCCTCCCACTCCTTGTGCGCCGCTGCCGGAATG

Organoid clones for gRNA AR\_2 : TCAAGGGAGGTTACGCCAA

20% of Knock-out

FILENAME —	INDEL —	% —	TCTTTCAAGGGAGGTTACGC CAAAGGATTTGGAAGGTGAGAGCTTGGGGTGCTCTGGCAGCAGTGAAGCAGG
AR2_2_CtrlAR1AR2_3_	-1	100.0	TCTTTCAAGGGAGGTTACG- CAAAGGATTTGGAAGGTGAGAGCTTGGGGTGCTCTGGCAGCAGTGAAGCAGG
AR2_1_CtrlAR1AR2_3_	0	100.0	TCTTTCAAGGGAGGTTACGC CAAAGGATTTGGAAGGTGAGAGCTTGGGGTGCTCTGGCAGCAGTGAAGCAGG
AR2_3_CtrlAR1AR2_3_	0	100.0	TCTTTCAAGGGAGGTTACGC CAAAGGATTTGGAAGGTGAGAGCTTGGGGTGCTCTGGCAGCAGTGAAGCAGG
AR2_4_CtrlAR1AR2_3_	0	100.0	TCTTTCAAGGGAGGTTACGC CAAAGGATTTGGAAGGTGAGAGCTTGGGGTGCTCTGGCAGCAGTGAAGCAGG
AR2_5_CtrlAR1AR2_3_	0	100.0	TCTTTCAAGGGAGGTTACGC CAAAGGATTTGGAAGGTGAGAGCTTGGGGTGCTCTGGCAGCAGTGAAGCAGG
AR2_6_CtrlAR1AR2_3_	0	100.0	TCTTTCAAGGGAGGTTACGC CAAAGGATTTGGAAGGTGAGAGCTTGGGGTGCTCTGGCAGCAGTGAAGCAGG
AR2_7_CtrlAR1AR2_3_	0	100.0	TCTTTCAAGGGAGGTTACGC CAAAGGATTTGGAAGGTGAGAGCTTGGGGTGCTCTGGCAGCAGTGAAGCAGG
AR2_8_CtrlAR1AR2_3_	0	100.0	TCTTTCAAGGGAGGTTACGC CAAAGGATTTGGAAGGTGAGAGCTTGGGGTGCTCTGGCAGCAGTGAAGCAGG
AR2_9_CtrlAR1AR2_3_	0	100.0	TCTTTCAAGGGAGGTTACGC CAAAGGATTTGGAAGGTGAGAGCTTGGGGTGCTCTGGCAGCAGTGAAGCAGG
AR2_10_CtrlAR1AR2_3_	0	80.4	TCTTTCAAGGGAGGTTACGC CAAAGGATTTGGAAGGTGAGAGCTTGGGGTGCTCTGGCAGCAGTGAAGCAGG
	-3	19.6	TCTTTCAAGGGAGGTTA--- CAAAGGATTTGGAAGGTGAGAGCTTGGGGTGCTCTGGCAGCAGTGAAGCAGG

Supplemental Figure 1

## Supplementary Table 1

**Supplementary Table 1.** Potential off-target sites for CRISPR/Cas9\_gRNA AR\_1

crRNA	DNA	Chromosome	Direction	Mismatches
ATGTACGCGTCGCTCCTGGGNGG	ATGTACaCGTaGCTCCTaGCGG	chr8	+	4
ATGTACGCGTCGCTCCTGGGNGG	ATGTcCaGTCGCTCtTGGGAGG	chr5	+	4
ATGTACGCGTCGCTCCTGGGNGG	AgGaACGCGTCGCcCCTGGcTGG	chr5	+	4
ATGTACGCGTCGCTCCTGGGNGG	ATGTACGCcTgGCTCCTGacTGG	chr1	-	4
ATGTACGCGTCGCTCCTGGGNGG	ATGTACcCtTCGCTCCaGGcTGG	chr1	-	4
ATGTACGCGTCGCTCCTGGGNGG	ATGTcCGgGTCGagCCTGGGAGG	chr2	-	4
ATGTACGCGTCGCTCCTGGGNGG	ATGTAtGtTaGaTCCTGGGGGG	chr2	-	4
ATGTACGCGTCGCTCCTGGGNGG	cTaaACGCcTCGCTCCTGGGAGG	chr2	+	4
ATGTACGCGTCGCTCCTGGGNGG	tGTAgGcTtCaCTCCTGGGAGG	chr17	+	4
ATGTACGCGTCGCTCCTGGGNGG	ATGTACaCtTtGCTCCTGGGTGG	chr9	+	3
ATGTACGCGTCGCTCCTGGGNGG	ATGTACGCGTCGCTCCTGGGAGG	chrX	+	0
ATGTACGCGTCGCTCCTGGGNGG	tGTAAaGCaTaGCTCCTGGGAGG	chr14	+	4
ATGTACGCGTCGCTCCTGGGNGG	ATGTAtcCGTgGCTtCTGGGAGG	chr14	+	4
ATGTACGCGTCGCTCCTGGGNGG	ATcTggGCGcCGCTCCTGGGTGG	chr6	-	4
ATGTACGCGTCGCTCCTGGGNGG	ATGTACcCGcaGCaCCTGGGCGG	chr11	-	4
ATGTACGCGTCGCTCCTGGGNGG	ATGTAtatGTgGCTCCTGGGAGG	chr11	-	4
ATGTACGCGTCGCTCCTGGGNGG	cTtaACGCGTCGCTCCTGGGCGG	chr13	-	3
ATGTACGCGTCGCTCCTGGGNGG	tGTAgGtGtGCTCCTGGGTGG	chr13	+	4
ATGTACGCGTCGCTCCTGGGNGG	cTGTAtcaGTCGCTCCTGGGGGG	chr3	-	4
ATGTACGCGTCGCTCCTGGGNGG	ATGTAaGCcTCGaTCCaGGGAGG	chr3	+	4

## Supplementary Table 2

**Supplementary Table 2.** Potential off-target sites for CRISPR/Cas9\_gRNA AR\_2

crRNA	DNA	Chromosome	Direction	Mismatches
TTCAAGGGAGGTTACGCCAANGG	TaCAAGGGAGGTTActCaAcAGG	chr8	+	4
TTCAAGGGAGGTTACGCCAANGG	TTCAAGGaGAaGTTcCGCaAAGGG	chr8	+	4
TTCAAGGGAGGTTACGCCAANGG	TTCAAGGcAGGggACGCCAgTGG	chr8	-	4
TTCAAGGGAGGTTACGCCAANGG	TTCAAGGaAGGTTcCctCAATGG	chr15	-	4
TTCAAGGGAGGTTACGCCAANGG	TTCAAGGGgaGTTActgCAAAGG	chr5	-	4
TTCAAGGGAGGTTACGCCAANGG	TTaAAGGGAGcTTcCGCCAgGGG	chr5	-	4
TTCAAGGGAGGTTACGCCAANGG	TTCAAGaGAGGTTAactCAAGGG	chr5	+	4
TTCAAGGGAGGTTACGCCAANGG	TTtAAaGGAGGTTAgGCaATGG	chr5	+	4
TTCAAGGGAGGTTACGCCAANGG	TTcAGGGAGGTTAaGaCAtGGG	chr1	+	4
TTCAAGGGAGGTTACGCCAANGG	TTCAAaaGgGGTTAaGCCAAGGG	chr1	-	4
TTCAAGGGAGGTTACGCCAANGG	TTCAAGaGAGiTTAgGCCAcAGG	chr7	+	4
TTCAAGGGAGGTTACGCCAANGG	TTCAAGGGAGccTACcCaAATGG	chr7	+	4
TTCAAGGGAGGTTACGCCAANGG	TcCtAGGGAGGTTAtGCCAgTGG	chr7	+	4
TTCAAGGGAGGTTACGCCAANGG	TcCAAGGGAGiTTAaGgCAAGGG	chr7	+	4
TTCAAGGGAGGTTACGCCAANGG	TTCAAGGGAAatTTAgGCCAcGGG	chr7	-	4
TTCAAGGGAGGTTACGCCAANGG	cTgAGGGAGGTTAgGCCAAAGG	chr2	-	4
TTCAAGGGAGGTTACGCCAANGG	TTCAAGtaAGiTTAtGCCAAAGG	chr2	-	4
TTCAAGGGAGGTTACGCCAANGG	acCAAGGGAGGTgAgGCCAAGGG	chr12	-	4
TTCAAGGGAGGTTACGCCAANGG	TTcAGGGAGGTTAaGgCAgAGG	chr4	+	4
TTCAAGGGAGGTTACGCCAANGG	TTCAAGGGcGGaTACaCgAAGGG	chr16	-	4
TTCAAGGGAGGTTACGCCAANGG	TTCAAGGGAGGTTACGCCAAAGG	chrX	+	0
TTCAAGGGAGGTTACGCCAANGG	TTCAAaaGgGGTTAaGCCAAGGG	chr14	+	4
TTCAAGGGAGGTTACGCCAANGG	TTCAAaaGgGGTTAaGCCAAGGG	chr14	+	4
TTCAAGGGAGGTTACGCCAANGG	TTCAAaaGgGGTTAaGCCAAGGG	chr14	+	4
TTCAAGGGAGGTTACGCCAANGG	TTCAAaaGgGGTTAaGCCAAGGG	chr14	+	4
TTCAAGGGAGGTTACGCCAANGG	TTCAAaaGgGGTTAaGCCAAGGG	chr14	+	4
TTCAAGGGAGGTTACGCCAANGG	TTCAAaaGgGGTTAaGCCAAGGG	chr14	+	4
TTCAAGGGAGGTTACGCCAANGG	TTCAAaaGgGGTTAaGCCAAGGG	chr14	+	4
TTCAAGGGAGGTTACGCCAANGG	TTCAAaaGgGGTTAaGCCAAGGG	chr14	-	4
TTCAAGGGAGGTTACGCCAANGG	TTCAAaaGgGGTTAaGCCAAGGG	chr14	-	4
TTCAAGGGAGGTTACGCCAANGG	TTCAAaaGgGGTTAaGCCAAGGG	chr14	-	4
TTCAAGGGAGGTTACGCCAANGG	TTCAAaaGgGGTTAaGCCAAGGG	chr14	-	4
TTCAAGGGAGGTTACGCCAANGG	acCAAGGGAGGTTACaCCAgGGG	chr14	+	4
TTCAAGGGAGGTTACGCCAANGG	TTcTAGGaAGGTcAcCaCCAAGGG	chr14	+	4
TTCAAGGGAGGTTACGCCAANGG	TcCAAGGGAGGTTAaGgaAATGG	chr6	-	4
TTCAAGGGAGGTTACGCCAANGG	aTAcGGGAGGTcAcCaCCAAGGG	chr6	-	4
TTCAAGGGAGGTTACGCCAANGG	TTgAAGGaAGGTTAgGCCAtAGG	chr6	+	4
TTCAAGGGAGGTTACGCCAANGG	TTCAAGaGAGcaTAaGCCAAAGG	chr6	+	4
TTCAAGGGAGGTTACGCCAANGG	TTgAAGGGAGgAgGCCAAGGG	chr11	+	4
TTCAAGGGAGGTTACGCCAANGG	TTCAAGGGAGGTTAtGagcAAGG	chr11	-	4
TTCAAGGGAGGTTACGCCAANGG	TTtcAGGGAGGTTActtCAAAGG	chr10	-	4
TTCAAGGGAGGTTACGCCAANGG	TTCAAGGcAGGTTAgGcGAcAGG	chr19	-	4
TTCAAGGGAGGTTACGCCAANGG	aTgAAGGGAGGTgACGaCAATGG	chr18	-	4
TTCAAGGGAGGTTACGCCAANGG	TTCAAGGGAGcTgAgGgCAAAGG	chr18	+	4
TTCAAGGGAGGTTACGCCAANGG	TTtAAGGGAGGaTAaaCCAAGG	chr18	-	4
TTCAAGGGAGGTTACGCCAANGG	TTtAGtGAGGTTACcCCAAAGG	chr18	+	4

### Supplementary Table 3

**Supplementary Table 3.** Potential off-target sites for CRISPR/Cas9\_gRNA CFTR\_1

crRNA	DNA	Chromosome	Direction	Mismatches
GTGGCGATCATGTTGCTGCGNGG	GTGGCcATCATGTTGgTGCtGGG	chr14	-	3
GTGGCGATCATGTTGCTGCGNGG	GTGGCGATCATGTTGCTGCGCGG	chr6	-	0
GTGGCGATCATGTTGCTGCGNGG	GTGGCcTTCATGTTGCTGCaCGG	chr13	-	3
GTGGCGATCATGTTGCTGCGNGG	tTGGcIATCATGTTGCTGCtGG	chr19	-	3

### Supplementary Table 4

**Supplementary Table 4.** Potential off-target sites for CRISPR/Cas9\_gRNA CFTR\_2

crRNA	DNA	Chromosome	Direction	Mismatches
AGTTCCGGATTCTGAACAGGNGG	AGTTtCtGtTTCTGAACAGGTGG	chr8	+	3
AGTTCCGGATTCTGAACAGGNGG	AGTTcTGGAcTCTGAgCAGGGGG	chr2	+	3
AGTTCCGGATTCTGAACAGGNGG	AGTTcTGGgTTCTGAACAtGTGG	chr17	+	3
AGTTCCGGATTCTGAACAGGNGG	AGTTCCGGATTCTGAACAGGGGG	chr6	+	0
AGTTCCGGATTCTGAACAGGNGG	AGcTCCGGATTCTGAgAgAGGAGG	chr13	+	3
AGTTCCGGATTCTGAACAGGNGG	AGTTcTGGgTTCTGAAGAgAGGAGG	chr13	+	3

**Supplementary Table 5.** sgRNAs and primers

Name	Sequence (5' to 3')
B182 eGFP	CGAGGAGCTGTTACCGGGG
Ms AR 1	ATGTACGCGTCGCTCCTGGG
Ms AR 2	TTCAAGGGAGGTTACGCCAA
Ms CFTR 1	GTGGCGATCATGTTGCTGCG
Ms CFTR 2	AGTTCCGGATTCTGAACAGG
Hu P53	AACCATTGTTCAATATCGTC
Hu CFTR	GGAGAACTGGAGCCTTCAGA
mNG126	GGCACCGGCAATCCAAATGA
mNG260	GTATCCGGAGCCATCTACCA
AR CTRL KO fw	ATCTGACAGTGCCAAGGAGTT
AR CTRL KO rv	CATGTAGACTACCCAAGTCCC
CFTR CTRL KO fw	TCTACGTCCAGACTTCAGTTCG
CFTR CTRL KO rv	ACTCCAATTATGGGGTTAGGATGAG
AR1 off 1 1 fw	TCTCTATGCTCTAGTGGGGTCTT
AR1 off 1 1 rv	GAACAGTGCCTAGCGAGGA
AR1 off 2 1 fw	AGTCCTGCATCACTTCGGA
AR1 off 2 1 rv	GCAGAAAGCGGAGTCCCGA
AR2 off 1 1 fw	ACTTTGCTAGCAGGCTTCAG
AR2 off 1 1 rv	ACAAGGCAAGTCTCTGGCAAT
AR2 off 2 1 fw	AGAGCTTGGCGCTTAGAGAG
AR2 off 2 1 rv	ACAGAACTCCAGTCCATGCG
CF1 off 1 1 fw	GCTACCAGCTAACCCACTC
CF1 off 1 1 rv	ACGCAGTCAGTGTAGGTCC
CF1 off 2 1 fw	ATGGTGAGTCTGGTGGTCACT
CF1 off 2 1 rv	ATGGCAACTCCTTTCTACCCC
CF2 off 1 1 fw	ATCTACACTGAGCCGGACCT
CF2 off 1 1 rv	CAGGTATAGATCGCGCGTGG
CF2 off 2 1 fw	TGCCAAATGTGTGCTTGCTT
CF2 off 2 1 rv	TCATTCATCCCTCTGCCTGTC
P53 fw 1	AGTCAGATCCTAGCGTCGAG
P53 rv 1	GACAGGAAGCCAAAGGGTGAA
CFTR fw 1	CACTCGACACAGAGTGAGCA
CFTR rv 1	TGCAAGCTTCTTAAAGCATAGGT



**Manuscript 2**



## **Probing the role of UBTD1 as a modulator of cell adhesion strength in prostate organoids**

Tiroille. V.<sup>1,2</sup>, Bokobza. E.<sup>1,2</sup>, Voyton. C., Pisano. S.<sup>5</sup>, Obeid. P.<sup>3</sup>, Larbret. F.<sup>1</sup>, Krug. A.<sup>1,2</sup>, Dolfi. B.<sup>1,2</sup>, Guinamard. R.<sup>1</sup>, Irondelle. M.<sup>2</sup>, Ambrosetti. D.<sup>6</sup>, Gidrol. X.<sup>3</sup>, Verhoeyen. E.<sup>1,4</sup>, Bost. F.<sup>1</sup> & Clavel. S.<sup>1,2</sup>

1. Centre Méditerranéen de Médecine Moléculaire (C3M), Inserm U1065, Nice Cedex 3, France
2. Université Côte d'Azur, Nice, France
3. Univ. Grenoble Alpes, CEA, INSERM U1038 – IRIG, BGE, Biomics 38000 Grenoble, France
4. CIRI, Centre International de Recherche en Infectiologie Univ Lyon, Inserm, U1111, Université Claude Bernard Lyon 1, CNRS, UMR5308, ENS de Lyon, F-69007 Lyon, France
5. Institute for Research on Cancer and Aging (IRCAN), 06000, Nice
6. Department of Pathology, Nice University Hospital, University of Nice Sophia Antipolis, Nice, France

Keywords : UBTD1, Cell junction, Prostate, Organoid, EpCAM

Acknowledgement : This work has been supported by the French government, through the UCAJEDI Investments in the Future project managed by the National Research Agency (ANR) with the reference number ANR-15-IDEX-01. V.T. and A.K. are supported by the French Ministry of Research. FB is a CNRS investigator.

# **Probing the role of UBTD1 as a modulator of cell adhesion strength in prostate organoids**

## **Abstract**

Morphogenesis and tissue remodeling are finely regulated processes governed by cell-cell adhesions. However, the spatial and temporal control of adhesion molecules remains partially unexplored. Here we studied the role of UBTD1 as a modulator of the strength of adherens in the prostate epithelium. We showed that down-regulation of UBTD1 disrupted the self-organization of cells in three dimensions. Conversely, we demonstrated that overexpression of UBTD1 induced more regular epithelial monolayers and increased cell surface tension. Transcriptomic analyses revealed a gene expression profile of proteins involved in cell junctions affected by UBTD1 modulation. Using the prostate organoid model, we showed that UBTD1 expression in luminal cells disrupted cyst formation in mouse prostate organoids. Finally using a co-immunoprecipitation approach coupled to mass spectrometry, we showed that UBTD1 interacts with partners involved in cell-cell junctions and that these interactants have their expression modulated by UBTD1 deregulation. Our results show that a protein involved in protein degradation processes regulates the strength of adherens junctions.

## INTRODUCTION

The prostate is a male sex organ located just under the bladder. It is a gland with androgen-dependent maturation, whose function is to secrete fluid that contributes to ejaculation<sup>1</sup>. It contains a branched network of epithelial ducts composed of pseudostratified epithelium surrounded by a contractile stroma. The prostatic epithelium is composed of an outer layer of basal cells, and an inner layer of polarized luminal cells that provide the secretory function of the gland. In addition, this secretory gland is subjected to contractions of the surrounding fibromuscular stroma which participates to its secretory function<sup>2</sup>.

Epithelial tissues are composed of polarized epithelial cells that act as barriers separating two body compartments<sup>3</sup>. They perform specific functions regulated by chemical and mechanical stimuli received from the surrounding environment. The integrity and functionality of each epithelium is dependent on the formation and maintenance of junctions between the cells. Junctional complexes include adherens and tight junctions<sup>3,4</sup>. These junctions ensure, respectively, an engagement of the cell-cell contacts and a maintenance of the impermeability of the epithelial barrier. Both types of junctions are linked to the actin cortex underlying the cytoplasmic membrane. The initiation, maturation and maintenance of these adherens junctions is coordinated with the actin cortex remodeling. It must be noted that the loss of cell-cell junctions in the prostate epithelium is one major feature of prostate adenocarcinoma<sup>5</sup>.

Numerous studies have characterized the actors involved in different phases of adherens junction formation<sup>3,5-7</sup>. The actin polymerization regulatory Rho GTPases, Rac1 and CDC42, establish with Arp2/3 a branched actin network that pushes the cell membranes together to establish cell-cell contact<sup>8,9</sup>. Cadherins on the cell surface will adhere through homophilic interactions. During the maturation phase, the actin cytoskeleton is remodeled to form RhoA-dependent contractile linear actin filaments<sup>10</sup>. Finally, the stable junctions are maintained by a contractile actomyosin network dependent on myosin II<sup>3</sup>. These different steps ensure the stability of adherens junctions mediated by cadherins<sup>6</sup>. Another protein involved in the regulation of epithelial junctions has been discovered, the epithelial cell adhesion molecule (EpCAM; CD326)<sup>11</sup>. Next to being characterized as a biomarker in some cancers<sup>12,13</sup>, overexpression of EpCAM has been shown to establish homophilic interactions at cell junctions<sup>14</sup>. Furthermore, overexpression of EpCAM has been shown to destabilize E-cadherin-mediated junctions by disrupting the interactions of E-cadherin with the actin cytoskeleton mediated by alpha actinin<sup>15</sup>. In the prostate epithelium, the presence of all these partners is finely

orchestrated by post-translational modification of the proteins involved in regulating their degradation<sup>16</sup>.

One of these post-translational modification is ubiquitination, which consists in the attachment of one or more ubiquitins to a protein<sup>17,18</sup> and subsequently will lead to the degradation of the ubiquitinated protein by the proteasome. Ubiquitination involves three major enzymes: E1 (ubiquitin activation), E2 (ubiquitin conjugation), and E3 (ubiquitin ligation). Each of these enzymes interacts with a more or less broad spectrum of proteins. There are indeed a large number of E3 ligases that will have higher specificity with their substrate than the more rare E2 ligases that interact with many different proteins<sup>19,20</sup>. The modulation of the activity of the E2/E3 complex has been poorly studied up to now and thus few regulatory proteins of this complex have been reported<sup>20</sup>.

Ubiquitin domain-containing protein 1 (UBTD1) is a highly conserved protein in evolution. It belongs to a small protein family containing UBTD1 and UBTD2. This poorly characterized protein contains a ubiquitin-like domain (UbL)<sup>21</sup>. In previous studies it was demonstrated that UBTD1 interacts with the UBE2D family of E2 ubiquitin conjugating enzymes. Additionally, UBTD1 stabilized P53 by ubiquitinating MDM2, the E3 enzyme responsible for its degradation<sup>22</sup>. Similarly, it was recently confirmed that UBTD1 participated in the degradation of the transcriptional regulator yes-associated protein (YAP) by modifying its ubiquitination level<sup>23</sup>. Finally, a recent study showed the involvement of UBTD1 in coordinating EGFR signaling by controlling the cellular level of ceramide through the ubiquitination of several proteins involved in this process<sup>24</sup>. UBTD1 was found to be associated with the level of cancer aggressiveness, and survival of patients with prostate, liver and lung cancer<sup>21,23,25</sup>.

Organoids are a self-organized three-dimensional (3D) culture system derived from adult stem cells (ASCs)<sup>26-28</sup>. They recapitulate architecture, composition and functionality of their original epithelial tissues better than the traditionally used two-dimensional immortalized cell lines<sup>29,30</sup>. This model can be used to study stem cell differentiation and spatial organization processes<sup>31</sup>. We used here organoid technology to decipher the role of UBTD1 in processes associated with organogenesis or human pathologies..

Using 3D models we studies the role of UBTD1 in the control of cell junctions in the prostate epithelium.

## **MATERIALS AND METHODS**

### **Organoid culture**

Mouse prostate organoids were generated as described by Drost *et al.*<sup>29</sup>. Briefly, the prostates of 7-8-week-old mice were isolated, and minced in small fragments. Tissue fragments were digested with type II collagenase at 5mg/ml for 1 hour at 37°C and subsequently incubated with 1X TrypLE (Gibco, Waltham, USA) for 15 minutes at 37°C. Cells were washed between each step with 15 ml of advanced complete DMEM/F12 (adDMEM/F12 containing penicillin/streptomycin, 10 mM HEPES and 2 mM GlutaMAX (100× diluted)) (ThermoFisher, Waltham, USA). Then cells were passed through a 70-µm cell strainer (ThermoFisher, Waltham, USA) to remove excessively large debris. The cells were then labeled with CD49f-APC conjugated antibody and CD24-PE conjugated antibody (ThermoFisher, Waltham, USA) and sorted by flow cytometry (BD FACSAria™ Cell Sorter). The isolated cells were then washed with complete adDMEM/F12 and after centrifugation at 200g for 5 minutes, the cell pellet was re-suspended in growth factor reduced phenol red-free Matrigel (Corning, NY, USA) at a concentration of 200 cells per microliter of Matrigel. Mouse prostate organoids were maintained in complete adDMEM/F12 supplemented with 50 X diluted B27 (Life Technologies Carlsbad, USA), 1,25 mM N-acetyl-l-cysteine (Sigma-Aldrich, Saint-Louis, USA), 50 ng/ml EGF (PeproTech, Cranbury, USA), 200 nM A83-01 (Tocris Bioscience, Bristol, UK), 1% Noggin conditioned medium, 10% R-spondin 1 conditioned medium, 1 nM DiHydro-Testosterone (Sigma-Aldrich, Saint-Louis, USA) and 10 µM Y-27632 dihydrochloride (PeproTech Cranbury, USA). Culture medium was replenished every two days.

For passage of the organoid cultures, each drop of Matrigel containing the organoids was resuspended in 1 ml of ice cold complete adDMEM/F12, which were centrifuged for 5 minutes at 200g at 4 ° C. Prostate organoids were then incubated in TrypLE for 5 minutes at 37 ° C and mechanically dissociated by pipetting up and down with a P10 pipet tip. Cells were then washed with complete adDMEM/F12 and centrifuged at 200g at 4 ° C. Cells were seeded again in Matrigel at a concentration of 100 cells/µL. The appropriate medium was added to the cells and replenished every two days.

Organoids were passed every 7 to 10 days.

### **Epithelial monolayer & Acini Culture**

RWPE-1 cells were obtained from ATCC (CRL-11609; RRID:CVCL\_3791). RWPE-1 cells are a prostate epithelial cell line immortalized with human papillomavirus (HPV). This cell line can be cultured as a monolayer or in 3D<sup>32</sup>. All experiments were performed between passages 10 and 25.

For 2D-cultures, RWPE-1 cells were seeded (37°C, 5% CO<sub>2</sub>) in keratinocyte serum-free medium (K-SFM) with L-Glutamine supplemented with Epidermal Growth Factor (EGF) at 5 ng/ml final concentration and Bovine Pituitary Extract at 50 µg/ml final concentration (Life Technologies Carlsbad, USA). The cells were cultured without antibiotics. The cells were passaged every three days and maintained at an average confluence of 75%.

Prior to 3D culture of RWPE-1 cells, maintaining the cells in 2D at confluence of at least 75% is essential. The 3D epithelial structures formed by RWPE-1 cells are called acini. Acini were cultured in 96-well plates suitable for microscopy (Dutscher). A first layer of 70% concentrated matrigel (Corning 356231) diluted in complete K-SFM was deposited in the wells. The matrigel was allowed to solidify for 30 minutes at 37°C. During this time, cells maintained in 2D culture were rinsed, trypsinized and resuspended with 1X Soybean trypsin inhibitor (SBTI); after centrifugation for 5 minutes at 200g, cells were resuspended in K-SFM supplemented medium at a concentration of 6,000 cells per mL. 100 µL were, i.e. 600 cells, deposited on the solidified matrigel layer. The plate was incubated for 30 minutes at 37°C. Then, 100 µL per well of antibiotic-free '3D medium' (K-SFM without additives + EGF 20 ng/ml + 2% FCS) supplemented with 10% Matrigel was added to each well. The next day, 100 µL of 3D medium was replaced. Then, the medium was changed every 48h. Acini were cultured for 9 days.

### **Plasmid**

The cassettes encoding UBTD1-mNG, ΔN-UBTD1-mNG, UBTD1 G2A-mNG, UBTD1 C4A-mNG, UBTD1 G2A C4A-mNG, UBTD1-UBLd-mNG, UBTD1-UBDd-mNG were all inserted into the pHIV-SFFV-IRES GFP plasmid under the control of the spleen focus foamy virus (SFFV) promoter<sup>33</sup>. Lentiviral vector were produced using plasmids encoding GagPol HIV, VSV-G and all the different pHIV-SFFV-IRES. The VSV-G glycoprotein envelopes were expressed in the pHCMV-G expression plasmid.

The cassette encoding GFP or UBTD1-GFP were all inserted into the pPRIG plasmid under the control of the cytomegalovirus (CMV) promoter<sup>34,35</sup>.

Murine retroviral vector were produced using plasmids encoding GagPol MLV, VSV-G and the two plasmids pPRIG encoding for GFP and UBTD1-GFP.

### **Plasmid mutagenesis**

To induce point mutations in the myristoylation site of UBTD1, we used the QuikChange II Site-Directed Mutagenesis Kit (Agilent Technologies, Santa Clara, USA). Following manufacturer's instructions, we performed a thermal cycle to denature the template DNA. We annealed mutagenic primers (see supplementary data) containing the desired mutation and then extended these primers with PfuUltra DNA polymerase. We digested the template plasmid with the enzyme Dpn I. Dpn I digests parental methylated and hemimethylated DNA. Then we transformed competent bacteria with the product of the reaction. Then we sequenced the plasmids to confirm that the desired mutation was correctly introduced.

### **Production of Lentiviral vectors**

Lentiviral vectors (LV) were produced in 293T HEK cells.  $5 \cdot 10^6$  cells were plated per 10 cm plate 24h prior to transfection. To produce LVs, plasmids coding for HIVGagPol (8.6  $\mu\text{g}$ ), pHIVSFFV-Vector (8.6  $\mu\text{g}$ ) and VSVG (3  $\mu\text{g}$ ) were co-transfected with transfection reagent at a 2.6/1 ratio of Polyethylenimine (PEI; Polysciences, Warrington, USA) ( $\mu\text{g}$ )/total DNA ( $\mu\text{g}$ ). The medium was replaced 24 hours after transfection by 6 ml of OptiMEM (Life Technologies Carlsbad, USA) supplemented with penicillin – streptomycin and HEPES. The next day, the vector containing medium was clarified by centrifugation (2000 rpm for 5 min) and filtered through a 0.45  $\mu\text{m}$  pore-size filter before centrifugation overnight (3000g for 16h at 4 ° C). Supernatant was carefully removed by aspiration leaving a volume to obtain 100-150x concentration of the lentiviral vector preparation, which then can be stored at -80 °C.

### **Lentiviral transduction procedure**

Organoids were resuspended in ice-cold complete adDMEMF/12, then centrifuged at 200g for 5 minutes at 4 °C. Once the supernatant was aspirated, 1X TrypLE was added to the tube and incubated for 5 minutes at 37 ° C, while pipetting up and down to dissociate the organoids. After washing the cells with complete adDMEMF/12,  $1 \cdot 10^4$  cells were distributed in a 96-well plate in 100  $\mu\text{l}$  of complete adDMEMF/12 with 10  $\mu\text{M}$  Y-27632 to which the lentivectors were added. The plate was then centrifuged at 200g for 60 min at room temperature. The plate was incubated for 6 hours at 37 °C. The cells were then collected in Falcon15 tube containing 5 ml of complete adDMEMF/12 and centrifuged at 200g for 5 min. The supernatant was removed and the cells were resuspended in 100  $\mu\text{l}$  of Matrigel (356231) and drops of 40  $\mu\text{l}$  were

deposited in P24-well plates. After an incubation of 15 minutes at 37 ° C, 500 µl of mouse prostate organoid medium was added to each well as previously described.

To obtain a homogeneous organoid population expressing the integrated fluorescent cassette, we sorted the cells by flow cytometry (BD FACSAria™ Cell Sorter). After sorting we seeded the cells in Matrigel at a concentration of 200 cells/µL. Then the corresponding media was added and replenished every two days.

RWPE-1 cells were seeded in 96-well plates. Viral particles encoding GFP or UBTD1 GFP were added to the cells with an identical MOI of 1, to ensure a similar integrated copy number for both vectors. RWPE-1 were transduced with lentiviral vectors encoding control shRNA (shCTRL) or targeting UBTD1 (sh#2 and sh#4). Cells transduced with shRNAs were selected with puromycin. The RWPE-1 shCTRL, sh#2 and sh#4 lines were then transduced with the FUCCI probe (Ref. PLV-10146-50). The cells expressing the fluorescent probe were sorted by flow cytometry (BD FACSAria™ Cell Sorter).

### **Cell proliferation assay**

Proliferation determined with EdU was performed in 2D and 3D cultures. Click-iT™ Plus EdU Alexa Fluor™ 647 was used (ThermoFisher, Waltham, USA). For both 2D and 3D cell cultures, 5 µM EdU was added 12 hours before analysis according to manufacturer's instructions. Briefly, the cells were harvested, then fixed. The cells were permeabilized and then labeled with an anti-EdU antibody. The fluorescence of the anti-EdU label was analyzed by flow cytometry.

Proliferation of the 2D and 3D RWPE-1 cell cultures expressing shRNA was assessed with the FUCCI probe (PLV-10146-50, Takara, Kyoto, Japan). The FUCCI probe is a cell-cycle reporter vector that delivers fluorescent ubiquitination-based cell-cycle indicators.

The FUCCI probe contains a Geminin protein whose level fluctuates differentially throughout the cell cycle. As cells transition into S phase, Geminin levels rise, remaining high until the cells are back in G1. As Geminin is coupled to GFP, the evaluation of the probe fluorescence tells us, in which cell cycle phase the cells reside. Cells stably expressing the probe were harvested and analyzed by flow cytometry for their GFP fluorescence level.

### **Flow cytometry analysis**

The RWPE cells were rinsed and then trypsinized. They were then resuspended with PBS supplemented with 10% FBS.

The acini were resuspended with a P200 cone by mechanical agitation. They were then transferred to a falcon containing K-SFM ice-cold medium. Acini were centrifuged for 5 minutes at 200g at 4 ° C. The acini were then resuspended in 1 mL of 1X TrypLE. After a 5 minute incubation at 37 ° C. They were mechanically dissociated by pipetting up and down with a P10 / P1000 pipet tip. Cells were then washed with PBS 10% FBS and analyzed by flow cytometry for measuring the fluorescence of GFP or EdU labeling.

### **Immunofluorescent stainings and imaging**

For live imaging, organoids were observed with an Evos optical microscope. For immunofluorescence staining, organoids were harvested and washed once with ice cold complete addMEMF/12. They were fixed for 1 hour in PBS 4% PFA, permeabilized with 0.5% Triton X-100 for 30 minutes and then blocked with 2% Fetal Bovine Serum (FBS) in PBS for 1 hour at room temperature (RT). Primary antibodies were added to the cells for 2 hours at RT (list of antibodies in supplemental data). After washing with PBS, secondary antibodies coupled to AlexaFluor 488 or 594 (Life Technologies, Carlsbad, USA) were added for 1h30 at RT. DAPI was used to stain nuclear DNA. Organoids were mounted and imaged with a confocal Nikon microscope. Organoids were also cultivated in 96-well flat-bottom plates (Dutscher, Bernolsheim, France). They were then directly fixed and permeabilized with 4% PFA, 0.8% Triton X-100, 5 mM EGTA, 1 mM MgCl<sub>2</sub> in PBS. Antibody staining was performed as described above. Images were processed with the Imaris program for 3D reconstruction.

### **Immunohistofluorescence**

Histological sections were made from two paraffin-fixed post-prostatectomy samples of patients (Dr. Ambrosetti, anatomopathology department, CHU of Nice). Sections of 5 µm (Microme HM340E) were made, and then, after deparaffinization, they were treated with a demasking solution (10 nM sodium citrate, pH 5.5 and 6.5). After saturation (BSA 3%, 0.1% Tween20), the sections were incubated with primary antibodies targeting UBTD1 (HPA034825-Sigma), CK5 (ab193895), CK8 (ab53280), overnight at 4°C and then with adapted secondary antibodies for 1h at room temperature (Alexa Fluor® 594 anti-mouse, Alexa Fluor® 488 anti-rabbit). The nucleus was stained with DAPI and slides were sealed in mounting medium (ImmunoHistoMount™ - Sigma).

### **Stimulated-Emission-Depletion Microscopy**

Cells were seeded on 18x18mm, 0.17mm thick #1.5 coverslips previously coated with a solution of fibonectin diluted in PBS to a concentration of 20 µg/ml solution. The cells were seeded and left for 48h for complete adhesion. The cells were fixed with 4% PFA solution. F-actin was labeled with phalloidin Alexa Fluor™ 594 and endogenous UBTD1 using a specific STAR 635P secondary antibody. Cytoplasmic membrane was stained using Wheat Germ Agglutinin (WGA) conjugated with an Alexa Fluor™ 647 (pink). Acquisition was performed with a TCS SP8 STED 3X microscope (Leica Microsystems) in collaboration with the IPMC imaging platform.

### **Expansion**

RWPE-1 cells were seeded on 18 x 18 mm coverslips. As described in the article by Wassie et al.<sup>36</sup>, first, 'molecular handles' are covalently attached to the biological sample. The biosample is immersed in a monomer solution (containing sodium acrylate) that reacts by free-radical polymerization to form a densely cross-linked (NN'-methylenebisacrylamide cross-linking agent) and highly penetrating (sodium polyacrylate) polyelectrolyte hydrogel. This coats the biomolecules and/or markers, binding to the molecular handles so that the attached biomolecules and markers are mechanically coupled to the polymer mesh. The sample is chemically denatured to homogenize its mechanical properties. The sample is immersed in water, which allows the hydrogel to swell. After expansion, other markers can be applied.

### **Image analysis**

Confocal images of fixed samples were obtained on a Nikon A1R confocal microscope (Nikon, Tokyo, Japon). Bright field and fluorescent images were obtained on an EVOS fl AMF-4306 AMG microscope. Confocal images of organoids and acini were used for image.

The cell images were analyzed with the software CellProfiler. The morphological parameters of cells, organoids and acini were extracted with the MeasureObjectSizeShape module of CellProfiler. For in-depth analysis, we used the open source KNIME Analytics Platform. To evaluate the cell distribution within the organoid, the cells were identified with DAPI labeling. Then the position of the cells on the radius of the organoid was calculated. To simplify the calculations, the radius of each organoid was cut into bins, i.e. compartments in which each cell is classified. The bin 0 corresponded to the center of the organoid, the bin 10 corresponded to the edge of the organoid. To determine if the organoids were considered as cystic or compact, we calculated the percentage of cells present in bins 9, 10 and 11, which corresponded to the

edges of the organoid. We determined a reference cut-off based on organoids visually considered as cystic. Once the parameter was set, all images were analyzed with this same cut-off. To determine the average fluorescence of the CK5 and CK8 labels along the radius of the organoid, the fluorescence of each cell was determined, and then the cells were placed back on the radius of the organoid.

Cell fractionation imaging was also performed on CellProfiler from confocal images. Nuclei were identified based on DAPI staining. Epithelial cell outlines were determined with F-actin staining. The images shown in Supplementary Figure 1B represent the different masks set up on CellProfiler to separate the cytoplasmic membrane, cytosol, perinuclear region and nucleus. The imaging cell fractionation is performed on adherent cells.

The 3D reconstructions and 3D image analysis were performed with the Imaris software. The 3D reconstruction of the organoids in Supplementary Figure 6C was performed using confocal images with an interval of 2  $\mu\text{m}$ . Epithelial monolayer regularity was analyzed using F-actin staining with phalloidin. Cell monolayers were reconstituted with Imaris and the surface regularity was quantified.

### **Bleb induction**

Cell lines were established from RWPE-1 cells. They were transduced with retroviral vectors carrying GFP or UBTD1-GFP under a CMV promoter. The cells were grown in 96-well plates with a bottom adapted for microscopy (Dutscher, Bernolsheim, France) and were seeded 48h before Bleb formation was induced by treating the cells with ethanol 5% for 5 minutes and cytochalasin D at 2.5 $\mu\text{M}$  for 2 minutes. A PBS 4% PFA solution was used to fix the cells. The cells were permeabilized with Triton 0.1% and then stained. F-actin was stained with phalloidin (Life Technologies Carlsbad, USA), cell membranes were stained with Wheat Germ Agglutinin (ThermoFisher, Waltham, USA).

### **3D structure prediction of proteins**

The 3D protein structure was predicted for the human UBTD1 using the software for protein structure and function prediction I-TASSER<sup>37-39</sup>. Among the five predicted models, only the one with the highest score was displayed. To visualize the protein structure, we used the molecular visualization software PyMOL and highlighted the myristoylation sequences.

Alternative protein structure predictions of the human and mouse UBTD1 sequences were performed using the online 3D molecular structure prediction software AlphaFold<sup>40</sup>.

### **Sequence alignment**

The mouse and human UBTD1 sequences found on UniProtKB were aligned with the pairwise sequence alignment tool provided by EMBO-EBI online platform. The output format displayed the pairs.

### **Proteomic - Interactome analysis**

A 24-well plate of murine prostate organoids cultured for 7 days was lysed in RIPA buffer and frozen immediately in nitrogen. After immunoprecipitation using an anti-UBTD1 antibody (HPA034825-Sigma), the protein partners of UBTD1 were identified by mass spectrometry in collaboration with the Proteomics Platform of the Institute of Molecular and Cellular Pharmacology (IPMC). The UBTD1 interactome was then constructed with the Cytoscape software using the STRING database.

### **Atomic Force Microscopy - Young's modulus**

RWPE-1 cells stably expressing GFP or UBTD1-GFP were used to study the effect of UBTD1 overexpression. The stable cell lines expressing shCTRL, UBTD1 # 2 and # 4 were used to study the down regulation of UBTD1. The cells were seeded 72 hours before the measurements with the atomic force microscope (AFM) on a polystyrene dish of 35 mm in diameter. *“Before the measurement, the cells were washed twice with Leibovitz's medium (Life Technologies) supplemented with 10% inactivated fetal bovine serum (FBS). Samples were analyzed using a BioScope Catalyst atomic force microscope (Bruker Nano Surfaces, Santa Barbara, CA, USA) equipped with a NanoScope V controller and coupled to an optical microscope (Leica DMI6000B, Leica Microsystems Ltd. , UK). The measurements were performed at 37 ° C. For each sample, at least 30 cells were analyzed using the “Point and Shoot” method, collecting at least 200 force – distance curves at discrete points (on average five points for each cell in the perinuclear area). The experiments were performed using a probe with a borosilicate glass spherical tip (5  $\mu$ m diameter) and a cantilever with a nominal spring constant of 0.06 N / m (Novascan Technologies, Ames, IA USA). After determining both the deflection sensitivity of the system in the Leibovitz's medium using a clean Corning 35 mm polystyrene dish and the spring constant of the cantilever by means of the thermal tune method, force – distance curves were collected on samples using a velocity of 2  $\mu$ m / s, in relative trigger mode and by setting the trigger threshold to 2 nN. The apparent Young's modulus was calculated using the NanoScope Analysis 1.80 software (Bruker Nano Surfaces, Santa Barbara, CA, USA) applying to the force curves, after the baseline correction, the Hertz spherical indentation model using*

*a Poisson's ratio of 0.5. For each force curve, the force fit boundaries to perform the fit were chosen between 5% and 25%. To avoid any tilt effect due to the base correction step, only the force curves having their maximum value at 2 nN were taken into account for performing the fit and only the apparent Young's modulus values corresponding to a fit with  $R^2 > 0.90$  were accepted.” Modified from Torrino 2019.*

### **Cell extrusion**

To perform the extrusion assay, we first established stable cell lines from RWPE-1 cells. We transduced RWPE-1 epithelial cells with a lentiviral vector expressing an mCherry under the control of an SFFV promoter. Transduced cells were sorted by flow cytometry (BD FACSAria™ Cell Sorter) to obtain a homogeneous population expressing the fluorescent cassette. GFP and UBTD1-GFP lines were also sorted to obtain a GFP+ cell population. According to the protocol described in Teo *et al.*<sup>41</sup>, WT-mCherry and GFP/UBTD1-GFP or sh# cells were mixed at a 1:20 ratio, respectively. To quantify the percentage of apical extrusion of the epithelial monolayer, we counted the number of mCherry-positive cells that were surrounded by cells that were not expressing mCherry. The cells were seeded in 96-well plates with a bottom suitable for microscopy (Corning, NY, USA). Cells were seeded at day 0, medium was changed at day 2 and cells were fixed with 4% PFA in PBS at day 4.

Images were then acquired on a confocal microscope, and analyzed with CellProfiler. More detailed description can be found in the Image analysis section.

A proliferation control was performed on each of the cell lines to make sure that the differences observed were due to mechanical differences and not to a differential proliferation rates.

### **Western Blot**

Primary antibodies: anti-tubulin (10D8), anti-UBTD1 (HPA034825). HRP-conjugated donkey anti-mouse IgG (715-035-150) and HRP-conjugated anti-mouse IgG (711-035-152) from Jackson ImmunoResearch Laboratories (West Grove, USA).

### **RNA sequencing**

RWPE-1 cell lines were grown in 100 mm diameter dishes in complete K-SFM. Cells were seeded 72 h before harvesting to allow them to adhere and form junctions. Cells were rinsed, trypsinized and resuspended with SBTI. After centrifugation for 5 minutes at 200g, the supernatant was aspirated and the cell pellet was snap frozen in liquid nitrogen. RNA extraction

and subsequent analysis were done by the Beijing Genomics Institute (BGI, Shenzhen, China). All analyses were performed on the online software Dr.Tom provided by BGI.

### **Statistical Analysis**

We have applied either a Mann-Whitney test or a non-parametric Kruskal-Wallis test when we compared two or three experimental conditions, respectively. Experiments were performed at least three times.

## **RESULTS**

### **Mutation of the N-terminal myristoylation-like site disrupts membrane localization of UBTD1 in prostate epithelial cells**

In order to localize the UBTD1 protein in the epithelial gland, we stained a histological section of healthy adult human prostate (**Figure 1A**). Luminal cells were identified using anti-cytokeratin 8 (CK8) antibody staining. Basal cells were labeled with an anti-cytokeratin 5 antibody (CK5). UBTD1 detection showed strong expression in the contractile stromal cells surrounding the gland. In the gland, UBTD1 was mainly expressed in the CK5<sup>+</sup> basal cell layer. UBTD1 was not found in the CK8<sup>+</sup> luminal cells.

As shown in previous studies, UBTD1 localized in the prostate tissue to intercellular junctions where cell-cell contacts were established<sup>23</sup>. Next, we wanted to verify whether UBTD1 was localized to the cytoplasmic membrane or associated with the underlying actin cortex. We used high resolution imaging techniques to differentiate the membrane from the cortex. Using expansion microscopy (ExM), we identified the cytoplasmic membrane with Wheat Germ Agglutinin (WGA) coupled to a fluorophore. The actin cortex was labeled using phalloidin. UBTD1 did not appear to colocalize with the actin cortex but, in contrast, appeared to colocalize with the cytoplasmic membrane (**Figure S1 A**). To confirm these observations, we performed on the same tissue sections acquisitions using stimulated emission depletion (STED) microscopy. The UBTD1 spots colocalized with the cytoplasmic membrane labeling at the cell-cell contacts (**Figure 1B**). In addition, UBTD1 staining was situated above the actin cortex without co-localizing with it. On cell projections supported by an assembly of actin filaments, UBTD1 appeared to localize around the F-actin label. These first observations clearly indicated that UBTD1 localized to the cytoplasmic membrane and not to the actin cortex.

Blebs are spherical cell protrusions that are involved in several physiological events<sup>44</sup> such as locomotion, cell division. There are three distinct phases identified in bleb formation: bleb

initiation, bleb expression and cortex repolymerization and retraction. The first stage consists of local dissociation of the cortex from the membrane. The second stage consists of an entry of cytosolic fluid between the membrane and the cortex, which results in an increase in the volume of the bleb. The last step, which corresponds to the retraction of the bleb, involves a reassembly of the actin cortex inside the bleb. The acto-myosin contractile cortex will then retract the bleb. Here we took advantage of this type of cellular event, which can easily be triggered by exposure to hypertonic vesiculation buffer or ethanol, to assess whether UBTD1 was more tightly attached to the cytoplasmic membrane or to the cortex<sup>42,43</sup>. We treated the cells with 5% ethanol to trigger blebbing, and then exposed them to cytochalasin D (CytoD). CytoD blocks actin polymerization, and in the short term stimulates bleb formation. We observed that UBTD1 remained tightly attached to the membrane in bleb structures (**Figure 1C**). This confirmed that UBTD1 is indeed associated with the cytoplasmic membrane in prostate epithelial cells and not with the cortex.

To reveal how UBTD1 is addressed to the cytoplasmic membrane, we focused on the different domains that were included in the sequence of UBTD1 (**Figure 1D**). As shown in the predicted 3D structure (**Figure 1E**), we identified a potential myristoylation site located at the N-terminal part of the protein. Myristoylation of proteins can dictate their localization towards the membrane in many different situations<sup>44</sup>. It consists in the addition of a myristic acid by N-myristoyltransferase (NMT) at the N-terminal part of a protein that enables protein-lipid interactions. We generated several mutants for the potential myristoylation site of the UBTD1 protein coupled to the fluorescent protein, mNeonGreen. Deletion of the entire potential myristoylation site ( $\Delta$ N-UBTD1-mNG) resulted in delocalization of UBTD1 from the cytoplasmic membrane (**Figure 1D**). Quantification by imaging cell fractionation showed a significant difference in the proportion of  $\Delta$ N-UBTD1 localized at the cytoplasmic membrane compared to its native form (**Figure 1F1E**). Using a directed mutagenesis approach, we generated single point mutations in the N-terminal sequence of UBTD1. The glycine 2 mutation (UBTD1-G2A-mNG) also induced significant delocalization of UBTD1 from the cytoplasmic membrane. This mutant form of UBTD1 localized predominantly in the nucleus, in the perinuclear region, and in the cytosol. Interestingly, the cysteine 4 mutation (UBTD1-C4A-mNG) did not induce a significant delocalization of UBTD1 from the cytoplasmic membrane. UBTD1-C4A-mNG relocated mainly to the perinuclear region. Finally, when glycine 2 and cysteine 4 were mutated simultaneously (UBTD1-G2A-C4A-mNG), the protein was distributed in the cell similarly to the  $\Delta$ N-UBTD1-mNG and UBTD1-G2A-mNG mutant proteins.

Taken together, UBTD1 myristoylation appears to be required for its cytoplasmic membrane localization in prostate epithelial cells.

### **The expression level of UBTD1 is related to 3D cell organization processes**

To better understand the function of UBTD1 in epithelial cells, we also took advantage of a versatile 3D-cell culture model. The epithelial cell line RWPE-1 can be grown in 3D in a gel mimicking the extracellular matrix (ECM). The 3D culture in an ECM-mimicking environment enables the study of spatial self-organization processes of cells. This model allows the identification of genes regulating cell-cell or cell-matrix contacts<sup>45,46</sup>. RWPE-1 cells grown in matrigel (synthetic ECM) form gland-like structures, called acini, with a lumen in the center surrounded by a single cell layer. The formation acini relies on two distinct phases: a first phase of proliferation from day 0 to day 6 (**Figure 2A**), followed by a structuring phase from day 6 to day 10. This second phase of acini formation is conditioned by the maturation of cell-cell junctions and the establishment of apico-basal polarity. In a WT acini cultured until day 10, UBTD1 is localized in basolateral position of the cytoplasmic membrane (**Figure 2B**). To understand the role of UBTD1 in this simplified gland-like model, we first downregulated UBTD1 expression. We established stable cell lines using a lentiviral vector encoding a shRNA targeting UBTD1 mRNA. ShRNA #2 and #4 decreased UBTD1 protein expression by 78 and 76%, respectively (**Figure S3E**). As seen in the bright-field images, downregulation of UBTD1 with shRNA #2 and #4 disrupted cell organization and prevented the formation of mature acini (**Figure 2C**). Morphological parameter quantification based on confocal images (**Figure 2D**) showed a significant increase in acini area and perimeter in the conditions with shRNA #2 and #4 compared to the shRNA control (shCTRL) (**Figure 2E**). We then quantified the proliferation level at day 10, when the structures are organized. Image analysis already showed a significant increase in the number of cells per acini when UBTD1 was downregulated (**Figure 2F**). To quantify the level of acini proliferation, we established stable cell lines expressing the FUCCI cell cycle probe. At day 10, 19% of the cells are in S/G2/M phase in the shCTRL acini (Fig. 2F), while UBTD1 down regulation induced a significant increase in proliferation (39% and 35%) associated with acini disorganization. Interestingly, cell death, which is involved in lumen formation tends to decrease when UBTD1 is downregulated compared to the shCTRL condition (**Figure 2G**).

To conclude, down-regulation of UBTD1 disrupts the spatial organization of cells and induces a strong cell proliferation.

Conversely, we overexpressed UBTD1 in RWPE-1 cells by establishing stable lines expressing GFP or UBTD1-GFP (cytoplasmic membrane localized form).

The effect of UBTD1 overexpression seems less pronounced than the downregulation (**Figure 2H**). Nevertheless, acini overexpressing UBTD1 have a significantly larger area and perimeter than control acini (**Figure 2I**). In addition, the average distance of the cells from the center of the acini is also significantly increased. Labeling with the polarity marker giantin shows more uniformly oriented cells when UBTD1 is overexpressed (**Figure 2H**). We observe well organized UBTD1 overexpressing acini as early as day 6 (**Figure 2J**). No significant changes in proliferation and cell death were observed (**Figure 2L**).

Overexpression of UBTD1 induces acini that appear more mature, with visually better polarized cells. We hypothesize that cell junctions, which is a primordial process in acini organization, has been disrupted by the dysregulation of UBTD1 expression.

### **Overexpression of UBTD1 increases cell surface tension and induces more regular monolayers**

Cell-cell junction assembly during morphogenesis is accompanied by rearrangements of the actin cytoskeleton. These rearrangements can affect the shape, motility and polarity of epithelial cells<sup>9</sup>. Previous studies have shown that actin network rearrangements are accompanied by a change in cell stiffness<sup>47</sup>. In addition, increased cell-cell adhesions at a tissue scale increases tissue surface tension<sup>48</sup>. Here we used atomic force microscopy (AFM) to directly measure the surface tension of RWPE-1 epithelial cells<sup>49</sup>. With a spherical tip on a cantilever, we determined the surface tension of the different RWPE-1 cell lines (**Figure 3A**). Overexpression of UBTD1 significantly increased cell surface tension (**Figure 3B**). Conversely, downregulation of UBTD1 decreased surface tension (**Figure 3C**). Thus, the expression level of UBTD1 directly impacts the surface tension of RWPE-1 epithelial cells.

Another feature of cell junction establishment is the surface integrity of an epithelium. In culture, normal epithelial cells stop to proliferate to form a flat monolayer<sup>6</sup>. Here we analyzed the regularity of RWPE-1 monolayer grown to confluence (**Figure 3D,E**). Reconstitution of the epithelium in the Z axis shows more regularly organized cells when UBTD1-GFP is overexpressed compared to GFP (**Figure 3D**). Accordingly, UBTD1 overexpressing cells displayed a different morphology when compared to control GFP+ cells. The mean eccentricity was significantly increased. Downregulation of UBTD1 resulted in an less organized epithelium (**Figure 3F,G**). As seen in the Z plane image, cells treated with shRNA #2 and #4

started to grow on top of each other. Surprisingly, no change in cell shape is observed (**Figure 3F,G**).

To complete our observations, we then decided to focus on the phenomenon of cell extrusion. Live cell extrusion requires the formation of a contractile ring of actomyosin by adjoining cells surrounding a cell to be extruded. This contraction ring will induce an expulsion of the surrounded cells<sup>41</sup>. Here we examined the functional consequences of UBTD1 deregulation on apical extrusion. We used a cell mix to test the induction of live cell extrusion. We stably expressed mCherry in RWPE-1 WT cells that we mixed in minority (1:20) with either GFP or UBTD1-GFP expressing cells (**Figure 3H**). As a result, WT mCherry-positive cells surrounded by UBTD1-GFP cells had a higher extrusion rate compared to when they were surrounded by control GFP+ cells (**Figure 3I,J**). Importantly, no difference in proliferation rate was observed between GFP and UBTD1-GFP cells. In accordance, morphological changes of red cells were observed between the two conditions (**Figure 3K**). Their mean eccentricity was significantly higher when they were surrounded by UBTD1-GFP cells compared with GFP. We then mixed WT mCherry cells with UBTD1 downregulated cells at the same 1:20 ratio (**Figure S3 A**). Surprisingly, downregulation of UBTD1 also increased the apical extrusion of mCherry positive WT cells (**Figure S3 B,C**). Red cell eccentricity was decreased when they were surrounded by cells treated with shRNA #2 and #4 compared to shCTRL (**Figure S3 D**). Overall, dysregulation of UBTD1 modifies cell surface tension. It affects the integrity of the epithelial surface and induces changes in live cell extrusion rate.

### **Gene expression profile of proteins involved in cell junctions is affected by UBTD1 modulation**

To identify factors that would control these changes in cell shape and rigidity, we examined the transcriptomic profiles of RWPE-1 prostate epithelial cells over- or under-expressing UBTD1. We performed bulk transcriptomic analysis on 20 independent samples of each of the established cell lines. To compare genes that shared expression between basal expression conditions and when UBTD1 was overexpressed, principal component analysis (PCA) was performed (**Figure S4A**). PCAs showed biological replicates clustered together, confirming the robustness of the analysis. It showed that GFP and UBTD1-GFP cells were separated along PC1 and PC2 (**Figure S4A**). Presentation by volcano plot, which showed differentially expressed genes (DEGs), revealed that overexpression of UBTD1-GFP greatly affected the transcriptomic profile of RWPE-1 epithelial cells (**Figure 4A,B**). PCA performed separately on shCTRL, shUBTD1 #2 and #4 samples also showed differences in their transcriptomic

profiles (**Figure 4 A,B**). However, shUBTD1 #4 did not induce such a strong change in the transcriptomic profile compared to sh#2 (**Figure S4B**). We then performed a classification of the DEGs in the different conditions based on the Gene Ontology (GO) functional classification (**Figure 4C**). In the condition where UBTD1-GFP was overexpressed, and in the condition treated with shRNA #2, the GOs of the cellular components were generally associated with membrane, membrane-associated proteins and cell junctions. Locomotion, biological adhesion and developmental processes were also found in GOs associated with biological process (**Figure 4C**).

We then performed Gene Set Enrichment Analysis (GSEA) to determine if an a priori defined set of genes show statistically significant differences between the conditions (**Figure 4D**). Consistent with the differences we observed in processes involved in cell junctions, i.e. cell shape and cell rigidity, GSEA grouped genes involved in cell-cell junctions. When UBTD1 was downregulated with shUBTD1#2, many genes involved in cell-cell junctions and basolateral membrane were upregulated. GSEAs showed a set of genes involved in cell junctions that appeared to be more expressed in the GFP condition compared to UBTD1-GFP. Similarly, genes involved in the apical plasma membrane were upregulated with UBTD1-GFP.

Overall, these findings suggest that the observed changes in cell shape, cell stiffness and epithelial integrity are coupled with transcriptional changes in genes involved in cell junctions.

### **UBTD1 expression in luminal cells disrupts cyst formation in mouse prostate organoids**

In order to assess the role of UBTD1 in the maintenance of cell-cell junctions, we then used the murine prostate organoid model. Prostate organoids were generated by isolating adult stem cell (ASCs) from mouse prostate tissue. As described in previous studies<sup>29,50</sup>, ASCs were seeded into matrigel and were grown with organoid culture medium for 9 days. The organoids grow in distinct phases. As described in the illustration (**Figure S5A**), basal CK5+ ASCs proliferate, and start to differentiate into luminal cells from day 4. The CK8+ luminal cells, located in the center of the organoid will start to secrete fluid under the influence of dihydrotestosterone (DHT) between day 5 and day 6. Fluid secretions by luminal cells will induce the formation of a lumen in the center of the organoid from day 6. Luminal cells will secrete until they form a fully mature cystic organoid at day 9. As described in recent studies, lumen formation depends on the cell junctions of the secretory cells. Microlumens, initiated by secretory cells, fuse together by hydraulic fracturing of cell-cell contacts<sup>51</sup>.

Consistently with what is shown in **Figure 1A**, UBTD1 is only expressed in basal CK5+ cells of WT mouse prostate organoids (**Figure S5B**). Subsequently, we established stable organoid

lines, through transduction of a murine retroviral vector, expressing GFP or UBTD1-GFP in basal and luminal cells (**Figure 5A**).

At the 1 nM reference concentration of DHT<sup>29</sup>, bright field images of organoids labeled for their nuclei show more compact organoids with UBTD1 GFP, with a significantly reduced area (**Figure 5A,B**). This is reflected in the differential cell distribution along the organoid radius (**Figure 5C**). Indeed, the percentage of cystic organoid formed is significantly reduced with UBTD1-GFP compared to the GFP condition (**Figure 5D**). Confocal images of the center of GFP and UBTD1-GFP organoids highlight a different distribution of CK5 and CK8 cells (**Figure 5E**). As shown with quantification of the mean intensity of CK5 and CK8 markers along the organoid radius, when UBTD1-GFP is expressed, luminal cells remain localized in the center of the organoid (**Figure 5F**).

It was shown in previous studies that the swelling of organoids was dependent on the stimulation of luminal cells by DHT<sup>50</sup>. Therefore, we treated organoids expressing GFP or UBTD1-GFP with increasing doses of DHT to stimulate fluid secretion from luminal cells (**Figure 5A**). GFP organoids showed a compact profile at 0 nM DHT, with 0% cystic organoid formed (**Figure 5B,D**). Approximately 40% of GFP organoids became cystic at 0.5 nM DHT (**Figure 5D**). As shown with the cell distribution along the organoid radius (**Figure 5C**), at 1, 3 and 5 nM DHT, 60-90% of the GFP organoids were cystic (**Figure 5D**). Strikingly, UBTD1-GFP organoids became cystic when overstimulated with DHT (**Figure 5A,D**). As shown with the cell distribution, the percentage of cystic organoids increased to 60% at 3 nM DHT, showing no significant difference with the GFP condition (**Figure 5 B,D**).

Overall, transduction of mouse prostate organoids with UBTD1-GFP prevented lumen formation at 1nM DHT. However, when fluid secretion by luminal cells was overstimulated with DHT (3 nM) organoid regained lumen formation in the case of UBTD1 overexpression.

### **Analysis of UBTD1 interactome reveals cytoplasmic membrane and actin cortex associated partners**

Next, we used co-immunoprecipitation to isolate the interactants of the endogenous UBTD1 protein expressed in mouse prostate organoids. Using mass spectrometry (MS), we obtained a high quality network of interactions among the 182 identified proteins. This interactome connects part of the regulatory system of cell junctions to functional complexes associated with the actin cytoskeleton and its regulatory partners. A cluster associated with the ribosome and the proteasome was also identified. These data provide a large source of information that can be used to understand the connected roles of UBTD1 in other signaling pathways.

Notably, the cluster involving actin cytoskeleton regulatory proteins provides valuable information (**Figure 6 A,B**). We identified the Rho GTPases involved in the remodeling of the actin cytoskeleton that takes place during the establishment of cell-cell junctions, i.e. Rac3, CDC42 and RhoA<sup>3</sup>. Rho GDP-dissociation inhibitor 1 (ARHGDI1) was also identified as an interactant of UBTD1. We also identified ezrin and vinculin, which belong to the ERM family of proteins, responsible for binding the actin cytoskeleton to the cytoplasmic membrane<sup>52</sup>. Interestingly, we also identified the epithelial cell adhesion molecule (EpCAM), which participates in the regulation of adherent junctions<sup>11</sup>.

Overall, the identification of UBTD1 interactors. It provides potential partners that could explain the phenotypes associated with UBTD1 dysregulation.

### **UBTD1 interactants are modulated by UBTD1 deregulation**

In order to get insights into the identified interactants of UBTD1, we used open access data from single cell RNA sequencing performed on an intact human prostate. We used this data to identify in which cell type of the prostate gland the identified proteins were expressed. The ERM proteins ezrin and vinculin, have a higher average expression in luminal cells than in basal cells. Rho GTPases are expressed at the mRNA level in both basal and luminal cells. Interestingly, the Rho GDP-dissociation inhibitor ARHGDI1 has a higher average expression in basal cells. Finally, the epithelial cell adhesion molecule (EpCAM) was shown to be expressed in both basal and luminal cells (**Figure 7A,B**).

We then analyzed the protein atlas data base to determine, at the protein level, where these proteins are expressed in the human adult prostate (**Figure 7C**). CD44, vinculin, CAPN1, IQGAP1 and RAC3 showed high expression in basal cells, and for some, co-expression in luminal cells. Interestingly, EpCAM showed a predominantly localized protein expression at the intercellular junctions of luminal cells (**Figure 7C**). We then performed a more in depth analysis of expression levels of these genes in RWPE-1 cells (**Figure 7D**). The majority of these genes did not show significant changes in their transcriptional expression. However, we noted that CD44, VCL, and UBE2N showed transcriptional changes opposite to the expression level of UBTD1. We also noted that EpCAM and ARHGDI1 showed changes that followed the expression of UBTD1. When UBTD1 was overexpressed, these genes were upregulated, when UBTD1 was downregulated, the expression of these genes tended to decrease.

These information gave insights about potential mechanisms involved in prostate organoid organization due to interactions that UBTD1 could have with the partners identified by mass spectrometry.

## **DISCUSSION**

Here we dissected the cellular localization and the role of UBTD1 in the prostate epithelium. We showed by a directed mutagenesis approach that the intracellular localization of UBTD1 depends on an N-terminal myristoylation site. We studied the influence of UBTD1 on cell shape and rigidity and its impact on 3D cell organization processes. We also showed that de-regulating expression of UBTD1 in luminal cells disrupted lumen formation in a 3D prostate organoid model. Finally, using a transcriptomics and co-immunoprecipitation approach associated with mass spectrometry, we identified genes interacting with UBTD1.

We began by investigating which role UBTD1 might have in gland homeostasis using a 3D model of cellular self-organization<sup>45,46</sup>. The model, called acini, which reproduces a simplified prostate gland, indicated the necessity of UBTD1 for these organizational processes.

These organizational processes are largely dependent on the mechanisms of cell-cell junctions and the establishment of apical-basal polarity, we next investigated the cellular processes associated with cell-junction formation<sup>6,7,45,53</sup>.

The establishment and maturation of cell-cell junctions is associated with a remodeling of the actin cytoskeleton<sup>3,54</sup>. Cell junctions are initiated with a cortex composed of short branched actin filaments, mature junctions are stabilized by long contractile actin filaments<sup>55,56</sup>. As shown in previous studies, the nature of the actin cortex influences the cortical tension and consequently the cell surface tension<sup>47,57</sup>. The measurement of the surface tension of cells expressing different levels of UBTD1 indicated and validated this feature of cell junction establishment. Along with that, UBTD1 also affected cell shape, and the integrity of a 2D grown epithelial monolayer<sup>58</sup>.

We then showed the effect of over-expression of UBTD1 in murine prostate organoids. As shown in previous studies, prostate organoid swelling is dependent on stimulation of luminal cells by DHT<sup>50</sup>. A study published in 2019 supported the importance of E-cadherin-mediated intercellular junctions for lumen formation in mouse blastocysts<sup>51,59</sup>. Fluid secretion by the cells stimulated the formation of microlumen, which then fused by hydraulic fracturing of the intercellular junctions. We took advantage of this information and expressed UBTD1 in luminal

prostate cells. Expression of UBTD1 in luminal cells prevented cyst formation in prostate organoids at 1 nM DHT. In order to stimulate fluid secretion by the prostate luminal cells, we treated the organoids with increasing doses of DHT. This restored lumen formation. To comfort the idea that the hydraulic fracturing process of the adherens junctions of prostate luminal cells was indeed responsible for lumen formation, we could downregulate the level of E-cadherin in UBTD1-GFP expressing organoids.

The identification of interactants of the endogenous form of UBTD1 in basal cells of mouse prostates organoids showed numerous proteins associated with the regulation of the actin cytoskeleton. Among the identified proteins, the expression levels of EpCAM showed to be significantly changed by UBTD1 dysregulation. As previously shown, EpCAM, which is expressed at the mRNA level in basal and luminal cells, is only found at the protein level in the intercellular junctions of polarized luminal cells. EpCAM has been shown to decrease the strength of cell junctions by destabilizing E-cadherin<sup>41,15</sup>.

Consistent with the previously demonstrated role of UBTD1 in protein degradation processes mediated by E2/E3-dependent ubiquitination<sup>21,23,24</sup>, we hypothesize that UBTD1 participates in the regulation of E-cadherin-dependent adherens junctions by affecting the level of EpCAM degradation. To address this question, we should overexpress EpCAM in UBTD1-GFP expressing organoids to see if we would reform a lumen at a DHT concentration of 1nM. Consistent with this, we could monitor the levels of EpCAM degradation and ubiquitination based on UBTD1 expression levels.

Using predictive software we identified an N-terminal myristoylation site responsible for the cytoplasmic membrane localization of UBTD1. Like nuclear proteins that can only perform their function when they are imported into the nucleus, a membrane-associated protein, such as UBTD1, will only perform its membrane function once localized to the membrane<sup>44,60,61</sup>. Characterizing the interactants associated with different UBTD1 mutants would help us to identify specific membrane-associated partners. Finally, to correlate the intracellular localization of UBTD1 with its functionality, we could establish organoid lines expressing each of the mutants of UBTD1. The resulting phenotype would inform us on its functionality.

Overall, this study investigated a novel role of UBTD1 in prostate epithelial cells. We showed here that UBTD1 is a regulator of adherens junctions in prostate epithelial cells.

## REFERENCES

1. Toivanen, R. & Shen, M. M. Prostate organogenesis: tissue induction, hormonal regulation and cell type specification. *Development* 144, 1382–1398 (2017).
2. Xie, Q. *et al.* Dissecting cell-type-specific roles of androgen receptor in prostate homeostasis and regeneration through lineage tracing. *Nat Commun* 8, 14284 (2017).
3. Arnold, T. R., Stephenson, R. E. & Miller, A. L. Rho GTPases and actomyosin: Partners in regulating epithelial cell-cell junction structure and function. *Experimental Cell Research* 358, 20–30 (2017).
4. Yap, A. S., Gomez, G. A. & Parton, R. G. Adherens Junctions Revisualized: Organizing Cadherins as Nanoassemblies. *Developmental Cell* 35, 12–20 (2015).
5. Wang, X. *et al.* E-cadherin bridges cell polarity and spindle orientation to ensure prostate epithelial integrity and prevent carcinogenesis in vivo. *PLoS Genet* 14, e1007609 (2018).
6. Mendonsa, A. M., Na, T.-Y. & Gumbiner, B. M. E-cadherin in contact inhibition and cancer. *Oncogene* 37, 4769–4780 (2018).
7. Jung, H.-Y. *et al.* Apical–basal polarity inhibits epithelial–mesenchymal transition and tumour metastasis by PAR-complex-mediated SNAIL1 degradation. *Nat Cell Biol* 21, 359–371 (2019).
8. Müller, P. M. *et al.* Systems analysis of RhoGEF and RhoGAP regulatory proteins reveals spatially organized RAC1 signalling from integrin adhesions. *Nat Cell Biol* 22, 498–511 (2020).
9. Jamora, C. & Fuchs, E. Intercellular adhesion, signalling and the cytoskeleton. *Nat Cell Biol* 4, E101–E108 (2002).
10. Marjoram, R., Lessey, E. & Burridge, K. Regulation of RhoA Activity by Adhesion Molecules and Mechanotransduction. *Current Molecular Medicine* 14, 199–208 (2014).

11. Schnell, U., Cirulli, V. & Giepmans, B. N. G. EpCAM: Structure and function in health and disease. *Biochimica et Biophysica Acta (BBA) - Biomembranes* 1828, 1989–2001 (2013).
12. Spizzo, G. *et al.* Prognostic significance of Ep-CAM AND Her-2/neu overexpression in invasive breast cancer: Ep-CAM AND Her-2/neu Overexpression. *Int. J. Cancer* 98, 883–888 (2002).
13. Varga, M. *et al.* Overexpression of Epithelial Cell Adhesion Molecule Antigen in Gallbladder Carcinoma Is an Independent Marker for Poor Survival. *Clin Cancer Res* 10, 3131–3136 (2004).
14. Litvinov, S. V., Velders, M. P., Bakker, H. A., Fleuren, G. J. & Warnaar, S. O. Ep-CAM: a human epithelial antigen is a homophilic cell-cell adhesion molecule. *Journal of Cell Biology* 125, 437–446 (1994).
15. Litvinov, S. V. *et al.* Epithelial Cell Adhesion Molecule (Ep-CAM) Modulates Cell–Cell Interactions Mediated by Classic Cadherins. *Journal of Cell Biology* 139, 1337–1348 (1997).
16. Rape, M. Ubiquitylation at the crossroads of development and disease. *Nat Rev Mol Cell Biol* 19, 59–70 (2018).
17. Komander, D. & Rape, M. The Ubiquitin Code. *Annu. Rev. Biochem.* 81, 203–229 (2012).
18. Yau, R. & Rape, M. The increasing complexity of the ubiquitin code. *Nat Cell Biol* 18, 579–586 (2016).
19. Schulman, B. A. & Wade Harper, J. Ubiquitin-like protein activation by E1 enzymes: the apex for downstream signalling pathways. *Nat Rev Mol Cell Biol* 10, 319–331 (2009).
20. Ye, Y. & Rape, M. Building ubiquitin chains: E2 enzymes at work. *Nat Rev Mol Cell Biol* 10, 755–764 (2009).

21. Uhler, J. P. *et al.* The UbL protein UBTD1 stably interacts with the UBE2D family of E2 ubiquitin conjugating enzymes. *Biochemical and Biophysical Research Communications* 443, 7–12 (2014).
22. Zhang, X.-W. *et al.* UBTD1 induces cellular senescence through an UBTD1-Mdm2/p53 positive feedback loop: Cellular senescence induced by UBTD1-Mdm2/p53 positive feedback loop. *J. Pathol.* 235, 656–667 (2015).
23. Torrino, S. *et al.* UBTD1 is a mechano-regulator controlling cancer aggressiveness. *EMBO Rep* 20, (2019).
24. Torrino, S. *et al.* UBTD1 regulates ceramide balance and endolysosomal positioning to coordinate EGFR signaling. *eLife* 10, e68348 (2021).
25. Yang, N. *et al.* CXCR4 mediates matrix stiffness-induced downregulation of UBTD1 driving hepatocellular carcinoma progression via YAP signaling pathway. *Theranostics* 10, 5790–5801 (2020).
26. Sato, T. *et al.* Single Lgr5 stem cells build crypt-villus structures in vitro without a mesenchymal niche. *Nature* 459, 262–265 (2009).
27. Sato, T. *et al.* Paneth cells constitute the niche for Lgr5 stem cells in intestinal crypts. *Nature* 469, 415–418 (2011).
28. Sato, T. *et al.* Long-term Expansion of Epithelial Organoids From Human Colon, Adenoma, Adenocarcinoma, and Barrett’s Epithelium. *Gastroenterology* 141, 1762–1772 (2011).
29. Drost, J. *et al.* Organoid culture systems for prostate epithelial and cancer tissue. *Nat Protoc* 11, 347–358 (2016).
30. Clevers, H. Modeling Development and Disease with Organoids. *Cell* 165, 1586–1597 (2016).

31. Matano, M. *et al.* Modeling colorectal cancer using CRISPR-Cas9–mediated engineering of human intestinal organoids. *Nat Med* 21, 256–262 (2015).
32. Bello, D. Androgen responsive adult human prostatic epithelial cell lines immortalized by human papillomavirus 18. *Carcinogenesis* 18, 1215–1223 (1997).
33. Lévy, C. *et al.* Measles virus envelope pseudotyped lentiviral vectors transduce quiescent human HSCs at an efficiency without precedent. *Blood Advances* 1, 2088–2104 (2017).
34. Albagli-Curiel, O., Lecluse, Y., Pognonec, P., Boulukos, K. E. & Martin, P. A new generation of pPRIG-based retroviral vectors. *BMC Biotechnol* 7, 85 (2007).
35. Martin, P., Albagli, O., Poggi, M., Boulukos, K. & Pognonec, P. Development of a new bicistronic retroviral vector with strong IRES activity. *BMC Biotechnol* 6, 4 (2006).
36. Wassie, A. T., Zhao, Y. & Boyden, E. S. Expansion microscopy: principles and uses in biological research. *Nat Methods* 16, 33–41 (2019).
37. Yang, J. *et al.* The I-TASSER Suite: protein structure and function prediction. *Nat Methods* 12, 7–8 (2015).
38. Yang, J. & Zhang, Y. I-TASSER server: new development for protein structure and function predictions. *Nucleic Acids Res* 43, W174–W181 (2015).
39. Roy, A., Kucukural, A. & Zhang, Y. I-TASSER: a unified platform for automated protein structure and function prediction. *Nat Protoc* 5, 725–738 (2010).
40. Jumper, J. *et al.* Highly accurate protein structure prediction with AlphaFold. *Nature* 596, 583–589 (2021).
41. Teo, J. L. *et al.* Caveolae Control Contractile Tension for Epithelia to Eliminate Tumor Cells. *Developmental Cell* 54, 75-91.e7 (2020).
42. Monasterio, B. G. *et al.* Patches and Blebs: A Comparative Study of the Composition and Biophysical Properties of Two Plasma Membrane Preparations from CHO Cells. *IJMS* 21, 2643 (2020).

43. Charras, G. T., Hu, C.-K., Coughlin, M. & Mitchison, T. J. Reassembly of contractile actin cortex in cell blebs. *Journal of Cell Biology* 175, 477–490 (2006).
44. Wang, B. *et al.* Protein N-myristoylation: functions and mechanisms in control of innate immunity. *Cell Mol Immunol* 18, 878–888 (2021).
45. Debnath, J. & Brugge, J. S. Modelling glandular epithelial cancers in three-dimensional cultures. *Nat Rev Cancer* 5, 675–688 (2005).
46. Dolega, M. E. *et al.* Label-free analysis of prostate acini-like 3D structures by lensfree imaging. *Biosensors and Bioelectronics* 49, 176–183 (2013).
47. Chugh, P. *et al.* Actin cortex architecture regulates cell surface tension. *Nat Cell Biol* 19, 689–697 (2017).
48. Lecuit, T. & Lenne, P.-F. Cell surface mechanics and the control of cell shape, tissue patterns and morphogenesis. *Nat Rev Mol Cell Biol* 8, 633–644 (2007).
49. Lee, H. D. *et al.* Direct Surface Tension Measurements of Individual Sub-Micrometer Particles Using Atomic Force Microscopy. *J. Phys. Chem. A* 121, 8296–8305 (2017).
50. Karthaus, W. R. *et al.* Identification of Multipotent Luminal Progenitor Cells in Human Prostate Organoid Cultures. *Cell* 159, 163–175 (2014).
51. Dumortier, J. G. *et al.* Hydraulic fracturing and active coarsening position the lumen of the mouse blastocyst. *Science* 365, 465–468 (2019).
52. Fehon, R. G., McClatchey, A. I. & Bretscher, A. Organizing the cell cortex: the role of ERM proteins. *Nat Rev Mol Cell Biol* 11, 276–287 (2010).
53. Lenne, P.-F., Rupprecht, J.-F. & Viasnoff, V. Cell Junction Mechanics beyond the Bounds of Adhesion and Tension. *Developmental Cell* 56, 202–212 (2021).
54. Hartsock, A. & Nelson, W. J. Adherens and tight junctions: Structure, function and connections to the actin cytoskeleton. *Biochimica et Biophysica Acta (BBA) - Biomembranes* 1778, 660–669 (2008).

55. Cavey, M. & Lecuit, T. Molecular Bases of Cell-Cell Junctions Stability and Dynamics. *Cold Spring Harbor Perspectives in Biology* 1, a002998–a002998 (2009).
56. Efimova, N. & Svitkina, T. M. Branched actin networks push against each other at adherens junctions to maintain cell–cell adhesion. *Journal of Cell Biology* 217, 1827–1845 (2018).
57. Fagotto, F. The cellular basis of tissue separation. *Development* 141, 3303–3318 (2014).
58. Chalut, K. J. & Paluch, E. K. The Actin Cortex: A Bridge between Cell Shape and Function. *Developmental Cell* 38, 571–573 (2016).
59. Goodwin, K. & Nelson, C. M. Mechanics of Development. *Developmental Cell* 56, 240–250 (2021).
60. Stewart, M. Molecular mechanism of the nuclear protein import cycle. *Nat Rev Mol Cell Biol* 8, 195–208 (2007).
61. Bouamr, F., Scarlata, S. & Carter, C. Role of Myristylation in HIV-1 Gag Assembly †. *Biochemistry* 42, 6408–6417 (2003).

**Figure 1. UBTD1 is localized to the cytoplasmic membrane of prostate basal cells via its N-terminal myristoylation site.**

- A. Representative immunofluorescence (IF) image of healthy human prostate section. Staining for basal cell marker CK5 (pink), luminal cell marker CK8 (red) and UBTD1 (green). Nuclei were stained with DAPI (blue). Scale bar, 40  $\mu\text{m}$  and 10  $\mu\text{m}$ .
- B. Representative immunofluorescence image of human prostate cytoplasmic cell membrane done with stimulated-emission-depletion (STED) microscope. Staining for F-actin with phalloidin Alexa Fluor™ 594 (red) and UBTD1 (green) using a STAR 635P secondary antibody. Cytoplasmic membrane was stained using Wheat Germ Agglutinin (WGA) conjugated with an Alexa Fluor™ 647 (pink). Scale bar, 5  $\mu\text{m}$ , 2  $\mu\text{m}$ , 1  $\mu\text{m}$ .
- C. Representative immunofluorescence image of a blebbing cell. Blebbing in human prostate epithelial cell was induced by treatment with EtOH 5% and Cytochalasin D (CytoD) 2.5 $\mu\text{M}$ . Staining for F-actin with phalloidin Alexa Fluor™ 594 (red) and UBTD1 (green). Cytoplasmic membrane was stained using WGA conjugated with an Alexa Fluor™ 647 (pink). Scale bar, 5  $\mu\text{m}$ .
- D. Schematic representation of the constructs used to achieve expression of the mutated form of UBTD1. UBTD1 was coupled in C-terminal with mNeonGreen. Total myristoylation site was removed in  $\Delta\text{N}$ -UBTD1. Single point mutations were realised on UBTD1 N-terminal myristoylation site (G2A, C4A and G2A/C4A). Immunofluorescence pictures of mutated form of UBTD1. F-actin was stained with phalloidin (red), nuclei were stained with DAPI (blue). Scale bar, 10  $\mu\text{m}$ .
- E. Representative images of the 3D structure of UBTD1. The entire myristoylation site was highlighted with a green color. Glycine number 2 and cysteine number 4 were highlighted with a orange color. The prediction of the 3D structure was carried out using the open access online software I-TASSER.
- F. Quantification of confocal images for UBTD1's location in the cell using CellProfiler. Cells were divided into four compartments: nucleoplasm, perinuclear region, cytosol, cytoplasmic membrane. A two-way ANOVA test was performed. (means  $\pm$  SEM; n = 3; \*p<0.05; \*\*p<0.01, \*\*\*p<0.001; ns= not significant)

**Figure 2. UBTD1 expression levels affect cells organization in three dimensions.**

- A. Experimental scheme for the culture of epithelial cells in three dimensions from seeding to the final epithelial polarization at day 10. Scheme modified from Jung *et al.* 2019.
- B. Immunofluorescence images for E-cadherin (red), UBTD1 (green), nuclei (DAPI) in RWPE-1 cells after ten days of culture.
- C. Representative bright-field images of acini down regulated for UBTD1 at day 10. Scale bar, 50  $\mu\text{m}$ .
- D. Representative immunofluorescence images of the center of acini at day 10 treated with the different shRNAs. Staining for F-actin (white) and E-cadherin (cyan). Nuclei were stained with DAPI (blue). Scale bar, 50  $\mu\text{m}$ .
- E. Morphological parameters of acini were evaluated using CellProfiler. Acini area and perimeter are represented here.  $n = 25$  acini per condition from 3 independent experiments were analyzed. A one-way ANOVA test was performed (means  $\pm$  SD;  $n = 3$ ; \*\*\* $p < 0.001$ ).
- F. Cell proliferation inside the acini was assessed using an imaging analysis approach and cytometry approach. The number of cells per acini was evaluated using CellProfiler. Quantification was done on sections of the center of the acini at day 10. The proliferation was quantified using the FUCCI fluorescent sensor. FUCCI probe consist of a geminin coupled to a GFP expressed during the S/G2/M of the cell cycle. A one-way ANOVA test was performed (means  $\pm$  SD;  $n = 3$ ; \* $p < 0.05$ ; \*\* $p < 0.01$ , \*\*\* $p < 0.001$ ).
- G. Representative immunofluorescence images of the center of acini at day 10 treated with the different shRNAs. Staining for F-actin (pink) and caspase-3 (white). Nuclei were stained with DAPI (blue). Scale bar, 50  $\mu\text{m}$ . Cell death quantification was assessed using an automated fluorescence cell counter which also quantifies cell viability. A one-way ANOVA test was performed (means  $\pm$  SD;  $n = 3$ ).
- H. Representative immunofluorescence images of the center of GFP or UBTD1-GFP expressing acini at day 10. Staining for integrin- $\beta 4$  (red) and giantin (white) on the left panel. Staining for F-actin (white) and E-cadherin (cyan) on the right panel. Nuclei were stained with DAPI (blue). Scale bar, 15  $\mu\text{m}$ , 50  $\mu\text{m}$ .
- I. Morphological parameters of acini were evaluated using CellProfiler on acini sections acquired on a confocal microscope. Acini area and perimeter are represented here. The average distance of cells from the center of acini was also quantified.  $n = 25$  acini

per condition from 3 independent experiments were analyzed. A one-way ANOVA test was performed (means  $\pm$  SD; n = 3; \*\*p<0.01).

- J. Representative bright-field images of GFP or UBTD1 expressing acini at day 3, 6 and 10. Scale bar, 100  $\mu$ m.
- K. Cell proliferation inside the acini was assessed using an imaging analysis approach and cytometry approach. The number of cells per acini was evaluated using CellProfiler. Quantification was done on sections of the center of the acini at day 10. The level of proliferation of epithelial cells expressing GFP or UBTD1-GFP was quantified by assessing the amount of EdU incorporated by the cells. Quantification was performed by flow cytometry. A one-way ANOVA test was performed (means  $\pm$  SD; n = 3; \*p<0.05; ns= not significant).
- L. Representative immunofluorescence images of the center of GFP or UBTD1-GFP expressing acini at day. Staining for F-actin (pink) and caspase-3 (white). Nuclei were stained with DAPI (blue). Scale bar, 50  $\mu$ m. Cell death quantification was assessed using an automated fluorescence cell counter which also quantifies cell viability. A t-test was performed (means  $\pm$  SD; n = 3; ns= not significant).

**Figure 3. UBTD1 expression levels affect cell shape and rigidity in an epithelial monolayer.**

- A. Schematic of indentation on an isolated cell. The AFM probe is made of silicon in a form of long, flexible levers with a probing tip mounted at its free end (Lekka 2016).
- B. Measure of cellular deformability using atomic force microscopy (AFM). The elastic properties of cells are delivered from indentation experiments and described quantitatively by Young's modulus. Cellular deformability was measured on adherent epithelial cells overexpressing UBTD1 (UBTD1-GFP). A t-test was performed (median  $\pm$  interquartile range; n = 3; \*p<0.05).
- C. Cellular deformability was measured on adherent epithelial cells expressing less UBTD1 protein (shUBTD1 #2, #4). A Kruskal-Wallis test was performed (median  $\pm$  interquartile range; n = 3; \*\*p<0.01, \*\*\*p<0.001).
- D. The surface regularity of the epithelial monolayer was measured on confocal images using Imaris software. Surface regularity was assessed on cells either overexpressing or under expressing UBTD1. A one-way ANOVA test was performed (means  $\pm$  SD; n = 3; \*\*\*p<0.001; ns= not significant).

- E. Representative pictures of 3D reconstructed objects based on images acquired with confocal microscope (top). Cross-section in the z-plane of epithelial monolayers (bottom). The 3D reconstruction was based on F-actin labeling with the Imaris software
- F. Representative immunofluorescence images of human prostate epithelial cell monolayer. Staining for F-actin (white), nuclei were stained with DAPI (blue). Scale bar, 40  $\mu\text{m}$ , 200  $\mu\text{m}$ .
- G. Morphological parameters of cells were measured using CellProfiler. Cells mean eccentricity and cells mean form factors are evaluated here. Measurements were made on epithelial monolayer either overexpressing UBTD1 (UBTD1-GFP) or expressing less UBTD1 protein (shUBTD1 # 2, # 4). GFP and shCTRL were the controls for both conditions respectively. A 2way ANOVA test was performed (means  $\pm$  SD; n = 3; \*\*\*p<0.001; ns= not significant).
- H. Schematic illustration of mCherry expressing wild-type (WT) cells surrounded by either GFP expressing cells or UBTD1-GFP expressing cells. Schema modified from Teo *et al.* 2020.
- I. Representative images of epithelial monolayers containing WT mCherry cells with GFP or UBTD1-GFP expressing cells. Visualization from the top or XZ plane. Scale bar, 100  $\mu\text{m}$ .
- J. Quantification of red cell extrusion was done by image analysis using CellProfiler. The level of proliferation of epithelial cells expressing GFP or UBTD1-GFP was quantified by assessing the amount of EdU incorporated by the cells. Quantification was performed by flow cytometry. A one-way ANOVA test was performed (means  $\pm$  SD; n = 3; \*\*\*p<0.001; ns= not significant).
- K. Morphological parameters of red cells were evaluated using imaging analysis. Red cells eccentricity and compactness are represented here. A one-way ANOVA test was performed (means  $\pm$  SD; n = 3; \*\*\*p<0.001).

**Figure 4. UBTD1 affects the expression levels of genes associated with processes involving the cytoplasmic membrane, actin cortex and cell junctions.**

- A. Annotation and GO classification of differentially expressed genes (DEGs). The X-axis represents the number of genes annotated to the GO entry, and the Y-axis

represents the GO functional classification. Only GFP vs UBTD1-GFP and shCTRL vs sUBTD1#2 conditions are shown here.

- B. Volcano map of DEGs. The X-axis represents the fold change of the difference after conversion to  $\log_2$ , and the Y-axis represents the significance value after conversion to  $-\log_{10}$ . Red represents DEG up regulated, blue represents DEG down regulated, and gray represents non-DEG.
- C. GO cellular component enrichment bubble chart. X-axis is the enrichment ratio [the ratio of the number of genes annotated to an entry in the selected gene set to the total number of genes annotated to the entry in the species, calculated as Rich Ratio = Term Candidate Gene Num/Term Gene Num] It is GO Term. The size of the bubble represents the number of DEGs annotated to a GO Term. The color represents the enriched significance. The redder the color, the smaller the significance value.
- D. Gene Set Enrichment Analysis (GSEA) of statistically significant and consistent differences between two conditions. Here are represented GSEA for GFPvs UBTD1-GFP and shCTRLvs shUBTD1#2. The graph is divided into four parts. The X-axis always indicates the rank of the change value (change value generally refers to  $\text{signal}^2/\text{noise}$  or  $\log_2\text{ratio}$ , hereinafter referred to as "score") before and after processing of all genes (the expression level is greater than 0). The change values are sorted in descending order from the left to right, namely, the maximum change value are sorted as 1.
  1. Part one, the green fold line indicates the change curve of the gene enrichment score (ES), and the Y-axis is the ES value. It is necessary to pay attention to the crest value or wave trough value of the polyline. When the absolute value of the crest is greater than the absolute value of the wave trough, it indicates that the gene on the left side of the crest (that is, the leading edge subset) is related to the phenotype of the treatment group; when the absolute value of the wave trough is higher, it indicates the right gene of wave trough is related to the phenotype of the control group.
  2. Part two, Each black vertical line represents one gene, this section shows all genes in a certain category (such as a pathway or a GO entry). The height of Y-axis is fixed, without special meaning
  3. Part three, The heatmap represents the  $\text{signal}^2/\text{noise}/\log_2\text{ratio}$  value of all expressed genes. Here, the average score of multiple genes in a certain interval is used as a representative display. Red indicates the value  $> 0$ , and blue indicates the value  $< 0$ . The darker the color, the higher the absolute value.

4. Part four, The Y-axis of the gray histogram represents the signal2noise/log2ratio values of all the expressed genes. Here, the score values of 1000 genes are selected as models from all genes at a certain interval.

**Figure 5. UBTD1 overexpression prevents cyst formation in mouse prostate organoids at normal DHT concentration.**

- A. Representative immunofluorescence images of GFP and UBTD1-GFP expressing organoids treated with different concentrations of dihydrotestosterone (DHT). Staining at day 9 for nuclei with DAPI (white). Scale bar, 200  $\mu\text{m}$ .
- B. Representative immunofluorescence images of the center of GFP and UBTD1-GFP expressing organoids with staining for basal cell marker CK5 (cyan) and luminal cell marker CK8 (red) at day 9. Scale bar, 50  $\mu\text{m}$ .
- C. Quantification of confocal images of the center of GFP and UBTD1-GFP expressing organoids at 1 nM of DHT at day 9. Fluorescence intensities were normalized between the smallest and the largest values in each data set. X axis represents cell location along the organoid radius (0: organoid center, 10: organoid edge). n = 52 GFP organoids and n = 53 organoids from 3 independent batches were analyzed.
- D. Cell distribution along the organoid radius for GFP and UBTD1-GFP expressing organoids treated with different DHT concentrations, i.e. 0, 0.5, 1, 3 and 5 nM. On the Y axis, 1 and 13 correspond respectively to the center and the edge of the organoid. Scale bars correspond to the percentage of cell present in each bin. The darker the color, the fewer cells there are, and the lighter the color, the more cells. The quantification was done on confocal images of the center of GFP and UBTD1-GFP expressing organoids. n > 50 organoids from 3 independent batches were analyzed for each condition.
- E. Area occupied by individual organoids. Quantification of confocal images of the center of GFP and UBTD1-GFP expressing organoids treated with multiple DHT concentrations, i.e. 0, 0.5, 1, 3 and 5 nM. n > 50 organoids from 3 independent batches were analyzed for each condition. A one-way ANOVA test was performed (means  $\pm$  SEM; n = 3; \*p<0.05; \*\*p<0.01, \*\*\*p<0.001; ns= not significant)..
- F. Percentage of cystic organoids. Quantification of confocal images of the center of GFP and UBTD1-GFP expressing organoids treated with multiple DHT concentrations, i.e. 0, 0.5, 1, 3 and 5 nM. n > 50 organoids from 3 independent batches

were analyzed for each condition. A one-way ANOVA test was performed, (means  $\pm$  SEM; n = 3; \*p<0.05; \*\*p<0.01, \*\*\*p<0.001; ns= not significant)..

**Figure 6. UBTD1 interactome is highly connected with cellular processes involved in actin cortex-membrane dialogue.**

- A. Go component of the proteins contained in the "regulation of actin cytoskeleton" cluster.
- B. Go function of the proteins contained in the "regulation of actin cytoskeleton" cluster.

**Figure 7. UBTD1 interactants display cell type specific expression and have an expression modulated with UBTD1 dysregulation**

- A. Single cell RNA sequencing profile of an intact human adult prostate. Expression profile of the different UBTD1 interactors in the different cell populations identified by single cell.
- B. Average expression profile of UBTD1 interacting genes in basal, basal hillock, luminal 1 and luminal 2 cells.
- C. Immunohistochemical staining of human prostate histological sections were taken from the Human Protein Atlas.
- D. Expression profile at mRNA level of the different genes interacting with UBTD1 in human prostate RWPE-1 cells. A one-way ANOVA test was performed (means  $\pm$  SD; n = 3; \*p<0.05; \*\*p<0.01, \*\*\*p<0.001; ns= not significant).

### Supplemental Figure 1.

- A. Confocal immunofluorescence images of human prostate epithelial cells stained using expansion microscopy technique. Staining for F-actin with phalloidin Alexa Fluor™ 594 (red) and UBTD1 (green). Cytoplasmic membrane was stained using WGA conjugated with an Alexa Fluor™ 647 (pink). Scale bar, 20  $\mu\text{m}$ , 5  $\mu\text{m}$ .
- B. Images representing the analysis pipeline made on CellProfiler.
- C. Image of the 3D structure prediction of human UBTD1 made with AlphaFold2 (Jumper, J *et al.* 2021). The graph on the right illustrates the predicted aligned errors. The color at position (x, y) indicates AlphaFold's expected position error at residue x, when the predicted and true structures are aligned on residue y.
- D. Image of the 3D structure prediction of mouse UBTD1 made with AlphaFold2 (Jumper, J *et al.* 2021). The graph on the right illustrates the predicted aligned errors.
- E. Alignment of human and mouse UBTD1 protein sequences using the Pairwise Sequence Alignment tool provided by EMBL-EBI. Mouse and human amino acids sequences have a similarity of 99.6%.

### Supplemental Figure 2.

- A. Representative masks of identified acini generated on CellProfiler.
- B. Representative IF pictures of acini with the FUCCI probe.
- C. Percentage of formed acini assessed by counting the number cystic acini.
- D. Additional morphological parameters assessed on acini sections. A one-way ANOVA test was performed (means  $\pm$  SD; n = 3; \*p<0.05; \*\*p<0.01, \*\*\*p<0.001; ns= not significant).
- E. Representative masks of identified acini, cells and cytoplasm generated on CellProfiler on GFP and UBTD1-GFP expressing acini.
- F. Percentage of formed acini assessed by counting the number cystic acini.
- G. Additional morphological parameters assessed on acini sections. A one-way ANOVA test was performed (means  $\pm$  SD; n = 3; \*p<0.05; \*\*p<0.01, \*\*\*p<0.001; ns= not significant).
- H. Representative masks of GFP and UBTD1-GFP expressing acini. The percentage of contact between cells is represented here by a color gradient. The number of neighboring cells is represented by a color gradient. The quantification of these parameters was assessed across the acini radius (right panels).

### Supplemental Figure 3.

- A. Schematic illustration of mCherry expressing wild-type (WT) cells surrounded by either shCTRL cells or shUBTD1 #2 and #4 expressing cells. Schema modified from Teo *et al.* 2020.
- B. Quantification of red cell extrusion was done by image analysis using CellProfiler. The level of proliferation of epithelial cells expressing shCTRL cells or shUBTD1 #2 and #4 was quantified by using the fluorescent FUCCI cell cycle sensor. The fluorescence quantification was performed by flow cytometry. A one-way ANOVA test was performed (means  $\pm$  SD; n = 3; \*p<0.05; \*\*p<0.01, \*\*\*p<0.001; ns= not significant).
- C. Representative images of epithelial monolayers containing WT mCherry cells with shCTRL cells or shUBTD1 #2 and #4 expressing cells. Visualization from the top or XZ plane. Scale bar, 100  $\mu$ m.
- D. Morphological parameters of red cells were evaluated using imaging analysis. A one-way ANOVA test was performed (means  $\pm$  SD; n = 3; \*p<0.05; \*\*p<0.01, \*\*\*p<0.001; ns= not significant).
- E. Western Blot of the different RWPE-1 stable cell lines treated with shCTRL, sh#2 and sh#4.

### Supplemental Figure 4.

- A. Principal component analysis. The X and Y axes represent a new data set of the corresponding principal components obtained after the dimension reduction of the sample expression, which is used to represent the gap between the samples; the values in brackets on the axis labels represent the percentage of the overall variance explained by the corresponding principal components. The dots represent each sample, and the same color represents the same sample group.
- B. Volcano map of DEGs. The X-axis represents the fold change of the difference after conversion to log<sub>2</sub>, and the Y-axis represents the significance value after conversion to -log<sub>10</sub>. Red represents DEG up regulated, blue represents DEG down regulated, and gray represents non-DEG.
- C. Correlation heatmap. The X and Y axes represent each sample. Color represents the correlation coefficient (blue colors represent higher correlations, red colors represent lower correlations).

- D. Stacked graph of expression quantity. The X-axis indicates the sample name, the Y-axis indicates the number of genes, and the shades of color indicate different expression levels: FPKM  $\leq 1$  is a gene with a very low expression level, FPKM between 1 and 10 is a gene with a lower expression level, FPKM Genes with  $\geq 10$  are high and moderately expressed.
- E. Boxplot of expression quantity. The X axis is the sample name and the Y axis is  $\log_{10}(\text{FPKM} + 1)$ . The boxplot of each area corresponds to five statistics (Maximum, upper quartile, median, lower quartile, minimum) where outliers are not considered for upper and lower limits).
- F. DEGs cluster heatmaps. The horizontal axis is the  $\log_2$  of sample (expression value +1), and the vertical axis is the gene. Under the default color matching, the warmer the color block is, the higher the expression level is, and the colder the color block is, the lower the expression level is.
- G. DEGs heatmaps of the GO term Desmosome. The horizontal axis is the  $\log_2$  of sample (expression value +1), and the vertical axis is the gene. Under the default color matching, the warmer the color block is, the higher the expression level is, and the colder the color block is, the lower the expression level is.
- H. DEGs heatmaps of the GO term GAP Junction. The horizontal axis is the  $\log_2$  of sample (expression value +1), and the vertical axis is the gene. Under the default color matching, the warmer the color block is, the higher the expression level is, and the colder the color block is, the lower the expression level is.

### **Supplemental Figure 5.**

- A. Simplified model of prostate organoid growth.
- B. Representative immunofluorescence images of the center of WT mouse prostate organoids with staining for basal cell marker CK5 (pink) and luminal cell marker CK8 (red) and UBTD1 (green) at day 9. Nuclei were stained with DAPI (blue). Scale bar, 80  $\mu\text{m}$ , 40  $\mu\text{m}$ .
- C. Representative bright-field images of GFP and UBTD1-GFP expressing organoids at 1 nM of DHT at day 9. Scale bar, 200  $\mu\text{m}$ .
- D. Representative images of 3D reconstructed GFP and UBTD1-GFP organoids. Staining for basal cell marker CK5 (cyan), luminal cell marker CK8 (red), GFP and UBTD1-GFP (green). Scale bar, 100  $\mu\text{m}$ .

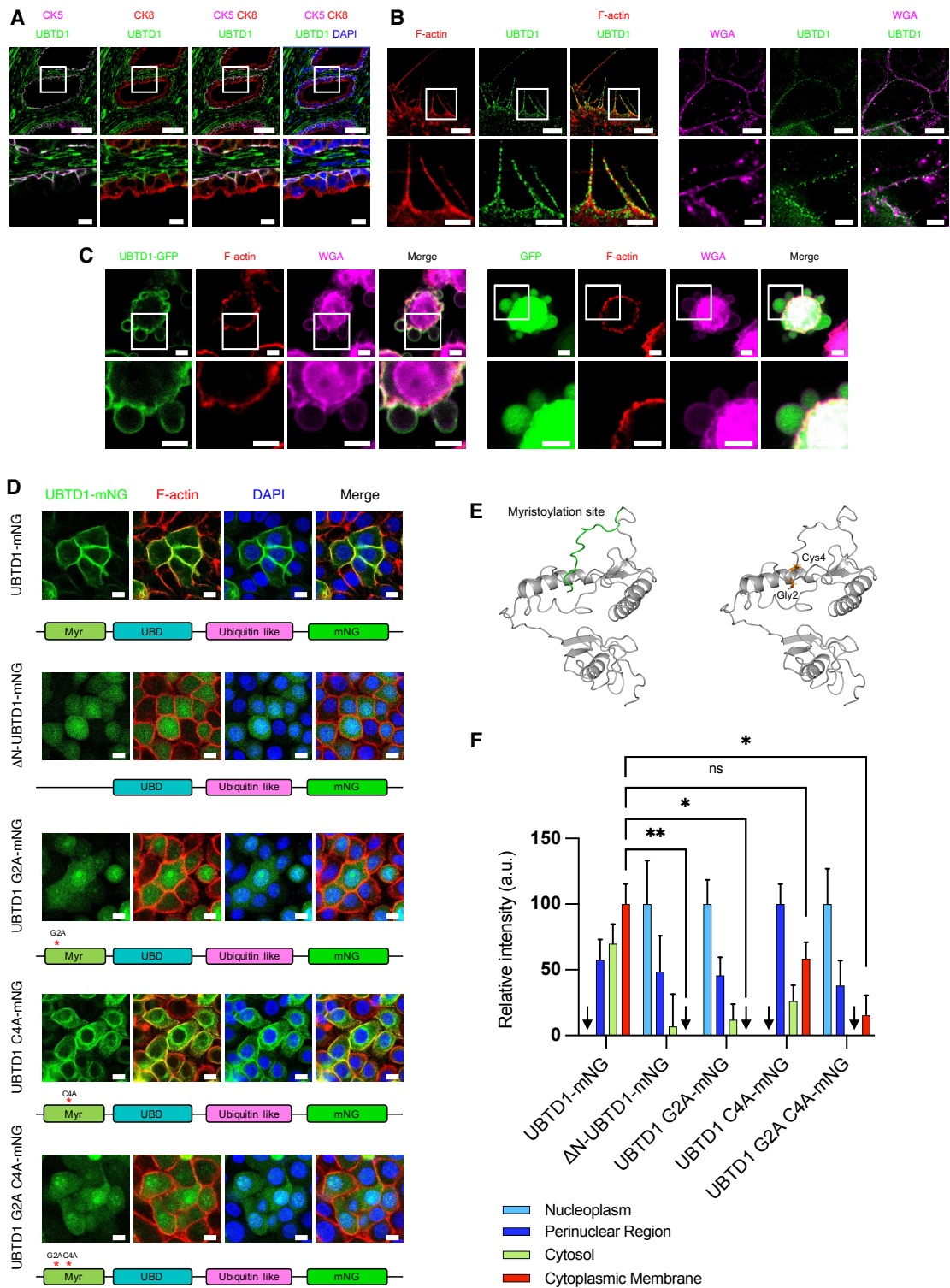


Figure 1

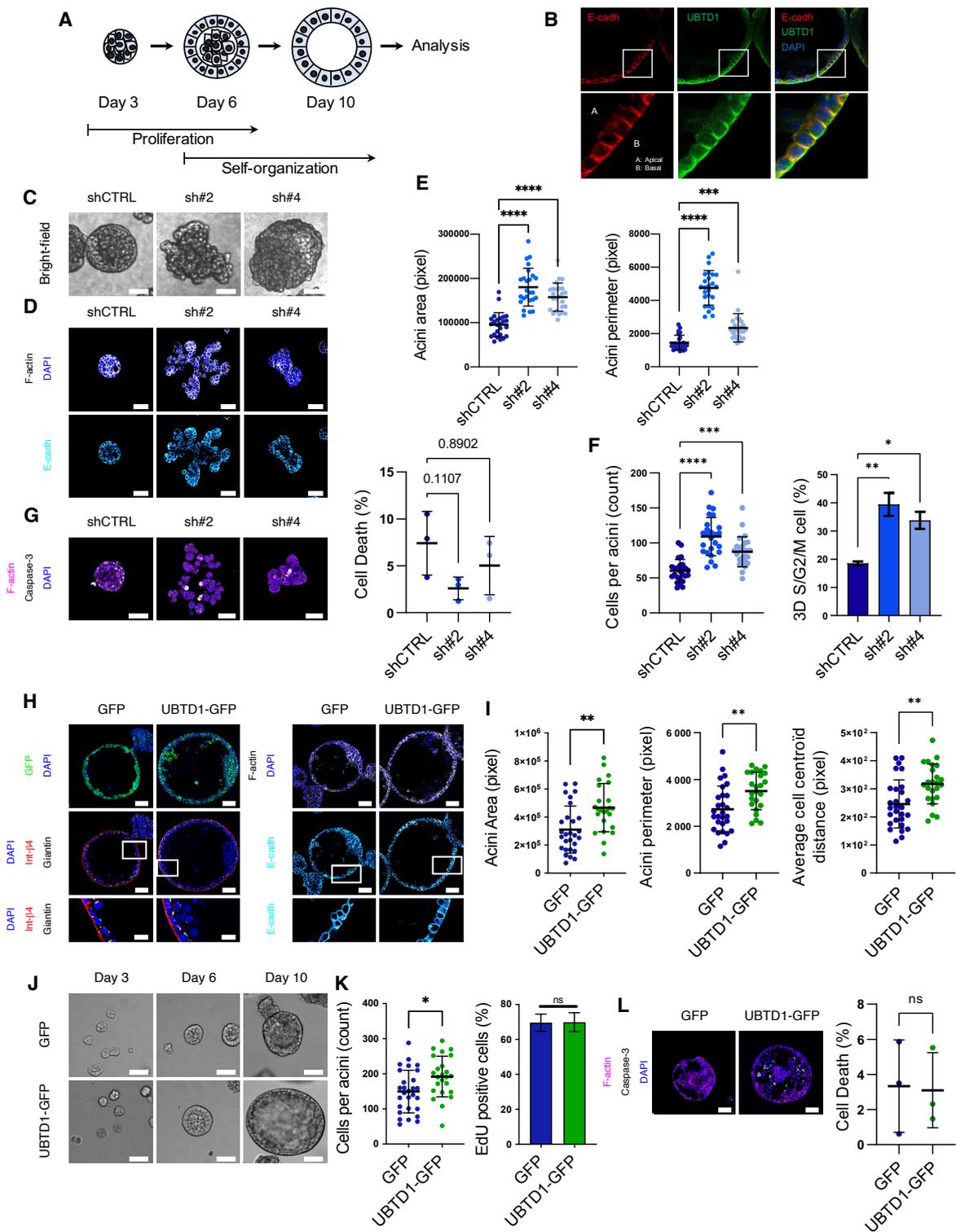


Figure 2

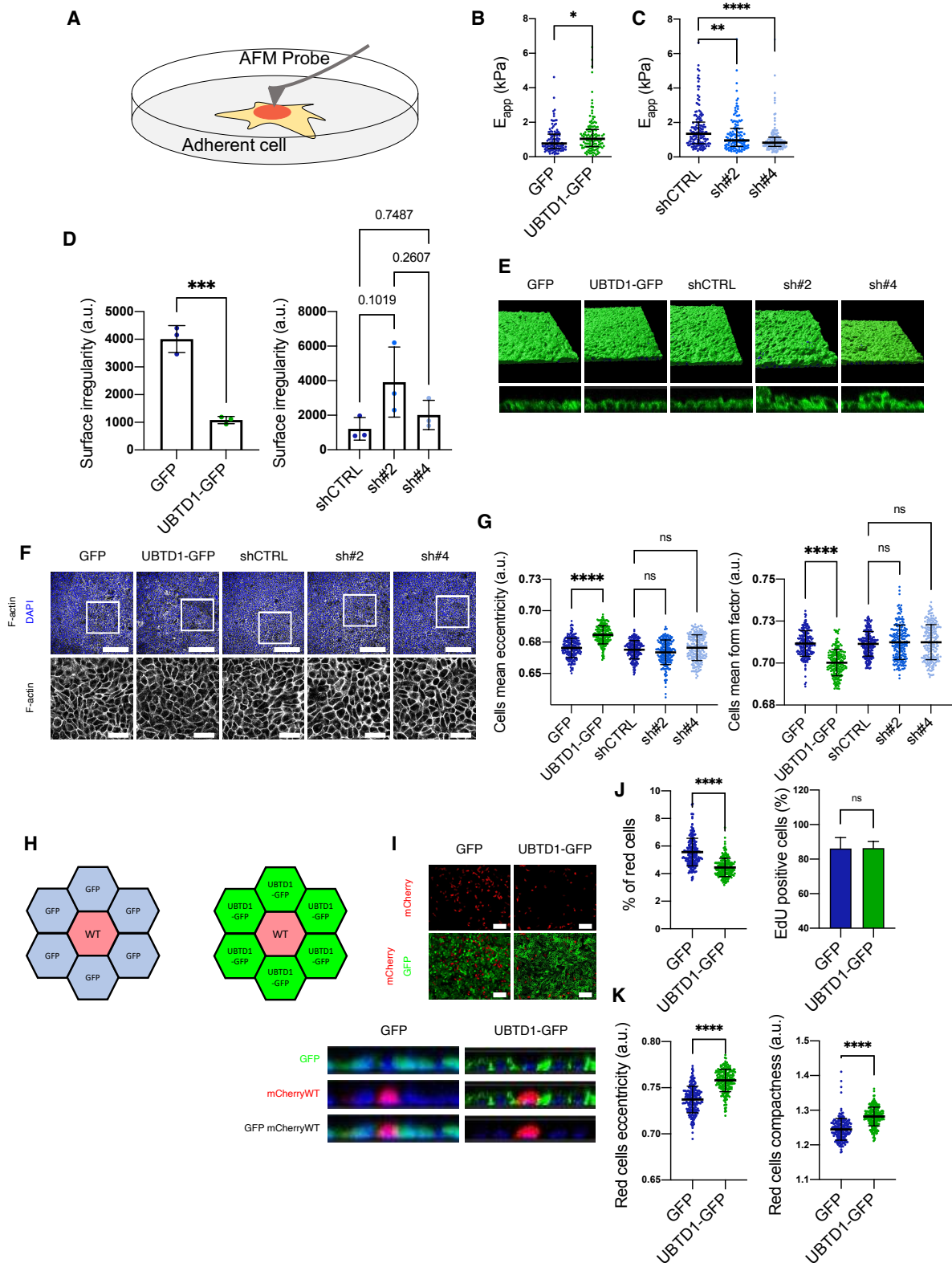


Figure 3

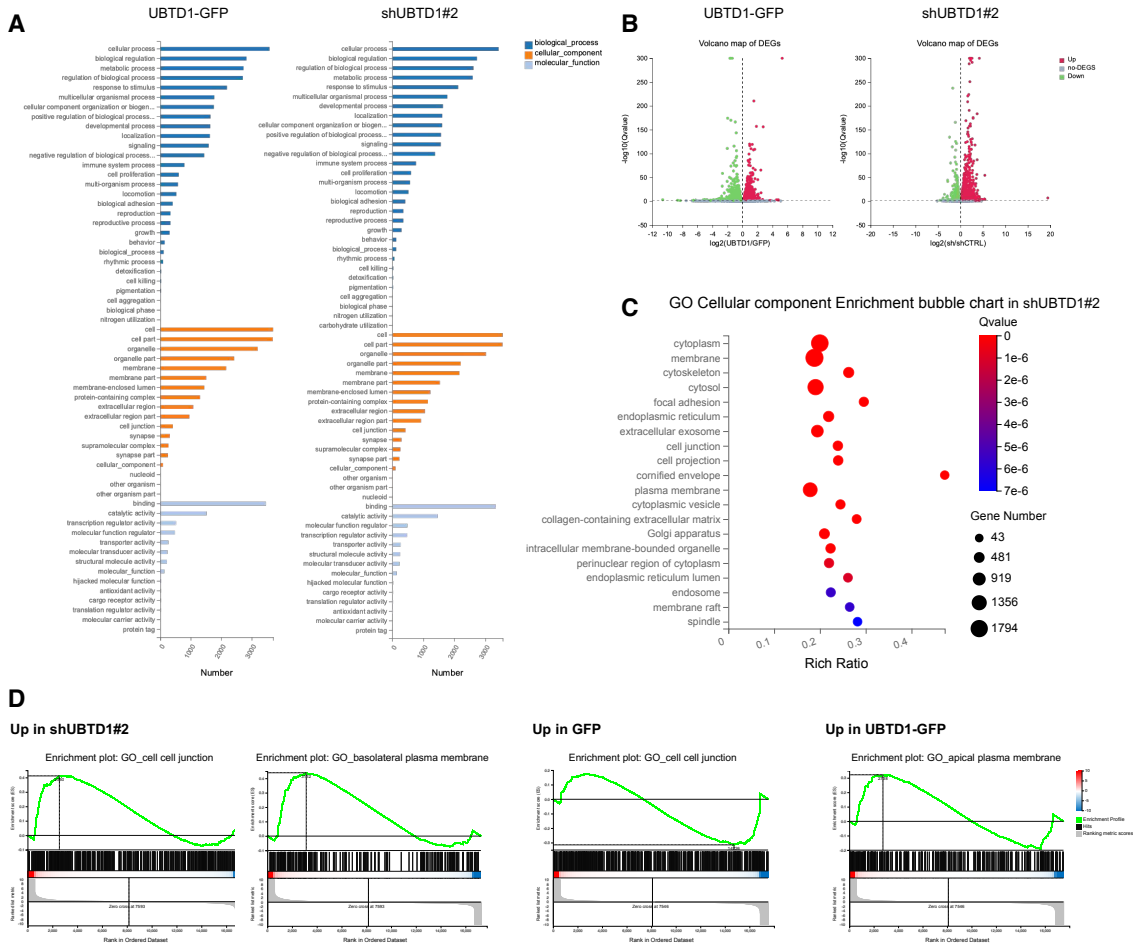


Figure 4

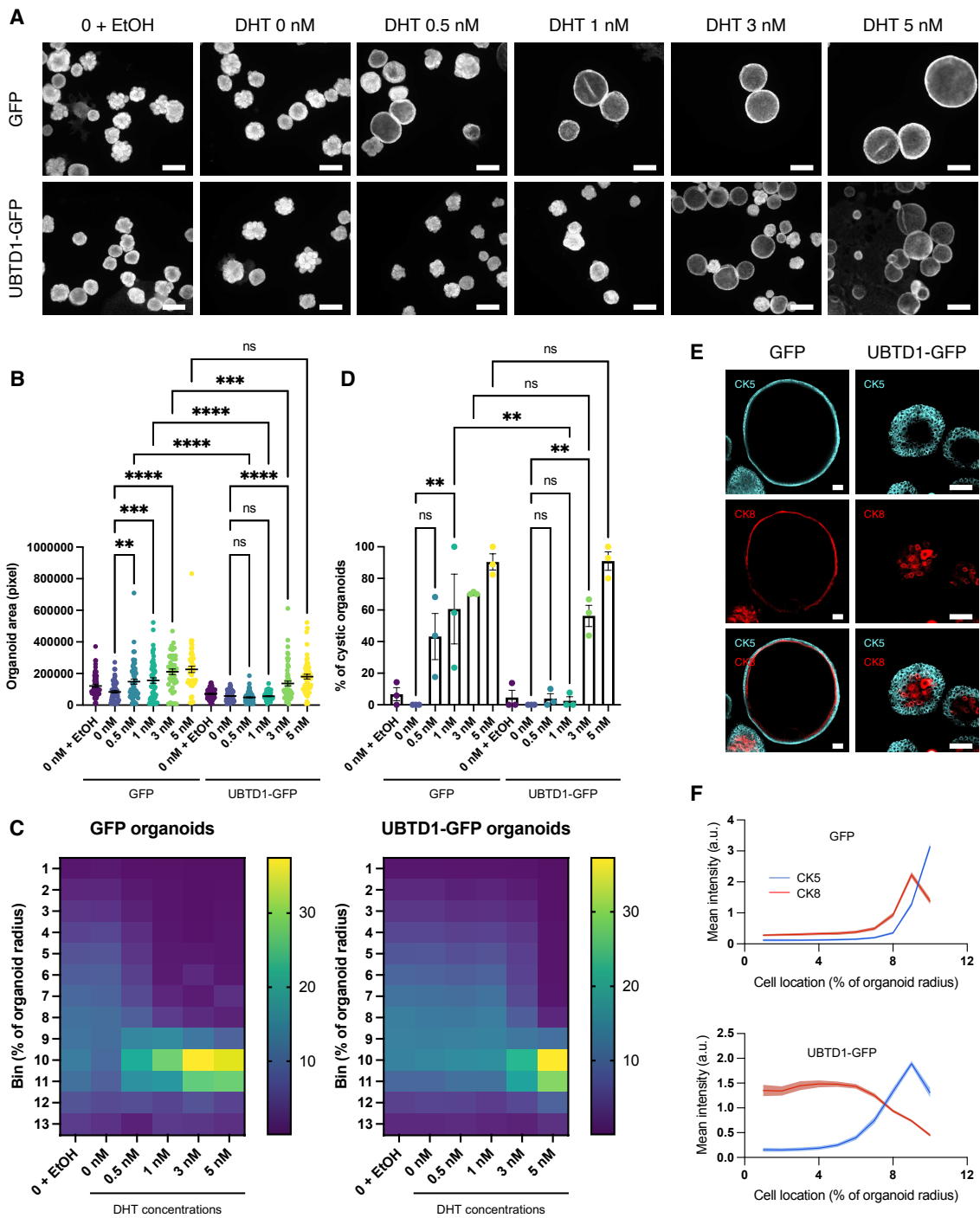


Figure 5

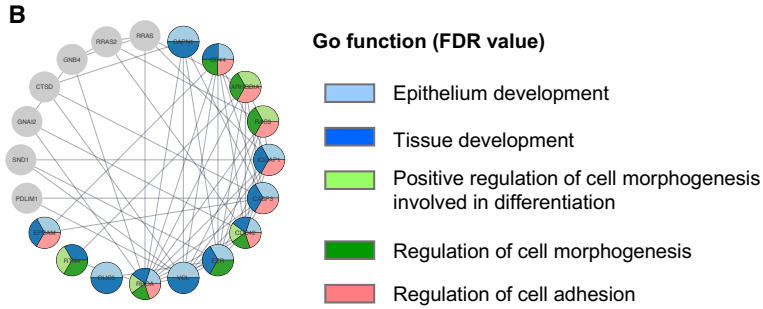
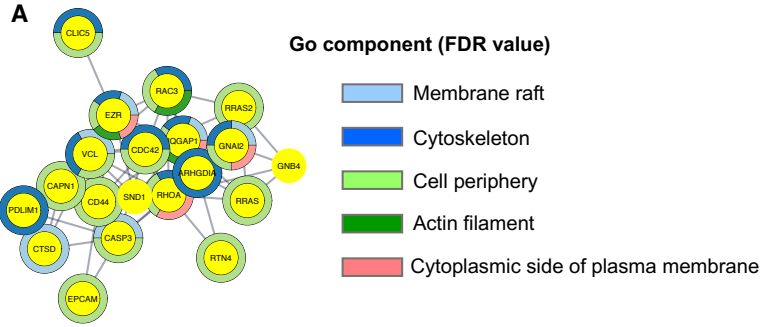


Figure 6

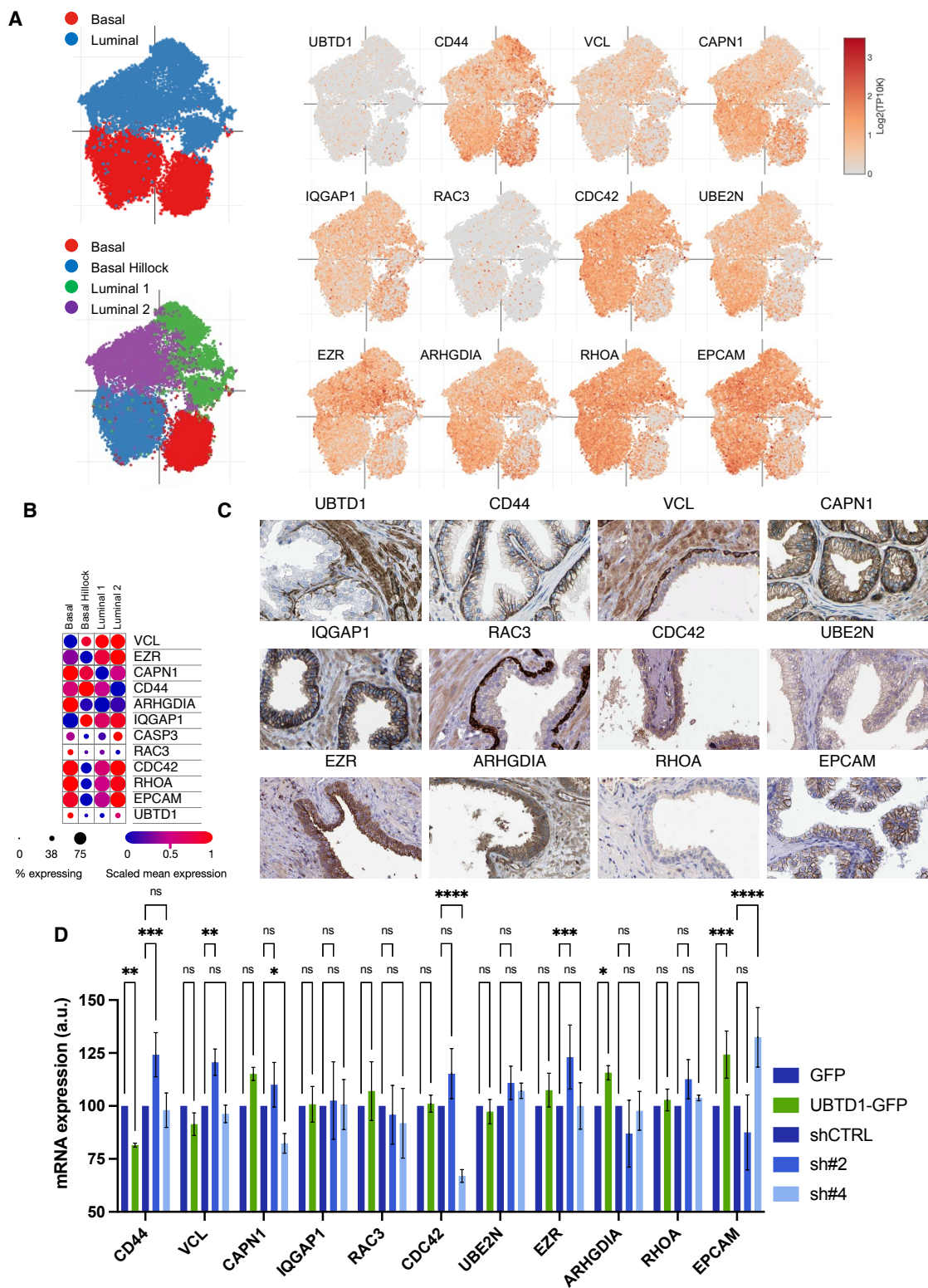
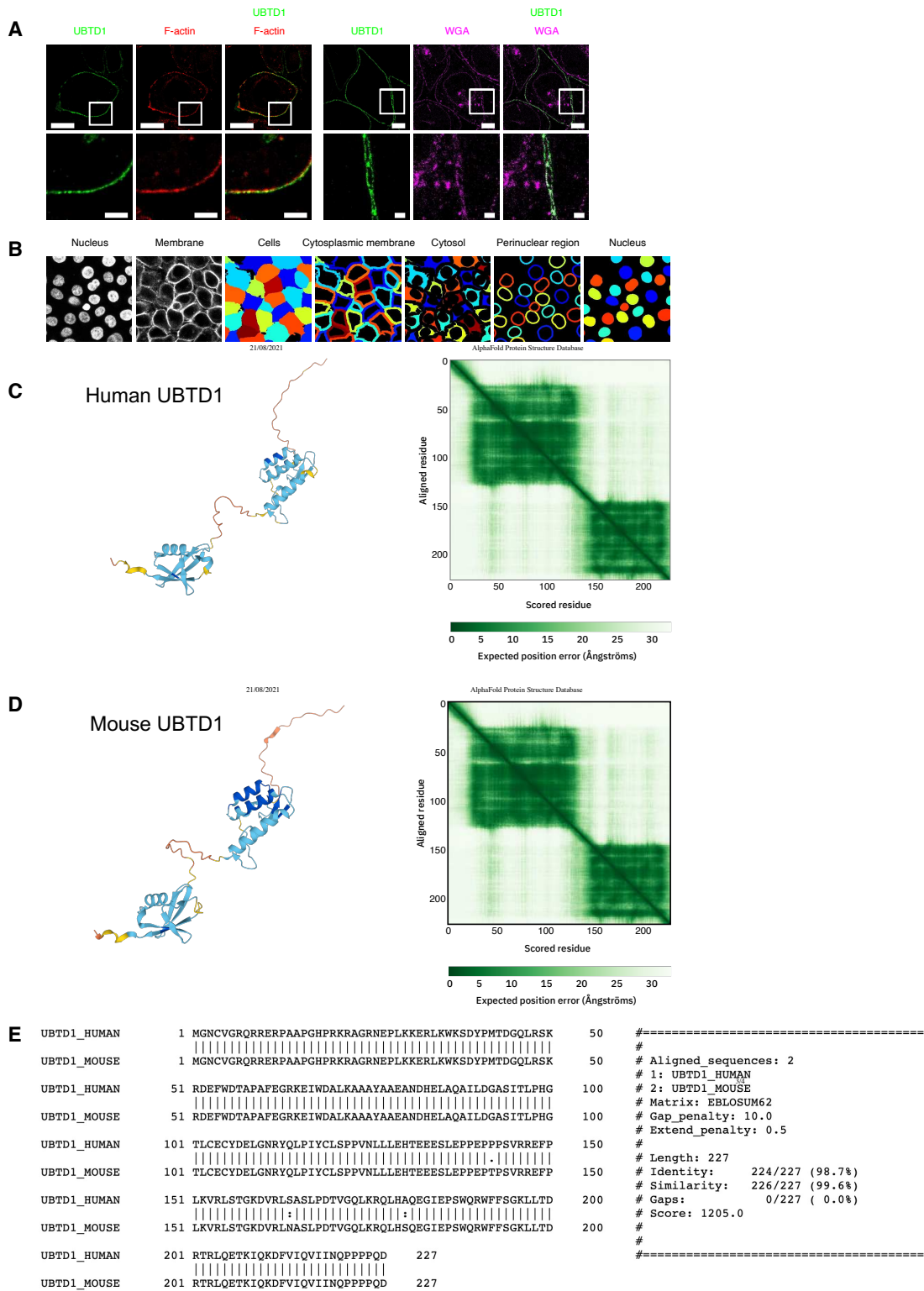
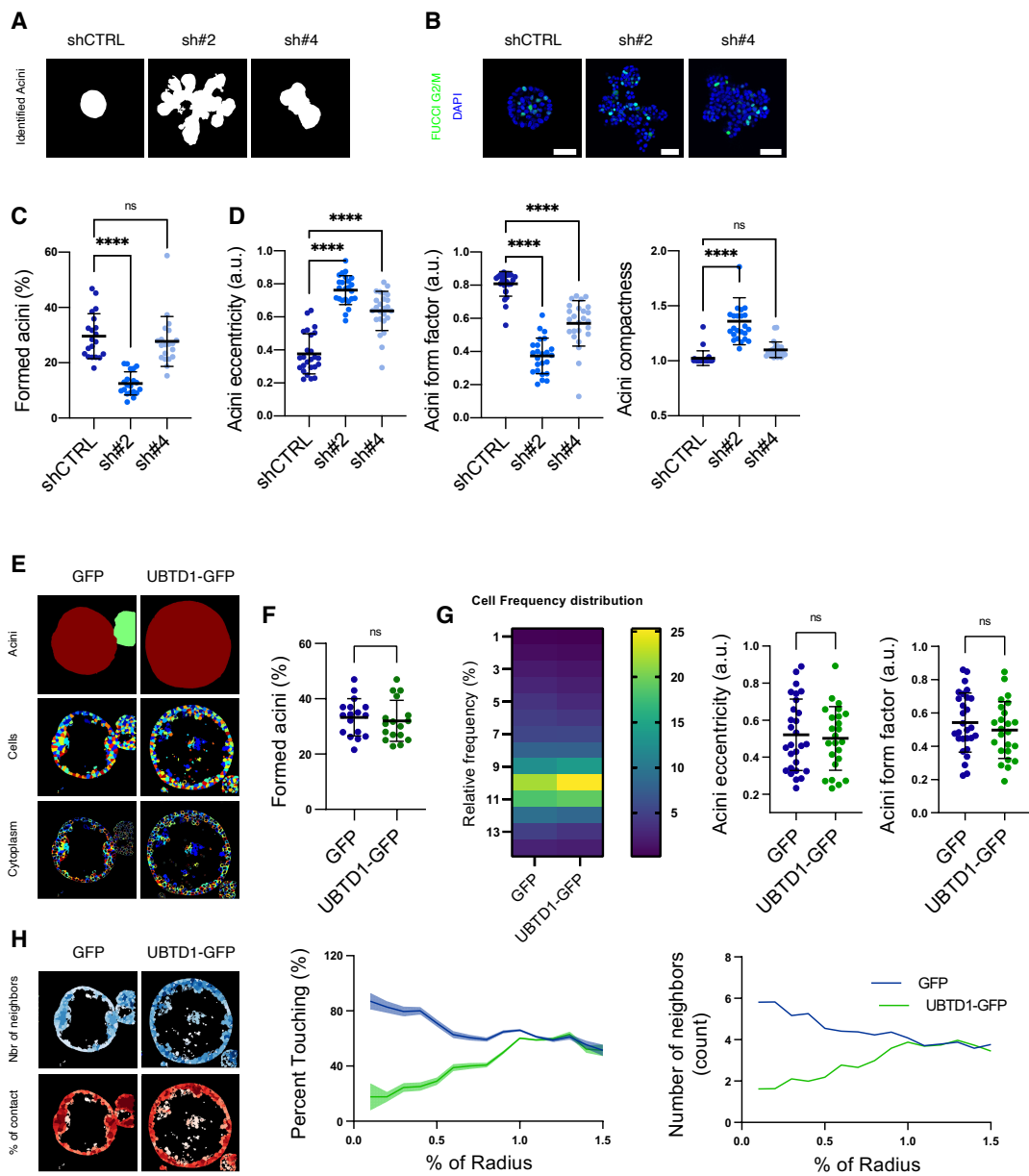


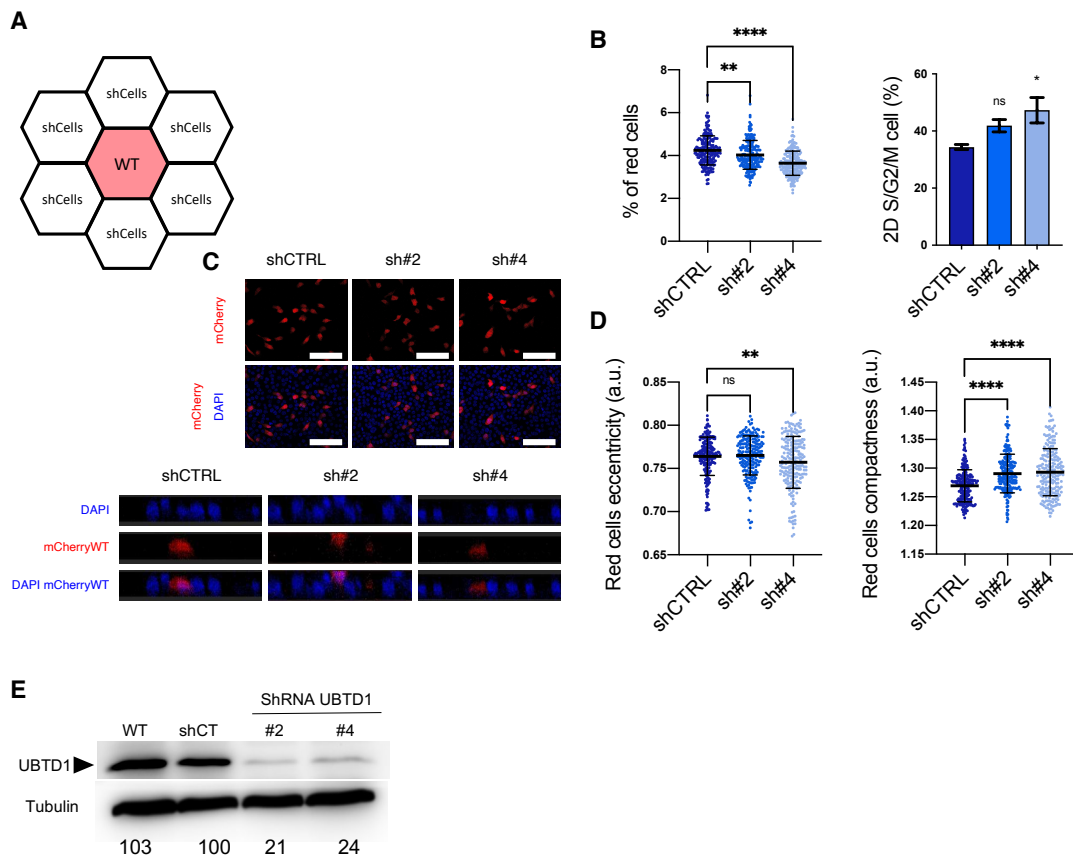
Figure 7



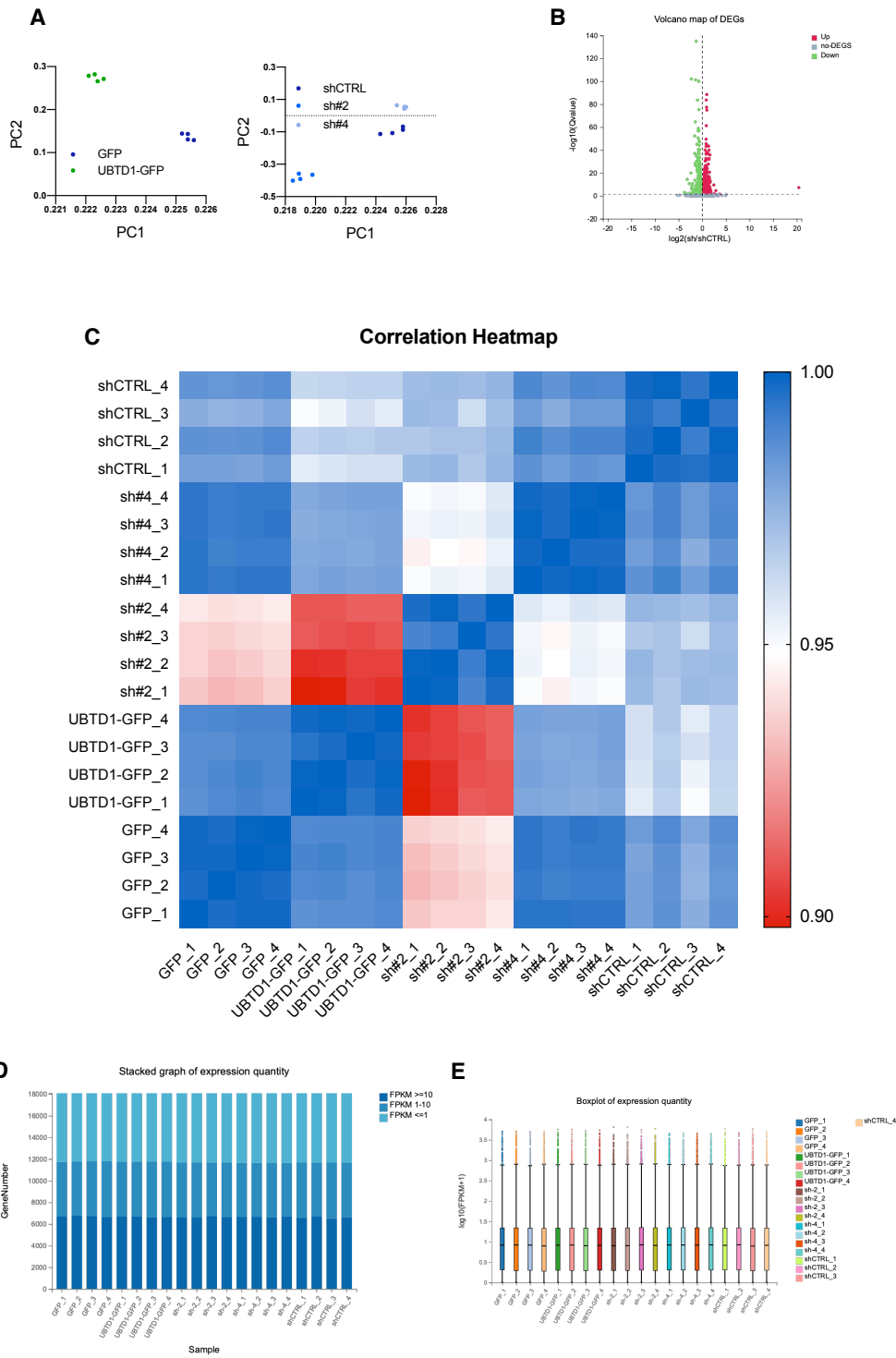
Supplemental Figure 1



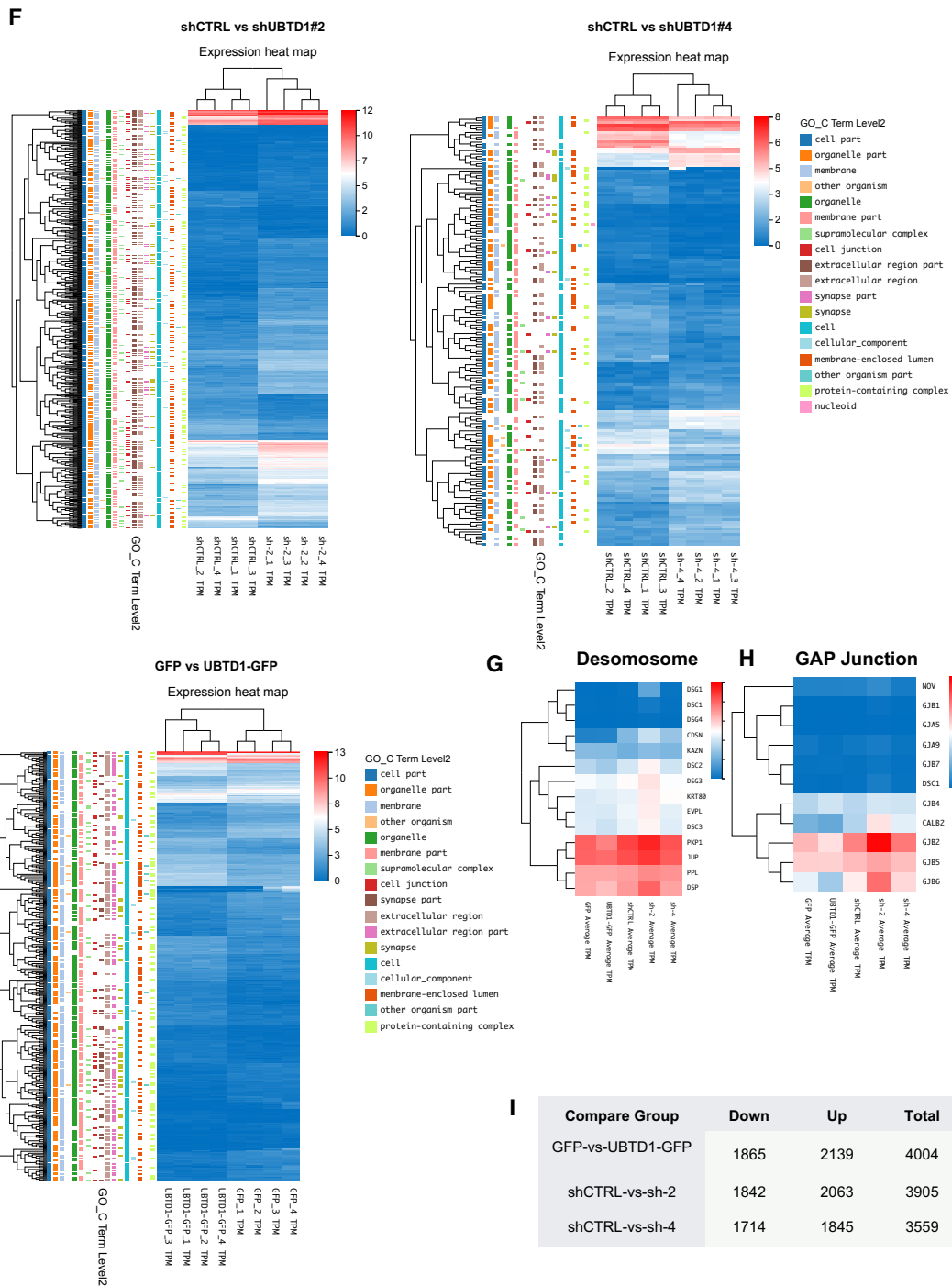
Supplemental Figure 2



Supplemental Figure 3



Supplemental Figure 4



Supplemental Figure 4



**Table 2.** List antibodies used for IF staining and western blot.

<b>Product Name</b>	<b>Reference</b>
CK5-AF647	ab193895
CK8	ab53280
UBTD1	HPA034825
Alexa Fluor™ 594 Phalloidin	A12381
Wheat Germ Agglutinin, Alexa Fluor™ 647 Conjugate	W32466
E-Cadherin	61081
Caspase-3	AB3623
Integrin B4	MAB1964
Beta Tubulin (BT7R)	MA5-16308

Supplemental Information



## **DISCUSSION AND PERSPECTIVES**



## Discussion and perspectives

During my thesis, I worked on the prostate organoid model with two main objectives: (1) to develop genome engineering techniques and (2) to study the role of the UBTD1 protein.

As mentioned previously, genome engineering is the modification of genes at specific loci in a more physiological manner than ectopic inputs of DNA. Genome editing allows for addition or removal of mutations, insertion or deletion of genes or gene parts. In the past decades, the CRISPR-Cas9 technology, based on RNA-programmable endonucleases, has revolutionized genome editing, making it easier, faster, and more efficient than previous techniques<sup>159</sup>. Nevertheless, constraints limit the use of this method for certain models, such as organoids. Indeed, the efficiency of delivery and the levels of toxicity can be limiting and become a barrier to genome editing<sup>142,175</sup>.

Adult Stem Cell based organoid technology recapitulates the architecture and functionality of the organ of origin better than immortalized 2D cell line models<sup>115</sup>. The generation of organoids from genetically engineered mice has allowed the study of many genes. However, organoids derived from human ASCs require efficient genome editing techniques.

In the first paper of my thesis, we developed the use of nanoblades to efficiently edit the genome of organoids *in vitro*.

We showed that nanoblades could achieve levels of genome editing that exceeded all other delivery methods in organoids. We showed that in addition to this high efficiency, nanoblades permitted to edit organoids with low cellular toxicity.

Because they have two advantages : they can carry a cargo and function as a delivery vehicle, Nanoblades allow high-level genome editing in organoids whereas previous studies reported much lower levels of gene editing. Until recently, the majority of studies containing gene editing in organoids relied on the electroporation of plasmids coding for Cas9<sup>142,205</sup>. These studies described the use of the CRISPR-Cas9 system to correct the CFTR channel mutation in organoids derived from cystic fibrosis patients<sup>142</sup>. The other study published by the same group reported the use of CRISPR Cas9 to induce sequential mutations to reproduce a mutational signature in colon cancer<sup>205</sup>. Both studies used liposomal transfection of plasmids encoding the CRISPR-Cas9 machinery. Although functional, the editing levels did not exceed 1%, making these approaches laborious and time consuming. A study published in 2015 reported the use of electroporation to deliver plasmids encoding Cas9 and sgRNA<sup>175</sup>. This technique exceeded the efficiency level of liposomal transfection. Nevertheless, the editing levels did not exceed 2%. Viruses have been shown to be extremely efficient at genetically manipulating cells. The efficiency of the best viral vectors can reach 100% transduction of the targeted cells<sup>180</sup>. We showed in our work the use of VLPs to bring the CRISPR-Cas9 machinery and sgRNAs to genetically edit organoids.

To set up the method we performed GFP knockouts in GFP labeled organoids. As a proof of concept, we also performed knockouts of the AR and CFTR genes. We obtained editing levels reaching 80% when targeting GFP and 20 to 30% for endogenous genes. For all the genes tested, the nanoblades did not induce a high level of toxicity in these cells in contrast to other

methods like electroporation. These methods induce toxicity and nevertheless permit only very low gene editing efficiency.

As mentioned above, another important point is the type of material brought (the cargo). With nanoblades, we deliver the CRISPR-Cas9 gene editing machinery in the form of RNPs that are incorporated in viral like particles and are introduced into the target cells via nanoblade envelope-cell fusion, which is a soft process not toxic for cells. As shown in other studies, this type of cargo increases the level of gene editing compared to electroporation of plasmids or mRNAs coding for Cas9 or sgRNAs<sup>174</sup>. Indeed, in a study published by Emma Rawlins' group, they compared the efficiency of different cargo delivered by nucleofection<sup>174</sup>. They showed that the electroporation of RNPs outperformed the efficiency levels of other types of cargo, i.e. DNA plasmid. The percentage of INDELS induced by electroporation of plasmid encoding Cas9 and sgRNA was about 5%, at the maximum plasmid dose, while it reached 25% with RNPs coupled with sgRNA (**Table 2**).

**Table 2. Gene editing efficiency in organoids.**

Delivery vehicle	Editing efficiency in organoids	Cargo	Organoid text refs
Microinjection	Not reported in organoids	DNA plasmid ; mRNA ; RNPs	
Electroporation	<25%	DNA plasmid ; mRNA ; RNPs	Beumer <i>et al.</i> 2021 Sun <i>et al.</i> 2021, Geurts <i>et al.</i> 2021, Artegiani <i>et al.</i> 2020, Artegiani <i>et al.</i> 2019, Fujii <i>et al.</i> 2015, etc.
Liposome transfection	<1%	DNA plasmid ; mRNA ; RNPs	Fujii <i>et al.</i> 2015, Drost <i>et al.</i> 2015, Schwank <i>et al.</i> 2013
Lentivirus (LV)	~%	DNA plasmid	Sun <i>et al.</i> 2021
Virus-like particule (VLP)	30 to 80%	RNPs	Tirolle <i>et al.</i> submitted

The other advantage of RNPs is their short transient presence in the cell. Indeed, RNPs have a lifetime limited to the half-life of the protein, compared to plasmids encoding Cas9 which persist for a longer period. This difference has been shown to influence the gene editing at off-target genomic site by the Cas9 protein<sup>206</sup>.

With nanoblades, we reported no off-target INDELS in mouse prostate and colon organoids. Summarizing, nanoblades have shown to be a very efficient technology to induce *in vitro* knockouts in mouse organoids.

Interestingly, we observed that AR knockout in prostate organoids prevented the formation of a lumen in the center of the organoid. As shown in a previous study, AR knockout in mice can disrupt the differentiation of mouse prostate luminal cells<sup>207</sup>. It is therefore interesting to note that prostate organoid swelling can be directly affected by luminal cell differentiation. This robust and easily quantifiable read-out paves the way for using this model to study prostate luminal cell differentiation. To take this observation further, analyses of the level of differentiation of the organoids would be interesting. Indeed, if changes in organoid morphology reflect the level of luminal cell differentiation, this makes the model attractive for testing drugs affecting the metabolism or differentiation of prostate luminal cells. Testing endocrine disruptors<sup>23</sup>, known to disrupt androgenic pathways, and therefore luminal cell

differentiation, would then be an excellent opportunity to challenge the prostate organoid model.

More generally, genome editing combined with organoids offers opportunities to easily study genes involved in organogenesis or the development of human pathology<sup>115,148</sup>. In order to push the use of nanoblades technology further, it will be interesting to see the levels of efficiency achievable in human organoids. Without thinking directly about gene therapy, it would accelerate and facilitate the study of genes in a model more relevant than mouse organoids.

In the long term, and in view of the developments made by the laboratories leading the research using organoids, efficient and non-toxic gene editing techniques will be necessary to consider approaches in gene therapy<sup>148</sup>. Indeed, the *ex vivo* correction of a patient's genetic mutation and regrafting in the same patient opens the way to promising treatment perspectives for genetic pathologies, such as cystic fibrosis.

Nevertheless, limitations not directly linked to the nanoblades technology but rather to the CRISPR-Cas9 technology itself do not allow yet to envisage therapies directly applied to patients. Indeed, it has been demonstrated that the DSBs cuts induced by Cas9 could induce off-target effects but also large chromosomal rearrangements<sup>208</sup>. Recently developed technologies such as base and prime editing have been shown to be more precise and to induce less chromosomal rearrangements. Indeed, to increase the precision of gene editing and reduce off-target cuts, other tools derived from the CRISPR Cas9 system are continuously developed, with increased possibilities and better specificity. There are indeed two main categories of CRISPR-based genome editing agents available today, namely, base editors and prime editors<sup>209-211</sup>. Base editors allow to generate single nucleotide changes in gDNA, while prime editors use Cas9 fused to a reverse transcriptase, programmed with a prime editing guide RNA (pegRNA) that specifies the target site and the desired sequence<sup>211</sup>. To explain in more detail, base editing is achieved by fusing C or A deaminase moieties to D10A Cas9 nickase. It should be noted however that these base editors have major limitations, they can currently only induce 6 (C→T, A→G, C→G, G→A, T→C, G→C) of the 12 possible point mutations. The other possibility to induce small sequence changes, point mutations, small insertions and small deletions, is prime editing. It involves a fusion of the H840A Cas9 nickase to the Reverse transcriptase of the Moloney Murine Leukemia Virus and modified guide RNAs carrying sequence templates to be copied into the target genomic site. However only one DNA strand is modified, and stable insertion depends on copying the modification onto the other DNA strand. These technologies or others coupled with the nanoblades delivery method would open wider possibilities of gene editing in models difficult to manipulate, such as organoids.

Another more direct prospect with nanoblades and organoids is the creation of an efficient and non-toxic technique to generate knock-ins. The knock-in consists in the integration of an exogenous DNA sequence at a precise locus in the genome. A study published by Benedetta Artegiani and her colleagues in 2020 already reported the generation of knock-ins in human organoids using homology-independent CRISPR-Cas9 precision genome editing<sup>132,176</sup>. They reported efficiency levels ranging from 6 to 40 percent depending on the targeted gene. More precisely, they obtained a maximum efficiency of 40% within the transfected population, which was 9%, meaning that they did not exceed efficiency levels of 5%<sup>176</sup>. Interestingly, inhibition

of TP53 by transient overexpression of a dominant negative form of TP53 appeared to increase the levels of knock-ins. This study which set-up an efficient knock-in approach in organoids highlights important points in a knock-in strategy. Nevertheless, as mentioned for knock-out, improvements in efficiency could be brought by modifying the delivery vehicle. Indeed, this study is based on the electroporation of plasmid DNA into the cells. However, the efficiency levels remain low. The use of viral vectors could probably increase the efficiency levels.

Together with the retrovirus-like system used for nanoblades, we could use the Integrase-Deficient Lentivirus (IDLV) system to efficiently deliver a DNA donor template for sites specific homologous recombination into targeted cells (**Figure 24**). IDLV technologies deliver RNA that is then reverse transcribed into DNA, once introduced into the cell. Unlike classical lentiviral vectors, the genetic information will not be integrated into the genome via mechanisms mediated by the viral machinery. This type of vector is therefore ideal for introducing a DNA template into a cell efficiently, without integrating it into the genome. Another type of viral particle, the Adeno-Associated Virus (AAVs), allows to introduce a template directly into the cells in the form of DNA. AAVs are as IDLV non-integrating vectors so only transiently present in dividing cells. As already shown in previous studies, these systems, coupled with nanoblades, would probably allow to reach higher levels of knock-in than other current techniques of delivery in organoids with minimal toxicity induction<sup>198</sup>. However, it is possible that for technical reasons related to the presence time of Cas9 provided by the nanoblades and the handling time of the organoids outside their adapted culture environment, AAVs might be more efficient than IDLVs. On the other hand, as already shown in another study, the different knock-in approaches can influence the level of efficiency<sup>176</sup>. Indeed, HDR mediated gene integration requires that the cells are in the S phase of the cell cycle whereas NHEJ takes place in all phases of the cycle. In the paper published by Artegiani et al, they reported a 10-fold increase in the level of knock-in efficiency mediated by NHEJ compared to HDR. It will be interesting to test these two types of integration in the genome with the delivery vehicles mentioned above.

Overall, gene editing technologies coupled with the organoid model open interesting and innovative research perspectives.

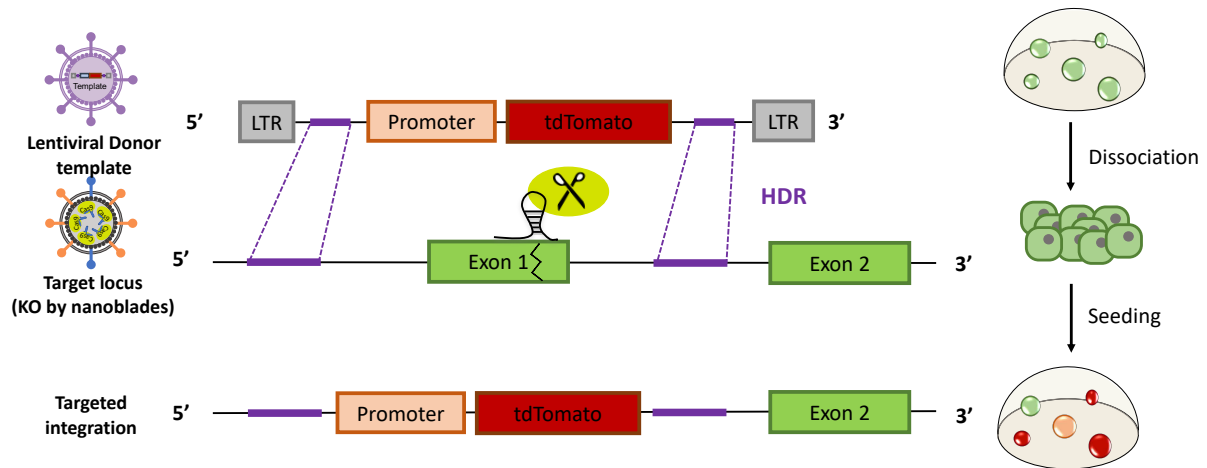


**Figure 24. Knock-in of a reporter gene to reveal nanoblade induced-KO in organoids.** Combining nanoblades targeting a genomic locus with integration deficient lentiviral vectors encoding for the donor template carrying the reporter expression cassette flanked by the two homology arms directed to the genomic region of interest .

The second objective of my thesis was to study the role of the UBTD1 protein in cell junctions. As mentioned before, UBTD1 or UBiquitin Domain containing 1, is a highly conserved protein in evolution. It belongs to a small protein family containing UBTD1 and UBTD2. This 25.9kDa protein contains a characterized UBL domain and a UBD domain. It also contains potential NLS sites. In a previous study, UBTD1 was shown to interact with members of the UBE2D family of E2 ubiquitin ligases<sup>92</sup>. UBTD1 was also shown to stabilize P53 by controlling the ubiquitination of MDM2, the E3 responsible for its degradation<sup>93</sup>. Our laboratory showed that UBTD1 participated in the degradation of YAP by modifying its ubiquitination levels<sup>94</sup>. Finally, in a recent study, we demonstrated that UBTD1 coordinate EGFR signaling by controlling cellular ceramide levels, via the ubiquitination of several proteins involved in this process (Torrino et al. 2021, see article in appendice).

All these previous studies suggest that UBTD1 acts as a platform to mediate the ubiquitination of several substrates.

We showed that UBTD1 localizes to the membrane-actin cortex region after the initiation of cell-cell contacts<sup>94</sup>. In my thesis I was interested in understanding where precisely UBTD1 was localized and through which mechanism. We showed that UBTD1 localized at the cytoplasmic membrane of prostate epithelial cells. We also showed that deletion of an N-terminal myristoylation site of the protein disrupted this membrane localization (**Figure 25**). In order to fully understand how myristoylation affects the localization of UBTD1, it would be interesting to decipher the myristoylation itself. Indeed, this type of myristoylation is achieved by N-myristoyltransferase (NMT). The deletion of the myristoylation site disrupted its membrane localization, an interesting question is: what controls the induction of myristoylation on UBTD1? It will be noteworthy in the future to inhibit these myristoylation enzymes. Furthermore, considering the dynamics associated with the localization of UBTD1, i.e. its localization at the membrane during the establishment of cell-cell contacts, it will be of interest to see if conformational changes of the protein itself occur. In this case, it will require the

analysis of potential phosphorylation sites on the protein. We can hypothesize that the enzymes responsible for myristoylation are not regulated, and are constantly active. In this case, the myristoylation changes of UBTD1 could potentially come from a conformational change, making the myristoylation site accessible under specific conditions. To further analyze the conformational changes of the protein, crystallographic analysis will be necessary.

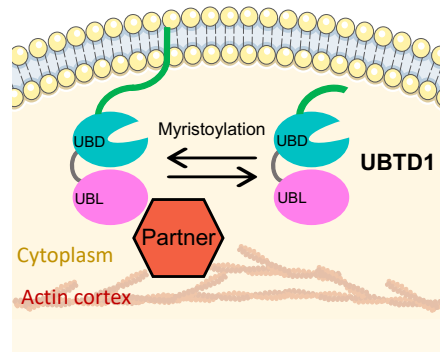


**Figure 25. Simplified representation of the anchoring of UBTD1 to the cytoplasmic membrane. UBTD1 is localized in the cytosol when its myristoylation site is deleted.**

Regarding its localization to the cytoplasmic membrane during the establishment of cell-cell contacts, we were interested in its potential role in the control of cell-cell junctions. We started by modulating UBTD1 expression in a 3D culture system to study cell organization processes related to cell junctions. We observed that downregulation of UBTD1 prevented this cell self-organization. Conversely, overexpression of UBTD1 seemed to increase cell organization. Acini, are ideal to study changes that are not easily visible in 2D cultures. Indeed, this model is ideal to exacerbate phenotypes associated with the organization of epithelium not visible in 2D. The simplicity of the analysis of the main read-out, namely the formation of the acini, makes it a very practical tool. However, the analysis of more precise features, such as cell polarity or cell shape, is more difficult. Indeed, acini grow randomly, and the percentage of acini formed varies from one experiment to another. Moreover, the shape and the level of organization varies from one acini to another, which makes the image analysis difficult and variable. In addition, it results in a very high background noise. This model is therefore not ideal for studying the precise characteristics associated with cell-cell interactions.

We then measured read-outs associated with the formation of cell junctions on the same cell line. We observed that overexpression of UBTD1 increased cell surface tension in a monolayer epithelium. Conversely, downregulation of UBTD1 decreased this surface tension. Cell shape was modified when UBTD1 was overexpressed. Z-plane organization was affected in monolayer epithelial cells under-expressing UBTD1. As shown in a previous study, downregulation of UBTD1 is associated with modification of genes involved in epithelial-mesenchymal transition (EMT)<sup>94</sup>. Even if the data obtained with these experiments are robust and reproducible, they are only partial and do not allow to fully understand the events triggered by UBTD1. From a physical point of view, the measurement of the surface tension allowed us to see that UBTD1 played a role in the cell tension. We concluded in the article that this measurement reflected changes associated with the establishment of cell junctions. However, as published in other studies using this type of technique<sup>212</sup>, the measurement of surface tension is not sufficient to conclude that the organization of the actin cortex has changed. Indeed,

research conducted by Ewa Palluch's group associated modifications of cellular rigidity with modifications of the organization of the actin cortex, however, these experiments were done by measuring cortical tension. Moreover, the measurement of surface tension that we did could also be affected by a modification of the membrane tension. Analyses of the latter using the optical tweezers technique would provide a clear answer to these first observations.

To further decipher the genes associated with UBTD1 downregulation in healthy epithelial cells, we performed bulk RNAseq. We identified numerous sets of genes associated with cell junctions that were affected by under or over-expression of UBTD1. These initial results supported the idea that UBTD1 affects processes associated with cell junctions.

As we have shown, UBTD1 is expressed only in basal cells of the prostate epithelium. UBTD1 is not found in luminal cells. We then took advantage of this information and chose to use the prostate organoid model. I developed this model in the laboratory after an internship in the Clevers's laboratory at the beginning of my thesis. This model derived from ASCs partially recapitulates the architecture and cellular composition of the original gland. It contains in its mature form, a layer of basal cells in contact with the ECM and a layer of luminal cells surrounding the organoid lumen. We then decided to express UBTD1 constitutively in the basal cells and in the luminal cells of the prostate organoids. We obtained compact organoids containing basal cells in the periphery and luminal cells in the center. However, no lumen was formed between the luminal cells in the center of the organoid under "physiological" conditions. As shown in a study published in 2019, the mechanisms of lumen formation within blastocyst structures is mediated by hydraulic fracturing of cell junctions between cells in the center of the blastocyst<sup>28</sup>. It was shown that the decrease of intercellular junctions facilitated the formation of lumen.

It was also shown in the study published by Karthaus et al, that prostate organoid swelling was stimulated with DHT<sup>20</sup>. Taking into account this information, we decided to force the secretion of luminal cells by overstimulating them with DHT. We observed the reformation of lumen in the organoids in the presence of concentrations three times higher than the reference concentrations<sup>20,101</sup>. We can imagine that the hydraulic fracturing mechanisms were restored. However, this hypothesis remains to be demonstrated with further experiments. We could indeed imagine playing on the expression levels of EpCAM, to see if a higher expression would restore lumen formation at 1 nM DHT. We could also induce a knock-out or a knock-down of E-cadherin in luminal cells. The decrease of junctions via the decrease of E-cadherin could also counterbalance the expression of UBTD1 in luminal cells. However, these hypotheses remain uncertain. Ideally, we would like to know the precise interactant(s) of UBTD1 and see if their increase or decrease could restore lumen formation. Taking a step back on the use of the organoid model, we have here a very limited use of it. Indeed, we only played on the junctions between the luminal cells of the prostate and visually analyzed the results of the expression of UBTD1. It could be interesting to analyze if the differentiation of the cells is affected. Nevertheless, the organoid remains an *in vitro* model, and morphological modifications are not necessarily associated with modifications of the differentiation level. Several modifications can indeed induce the same morphological phenotype. Indeed, AR knock-out and constitutive expression of UBTD1 in all cells induced compact organoids with luminal cells in the center and basal cells in the periphery. The interpretation of these morphological phenotypes should be taken with caution and should be associated with further experiments.

The concept of hydraulic fracturing should also be confirmed in this type of organoid by further analysis. Indeed, the precision of the imaging done here does not really allow to confirm if this type of mechanism is affected. In the study cited above<sup>28</sup>, live imaging was performed at a much higher resolution.

To dig deeper into the potential UBTD1 partners linked to this phenotype, we performed a mass spectrometry analysis of endogenous UBTD1 interactants isolated by co-immunoprecipitation. We identified several partners associated with cell junctions. One of them caught our attention, indeed the cell adhesion molecule (EpCAM) is identified as interacting with UBTD1. However, EpCAM is found to be expressed predominantly at the protein level in luminal prostate cells<sup>83</sup>. It is also known that EpCAM is responsible for loose junctions between epithelial cells, i.e. weak junctions. It exerts this role by destabilizing the binding of E-cadherin to the cytoskeleton in adherens junctions. Its high expression at the level of cell-cell contacts between luminal cells of the prostate suggests that the junctions between the cells are quite weak<sup>83</sup>.

The hypothesis we formulated here is that UBTD1 would modulate the strength of cell-cell junctions by controlling the degradation of EpCAM. A first preliminary result showed that its expression at the messenger level was modified when UBTD1 was deregulated. When UBTD1 was overexpressed EpCAM appeared to be downregulated and vice versa. This suggests compensatory mechanisms at the transcriptional level due to potential protein degradation. Nevertheless, experiments will be necessary to confirm that UBTD1 plays a role in EpCAM degradation, for example by evaluating its ubiquitination levels. The evaluation of the amount of EpCAM protein will allow us to assess whether EpCAM is more or less degraded depending on the level of UBTD1 expression. Nevertheless, as mentioned in the literature, ubiquitination does not only induce protein degradation, but it can also induce changes in protein-protein interactions<sup>85</sup>. In this case the experiments to be performed will be different, and the simple evaluation of the protein level of EpCAM will not be sufficient.

On the other hand, in view of the protein interactants of UBTD1, the hypothesis that UBTD1 plays a role in the degradation of EpCAM is the most straight forward. However, UBTD1 also seems to interact with vinculin, and subunits of the Arp2/3 complex (data not shown). Arp2/3 being the main actor of the branched polymerization of the actin cytoskeleton<sup>81</sup>. As seen in the literature, the regulation of the branching polymerization of the actin cytoskeleton is a key step in the initiation and maturation of adherens junctions<sup>213</sup>. Vinculin could also be a candidate to explain these phenotypes, given its key role in adherens junctions<sup>214</sup>.

Mechanistic studies will therefore be necessary to fully understand how UBTD1 affects cell junctions. Overall UBTD1 seems to be a promising player as a modulator of the strength of intercellular junctions in an epithelium.

Given the use of nanoblades in organoids, the logical next step would have been to perform a UBTD1 knockout in organoids to further dissect its role in cell junctions.

In the future, it will be interesting to study more precisely the two main domains of UBTD1 to see if we observe mechanisms similar to those observed on other UBL proteins. Indeed, other proteins have been reported to contain UBL and UBD domains<sup>91</sup>. In these proteins, conformational changes were necessary for them to be functional. The study of conformational changes in the UBTD1 protein is essential to understand more precisely its function and regulation.

It will also be interesting to dissect the roles of UBTD1 and UBTD2, to see if they do not compensate each other in some organs. Indeed, UBTD2 is part of the same family as UBTD1, but their expressions can vary from one organ to another.

Overall, UBTD1 seems to be a very versatile protein that interacts with many other proteins. Understanding how UBTD1 interacts with these proteins will be a key step to fully understand the protein.



## **REFERENCES**



1. Toivanen, R. & Shen, M. M. Prostate organogenesis: tissue induction, hormonal regulation and cell type specification. *Development* **144**, 1382–1398 (2017).
2. Berman, D. M. *et al.* Roles for Hedgehog signaling in androgen production and prostate ductal morphogenesis. *Developmental Biology* **267**, 387–398 (2004).
3. Hayward, S. *et al.* Epithelial development in the rat ventral prostate, anterior prostate and seminal vesicle.
4. Cunha, G. R. & Lung, B. The possible influence of temporal factors in androgenic responsiveness of urogenital tissue recombinants from wild-type and androgen-insensitive (Tfm) Mice. *J. Exp. Zool.* **205**, 181–193 (1978).
5. Cunha, A. *et al.* Normal and Abnormal Development Urogenital Tract. *Journal of Andrology* **13**, 465–475 (1992).
6. Donjacour, A. A., Thomson, A. A. & Cunha, G. R. FGF-10 plays an essential role in the growth of the fetal prostate. *Developmental Biology* **261**, 39–54 (2003).
7. Mirosevich, J., Gao, N. & Matusik, R. J. Expression of Foxa transcription factors in the developing and adult murine prostate: Foxa Expression in the Murine Prostate. *Prostate* **62**, 339–352 (2005).
8. Gao, N. *et al.* Forkhead box A1 regulates prostate ductal morphogenesis and promotes epithelial cell maturation. *Development* **132**, 3431–3443 (2005).
9. Wang, S. *et al.* Prostate-specific deletion of the murine Pten tumor suppressor gene leads to metastatic prostate cancer. *Cancer Cell* **4**, 209–221 (2003).
10. Economides, K. D. & Capecchi, M. R. *Hoxb13* is required for normal differentiation and secretory function of the ventral prostate. *Development* **130**, 2061–2069 (2003).
11. Freestone, S. H. *et al.* Sonic hedgehog regulates prostatic growth and epithelial differentiation. *Developmental Biology* **264**, 352–362 (2003).
12. Lamm, M. L. G. *et al.* Mesenchymal Factor Bone Morphogenetic Protein 4 Restricts Ductal Budding and Branching Morphogenesis in the Developing Prostate. *Developmental Biology* **232**, 301–314 (2001).
13. Donjacour, A. The Effect of Androgen Deprivation on Branching Morphogenesis in the Mouse Prostate' g2. 14.
14. Lung, B. & Cunha, G. R. Development of seminal vesicles and coagulating glands in neonatal mice. I. The morphogenetic effects of various hormonal conditions. *Anat. Rec.* **199**, 73–88 (1981).
15. Price, D. Normal development of the prostate and seminal vesicles of the rat with a study of experimental postnatal modifications. *Am. J. Anat.* **60**, 79–127 (1936).
16. Wuidart, A. *et al.* Quantitative lineage tracing strategies to resolve multipotency in tissue-specific stem cells. *Genes Dev.* **30**, 1261–1277 (2016).
17. Ousset, M. *et al.* Multipotent and unipotent progenitors contribute to prostate postnatal development. *Nat Cell Biol* **14**, 1131–1138 (2012).
18. Guo, W. *et al.* Single-cell transcriptomics identifies a distinct luminal progenitor cell type in distal prostate invagination tips. *Nat Genet* **52**, 908–918 (2020).
19. Karthaus, W. R. *et al.* Regenerative potential of prostate luminal cells revealed by single-cell analysis. *Science* **368**, 497–505 (2020).
20. Karthaus, W. R. *et al.* Identification of Multipotent Luminal Progenitor Cells in Human Prostate Organoid Cultures. *Cell* **159**, 163–175 (2014).
21. Szczyrba, J. *et al.* Neuroendocrine Cells of the Prostate Derive from the Neural Crest. *Journal of Biological Chemistry* **292**, 2021–2031 (2017).
22. Borowsky, A. D. *et al.* Inflammation and Atrophy Precede Prostatic Neoplasia in a PhIP-Induced Rat Model. *Neoplasia* **8**, 708–715 (2006).
23. Bokobza, E. *et al.* The Adipose Tissue at the Crosstalk Between EDCs and Cancer Development. *Front. Endocrinol.* **12**, 691658 (2021).

24. Shen, M. M. & Abate-Shen, C. Molecular genetics of prostate cancer: new prospects for old challenges. *Genes Dev.* **24**, 1967–2000 (2010).
25. Hartsock, A. & Nelson, W. J. Adherens and tight junctions: Structure, function and connections to the actin cytoskeleton. *Biochimica et Biophysica Acta (BBA) - Biomembranes* **1778**, 660–669 (2008).
26. Takeichi, M. Functional correlation between cell adhesive properties and some cell surface proteins. *Journal of Cell Biology* **75**, 464–474 (1977).
27. Larue, L., Ohsugi, M., Hirchenhain, J. & Kemler, R. E-cadherin null mutant embryos fail to form a trophectoderm epithelium. *Proceedings of the National Academy of Sciences* **91**, 8263–8267 (1994).
28. Dumortier, J. G. *et al.* Hydraulic fracturing and active coarsening position the lumen of the mouse blastocyst. *Science* **365**, 465–468 (2019).
29. Mendonsa, A. M., Na, T.-Y. & Gumbiner, B. M. E-cadherin in contact inhibition and cancer. *Oncogene* **37**, 4769–4780 (2018).
30. Halbleib, J. M. & Nelson, W. J. Cadherins in development: cell adhesion, sorting, and tissue morphogenesis. *Genes & Development* **20**, 3199–3214 (2006).
31. Guillot, C. & Lecuit, T. Adhesion Disengagement Uncouples Intrinsic and Extrinsic Forces to Drive Cytokinesis in Epithelial Tissues. *Developmental Cell* **24**, 227–241 (2013).
32. Pokutta, S. & Weis, W. I. Structure of the Dimerization and  $\beta$ -Catenin-Binding Region of  $\alpha$ -Catenin. *Molecular Cell* **11**.
33. Patel, S. D. *et al.* Type II Cadherin Ectodomain Structures: Implications for Classical Cadherin Specificity. *Cell* **124**, 1255–1268 (2006).
34. Vestweber, D. & Kemler, R. Identification of a putative cell adhesion domain of uvomorulin. *The EMBO Journal* **4**, 3393–3398 (1985).
35. Thoreson, M. A. *et al.* Selective Uncoupling of P120ctn from E-Cadherin Disrupts Strong Adhesion. *Journal of Cell Biology* **148**, 189–202 (2000).
36. Reynolds, A. B., Roesel, D. J., Kanner, S. B. & Parsons, J. T. Transformation-Specific Tyrosine Phosphorylation of a Novel Cellular Protein in Chicken Cells Expressing Oncogenic Variants of the Avian Cellular src Gene. *MOL. CELL. BIOL.* **9**, 10 (1989).
37. Staddon, J. M., Smales, C., Schulze, C. & Esch, F. S. p120, a p120-Related Protein (p100), and the Cadherin/Catenin Complex. *The Journal of Cell Biology* **130**, 13 (1995).
38. Keirsebilck, A. *et al.* Molecular Cloning of the Human p120ctn/Catenin Gene (CTNND1): Expression of Multiple Alternatively Spliced Isoforms. *Genomics* **50**, 129–146 (1998).
39. Anastasiadis, P. Z. *et al.* Inhibition of RhoA by p120 catenin. *Nat Cell Biol* **2**, 637–644 (2000).
40. Ishiyama, N. *et al.* Dynamic and Static Interactions between p120 Catenin and E-Cadherin Regulate the Stability of Cell-Cell Adhesion. *Cell* **141**, 117–128 (2010).
41. Petrova, Y. I., Spano, M. M. & Gumbiner, B. M. Conformational epitopes at cadherin calcium-binding sites and p120-catenin phosphorylation regulate cell adhesion. *MBoC* **23**, 2092–2108 (2012).
42. Castaño, J. *et al.* Specific Phosphorylation of p120-Catenin Regulatory Domain Differently Modulates Its Binding to RhoA. *Mol Cell Biol* **27**, 1745–1757 (2007).
43. Goodwin, M., Kovacs, E. M., Thoreson, M. A., Reynolds, A. B. & Yap, A. S. Minimal Mutation of the Cytoplasmic Tail Inhibits the Ability of E-cadherin to Activate Rac but Not Phosphatidylinositol 3-Kinase. *Journal of Biological Chemistry* **278**, 20533–20539 (2003).
44. Stairs, D. B. *et al.* Deletion of p120-Catenin Results in a Tumor Microenvironment with Inflammation and Cancer that Establishes It as a Tumor Suppressor Gene. *Cancer Cell* **19**, 470–483 (2011).

45. McCrea, P. D. & Gumbiner, B. M. Purification of a 92-kDa cytoplasmic protein tightly associated with the cell-cell adhesion molecule E-cadherin (uvomorulin). *Journal of Biological Chemistry* **266**, 4514–4520 (1991).
46. Lickert, H., Bauer, A., Kemler, R. & Stappert, J. Casein Kinase II Phosphorylation of E-cadherin Increases E-cadherin/ $\beta$ -Catenin Interaction and Strengthens Cell-Cell Adhesion. *Journal of Biological Chemistry* **275**, 5090–5095 (2000).
47. Huber, A. H. & Weis, W. I. The Structure of the  $^N$ -Catenin/E-Cadherin Complex and the Molecular Basis of Diverse Ligand Recognition by  $^N$ -Catenin. 12.
48. Lilien, J., Balsamo, J., Arregui, C. & Xu, G. Turn-off, drop-out: Functional state switching of cadherins. *Dev. Dyn.* **224**, 18–29 (2002).
49. Chen, Y.-T., Stewart, D. B. & Nelson, W. J. Coupling Assembly of the E-Cadherin/ $^N$ -Catenin Complex to Efficient Endoplasmic Reticulum Exit and Basal-lateral Membrane Targeting of E-Cadherin in Polarized MDCK Cells. *The Journal of Cell Biology* **144**, 13 (1999).
50. Huber, A. H., Nelson, W. J. & Weis, W. I. Three-Dimensional Structure of the Armadillo Repeat Region of  $^N$ -Catenin. 12.
51. Fukata, M. *et al.* Cdc42 and Rac1 Regulate the Interaction of IQGAP1 with  $\beta$ -Catenin. *Journal of Biological Chemistry* **274**, 26044–26050 (1999).
52. Clevers, H. Wnt/ $\beta$ -Catenin Signaling in Development and Disease. *Cell* **127**, 469–480 (2006).
53. Morin, P. J.  $\beta$ -catenin signaling and cancer. *Bioessays* **21**, 1021–1030 (1999).
54. Pradhan, D., Lombardo, C. R., Roe, S., Rimm, D. L. & Morrow, J. S.  $\alpha$ -Catenin Binds Directly to Spectrin and Facilitates Spectrin-Membrane Assembly in Vivo. *Journal of Biological Chemistry* **276**, 4175–4181 (2001).
55. Gates, J. & Peifer, M. Can 1000 Reviews Be Wrong? Actin,  $\alpha$ -Catenin, and Adherens Junctions. *Cell* **123**, 769–772 (2005).
56. Drees, F., Pokutta, S., Yamada, S., Nelson, W. J. & Weis, W. I.  $\alpha$ -Catenin Is a Molecular Switch that Binds E-Cadherin- $\beta$ -Catenin and Regulates Actin-Filament Assembly. *Cell* **123**, 903–915 (2005).
57. Biswas, K. H. Regulation of  $\alpha$ -catenin conformation at cadherin adhesions. *JBSE* **13**, 17-00699-17–00699 (2018).
58. Choi, S. H., Estaras, C., Moresco, J. J., Yates, J. R. & Jones, K. A.  $\alpha$ -Catenin interacts with APC to regulate  $\alpha$ -catenin proteolysis and transcriptional repression of Wnt target genes. *Genes & Development* **27**, 2473–2488 (2013).
59. Geiger, B. A 130K protein from chicken gizzard: Its localization at the termini of microfilament bundles in cultured chicken cells. *Cell* **18**, 193–205 (1979).
60. Burridge, K. & Feramisco, J. Microinjection and localization of a 130K protein in living fibroblasts: a relationship to actin and fibronectin. *Cell* **19**, 587–595 (1980).
61. Carisey, A. & Ballestrem, C. Vinculin, an adapter protein in control of cell adhesion signalling. *European Journal of Cell Biology* **90**, 157–163 (2011).
62. Dufour, S., Mège, R.-M. & Thiery, J. P.  $\alpha$ -catenin, vinculin, and F-actin in strengthening E-cadherin cell–cell adhesions and mechanosensing. *Cell Adhesion & Migration* **7**, 345–350 (2013).
63. Chen, H., Cohen, D. M., Choudhury, D. M., Kioka, N. & Craig, S. W. Spatial distribution and functional significance of activated vinculin in living cells. *Journal of Cell Biology* **169**, 459–470 (2005).
64. Vasioukhin, V., Bauer, C., Yin, M. & Fuchs, E. Directed Actin Polymerization Is the Driving Force for Epithelial Cell–Cell Adhesion. *Cell* **100**, 209–219 (2000).
65. Hazan, R. B., Kang, L., Roe, S., Borgen, P. I. & Rimm, D. L. Vinculin Is Associated with the E-cadherin Adhesion Complex. *Journal of Biological Chemistry* **272**, 32448–32453

(1997).

66. Bertocchi, C., Ravasio, A., Ong, H. T., Toyama, Y. & Kanchanawong, P. *Mechanical Roles of Vinculin/ $\beta$ -catenin interaction in Adherens Junction*. <http://biorxiv.org/lookup/doi/10.1101/770735> (2019) doi:10.1101/770735.
67. Hetrick, B., Han, M. S., Helgeson, L. A. & Nolen, B. J. Small Molecules CK-666 and CK-869 Inhibit Actin-Related Protein 2/3 Complex by Blocking an Activating Conformational Change. *Chemistry & Biology* **20**, 701–712 (2013).
68. Mergault, C. *et al.* Inhibition of the Arp2/3 complex represses human lung myofibroblast differentiation and attenuates bleomycin-induced pulmonary fibrosis. *Br J Pharmacol* bph.15675 (2021) doi:10.1111/bph.15675.
69. Bustelo, X. R., Sauzeau, V. & Berenjano, I. M. GTP-binding proteins of the Rho/Rac family: regulation, effectors and functions in vivo. *Bioessays* **29**, 356–370 (2007).
70. Boureux, A., Vignal, E., Faure, S. & Fort, P. Evolution of the Rho Family of Ras-Like GTPases in Eukaryotes. *Molecular Biology and Evolution* **24**, 203–216 (2007).
71. Müller, P. M. *et al.* Systems analysis of RhoGEF and RhoGAP regulatory proteins reveals spatially organized RAC1 signalling from integrin adhesions. *Nat Cell Biol* **22**, 498–511 (2020).
72. Arnold, T. R., Stephenson, R. E. & Miller, A. L. Rho GTPases and actomyosin: Partners in regulating epithelial cell-cell junction structure and function. *Experimental Cell Research* **358**, 20–30 (2017).
73. Yang, W.-H. *et al.* RAC1 activation mediates Twist1-induced cancer cell migration. *Nat Cell Biol* **14**, 366–374 (2012).
74. Zhang, S. *et al.* RhoA Regulates G<sub>1</sub>-S Progression of Gastric Cancer Cells by Modulation of Multiple INK4 Family Tumor Suppressors. *Mol Cancer Res* **7**, 570–580 (2009).
75. Vicente-Manzanares, M., Ma, X., Adelstein, R. S. & Horwitz, A. R. Non-muscle myosin II takes centre stage in cell adhesion and migration. *Nat Rev Mol Cell Biol* **10**, 778–790 (2009).
76. Naydenov, N. G. *et al.* Nonmuscle Myosin IIA Regulates Intestinal Epithelial Barrier in vivo and Plays a Protective Role During Experimental Colitis. *Sci Rep* **6**, 24161 (2016).
77. Weng, M. & Wieschaus, E. Myosin-dependent remodeling of adherens junctions protects junctions from Snail-dependent disassembly. *Journal of Cell Biology* **212**, 219–229 (2016).
78. Yonemura, S., Wada, Y., Watanabe, T., Nagafuchi, A. & Shibata, M.  $\alpha$ -Catenin as a tension transducer that induces adherens junction development. *Nat Cell Biol* **12**, 533–542 (2010).
79. Leerberg, J. M. *et al.* Tension-Sensitive Actin Assembly Supports Contractility at the Epithelial Zonula Adherens. *Current Biology* **24**, 1689–1699 (2014).
80. Sjöblom, B., Salmazo, A. & Djinović-Carugo, K.  $\alpha$ -Actinin structure and regulation. *Cell. Mol. Life Sci.* **65**, 2688–2701 (2008).
81. Tang, V. W. & Briehar, W. M.  $\alpha$ -Actinin-4/FSGS1 is required for Arp2/3-dependent actin assembly at the adherens junction. *Journal of Cell Biology* **196**, 115–130 (2012).
82. Bois, P. R. J., Borgon, R. A., Vornrhein, C. & Izard, T. Structural Dynamics of  $\alpha$ -Actinin–Vinculin Interactions. *MOL. CELL. BIOL.* **25**, 11 (2005).
83. Schnell, U., Cirulli, V. & Giepmans, B. N. G. EpCAM: Structure and function in health and disease. *Biochimica et Biophysica Acta (BBA) - Biomembranes* **1828**, 1989–2001 (2013).
84. Litvinov, S. V. *et al.* Epithelial Cell Adhesion Molecule (Ep-CAM) Modulates Cell–Cell Interactions Mediated by Classic Cadherins. *Journal of Cell Biology* **139**, 1337–1348 (1997).

85. Rape, M. Ubiquitylation at the crossroads of development and disease. *Nat Rev Mol Cell Biol* **19**, 59–70 (2018).
86. Komander, D. & Rape, M. The Ubiquitin Code. *Annu. Rev. Biochem.* **81**, 203–229 (2012).
87. Yau, R. & Rape, M. The increasing complexity of the ubiquitin code. *Nat Cell Biol* **18**, 579–586 (2016).
88. Schulman, B. A. & Wade Harper, J. Ubiquitin-like protein activation by E1 enzymes: the apex for downstream signalling pathways. *Nat Rev Mol Cell Biol* **10**, 319–331 (2009).
89. Ye, Y. & Rape, M. Building ubiquitin chains: E2 enzymes at work. *Nat Rev Mol Cell Biol* **10**, 755–764 (2009).
90. Hicke, L., Schubert, H. L. & Hill, C. P. Ubiquitin-binding domains. *Nat Rev Mol Cell Biol* **6**, 610–621 (2005).
91. Kerscher, O., Felberbaum, R. & Hochstrasser, M. Modification of Proteins by Ubiquitin and Ubiquitin-Like Proteins. *Annu. Rev. Cell Dev. Biol.* **22**, 159–180 (2006).
92. Uhler, J. P. *et al.* The UbL protein UBTD1 stably interacts with the UBE2D family of E2 ubiquitin conjugating enzymes. *Biochemical and Biophysical Research Communications* **443**, 7–12 (2014).
93. Zhang, X.-W. *et al.* UBTD1 induces cellular senescence through an UBTD1-Mdm2/p53 positive feedback loop: Cellular senescence induced by UBTD1-Mdm2/p53 positive feedback loop. *J. Pathol.* **235**, 656–667 (2015).
94. Torrino, S. *et al.* UBTD1 is a mechano-regulator controlling cancer aggressiveness. *EMBO Rep* **20**, (2019).
95. Torrino, S. *et al.* UBTD1 regulates ceramide balance and endolysosomal positioning to coordinate EGFR signaling. *eLife* **10**, e68348 (2021).
96. Yang, N. *et al.* CXCR4 mediates matrix stiffness-induced downregulation of UBTD1 driving hepatocellular carcinoma progression via YAP signaling pathway. *Theranostics* **10**, 5790–5801 (2020).
97. Kim, J., Koo, B.-K. & Knoblich, J. A. Human organoids: model systems for human biology and medicine. *Nat Rev Mol Cell Biol* **21**, 571–584 (2020).
98. Lancaster, M. A. & Knoblich, J. A. Organogenesis in a dish: Modeling development and disease using organoid technologies. *Science* **345**, 1247125 (2014).
99. Schutgens, F. & Clevers, H. Human Organoids: Tools for Understanding Biology and Treating Diseases. *Annu. Rev. Pathol. Mech. Dis.* **15**, 211–234 (2020).
100. Masters, J. R. HeLa cells 50 years on: the good, the bad and the ugly. *Nat Rev Cancer* **2**, 315–319 (2002).
101. Drost, J. *et al.* Organoid culture systems for prostate epithelial and cancer tissue. *Nat Protoc* **11**, 347–358 (2016).
102. Marino, S., Staines, K. A., Brown, G., Howard-Jones, R. A. & Adamczyk, M. Models of ex vivo explant cultures: applications in bone research. *BoneKEy Reports* **5**, (2016).
103. Rheinwatd, J. G. & Green, H. Se'iam Cultivation of Strains of Human Epider a Ke at nocyt..s. the Formation Keratinizin Co!onies fto Single Ce is. 12.
104. Li, M. L. *et al.* Influence of a reconstituted basement membrane and its components on casein gene expression and secretion in mouse mammary epithelial cells. *Proceedings of the National Academy of Sciences* **84**, 136–140 (1987).
105. Sato, T. *et al.* Single Lgr5 stem cells build crypt-villus structures in vitro without a mesenchymal niche. *Nature* **459**, 262–265 (2009).
106. Eiraku, M. *et al.* Self-organizing optic-cup morphogenesis in three-dimensional culture. *Nature* **472**, 51–56 (2011).
107. Sulston, J. E., Schierenberg, E., White, J. G. & Thomson, J. N. The embryonic cell lineage of the nematode *Caenorhabditis elegans*. *Developmental Biology* **100**, 64–119 (1983).

108. Harris, T. W. WormBase: a multi-species resource for nematode biology and genomics. *Nucleic Acids Research* **32**, 411D – 417 (2004).
109. Poulin, G., Nandakumar, R. & Ahringer, J. Genome-wide RNAi screens in *Caenorhabditis elegans*: impact on cancer research. *Oncogene* **23**, 8340–8345 (2004).
110. Lui, J. H., Hansen, D. V. & Kriegstein, A. R. Development and Evolution of the Human Neocortex. *Cell* **146**, 18–36 (2011).
111. Sanoh, S. *et al.* Predictability of Metabolism of Ibuprofen and Naproxen Using Chimeric Mice with Human Hepatocytes. *Drug Metab Dispos* **40**, 2267–2272 (2012).
112. Sato, T. *et al.* Long-term Expansion of Epithelial Organoids From Human Colon, Adenoma, Adenocarcinoma, and Barrett’s Epithelium. *Gastroenterology* **141**, 1762–1772 (2011).
113. Gao, D. *et al.* Organoid Cultures Derived from Patients with Advanced Prostate Cancer. *Cell* **159**, 176–187 (2014).
114. Barker, N. *et al.* Identification of stem cells in small intestine and colon by marker gene *Lgr5*. *Nature* **449**, 1003–1007 (2007).
115. Clevers, H. Modeling Development and Disease with Organoids. *Cell* **165**, 1586–1597 (2016).
116. Hu, H. *et al.* Long-Term Expansion of Functional Mouse and Human Hepatocytes as 3D Organoids. *Cell* **175**, 1591-1606.e19 (2018).
117. Peng, W. C. *et al.* Inflammatory Cytokine TNF $\alpha$  Promotes the Long-Term Expansion of Primary Hepatocytes in 3D Culture. *Cell* **175**, 1607-1619.e15 (2018).
118. Basak, O. *et al.* Induced Quiescence of *Lgr5*<sup>+</sup> Stem Cells in Intestinal Organoids Enables Differentiation of Hormone-Producing Enteroendocrine Cells. *Cell Stem Cell* **20**, 177-190.e4 (2017).
119. Beumer, J. *et al.* Enteroendocrine cells switch hormone expression along the crypt-to-villus BMP signalling gradient. *Nat Cell Biol* **20**, 909–916 (2018).
120. Barker, N. *et al.* *Lgr5*<sup>+</sup>ve Stem Cells Drive Self-Renewal in the Stomach and Build Long-Lived Gastric Units In Vitro. *Cell Stem Cell* **6**, 25–36 (2010).
121. Stange, D. E. *et al.* Differentiated *Troy*<sup>+</sup> Chief Cells Act as Reserve Stem Cells to Generate All Lineages of the Stomach Epithelium. *Cell* **155**, 357–368 (2013).
122. Bartfeld, S. *et al.* In Vitro Expansion of Human Gastric Epithelial Stem Cells and Their Responses to Bacterial Infection. *Gastroenterology* **148**, 126-136.e6 (2015).
123. Pleguezuelos-Manzano, C. *et al.* Mutational signature in colorectal cancer caused by genotoxic pks<sup>+</sup> *E. coli*. *Nature* **580**, 269–273 (2020).
124. Salama, N. R., Hartung, M. L. & Müller, A. Life in the human stomach: persistence strategies of the bacterial pathogen *Helicobacter pylori*. *Nat Rev Microbiol* **11**, 385–399 (2013).
125. Ramani, S., Atmar, R. L. & Estes, M. K. Epidemiology of human noroviruses and updates on vaccine development: *Current Opinion in Gastroenterology* **30**, 25–33 (2014).
126. Ettayebi, K. *et al.* Replication of human noroviruses in stem cell-derived human enteroids. *Science* **353**, 1387–1393 (2016).
127. Lamers, M. M. *et al.* SARS-CoV-2 productively infects human gut enterocytes. *Science* **369**, 50–54 (2020).
128. Huch, M. & Koo, B.-K. Modeling mouse and human development using organoid cultures. *Development* **142**, 3113–3125 (2015).
129. Rusnati, M. *et al.* Recent Strategic Advances in CFTR Drug Discovery: An Overview. *IJMS* **21**, 2407 (2020).
130. Dekkers, J. F. *et al.* A functional CFTR assay using primary cystic fibrosis intestinal organoids. *Nat Med* **19**, 939–945 (2013).
131. Sato, T. *et al.* Paneth cells constitute the niche for *Lgr5* stem cells in intestinal crypts.

*Nature* **469**, 415–418 (2011).

132. Artegiani, B. *et al.* Probing the Tumor Suppressor Function of BAP1 in CRISPR-Engineered Human Liver Organoids. *Cell Stem Cell* **24**, 927-943.e6 (2019).
133. van de Wetering, M. *et al.* Prospective Derivation of a Living Organoid Biobank of Colorectal Cancer Patients. *Cell* **161**, 933–945 (2015).
134. Fujii, M. *et al.* A Colorectal Tumor Organoid Library Demonstrates Progressive Loss of Niche Factor Requirements during Tumorigenesis. *Cell Stem Cell* **18**, 827–838 (2016).
135. Jacob, F. *et al.* Human Pluripotent Stem Cell-Derived Neural Cells and Brain Organoids Reveal SARS-CoV-2 Neurotropism Predominates in Choroid Plexus Epithelium. *Cell Stem Cell* **27**, 937-950.e9 (2020).
136. Sachs, N. *et al.* A Living Biobank of Breast Cancer Organoids Captures Disease Heterogeneity. *Cell* **172**, 373-386.e10 (2018).
137. Lo, Y.-H., Karlsson, K. & Kuo, C. J. Applications of organoids for cancer biology and precision medicine. *Nat Cancer* **1**, 761–773 (2020).
138. Vlachogiannis, G. *et al.* Patient-derived organoids model treatment response of metastatic gastrointestinal cancers. *Science* **359**, 920–926 (2018).
139. Drost, J. *et al.* Use of CRISPR-modified human stem cell organoids to study the origin of mutational signatures in cancer. *Science* **358**, 234–238 (2017).
140. Shen, L. Mitigating Psychological Reactance: The Role of Message-Induced Empathy in Persuasion. *Human Communication Research* **36**, 397–422 (2010).
141. Driehuis, E. & Clevers, H. CRISPR/Cas 9 genome editing and its applications in organoids. *American Journal of Physiology-Gastrointestinal and Liver Physiology* **312**, G257–G265 (2017).
142. Schwank, G. *et al.* Functional Repair of CFTR by CRISPR/Cas9 in Intestinal Stem Cell Organoids of Cystic Fibrosis Patients. *Cell Stem Cell* **13**, 653–658 (2013).
143. Geurts, M. H. *et al.* Evaluating CRISPR-based prime editing for cancer modeling and CFTR repair in organoids. *Life Sci. Alliance* **4**, e202000940 (2021).
144. Park, J. S. *et al.* The effect of matrix stiffness on the differentiation of mesenchymal stem cells in response to TGF- $\beta$ . *Biomaterials* **32**, 3921–3930 (2011).
145. Kim, G.-A., Ginga, N. J. & Takayama, S. Integration of Sensors in Gastrointestinal Organoid Culture for Biological Analysis. *Cellular and Molecular Gastroenterology and Hepatology* **6**, 123-131.e1 (2018).
146. Cox, T. R. & Eler, J. T. Remodeling and homeostasis of the extracellular matrix: implications for fibrotic diseases and cancer. *Disease Models & Mechanisms* **4**, 165–178 (2011).
147. Kratochvil, M. J. *et al.* Engineered materials for organoid systems. *Nat Rev Mater* **4**, 606–622 (2019).
148. Hofer, M. & Lutolf, M. P. Engineering organoids. *Nat Rev Mater* **6**, 402–420 (2021).
149. Nikolaev, M. *et al.* Homeostatic mini-intestines through scaffold-guided organoid morphogenesis. *Nature* **585**, 574–578 (2020).
150. Wang, M., Glass, Z. A. & Xu, Q. Non-viral delivery of genome-editing nucleases for gene therapy. *Gene Ther* **24**, 144–150 (2017).
151. Sackmann Sala, L. *et al.* A rare castration-resistant progenitor cell population is highly enriched in Pten-null prostate tumours: Castration-resistant progenitors are enriched in Pten<sup>-/-</sup> prostates. *J. Pathol* **243**, 51–64 (2017).
152. Puca, L. *et al.* Patient derived organoids to model rare prostate cancer phenotypes. *Nat Commun* **9**, 2404 (2018).
153. Servant, R. *et al.* Prostate cancer patient-derived organoids: detailed outcome from a prospective cohort of 81 clinical specimens. *J. Pathol.* **254**, 543–555 (2021).
154. Lino, C. A., Harper, J. C., Carney, J. P. & Timlin, J. A. Delivering CRISPR: a review

- of the challenges and approaches. *Drug Delivery* **25**, 1234–1257 (2018).
155. Martin, F., Sánchez-Hernández, S., Gutiérrez-Guerrero, A., Pinedo-Gomez, J. & Benabdellah, K. Biased and Unbiased Methods for the Detection of Off-Target Cleavage by CRISPR/Cas9: An Overview. *IJMS* **17**, 1507 (2016).
  156. Gaj, T., Gersbach, C. A. & Barbas, C. F. ZFN, TALEN, and CRISPR/Cas-based methods for genome engineering. *Trends in Biotechnology* **31**, 397–405 (2013).
  157. Khalil, A. M. The genome editing revolution: review. 16 (2020).
  158. Ishino, Y., Shinagawa, H., Makino, K., Amemura, M. & Nakata, A. Nucleotide sequence of the iap gene, responsible for alkaline phosphatase isozyme conversion in *Escherichia coli*, and identification of the gene product. *J Bacteriol* **169**, 5429–5433 (1987).
  159. Doudna, J. A. & Charpentier, E. The new frontier of genome engineering with CRISPR-Cas9. *Science* **346**, 1258096 (2014).
  160. Bolotin, A., Quinquis, B., Sorokin, A. & Ehrlich, S. D. Clustered regularly interspaced short palindrome repeats (CRISPRs) have spacers of extrachromosomal origin. *Microbiology* **151**, 2551–2561 (2005).
  161. Pourcel, C., Salvignol, G. & Vergnaud, G. CRISPR elements in *Yersinia pestis* acquire new repeats by preferential uptake of bacteriophage DNA, and provide additional tools for evolutionary studies. *Microbiology* **151**, 653–663 (2005).
  162. Cradick, T. J., Ambrosini, G., Iseli, C., Bucher, P. & McCaffrey, A. P. ZFN-Site searches genomes for zinc finger nuclease target sites and off-target sites. *BMC Bioinformatics* **12**, 152 (2011).
  163. Langmead, B., Trapnell, C., Pop, M. & Salzberg, S. L. Ultrafast and memory-efficient alignment of short DNA sequences to the human genome. *Genome Biol* **10**, R25 (2009).
  164. Anderson, E. M. *et al.* Systematic analysis of CRISPR–Cas9 mismatch tolerance reveals low levels of off-target activity. *Journal of Biotechnology* **211**, 56–65 (2015).
  165. Bae, S., Park, J. & Kim, J.-S. Cas-OFFinder: a fast and versatile algorithm that searches for potential off-target sites of Cas9 RNA-guided endonucleases. *Bioinformatics* **30**, 1473–1475 (2014).
  166. Bloh, K. *et al.* Deconvolution of Complex DNA Repair (DECODR): Establishing a Novel Deconvolution Algorithm for Comprehensive Analysis of CRISPR-Edited Sanger Sequencing Data. *The CRISPR Journal* **4**, 120–131 (2021).
  167. Wang, X. *et al.* Whole-genome sequencing reveals rare off-target mutations in CRISPR/Cas9-edited grapevine. *Hortic Res* **8**, 114 (2021).
  168. Shim, G. *et al.* Therapeutic gene editing: delivery and regulatory perspectives. *Acta Pharmacol Sin* **38**, 738–753 (2017).
  169. Yang, H. *et al.* One-Step Generation of Mice Carrying Reporter and Conditional Alleles by CRISPR/Cas-Mediated Genome Engineering. *Cell* **154**, 1370–1379 (2013).
  170. Horii, T. *et al.* Validation of microinjection methods for generating knockout mice by CRISPR/Cas-mediated genome engineering. *Sci Rep* **4**, 4513 (2015).
  171. Wu, Y. *et al.* Correction of a Genetic Disease in Mouse via Use of CRISPR-Cas9. *Cell Stem Cell* **13**, 659–662 (2013).
  172. Xin, Y. & Duan, C. Microinjection of Antisense Morpholinos, CRISPR/Cas9 RNP, and RNA/DNA into Zebrafish Embryos. in *Hypoxia* (ed. Huang, L. E.) vol. 1742 205–211 (Springer New York, 2018).
  173. Ross, J. mRNA Stability in Mammalian Cells. *MICROBIOL. REV.* **59**, 28 (1995).
  174. Dawei, S., Lewis, E. & Emma L., R. *Organoid Easytag: an efficient workflow for gene targeting in human organoids*. <https://prelights.biologists.com?p=20966> (2020) doi:10.1242/prelights.20966.
  175. Fujii, M., Matano, M., Nanki, K. & Sato, T. Efficient genetic engineering of human intestinal organoids using electroporation. *Nat Protoc* **10**, 1474–1485 (2015).

176. Artegiani, B. *et al.* Fast and efficient generation of knock-in human organoids using homology-independent CRISPR–Cas9 precision genome editing. *Nat Cell Biol* **22**, 321–331 (2020).
177. Kim, S., Kim, D., Cho, S. W., Kim, J. & Kim, J.-S. Highly efficient RNA-guided genome editing in human cells via delivery of purified Cas9 ribonucleoproteins. *Genome Research* **24**, 1012–1019 (2014).
178. Wang, M. *et al.* Efficient delivery of genome-editing proteins using bioreducible lipid nanoparticles. *Proc Natl Acad Sci USA* **113**, 2868–2873 (2016).
179. Liang, X. *et al.* Rapid and highly efficient mammalian cell engineering via Cas9 protein transfection. *Journal of Biotechnology* **208**, 44–53 (2015).
180. Levine, F. & Friedmann, T. Gene therapy techniques. *Current Opinion in Biotechnology* **2**, 840–844 (1991).
181. Naso, M. F., Tomkowicz, B., Perry, W. L. & Strohl, W. R. Adeno-Associated Virus (AAV) as a Vector for Gene Therapy. *BioDrugs* **31**, 317–334 (2017).
182. Wu, Z., Yang, H. & Colosi, P. Effect of Genome Size on AAV Vector Packaging. *Molecular Therapy* **18**, 80–86 (2010).
183. Carroll, K. J. *et al.* A mouse model for adult cardiac-specific gene deletion with CRISPR/Cas9. *Proc Natl Acad Sci USA* **113**, 338–343 (2016).
184. Swiech, L. *et al.* In vivo interrogation of gene function in the mammalian brain using CRISPR-Cas9. *Nat Biotechnol* **33**, 102–106 (2015).
185. Ran, F. A. *et al.* In vivo genome editing using *Staphylococcus aureus* Cas9. *Nature* **520**, 186–191 (2015).
186. Garita-Hernandez, M. *et al.* AAV-Mediated Gene Delivery to 3D Retinal Organoids Derived from Human Induced Pluripotent Stem Cells. *IJMS* **21**, 994 (2020).
187. Maetzig, T., Galla, M., Baum, C. & Schambach, A. Gammaretroviral Vectors: Biology, Technology and Application. *Viruses* **3**, 677–713 (2011).
188. Naldini, L. *et al.* In Vivo Gene Delivery and Stable Transduction of Nondividing Cells by a Lentiviral Vector. *Science* **272**, 263–267 (1996).
189. Dull, T. *et al.* A Third-Generation Lentivirus Vector with a Conditional Packaging System. *J. Virol.* **72**, 8463–8471 (1998).
190. Derse, D. & Martarano, L. Construction of a Recombinant Bovine Leukemia Virus Vector for Analysis of Virus Infectivity. *J. VIROL.* **64**, 5 (1990).
191. Suerth, J. D., Maetzig, T., Galla, M., Baum, C. & Schambach, A. Self-Inactivating Alpharetroviral Vectors with a Split-Packaging Design. *J Virol* **84**, 6626–6635 (2010).
192. Watanabe, S. & Temin, H. M. Encapsidation sequences for spleen necrosis virus, an avian retrovirus, are between the 5' long terminal repeat and the start of the gag gene. *Proceedings of the National Academy of Sciences* **79**, 5986–5990 (1982).
193. Günzburgi, W. H. & Salmons, B. Mouse mammary tumor virus mediated transfer and expression of neomycin resistance to infected cultured cells. *Virology* **155**, 236–248 (1986).
194. Heckl, D. *et al.* Generation of mouse models of myeloid malignancy with combinatorial genetic lesions using CRISPR-Cas9 genome editing. *Nat Biotechnol* **32**, 941–946 (2014).
195. Petri, W. A. & Wagner, R. R. Reconstitution into liposomes of the glycoprotein of vesicular stomatitis virus by detergent dialysis. *Journal of Biological Chemistry* **254**, 4313–4316 (1979).
196. Naskalska, A. & Pyrc, K. Virus Like Particles as Immunogens and Universal Nanocarriers. *Pol J Microbiol* **64**, 3–13 (2015).
197. Mangeot, P. E. *et al.* Genome editing in primary cells and in vivo using viral-derived Nanoblades loaded with Cas9-sgRNA ribonucleoproteins. *Nat Commun* **10**, 45 (2019).
198. Gutierrez-Guerrero, A. *et al.* Baboon Envelope Pseudotyped “Nanoblades” Carrying

- Cas9/gRNA Complexes Allow Efficient Genome Editing in Human T, B, and CD34+ Cells and Knock-in of AAV6-Encoded Donor DNA in CD34+ Cells. *Front. Genome Ed.* **3**, 604371 (2021).
199. Cronin, J., Zhang, X.-Y. & Reiser, J. Altering the Tropism of Lentiviral Vectors through Pseudotyping. *CGT* **5**, 387–398 (2005).
200. Girard-Gagnepain, A. *et al.* Baboon envelope pseudotyped LVs outperform VSV-G-LVs for gene transfer into early-cytokine-stimulated and resting HSCs. *Blood* **124**, 1221–1231 (2014).
201. Finkelshtein, D., Werman, A., Novick, D., Barak, S. & Rubinstein, M. LDL receptor and its family members serve as the cellular receptors for vesicular stomatitis virus. *Proceedings of the National Academy of Sciences* **110**, 7306–7311 (2013).
202. Lieber, M. M., Livingston, D. M. & Kalter, S. S. Infectious C-type vtrus isolated from a baboon placenta. *4* (1974).
203. Bernadin, O. *et al.* Baboon envelope LVs efficiently transduced human adult, fetal, and progenitor T cells and corrected SCID-X1 T-cell deficiency. *Blood Advances* **3**, 461–475 (2019).
204. Colamartino, A. B. L. *et al.* Efficient and Robust NK-Cell Transduction With Baboon Envelope Pseudotyped Lentivector. *Front. Immunol.* **10**, 2873 (2019).
205. Drost, J. *et al.* Sequential cancer mutations in cultured human intestinal stem cells. *Nature* **521**, 43–47 (2015).
206. Vakulskas, C. A. *et al.* A high-fidelity Cas9 mutant delivered as a ribonucleoprotein complex enables efficient gene editing in human hematopoietic stem and progenitor cells. *Nat Med* **24**, 1216–1224 (2018).
207. Xie, Q. *et al.* Dissecting cell-type-specific roles of androgen receptor in prostate homeostasis and regeneration through lineage tracing. *Nat Commun* **8**, 14284 (2017).
208. Anderson, E. M. *et al.* Systematic analysis of CRISPR–Cas9 mismatch tolerance reveals low levels of off-target activity. *Journal of Biotechnology* **211**, 56–65 (2015).
209. Chen, P. J. *et al.* Enhanced prime editing systems by manipulating cellular determinants of editing outcomes. *Cell* **184**, 5635-5652.e29 (2021).
210. Anzalone, A. V. *et al.* Search-and-replace genome editing without double-strand breaks or donor DNA. *Nature* **576**, 149–157 (2019).
211. Anzalone, A. V., Koblan, L. W. & Liu, D. R. Genome editing with CRISPR–Cas nucleases, base editors, transposases and prime editors. *Nat Biotechnol* **38**, 824–844 (2020).
212. De Belly, H. *et al.* Membrane Tension Gates ERK-Mediated Regulation of Pluripotent Cell Fate. *Cell Stem Cell* **28**, 273-284.e6 (2021).
213. Efimova, N. & Svitkina, T. M. Branched actin networks push against each other at adherens junctions to maintain cell–cell adhesion. *Journal of Cell Biology* **217**, 1827–1845 (2018).
214. Bays, J. L. & DeMali, K. A. Vinculin in cell–cell and cell–matrix adhesions. *Cell. Mol. Life Sci.* **74**, 2999–3009 (2017).

## **ANNEXES**



## **ARTICLE 1**



# UBTD1 regulates ceramide balance and endolysosomal positioning to coordinate EGFR signaling

Stéphanie Torino<sup>1,2\*</sup>, Victor Tiroille<sup>2†</sup>, Bastien Dolfi<sup>3†</sup>, Maeva Dufies<sup>4</sup>, Charlotte Hinault<sup>2,5</sup>, Laurent Bonesso<sup>5</sup>, Sonia Dagnino<sup>6</sup>, Jennifer Uhler<sup>7</sup>, Marie Irondelle<sup>8</sup>, Anne-sophie Gay<sup>1</sup>, Lucile Fleuriot<sup>1</sup>, Delphine Debayle<sup>1</sup>, Sandra Lacas-Gervais<sup>9</sup>, Mireille Cormont<sup>10</sup>, Thomas Bertero<sup>1</sup>, Frederic Bost<sup>2\*</sup>, Jerome Gilleron<sup>10‡</sup>, Stephan Clavel<sup>2‡\*</sup>

<sup>1</sup>Université Côte d'Azur, CNRS, IPMC, Valbonne, France; <sup>2</sup>Université Côte d'Azur, Inserm, C3M, Team Targeting prostate cancer cell metabolism, Nice, France; <sup>3</sup>Université Côte d'Azur, Inserm, C3M, Team Metabolism and cancer, Nice, France; <sup>4</sup>Biomedical Department, Centre Scientifique de Monaco, Monaco, Monaco; <sup>5</sup>Biochemistry Laboratory, University Hospital, Nice, France; <sup>6</sup>MRC Centre for Environment and Health, Department of Epidemiology and Biostatistics, School of Public Health, Imperial College London, London, United Kingdom; <sup>7</sup>Department of Medical Biochemistry and Cell Biology, University of Gothenburg, Gothenburg, Sweden; <sup>8</sup>Inserm U1065, Université Côte d'Azur, Nice, France; <sup>9</sup>CCMA, UFR Sciences, Université Côte d'Azur, Nice, France; <sup>10</sup>Université Côte d'Azur, Inserm, C3M, Team Cellular and Molecular Pathophysiology of Obesity and Diabetes, Nice, France

**\*For correspondence:**

stephanie.torino@unice.fr (ST);  
Frederic.BOST@univ-cotedazur.fr  
(FB);  
Stephan.CLAVEL@univ-cotedazur.fr  
(SC)

<sup>†</sup>These authors contributed equally to this work

<sup>‡</sup>These authors also contributed equally to this work

**Competing interests:** The authors declare that no competing interests exist.

**Funding:** See page 21

**Received:** 12 March 2021

**Accepted:** 20 April 2021

**Published:** 22 April 2021

**Reviewing editor:** Roger J Davis, University of Massachusetts Medical School, United States

© Copyright Torino et al. This article is distributed under the terms of the [Creative Commons Attribution License](https://creativecommons.org/licenses/by/4.0/), which permits unrestricted use and redistribution provided that the original author and source are credited.

**Abstract** To adapt in an ever-changing environment, cells must integrate physical and chemical signals and translate them into biological meaningful information through complex signaling pathways. By combining lipidomic and proteomic approaches with functional analysis, we have shown that ubiquitin domain-containing protein 1 (UBTD1) plays a crucial role in both the epidermal growth factor receptor (EGFR) self-phosphorylation and its lysosomal degradation. On the one hand, by modulating the cellular level of ceramides through N-acylsphingosine amidohydrolase 1 (ASAH1) ubiquitination, UBTD1 controls the ligand-independent phosphorylation of EGFR. On the other hand, UBTD1, via the ubiquitination of Sequestosome 1 (SQSTM1/p62) by RNF26 and endolysosome positioning, participates in the lysosomal degradation of EGFR. The coordination of these two ubiquitin-dependent processes contributes to the control of the duration of the EGFR signal. Moreover, we showed that UBTD1 depletion exacerbates EGFR signaling and induces cell proliferation emphasizing a hitherto unknown function of UBTD1 in EGFR-driven human cell proliferation.

## Introduction

All living organisms perceive variations in their environment and translate them into intracellular signals via signaling pathways. In multicellular organisms, disturbances in this signal transduction mechanism induce inappropriate cell behavior and are associated with a plethora of diseases including cancer.

Cellular signaling can be viewed as a finely tuned 'space-time continuum' (*Scott and Pawson, 2009*). Receptors activated by their ligands at the plasma membrane are endocytosed, then moved

along endocytic compartments to be routed to the lysosomes for final degradation or recycled back to the cell surface. Thus, the signal delivered to the cell is the sum of the signals emitted by the activated receptor at the plasma membrane and during its intracellular trafficking (Bakker *et al.*, 2017). The responsiveness of these processes requires fast and accurate control in space and time, which is mainly ensured by post-translational modification (PTM) of proteins. Broadly, several aspects of cell signaling and receptor trafficking are regulated by proteolytic or non-proteolytic ubiquitination (Bakker *et al.*, 2017; Rape, 2018; Haglund and Dikic, 2005; Tokunaga *et al.*, 2009; Eden *et al.*, 2012).

Protein ubiquitination is a PTM that results in the covalent attachment of one or more ubiquitin to lysine residues of the substrate (Yau and Rape, 2016; Komander and Rape, 2012; Kerscher *et al.*, 2006). Ubiquitin conjugation occurs in a sequential three-step enzymatic process involving E1 (ubiquitin activation), E2 (ubiquitin conjugation), and E3 (ubiquitin ligation). In this hierarchical framework, there are only two E1s, over 30 E2s and hundreds of E3s in human, illustrating the large spectrum of E2s that contrasts with the high specificity of E3s in the recognition of substrates (Schulman and Harper, 2009; Ye and Rape, 2009). While the interaction of E3s with their substrates confers specificity to the system, E2s are more versatile and are commonly considered as 'ubiquitin carriers' with an auxiliary rather than control role. However, the modulation of the functionality of E2/E3 complexes by scaffold proteins has been poorly investigated and few proteins acting on these complexes have been characterized (Ye and Rape, 2009; Good *et al.*, 2011).

Ubiquitin domain-containing protein 1 (UBTD1) is an evolutionarily-conserved protein which interacts, both *in vitro* and *in vivo*, with some E2 and E3 enzymes of the ubiquitin-proteasome system (UPS) (Uhler *et al.*, 2014). Recently, we have shown that UBTD1 controls the degradation of the transcriptional regulator yes-associated protein (YAP) by modulating its ubiquitination (Torrino *et al.*, 2019). Mechanistically, UBTD1 is a component of the ubiquitination complex that allows the E3 ligase beta-transducin repeats-containing proteins ( $\beta$ -TRCP) to interact with YAP. Coherent with this E2/E3 regulatory function, UBTD1 has been reported to stabilize p53 (tumor protein P53) through ubiquitination and further degradation of mouse double minute 2 (MDM2), the E3 enzyme that degrades p53 (Zhang *et al.*, 2015). Importantly, a decreased expression of UBTD1 is associated with increased cancer aggressiveness and decreased overall patient survival in colorectal, liver, prostate, and lung cancer (Uhler *et al.*, 2014; Torrino *et al.*, 2019; Yang *et al.*, 2020). Based on these evidences, we have previously suggested that UBTD1 may be an E2/E3 scaffolding protein acting as a tumor suppressor (Torrino *et al.*, 2019).

To provide novel insights into UBTD1 functions, we here investigated the effect of its knockdown in a cell model by combining lipidomic, proteomic, and signaling screening. Through this integrated approach, we have uncovered an important role of UBTD1 in epidermal growth factor receptor (EGFR) degradation and signaling. Indeed, we showed that UBTD1 participates in the processing of EGFR-positive vesicles and controls late endosome/lysosome positioning through p62/SQSTM1 (Sequestosome 1) ubiquitination by RNF26. UBTD1 also regulates the ubiquitination of lysosomal ceramidase N-Acylsphingosine Amidohydrolase 1 (ASAH1) and modifies membrane lipid composition to limit EGFR auto-phosphorylation. UBTD1 coordinates in time and space the EGFR signaling pathway to avoid persistent and inappropriate signaling leading to uncontrolled cell proliferation.

## Results

### UBTD1 depletion induces EGFR self-phosphorylation by modifying membrane lipid composition through ASAH1 ubiquitination

In mammals, UBTD1 is expressed in many organs and cell types, however its molecular function is still largely unknown, and its cellular role remains elusive. To provide insights into its cellular functions, we first performed a phospho-kinase array allowing us to observe that UBTD1 depletion increased (>1.5 fold) phosphorylation of JNK1/2/3, GSK3  $\alpha/\beta$  (S9/21) and EGFR (Y1086) (Figure 1A, Figure 1—figure supplement 1A). EGFR phosphorylation presented the highest difference compared to control cells (>2 fold). Next, we confirmed by western-blot an increase in EGFR phosphorylation (Y1068 and Y1086) at steady state, and we also noticed an increase in the total amount of EGFR in UBTD1-depleted cells (Figure 1B, Figure 1—figure supplement 1B). Coherently with an increased EGFR signaling, UBTD1 depletion sharply increases cell proliferation (Figure 1C). These

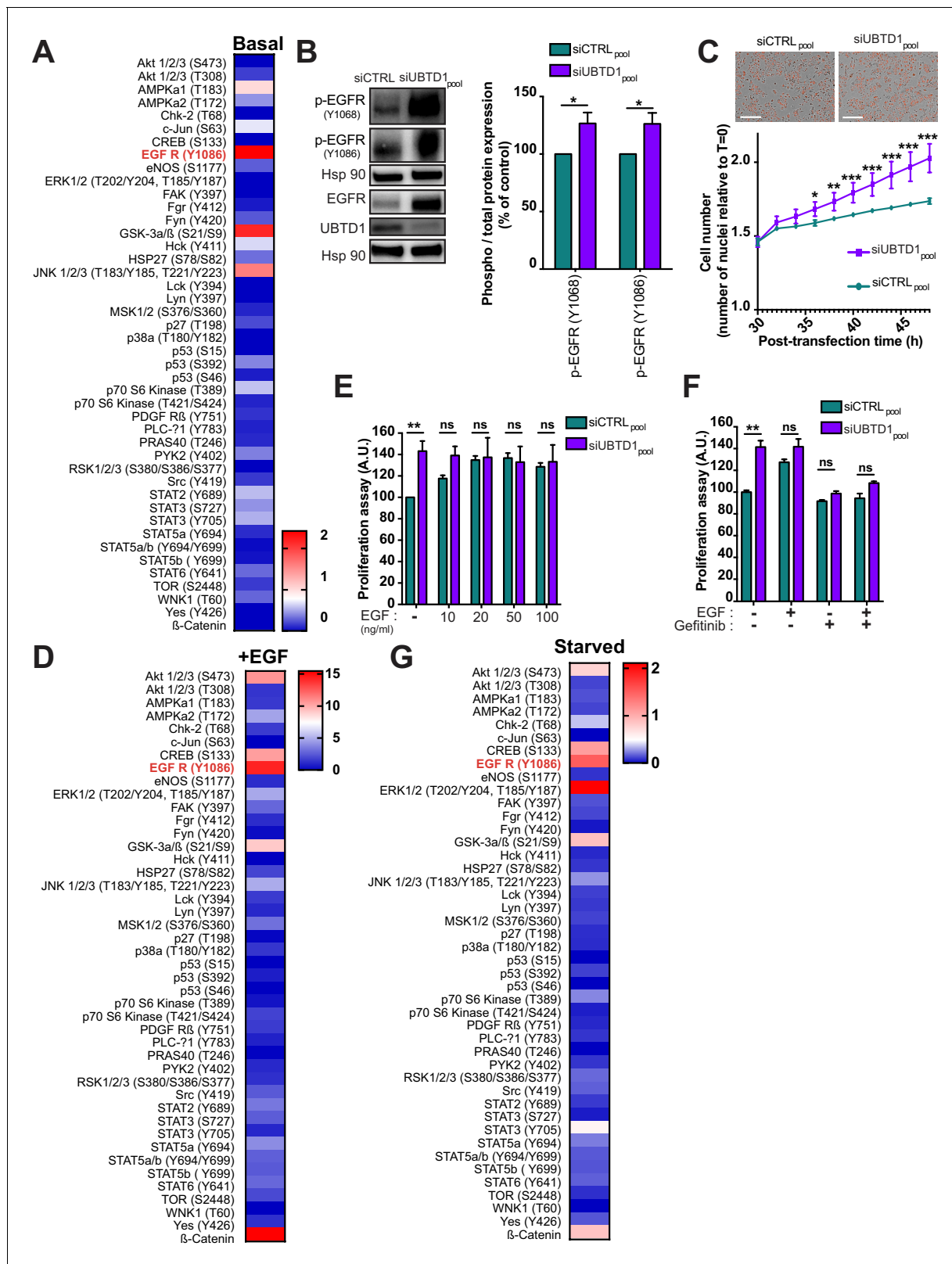


**Figure 1.** UBTD1 depletion exacerbates EGFR signaling to induce cell proliferation. (A–G) DU145 cells were transfected for 48 hr with the indicated siRNA (siCTRL<sub>pool</sub> or siUBTD1<sub>pool</sub>). (A, D, G) Heatmap of protein phosphorylation relative quantification from multiple signaling pathways in complete media (A), under EGF stimulation (D) at 50 ng/ml for 10 min or under serum-starved medium (G). Data quantification is carried out from dot blot (Figure 1—figure supplement 1A, C, H) and normalized to the siCTRL condition. (B) Immunoblot and quantification of p-EGFR (Y1068 or Y1086). Figure 1 continued on next page

Figure 1 continued

p-EGFR levels were quantified by calculating the ratio between p-EGFR and EGFR, both normalized to loading control signal. Immunoblot of UBTD1 shows the level of siRNA depletion. (C) Representative images and cell growth curves measured by videomicroscopy (Incucyte, Essen Bioscience). T = 0 corresponds to transfection time and the time window (30–50 hr) is presented. (E, F) Proliferation assay in the presence of different concentrations of EGF (E) and in the presence of EGF inhibitor (Gefitinib) (F). n ≥ 3 independent experiments. ns = non-significant, \*p<0.05; \*\*p<0.01, \*\*\*p<0.001; (C) Bonferroni's multiple comparison test; (E–F) two-way ANOVA and Bonferroni's multiple comparisons test; data are mean ± s.e.m.

The online version of this article includes the following source data and figure supplement(s) for figure 1:

**Source data 1.** Uncropped western blot for **Figure 1**.

**Source data 2.** Row data for **Figure 1** and for **Figure 1—figure supplement 1**.

**Figure supplement 1.** UBTD1 depletion exacerbates EGFR signaling.

**Figure supplement 1—source data 1.** Uncropped western blot for **Figure 1—figure supplement 1**.

observations led us to repeat the same experiment under EGF stimulation (**Figure 1D**, **Figure 1—figure supplement 1C**). As compared to EGF-treated-control cells, UBTD1 depletion drastically increased (5 to 20-fold) the phosphorylation of PKB/Akt,  $\beta$ -catenin, GSK3  $\alpha/\beta$ , CREB, ERK 1/2, and EGFR. In UBTD1 depleted cells, the phosphorylation status of EGFR is the most dramatically changed (15–20-fold), suggesting a close link between UBTD1 and EGFR. We then carefully evaluated, at steady state, the activation of the signaling pathways downstream of the EGFR (**Figure 1—figure supplement 1D–G**; Avraham and Yarden, 2011; Lemmon and Schlessinger, 2010; Wells, 1999; Grant et al., 2002). As expected, UBTD1 depletion increased STAT3 phosphorylation, nuclear translocation and STAT3 target gene expression: Bcl-2, HIF-2, and MMP-2,–9. Likewise, the phosphorylation of ERK (T202/Y204) and Akt (S473/T308) are increased in UBTD1-depleted cells. EGF promotes proliferation of control cells in a dose-dependent manner but does not further increase proliferation induced by UBTD1 depletion (**Figure 1E**), while the addition of Gefitinib, an EGFR inhibitor, totally abolishes the pro-proliferative effect of UBTD1 knockdown, indicating that this effect is EGFR-dependent but EGF-independent (**Figure 1F**). These converging results indicate that UBTD1 depletion increases EGFR phosphorylation and amplifies signaling cascades downstream of EGFR leading to increased proliferation.

We next wanted to elucidate the underlying mechanism by which UBTD1 controls EGFR phosphorylation. We performed a phospho-kinase array in serum free medium to determine whether some molecules present in the medium could be involved in EGFR activation (**Figure 1G**, **Figure 1—figure supplement 1H**; Sigismund et al., 2018). Surprisingly, although no growth factors were present in the medium, the levels of EGFR phosphorylation and its downstream targets (Akt, ERK, CREB, STATs) were still higher in UBTD1-depleted cells than in control cells. Therefore, we then postulated that UBTD1-depleted cells could secrete factors that elicit EGFR phosphorylation. Besides EGF, several other ligands can bind to and activate EGFR, including TGF- $\alpha$ , heparin-binding EGF-like growth factor (HB-EGF), amphiregulin, betacellulin, epigen, and epiregulin (Grant et al., 2002). Thus, we tested whether the knockdown of UBTD1 increases the mRNA expression and/or the secretion of these EGFR ligands. In UBTD1-depleted cells, neither the expression (**Figure 1—figure supplement 1I,K**) nor the secretion (**Figure 1—figure supplement 1J,L**) of the main EGFR ligands was increased. This data led us to consider that UBTD1 depletion induces ligand-independent EGFR phosphorylation.

Membrane lipid composition surrounding tyrosine kinase receptors can modulate their activation (Coskun et al., 2011; Ferguson et al., 2003; Meillet et al., 2000; Lambert et al., 2006; Todeschini et al., 2008). Thus, we isolated cell membranes and performed a lipidomic analysis. UBTD1 depletion induces major changes in membrane lipid composition and, notably, altered the ceramide subclass (**Figure 2A–B**, **Figure 2—figure supplement 1A**). Next, by MALDI-TOF/TOF mass spectrometry, which detects the non-lipidic moieties and the identity of the ceramide-backboned lipids, we identified, in UBTD1-depleted cells, a drop in GM2 and GM3 d18:1/16:0 gangliosides (**Figure 2C–D**). The GM3 ganglioside inhibits spontaneous EGFR autophosphorylation (Coskun et al., 2011; Meillet et al., 2000; Bremer et al., 1986). To test whether EGFR phosphorylation induced by UBTD1 depletion was caused by a decrease in GM3 content, we added GM3 to the culture medium. In UBTD1-depleted cells, addition of GM3 restores, in a dose-dependent manner, the level of EGFR phosphorylation observed in control cells and completely abolishes cell proliferation induced by UBTD1 knockdown (**Figure 2E,F**), suggesting that the increase in EGFR

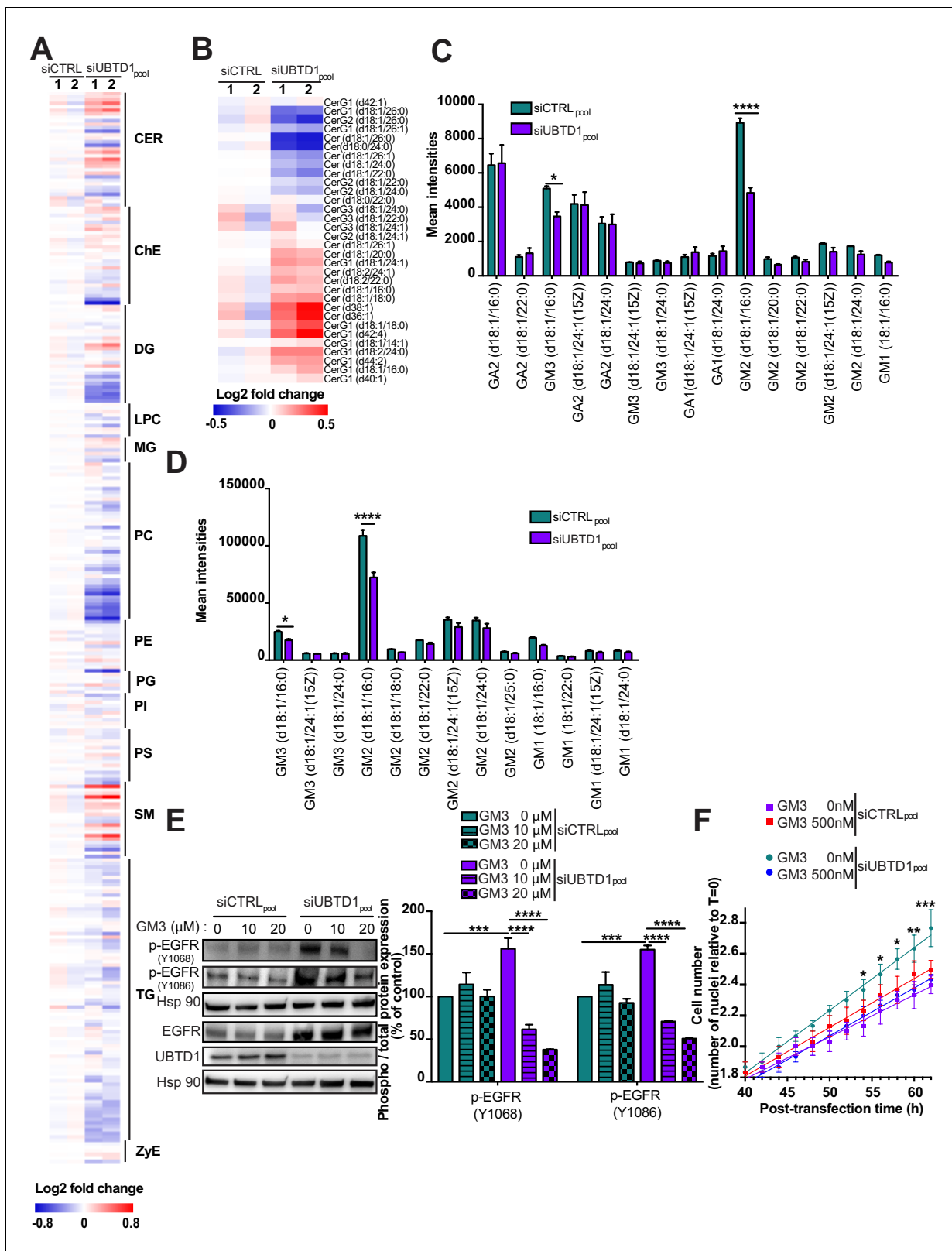


**Figure 2.** UBTD1 depletion induces EGFR self-phosphorylation by modifying membrane lipid composition. (A–F) DU145 cells were transfected for 48 hr with the indicated siRNA (siCTRL<sub>pool</sub> or siUBTD1<sub>pool</sub>). (A,B) Heatmap of all (A) lipids and (B) ceramide levels. The normalized expression of each lipid is shown in a scale range from blue to red. CER: ceramides; ChE: cholesterol ester; DG: diacylglycerols; LPC: lysophosphatidylcholines; MG: monoacylglycerols; PC: phosphatidylcholines; PE: phosphatidylethanolamines; PG: phosphatidylglycerol; PI: phosphatidylinositol; PS: phosphatidylserine; SM: sphingomyelin; ZyE: zwitterionic lipids. *Figure 2 continued on next page*

Figure 2 continued

phosphatidylserines; SM: sphingomyelins; TG: triglycerides; ZyE: zymosterols. (C,D) Mean intensities of positive-ion (C) and negative-ion (D) MS spectra from reflectron MALDI-TOF analyses. (E) Immunoblot and quantification of p-EGFR (Y1068 or Y1086) in the presence of different concentrations of GM3. p-EGFR levels were quantified by calculating the ratio between p-EGFR and EGFR, both normalized to loading control signal. Immunoblot of UBTD1 shows the level of siRNA depletion. (F) Representative cell growth curves measured by videomicroscopy (Incucyte, Essen Bioscience) in the presence of GM3. T = 0 corresponds to transfection time and the time window (40–60 hr) is presented.  $n \geq 3$  independent experiments. \* $p < 0.05$  \*\* $p < 0.01$ , \*\*\* $p < 0.001$ ; \*\*\*\* $p < 0.0001$ ; (C–F) two-way ANOVA and Bonferroni's multiple comparisons test; data are mean  $\pm$  s.e.m.

The online version of this article includes the following source data and figure supplement(s) for figure 2:

**Source data 1.** Uncropped western blot for **Figure 2**.

**Source data 2.** Row data for **Figure 2** and for **Figure 2—figure supplement 1**.

**Figure supplement 1.** Protein clustering and functional interaction analysis of the UBTD1 interactome.

**Figure supplement 1—source data 1.** Uncropped western blot for **Figure 2—figure supplement 1**.

phosphorylation and cell proliferation was due to a drop in GM3. To gain insight on how UBTD1 may alter ganglioside level, we performed an immunoprecipitation experiment using endogenous UBTD1 as a bait. Next, by mass spectrometry we identify UBTD1 partners and associated proteins. Using a mild stringency buffer (NP40) to preserve weak protein interactions, we identified a set of 463 proteins (**Figure 2—figure supplement 1**) distributed in different cell compartments including plasma membrane, endolysosome, and endoplasmic reticulum (ER) (**Figure 2—figure supplement 1**). Then, we generated a UBTD1 interactome and performed an unsupervised cluster analysis to define 14 protein clusters (**Figure 2—figure supplement 1B,C**). By assigning to these clusters their top biological functions, we identify a functional sub-network composed of seven proteins and associated with the ceramide metabolic pathway (**Figure 2—figure supplement 1D**). Within this cluster, we found two proteins directly involved either in the synthesis (ceramide synthase 2, CerS2) or in the degradation (lysosomal ceramidase, ASAH1) of ceramides. Although the protein level of CerS2 was unaffected by UBTD1 invalidation, the level of ASAH1 protein was significantly increased (**Figure 3A**). ASAH1 degradation was found to be controlled by the proteasome in a prostate cancer cell line (*Mizutani et al., 2015*). To test whether UBTD1 regulates the degradation of ASAH1, we blocked protein synthesis with cycloheximide (**Figure 3B**). In the UBTD1-depleted cells, we observed a substantial increase in ASAH1 protein lifetime compared to control cells. Next, we performed a ubiquitination assay (**Figure 3C**). UBTD1 knockdown drastically reduced ASAH1 ubiquitination, supporting that UBTD1 participates in ASAH1 degradation. Finally, to demonstrate that the increase of EGFR phosphorylation induced by UBTD1 depletion occurs through a defect of ASAH1 degradation, we knock down ASAH1 in UBTD1-depleted cells (**Figure 3D, Figure 2—figure supplement 1E**). The depletion of ASAH1 does not modify the phosphorylation of EGFR or its signaling as reflected by STAT3 phosphorylation. However, in UBTD1-depleted cells, the knockdown of ASAH1 severely decreases the phosphorylation of EGFR and STAT3 induced by UBTD1 depletion. Collectively, we here provided compelling evidence showing that UBTD1 depletion induces EGFR phosphorylation by decreasing GM3 level through impairment of ASAH1 ubiquitin-dependent degradation.

### UBTD1 is associated with EGFR and delays its lysosomal degradation

Although the change in the amount of ganglioside GM3 convincingly explains the effect of UBTD1 depletion on EGFR phosphorylation, the GM3 supplementation does not rescue the level of total EGFR, suggesting an additional role of UBTD1 on EGFR turnover. Thus, we evaluate the effect of UBTD1 depletion on EGFR turnover by blocking protein synthesis with cycloheximide (**Figure 4A, Figure 4—figure supplement 1A**). When treated with EGF, the level of EGFR decreases over time. Conversely, in UBTD1-depleted cells, the amount of EGFR remains constant for, at least, 3 hr after the addition of EGF, showing that UBTD1 acts post-transcriptionally on EGFR.

To decipher the underlying mechanism, we took advantage of the cluster functional analysis generated from the UBTD1 interactome (**Figure 2—figure supplement 1B,C**). Interestingly, we identified an extensive protein cluster functionally related to vesicle mediated transport and endocytosis, which includes EGFR (**Figure 2—figure supplement 1F**). This data provides an important clue to understand how UBTD1 can affect EGFR turnover. Indeed, the internalization of EGFR relies on its ubiquitination and we previously demonstrated that UBTD1 interacts with E2/E3 of the UPS (*Bakker et al., 2017; Uhler et al., 2014; Caldieri et al., 2018*). Therefore, we next hypothesized

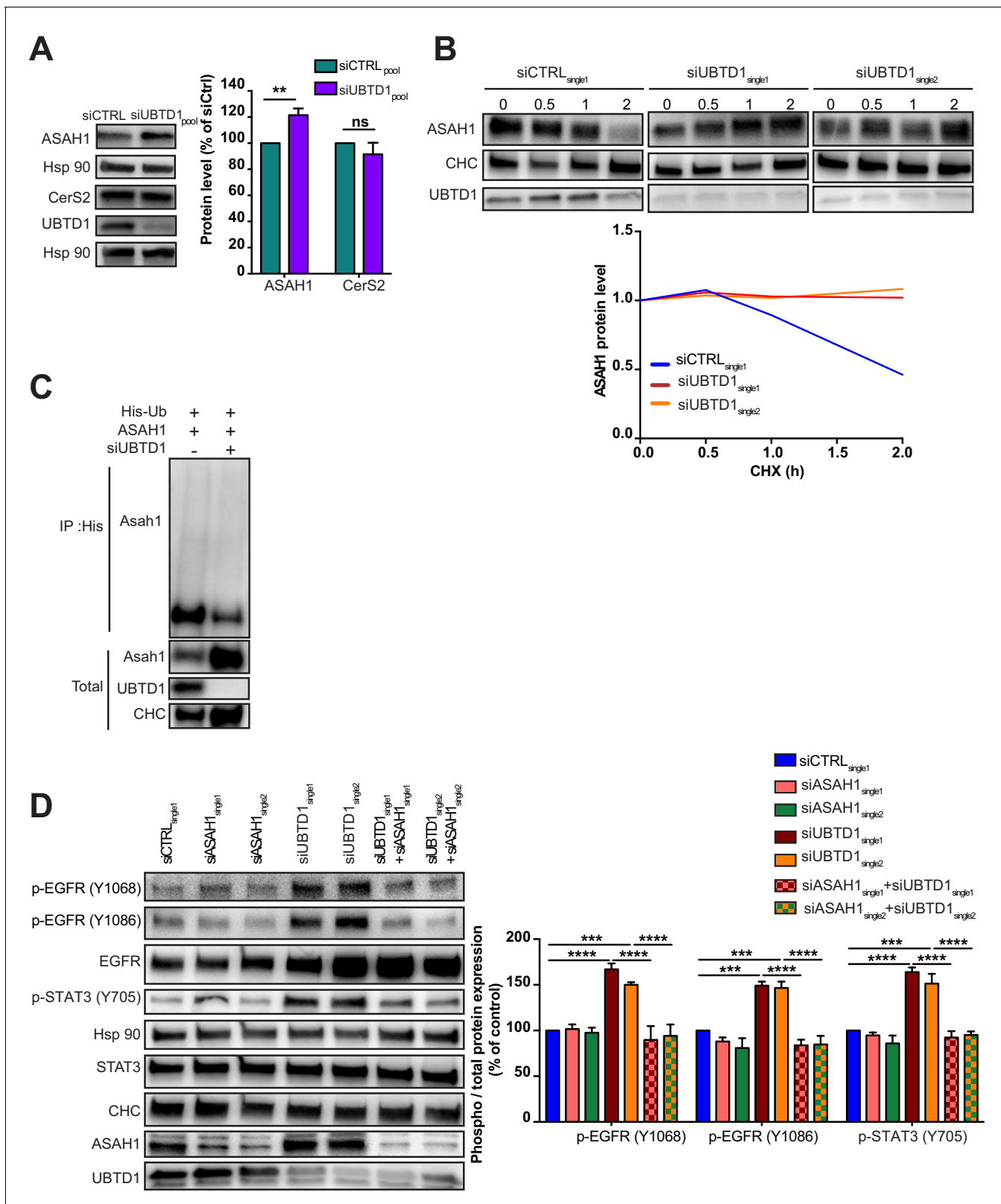


**Figure 3.** UBTD1 controls ASAHI ubiquitination to promote EGFR self-phosphorylation. (A–D) DU145 cells were transfected for 48 hr with the indicated siRNA (siCTRL<sub>pool</sub> or siUBTD1<sub>pool</sub> or siUBTD1<sub>single1</sub> or single2 or siASAHI single1 or single2). (A) Immunoblot and quantification of ceramide synthase 2 (CerS2) and the lysosomal ceramidase (ASAHI). (B) Immunoblots (up) and quantification (down) of ASAHI levels in cells treated with cycloheximide (CHX) at different time points. Immunoblot of UBTD1 shows the level of siRNA depletion. CHC was used as a loading control. (C) Figure 3 continued on next page

Figure 3 continued

Immunoblots show ASAH1 ubiquitylation in HEK cells in different experimental conditions. Cells were transfected, as indicated, with expression vectors for histidine-tagged ubiquitin (His-Ub) together with control siRNA or UBTD1 siRNA. His-Ub crosslinked forms of ASAH1 were purified (IP: His) and the immunoblot of ASAH1 showed ASAH1 ubiquitylation. The immunoblot of ASAH1 (bottom panel) was performed in parallel to verify the amounts of ASAH1 protein engaged in His-Ub purifications. The immunoblot of UBTD1 shows the level of siRNA depletion. (D) Immunoblot and quantification of p-EGFR (Y1068 or Y1086) and p-STAT3, p-ERK and p-AKT levels were quantified by calculating the ratio between phospho-protein and total-protein, both normalized to loading control signal. Immunoblot of UBTD1 shows the level of siRNA depletion.  $n \geq 3$  independent experiments; ns = non-significant, \*\* $p < 0.01$ , \*\*\* $p < 0.001$ ; \*\*\*\* $p < 0.0001$ ; (A,D) two-way ANOVA and Bonferroni's multiple comparisons test; data are mean  $\pm$  s.e.m. The online version of this article includes the following source data for figure 3:

**Source data 1.** Uncropped western blot for **Figure 3**.

**Source data 2.** Row data for **Figure 3**.

that UBTD1 depletion may impair EGFR ubiquitination. To test this possibility, we monitored by proximity ligation assay (PLA) the interaction between ubiquitin and EGFR with or without EGF stimulation (**Figure 4B**). As expected, in control cells, EGF treatment increased EGFR ubiquitination estimated by protein proximity. In UBTD1 knockdown cells, the amount of ubiquitinated EGFR increased similarly to control cells, demonstrating that UBTD1 depletion does not severely impair EGFR ubiquitination. Since the ubiquitination of the EGFR was not modified (**Figure 4—figure supplement 1B**), we then hypothesized that the intracellular trafficking of EGFR may be impaired. We first determined the amount of EGFR at the cell surface. Using an EGF binding assay, we did not detect any difference between control and UBTD1-depleted cells treated or not with EGF (**Figure 4C**). Next, we performed a time-course of EGF/EGFR endocytosis up to their lysosomal degradation in a pulse-chase experiment using a fluorescent-labeled EGF (**Figure 4D**). Cells were stimulated with a fluorescent-labeled EGF, and after washing to remove excess labeled EGF in the medium, the fluorescence detected in the cell corresponds to the EGF endocytosed through its receptor (*Hanafusa et al., 2011; Futter et al., 1996*). The amount of internalized EGF remained constant during the first 30 min in both control and UBTD1 knockdown cells, suggesting that the internalization remains similar. In control cells, the amount of EGF started to decay at 120 min, whereas in UBTD1-depleted cells degradation was delayed by at least one hour (**Figure 4D**). To determine in which compartment the EGF/EGFR complex was delayed, we combined a pulse-chase of labeled EGF with immuno-localization of early endosomes (EEA1) or late endosome/lysosome (LAMP1) markers. The arrival and departure of EGF in EEA1-positive compartments was similar in UBTD1-depleted and control cells (**Figure 4E**), confirming that UBTD1 depletion does not alter endocytosis and the first steps of EGFR intracellular trafficking. However, the extent of co-localization between EGF and LAMP1 strongly increased from the 120 min time point in cells depleted for UBTD1 and remained significantly higher for the last two time-points compared to controls (**Figure 4F**). These results underlined that UBTD1 depletion delays the delivery of EGF/EGFR to the degradative lysosomal compartment or impairs the degradative functions of lysosomes.

### UBTD1 depletion slows down EGFR degradation without affecting the overall endolysosomal kinetics

Endocytosis from the plasma membrane to the lysosomes is controlled at multiple stages which makes it virtually impossible to check one by one (*Bakker et al., 2017*). In our proteomic analysis, we identify many endocytosis-associated proteins as potential UBTD1 interactors (**Figure 2—figure supplement 1F**). Therefore, we further considered endocytosis as a global functional flux to evaluate the effect of UBTD1 depletion on its functioning. We first postulate that the delay in EGFR degradation we found in UBTD1-depleted cells can reflect a failure of the whole endolysosomal degradation route. To tackle this possibility, we analysed the impact of UBTD1 knockdown on the different endolysosomal compartment's morphology. During the pulse-chase of EGF, the size and number of EEA1- and LAMP1-positive vesicles was unchanged between control and UBTD1-depleted cells (**Figure 4—figure supplement 1C–F**). Consistent with this, the number and morphology of the early endosomes, late endosomes, and lysosomes were similar at the ultrastructural level (**Figure 4—figure supplement 1G,H**). Although the endocytic compartments were present and morphologically normal, the flux of cargoes along these compartments could be altered. To test it, we loaded the

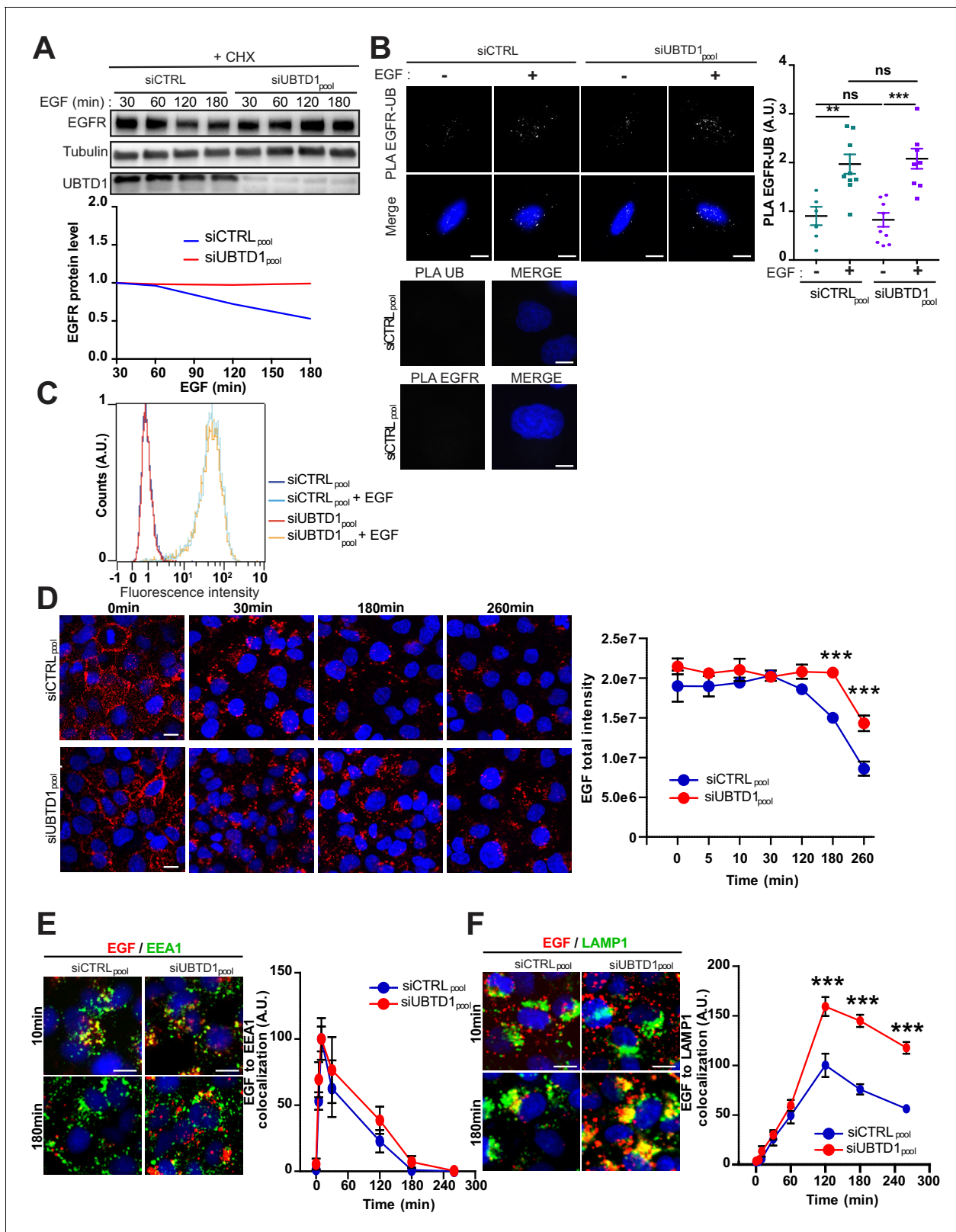


**Figure 4.** UBTD1 depletion slows-down EGFR degradation. (A–F) DU145 cells were transfected for 48 hr with the indicated siRNA (siCTRL<sub>pool</sub> or siUBTD1<sub>pool</sub>). (A) Immunoblots (up) and quantification (down) of EGFR levels in cells treated with cycloheximide (CHX) for 2 hr and in presence of EGF (50 ng/ml) at different time points. Immunoblot of UBTD1 shows the level of siRNA depletion. Tubulin was used as a loading control. (B) Proximal ligation assay monitoring and quantification of EGFR associated with ubiquitin in DU145 treated with EGF (50 ng/ml, 10 min). Nuclei were stained with DAPI. (C) Flow cytometry analysis of EGF (50 ng/ml, 10 min) in siCTRL<sub>pool</sub> and siUBTD1<sub>pool</sub> cells. (D) Immunofluorescence images and quantification of EGF total intensity in siCTRL<sub>pool</sub> and siUBTD1<sub>pool</sub> cells. (E) Immunofluorescence images and quantification of EGF to EEA1 colocalization in siCTRL<sub>pool</sub> and siUBTD1<sub>pool</sub> cells. (F) Immunofluorescence images and quantification of EGF to LAMP1 colocalization in siCTRL<sub>pool</sub> and siUBTD1<sub>pool</sub> cells. Error bars represent standard deviation. Statistical significance is indicated by asterisks: \*\* p < 0.01, \*\*\* p < 0.001, ns = not significant.

Figure 4 continued

DAPI (blue) on the MERGE image. (C) EGF binding to cell surfaces detected by flow cytometry. (D) EGF-alexa647 pulse chase images and quantification. (D) Representative images and quantification of EGF and EEA1 co-localization during EGF-alexa647 pulse chase. (E,F) Representative images and quantification of EGF and LAMP1 co-localization during EGF-Alexa647 pulse chase. Scale bar = 10  $\mu$ m. n  $\geq$  3 independent experiments; ns = non-significant; \*\*p<0.01; \*\*\*p<0.001; (B, D–F) Bonferroni's multiple comparison test; data are mean  $\pm$  s.e.m.

The online version of this article includes the following source data and figure supplement(s) for figure 4:

**Source data 1.** Uncropped western blot for **Figure 4**.

**Source data 2.** Row data for **Figure 4** and for **Figure 4—figure supplements 1–2**.

**Figure supplement 1.** UBTD1 depletion slows down EGFR degradation.

**Figure supplement 1—source data 1.** Uncropped western blot for **Figure 4—figure supplement 1**.

**Figure supplement 1—source data 2.** Uncropped western blot for **Figure 4—figure supplement 2**.

**Figure supplement 2.** UBTD1 depletion slows down RTK degradation.

cells with quantum dots coupled to BSA (DQ-BSA), a fluid phase cargo that fluoresces when reaching the lysosomes (*Marwaha and Sharma, 2017*). Both the number of DQ-BSA positive vesicles and the total DQ-BSA intensity were unchanged between control and UBTD1-depleted cells (**Figure 4—figure supplement 11–K**). Because the lysosomes were accessible to internalized cargoes and were functional (DQ-BSA fluoresces when lysosomes are functional), it is thus likely that the defect in EGFR degradation observed in UBTD1-depleted cells is not due to a general disruption of the endolysosomal degradation pathway, but is rather restricted to a subset of proteins including EGFR. To test whether this effect can be extended to other tyrosine kinase receptors, we performed pulse-chase experiments with a fluorescent-labeled HGF to monitor the temporal kinetics of its degradation in the lysosome. As for the EGF, in UBTD1-depleted cells, we observe a delay in the extinction of the intracellular fluorescent-HGF signal (**Figure 4—figure supplement 2A**). Next, we tested the effect of UBTD1 knockdown on the ubiquitination of c-Met. As with EGFR, we found that UBTD1 depletion does not alter c-Met ubiquitination (**Figure 4—figure supplement 2B,C**). Lastly, we wanted to know if, as for the EGFR, the depletion of UBTD1 affects the total amount of c-Met (**Figure 4—figure supplement 2D**). Indeed, in UBTD1-depleted cells, we observe an increase in the level of c-Met and TGF- $\beta$  R without any change in their mRNA expression (**Figure 4—figure supplement 2E**). Nevertheless, this mechanism seems to be restricted to tyrosine kinase receptors since we do not observe any change in the amount of IL2 or Transferrin receptors (**Figure 4—figure supplement 2D**). Collectively, this set of data shows that UBTD1 depletion alters degradation of some tyrosine kinase receptors including EGFR without interfering with the morphology or the functionality of the endolysosomal machinery.

### UBTD1 controls p62/SQSTM1 ubiquitination and endolysosomal vesicle positioning

Because the defect in EGFR degradation observed in UBTD1-depleted cells is specific to EGFR rather than a general defect in endocytic trafficking, and because we identify EGFR as a potential UBTD1 partner (**Figure 2—figure supplement 1F**), we decided to focus on UBTD1 and EGFR common interactors. Thus, we re-examined our proteomic data, generated a new protein-protein network centered around EGFR, and applied cell compartment filters to refine the analysis (**Figure 5A, B**). Using this approach, we identified a minimal interaction network between EGFR and p62/SQSTM1 (**Figure 5C**). Strikingly, p62/SQSTM1 was shown to be involved in the positioning of EGFR-positive endolysosome at the ER (*Jongsma et al., 2016*), which is critical for lysosomal function (*Pu et al., 2016*). We first confirmed that p62/SQSTM1 co-immunoprecipitated with UBTD1, demonstrating that these two proteins interact or, at least, are in the same protein complex (**Figure 5D**). Because interactions between endolysosome and the ER rule the spatial positioning of the endolysosomal vesicles, we analysed the pattern distribution of the early endosome (EEA1) and the late endosome/lysosome (LAMP1) vesicles in control and UBTD1-depleted cells. UBTD1 depletion does not affect the distribution of EEA1-positive vesicles nor their co-localization with the ER marker calreticulin (**Figure 5E, Figure 5—figure supplement 1A**). In contrast, UBTD1 depletion scatters LAMP1-positive vesicles and decreases the co-localization between LAMP1 and calreticulin (**Figure 5F, Figure 5—figure supplement 1B**). Consistent with this, in cells stably overexpressing GFP-tagged UBTD1, the LAMP1-positive vesicles, but not the EEA1-positive vesicles, were more clustered in the

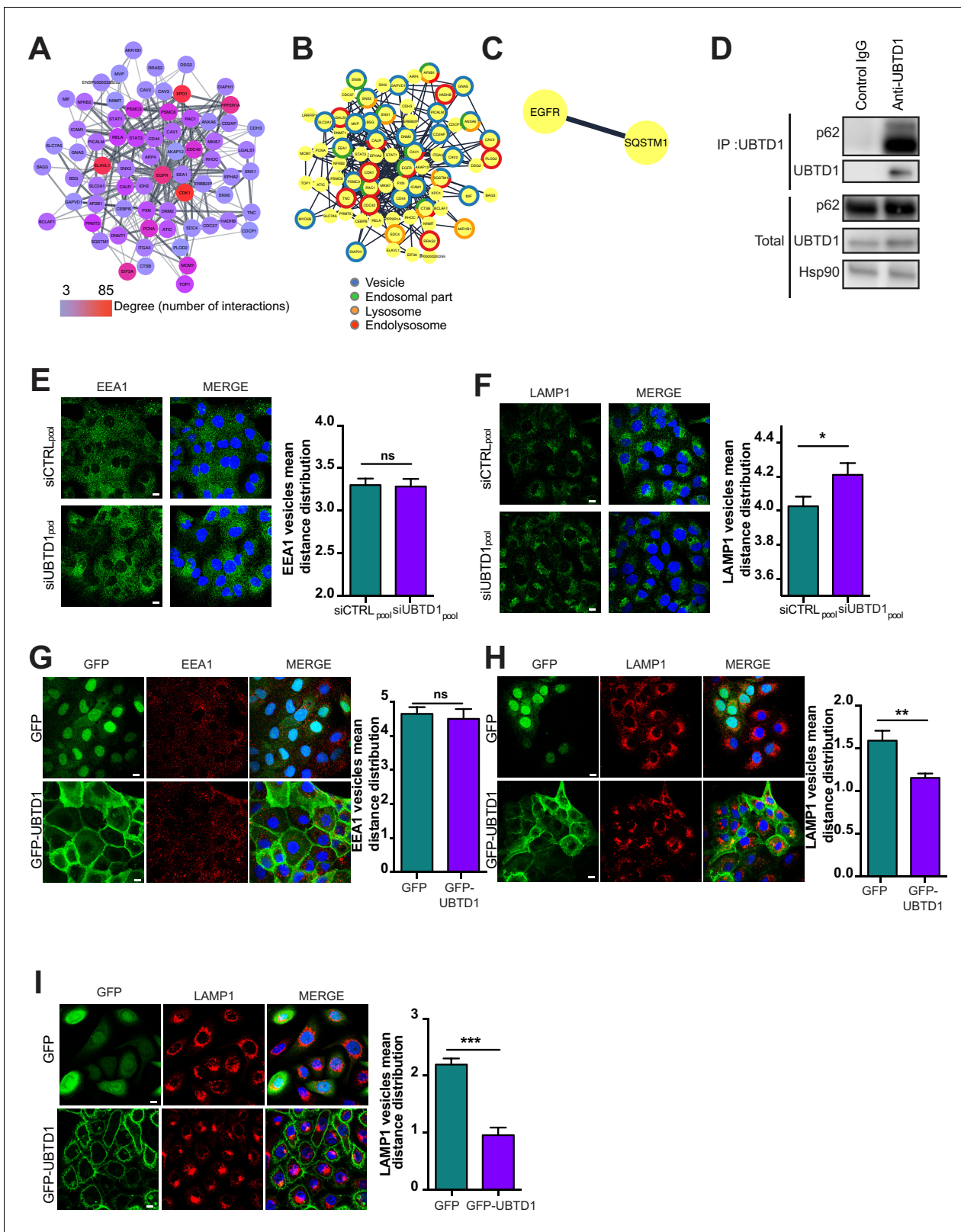


**Figure 5.** UBTD1 interacts with p62/SQSTM1 and controls endolysosomal vesicle positioning. (A) UBTD1 protein interactome in DU145 cell line centered on EGFR (first neighbors). Node color scale (from blue to red) illustrates the degree (number of interactors). The edges (connecting lines) represent the interactions between proteins reported in String database. The thickness of the edge represents the interaction score (string database, combined score). (B) Go Enrichment analysis (<http://geneontology.org>). Most relevant Go component are presented by using a split donut color code *Figure 5 continued on next page*

Figure 5 continued

(C) Minimal protein interaction network derived from graph (A) by applying subcellular localization filters focused on endosome, ER, and lysosome (StringApp, Cytoscape). (D) Co-immunoprecipitation in DU145 cells between endogenous p62 and UBTD1. UBTD1 was used as bait. The IgG isotype was used as a negative control. (E,F) DU145 cells were transfected for 48 hr with the indicated siRNA (siCTRLpool or siUBTD1pool). Representative confocal immunofluorescence images (left) and quantification (right) of EEA1 (E) or LAMP1 (F) vesicle distribution. (G,H) DU145 or (I) RWPE cells were stably transduced with GFP or GFP-UBTD1. Representative confocal immunofluorescence images (left) and quantification (right) of EEA1 (G) or LAMP1 (H,I) vesicles distribution. Scale bar = 10  $\mu$ m.  $n \geq 3$  independent experiments; ns = non-significant; \* $p < 0.05$ , \*\* $p < 0.01$ ; \*\*\* $p < 0.001$ ; (E–I) two-tailed t-test; data are mean  $\pm$  s.e.m.

The online version of this article includes the following source data and figure supplement(s) for figure 5:

**Source data 1.** Uncropped western blot for **Figure 5**.

**Source data 2.** Row data for **Figure 5** and for **Figure 5—figure supplement 1**.

**Figure supplement 1.** UBTD1 controls p62/SQSTM1 ubiquitination and endolysosomal vesicles positioning.

perinuclear region (**Figure 5G,H**). To validate this result further, we reproduced this experiment in a human epithelial cell line (RWPE1). Again, UBTD1 over-expression lead to a massive clustering of LAMP1-positive vesicles in the perinuclear region (**Figure 5I**). Taken together, both over- and down-expression experiments support a role for UBTD1 in controlling the positioning of the late endolysosomal degradative compartment.

Because p62/SQSTM1 is activated by ubiquitination via the ER-resident E3 ligase RNF26 (**Jongsma et al., 2016**), we performed a p62/SQSTM1 ubiquitination assay in UBTD1 depleted cells (**Figure 6A**). As depicted in **Figure 6A**, UBTD1 knockdown drastically reduced p62/SQSTM1 ubiquitination and increases both p62/SQSTM1 level and protein half-life (**Figure 6B,C**, **Figure 6—figure supplement 1A,B**). To confirm that UBTD1 acts on p62/SQSTM1 ubiquitination specifically via RNF26, we examined the interaction between p62/SQSTM1 and RNF26 in control and UBTD1-depleted cells (**Figure 6D**, **Figure 6—figure supplement 1C**). As shown in **Figure 6D**, UBTD1 sharply increases the proximity between P62/SQSTM1 and RNF26 thereby promoting the ubiquitination of P62/SQSTM1 by RNF26. We then verified that RNF26, by modulating cargoes trafficking, contributes to the net sum of EGFR present in the cell. The knockdown of RNF26 increases the amount of EGFR and p62 broadly corroborating the elegant experiments performed by **Jongsma et al., 2016** (**Figure 6E**). Interestingly, in UBTD1-depleted cells, RNF26 depletion does not have an additive effect on EGFR or P62 level, suggesting that UBTD1 and RNF26 act on the same molecular mechanism.

We then wondered whether the role of UBTD1 was related to the function of RNF26 or whether UBTD1 was more broadly associated with the ubiquitination of P62/SQSTM1. For this purpose, we stimulated autophagy in RWPE1 cells and then treated them with bafilomycin to block lysosome acidification (**Figure 6F**, **Figure 6—figure supplement 1D**). Despite an increase in autophagy in the UBTD1-depleted cell, we found that the general autophagic flow is not blocked and the accumulation kinetics of LC3II and P62/SQSTM1 are similar to control cells, confirming that UBTD1 acts on P62/SQSTM1 ubiquitination specifically via RNF26. These data demonstrate that UBTD1 controls late endosome/lysosome positioning and strongly suggest that the interaction of EGFR-positive vesicles with the ER is disrupted by a defect of p62/SQSTM1 ubiquitination by RNF26.

Collectively, we here showed that UBTD1 plays a crucial role in the post-translational regulation of the EGFR (**Figure 6—figure supplement 1E**). On the one hand, by modulating the cellular level of GM3 through ASAH1 ubiquitination, UBTD1 controls the ligand-independent phosphorylation of EGFR. On the other hand, UBTD1, via the ubiquitination of SQSTM1/p62 by RNF26 and positioning of late endosome/lysosome, participates in the lysosomal degradation of EGFR. The coordination of these two ubiquitin-dependent processes contributes to the control of the duration of the EGFR signal and cell proliferation. In conclusion, we have highlighted a yet unsuspected role of UBTD1 on receptor signaling which could be of major importance in certain human pathologies. Moreover, our data lead us to propose that UBTD1 may represent a multistrata coordinator orchestrating EGFR signaling in space and time.

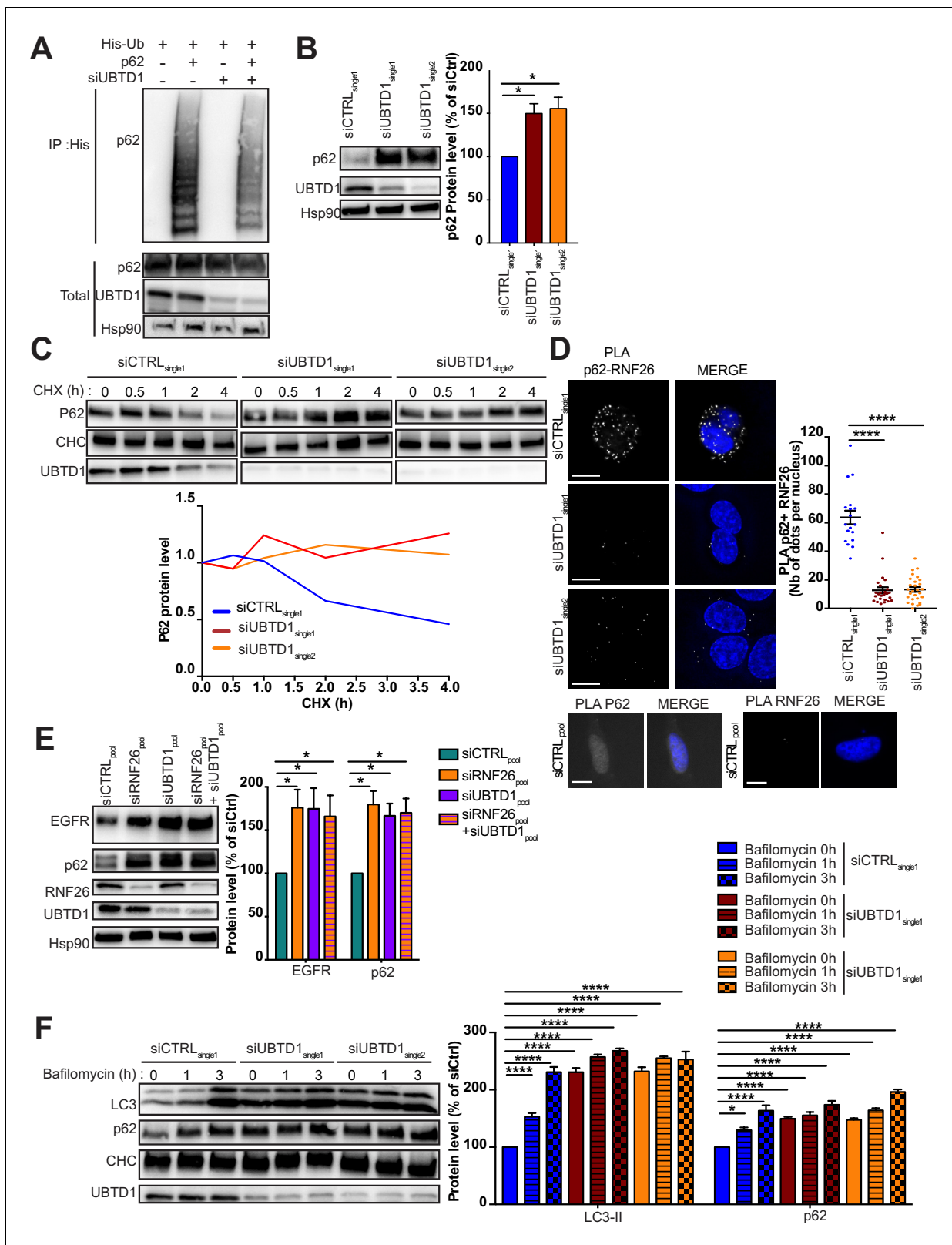


**Figure 6.** UBTD1 controls p62/SQSTM1 ubiquitination. (A–F) DU145 cells were transfected for 48 hr with the indicated siRNA (siCTRL<sub>pool</sub> or siUBTD1<sub>pool</sub> or siUBTD1<sub>single1</sub> or single2 or RNF26: siRNF26<sub>pool</sub>). (A) Immunoblots show p62 ubiquitylation in HEK cells in different experimental conditions. Cells were transfected, as indicated, with expression vectors for histidine-tagged ubiquitin (His-Ub) together with control siRNA or UBTD1 siRNA. His-Ub crosslinked forms of p62 were purified (IP: His) and the immunoblot of p62 showed p62 ubiquitylation. The immunoblot of p62 (bottom Figure 6 continued on next page

Figure 6 continued

panel) was performed in parallel to verify the amounts of p62 protein engaged in His-Ub purifications. The immunoblot of UBTD1 shows the level of siRNA depletion. (B) Immunoblot and quantification of p62. The immunoblot of UBTD1 shows the level of siRNA depletion. (C) Immunoblots (up) and quantification (down) of p62 levels in cells treated with cycloheximide (CHX) at different time points. Immunoblot of UBTD1 shows the level of siRNA depletion. CHC was used as a loading control. (D) Proximal ligation assay monitoring and quantification of p62 associated with RNF26. (E) Immunoblot and quantification of p62 and EGFR. The immunoblots of RNF26 and UBTD1 show the level of siRNA depletion. (F) Immunoblot and quantification of LC3 and p62 in cells treated or not with bafilomycin at different time points. The immunoblot of UBTD1 shows the level of siRNA depletion. Scale bar = 10  $\mu$ m.  $n \geq 3$  independent experiments; \* $p < 0.05$ , \*\*\*\* $p < 0.0001$ ; (B,D) Bonferroni's multiple comparison test; (E–F) two-way ANOVA and Bonferroni's multiple comparisons test; data are mean  $\pm$  s.e.m.

The online version of this article includes the following source data and figure supplement(s) for figure 6:

**Source data 1.** Uncropped western blot for **Figure 6**.

**Source data 2.** Raw data for **Figure 6** and for **Figure 6—figure supplement 1**.

**Figure supplement 1.** UBTD1 controls p62/SQSTM1 ubiquitination.

**Figure supplement 1—source data 1.** Uncropped western blot for **Figure 6—figure supplement 1**.

## Discussion

The ubiquitination process works in a hierarchical framework with few E2 enzymes allowing the ubiquitination of many substrates by association with multiple E3 enzymes (Ye and Rape, 2009). Previously, we found that UBTD1 interacts with a subset of E2s to form stable stoichiometric complexes (Uhler et al., 2014). Based on these biochemical results, it seems very likely that UBTD1, through its interaction with some E2s, can modify the ubiquitination of many proteins. Illustrating this assumption, we previously demonstrated that UBTD1 controls the ubiquitination of yes associated protein (YAP) and similar findings have been reported for MDM2 (mouse double minute two homolog) (Torrino et al., 2019; Zhang et al., 2015). However, these two specific examples presumably reflect only a small portion of the UBTD1 target proteins and, more importantly, of the cellular processes regulated by UBTD1. By using a holistic approach, we here provide evidence that UBTD1 coordinates the EGFR signaling pathway by controlling two distinct ubiquitin-mediated mechanisms. First, UBTD1 limits the self-phosphorylation of EGFR by modulating the ceramide (GM3) balance through the ubiquitin-dependent degradation of the acid ceramidase ASAH1. Additionally, UBTD1 controls the lysosomal degradation of EGFR by adjusting the spatial patterning of late endosome/lysosomes through RNF26-dependent ubiquitination of p62/SQSTM1. Together, the deregulation of these two molecular checkpoints causes EGFR self-phosphorylation and increases intracellular EGFR lifetime which leads to the persistence of its signaling and induces cell proliferation.

In UBTD1-depleted cells, the membrane lipid composition was altered by a decrease in ASAH1 ubiquitination. ASAH1 is synthesized in the ER as an inactive proenzyme and must be activated through autocleavage to become active in the lysosome (Brannigan et al., 1995; Gebai et al., 2018). This process is fundamental since ASAH1 is prominently involved in a genetic lysosomal storage disorder in human (Farber's disease) (Schuchman, 2016). However, the regulatory mechanism remains unclear. Interestingly, it has been reported that ASAH1 is regulated by the proteasome and that the deubiquitinase USP2 modulates protein half-life, clearly suggesting that, ASAH1 is controlled by a ubiquitination-mediated process before reaching the lysosome (Mizutani et al., 2015). Our findings reinforce this proposal by showing that UBTD1 acts on the ubiquitination of ASAH1. Furthermore, ASAH1 has been described by others as potentially interacting with the E3 ligase HERC2, which we also identified in our proteomic screen as a putative UBTD1 partner (Galligan et al., 2015). These data lead us to speculate that the lysosomal content of ASAH1 could be regulated by a ubiquitination process mediated by UBTD1 and HERC2. This hypothesis, although interesting, is still speculative and needs to be further explored in the future. Interestingly, Simmons' group nicely demonstrated that the ceramide GM3 prevents EGFR self-phosphorylation (Coskun et al., 2011). In accordance with this work, we observed that UBTD1 depletion, by decreasing cellular GM3 content, increases EGFR self-phosphorylation. In a broader view, we propose that UBTD1 regulates EGFR self-phosphorylation by controlling GM3 content through ASAH1 ubiquitination.

In a genome-wide screen analysis performed to identify endocytic trafficking master regulators, it has been reported that UBTD1 knockdown increases total EGF vesicle intensity, without major changes in vesicle number, elongation, area, or distance to the nucleus (Collinet et al., 2010).

Consistent with this finding, we here demonstrate that UBTD1 depletion drastically increases intracellular fluorescent-labeled EGF lifetime without altering the morphology or the distribution of the early endocytic vesicles. To discriminate at which stage EGF trafficking is corrupted, we analysed EGF kinetics throughout its endolysosomal trafficking. These functional experiments clearly emphasize that UBTD1 depletion only affects the late endosome/lysosome step of EGF transport while totally preserving the upstream EGF flux. As elegantly demonstrated by *Jongsma et al., 2016*, SQSTM1/P62 is necessary to control EGFR-positive vesicle spatial positioning. Briefly, ubiquitinated p62/SQSTM1 captures specific endolysosomal vesicle adaptors to permit transient ER/endolysosomal contacts which are required for trafficking of some cargoes including EGFR (*Jongsma et al., 2016*). This sophisticated process is orchestrated by the ubiquitination of p62/SQSTM1 by the ER-resident-E3 ligase, RNF26, and requires spatial and temporal coordination. Hence, we propose that UBTD1 impairs EGFR-positive vesicle positioning through a p62/SQSTM1-RNF26 mechanism close to the one described by *Jongsma et al., 2016*. Importantly, this process is presumably not restricted to EGFR since we observe, as anticipated by *Jongsma et al., 2016*, similar effects of UBTD1 depletion on other signaling receptors that use the same intracellular routing as EGFR such as c-Met or TGF- $\beta$  R (*Park and Richardson, 2020; Chen, 2009*). Although UBTD1 depletion affects p62/SQSTM1 ubiquitination by RNF26, it has a relatively minor impact on P62/SQSTM1-dependent autophagy demonstrating a high specificity toward some E3s rather than for the substrate in the ubiquitination process. We also noticed this E3-specificity of UBTD1 for the ubiquitination EGFR. Once the canonical clathrin-dependent EGFR endocytosis is saturated by an excess of EGF, EGFR is rapidly routed toward lysosomal degradation through clathrin-independent endocytosis (*Bakker et al., 2017; Todeschini et al., 2008*). This critical switch is controlled by the ubiquitination of EGFR by the E3 ligase c-Cbl and the E2 enzyme UBE2D3 (*Pu et al., 2016; Brannigan et al., 1995*). The depletion of UBTD1 had no effect either on the ubiquitination of EGFR or, indeed, on overall EGFR internalization suggesting that UBTD1 is not mandatory for UBE2D3-c-Cbl-mediated EGFR ubiquitination. Although UBTD1 is a molecular partner of some E2s (*Uhler et al., 2014*), it is likely that its function is specific to some E3s or context-dependent.

From the few works that have been published on UBTD1 and despite still incomplete knowledge about its cellular functions, it seems that a global picture is emerging. Although still largely speculative, we propose that UBTD1 is a rather stable partner of some E2s and its function could be to foster, in certain circumstances, the association between E2 and E3 within the ubiquitination complex. This scaffolding function, controlled by a still unknown mechanism, allows to finely control the ubiquitination of some substrates like P62/SQSTM1 or ASAH1.

EGFR plays a major role in cell proliferation and is frequently overexpressed or hyperactivated in many epithelial cancer cells (*Yarden and Pines, 2012*). Considering the dual role of UBTD1 on EGFR autophosphorylation and lysosomal degradation, it is not surprising that UBTD1 depletion exacerbates EGFR signaling and induces an EGFR-dependent cellular proliferation. This last finding underlines the importance of UBTD1 in EGFR-driven cell proliferation and may be further investigated in an EGFR hyper-activated state such as cancer. Collectively, we here demonstrated that UBTD1 acts as a coordinator of EGFR signaling, illustrating that the regulation of E2/E3 enzymes of the ubiquitination system by scaffold proteins may represent a critical but still underestimated control layer for coordination of some signaling pathways.

## Materials and methods

### Reagents and antibodies

EGF (50 ng/ml, AF-100–15) or 10 ng/ml (cell proliferation assay) and HGF (40 ng/ml, 100–39H) were purchased from PeproTech. Anti-UBTD1 (HPA034825, RRID:[AB\\_10602254](https://doi.org/10.1002/ab.10602254)), sodium chloride, DAPI, Gefitinib (0,5  $\mu$ M) (SML1657), cycloheximide (75  $\mu$ M), bafilomycinA1 (100 nM), and 2,5-dihydroxybenzoic acid (DHB) were purchased from Sigma-Aldrich. Anti-HSP90 (sc-13119, RRID:[AB\\_675659](https://doi.org/10.1002/ab.10675659)), anti-Tubulin (sc-398937), anti-RhoGDI (sc-360, RRID:[AB\\_2227516](https://doi.org/10.1002/ab.102227516)), and anti-Ubiquitin (sc-8017, RRID:[AB\\_2762364](https://doi.org/10.1002/ab.102762364)) were purchased from Santa Cruz Biotechnology. Anti-p-STAT3 (Tyr705) (clone D3A7, 9145, RRID:[AB\\_2491009](https://doi.org/10.1002/ab.102491009)), anti-STAT3 (clone 124H6, 9139, RRID:[AB\\_331757](https://doi.org/10.1002/ab.10331757)), anti-ERK (#9102, RRID:[AB\\_330744](https://doi.org/10.1002/ab.10330744)), anti-p-ERK (Thr202/Tyr204, #4370, RRID:[AB\\_2315112](https://doi.org/10.1002/ab.102315112)), anti-Akt (4691, RRID:[AB\\_915783](https://doi.org/10.1002/ab.102915783)), anti-p-Akt (Ser473) (#4060, RRID:[AB\\_2315049](https://doi.org/10.1002/ab.102315049)), anti-p-Akt (Thr308) (#13038), anti-c-Met

(#4560), anti-TGF- $\beta$  Receptor II (#79424, RRID:AB\_2799933), anti-p-EGFR Tyr1068 (#3777, RRID:AB\_2096270), anti-p-EGFR Tyr1086 (2234, RRID:AB\_331701), anti-LC3B (2775, RRID:AB\_915950), and anti-EGFR (2232, RRID:AB\_331707) were purchased from Cell Signaling Technology. Anti-EEA1 (610457, RRID:AB\_397830), anti-Clathrin Heavy Chain (610499) and anti-CD107a/LAMP1 (555798, RRID:AB\_396132) were purchased from BD Biosciences. Anti-SQSTM1/P62 (GTX100685, RRID:AB\_2038029) was purchased from Genetex, anti-ASAH1 (NBP1-89296, RRID:AB\_11025126) and anti-CerS2/LASS2 (NBP1-84537, RRID:AB\_11033791) from Novus Biologicals. Anti-calreticulin-ER Marker (ab2907, RRID:AB\_303402) and anti-RNF26 (ab236791) were purchased from Abcam. Anti-IL-2R (MAB623, RRID:AB\_2125599) was purchased from R and D Systems. DQ Red BSA (D12051) and anti-Transferrin Receptor (# 13–6800, RRID:AB\_2533029) were purchased from Invitrogen. Ganglioside GM3 (860058) was purchased from Avanti Polar Lipids. HRP-conjugated donkey anti-mouse IgG (715-035-150) and HRP-conjugated anti-mouse IgG (711-035-152) were purchased from Jackson ImmunoResearch Laboratories. Epidermal Growth Factor, biotinylated, complexed to Alexa Fluor 647 Streptavidin (Alexa Fluor 647 EGF complex) was purchased from Molecular Probes (Invitrogen, E35351). HGF was complexed to Alexa Fluor 647 (Labeling Kit) according to provider's protocol (A30009, Molecular Probes, Invitrogen).

## Cell culture

DU145 cells were purchased from the American Type Culture Collection (ATCC, RRID:CVCL\_0105). All cells used in this study were within 20 passages after thawing. DU145 cells were cultured (37°C, 5% CO<sub>2</sub>) in Dulbecco's modified Eagle's medium (DMEM, Gibco) supplemented with 10% fetal bovine serum (Gibco) and penicillin/streptomycin (1%, Gibco). The RWPE-1 cell line was obtained from ATCC (CRL-11609; RRID:CVCL\_3791). RWPE-1 cells were maintained in KSFM (Life Technologies) supplemented with 5 ng/mL epidermal growth factor (Life Technologies), 50 mg/mL bovine pituitary extract (Life Technologies), and 1% penicillin-streptomycin (Life Technologies). The cells were routinely cultured in a humidified atmosphere with 5% CO<sub>2</sub> at 37°C. All cell lines were found to be *Mycoplasma* free.

## siRNA and plasmid transfection

Transfections were performed with Lipofectamine RNAiMAX according to the manufacturer's instructions (Invitrogen) using siRNA SMARTpool or individual ON-TARGETplus (Horizon Discovery Ltd) Human UBTD1 (L-018385-00-0005), Human ASAH1 (L-005228-03-0005, J-005228-05-0002, J-005228-06-0002), Human RNF26 (L-007060-00-0005), or ON-TARGETplus Non-Targeting Control (D-001830–10, D-001810–01).

Sequences of single siRNA UBTD1Human have been synthesized by Eurogenetec using the following sequences: UBTD1single1 sense CAAGCGAGCAGGACGCAAU/antisense GGAGCAAACGGGAUGAGUU; UBTD1single2 sense GAAGCAGGUUCGAGCCAC/antisense CCACAAGGGCCAACCAGGA. Lipofectamine 2000 was used for plasmid transfection according to the manufacturer's instructions (11668, Invitrogen). Histidine-tagged ubiquitin (pCl-His-hUbi, #31815), EGFR-GFP (#32751), c-MET-GFP (#37560) and Ha-tagged p62 (HA-p62, #28027) plasmids were purchased from Addgene. ASAH1 human plasmid (RC212434) was purchased from Origene technologies. DNA constructs corresponding to the mature form of human UBTD1 were subcloned from pEGFP-N1 (Novagen) to a retroviral vector compatible plasmid (PPRIG) (Albagli-Curiel *et al.*, 2007). Cells were transduced with an MLV-based retroviral vector and selected by puromycin.

## Human phospho-kinase antibody array

Relative phosphorylation levels of 43 kinases and two related proteins were assessed using the Proteome Profiler Human Phospho-Kinase Array Kit (R and D Systems), according to the manufacturer's instructions. In brief, cell lysates were incubated overnight with nitrocellulose membranes of the Human Phospho-Kinase Array (R and D Systems). Membranes were then washed, incubated with biotinylated detection antibody cocktails, and then incubated with streptavidin-horseradish peroxidase and visualized using ECL (Millipore) and analysed on Pxi (Syngene). The signal of each capture spot was measured using the 'Protein Array Analyzer for ImageJ' and normalized to internal reference controls. Heatmaps were generated using Graphpad Prism software.

## Cell proliferation assay

After 48 hr of siRNA transfection, cells were seeded at  $5 \times 10^4$  cells/well in a 96-well plate and cultured for 24 hr prior to experiment. All conditions were performed in triplicate. Cells transfected with control siRNA served as control. Proliferation was measured using the Cell Proliferation ELISA BrdU kit (Roche Diagnostics GmbH), according to the manufacturer's instructions. Briefly, cells were labeled with BrdU at a final concentration of 10  $\mu$ M/well, for 12 hr at 37°C. The cells were then denatured with FixDenat solution and incubated for 120 min with 1:100 diluted mouse anti-BrdU conjugated to peroxidase. After two washings (PBS 1 $\times$ ), the substrate solution was added for 25 min and, after this period, the reaction was stopped with 1 M H<sub>2</sub>SO<sub>4</sub> solution. Absorbance was measured within 5 min at 450 nm with a reference wavelength at 690 nm using an ELISA plate reader.

## Kinetic growth assay

Cells were transduced with NuLight Red Lentivirus and selected with puromycin (1  $\mu$ g/ml) for 2 weeks (Essen Biosciences). After siRNA transfection, cells were allowed to grow (12-well plates) for 48 hr under a live cell imaging system (Essen Biosciences). The experiments were carried out three times independently. Nine images per well (six wells per condition) were taken every 2 hr for 48 hr and analysed with the Incucyte analysis software. The proliferation rate was calculated with the slope between 0 and 48 hr.

## Immunofluorescence and pulse-chase

For immunofluorescence analysis, the cells were fixed with PBS/PFA 4% for 10 min and permeabilized with PBS/Triton 100  $\times$  0.2% for 5 min. After blocking with PBS/BSA 0.2% for 1 hr, the cells were then incubated with primary antibodies (1/100) at room temperature for 1 hr. Secondary antibodies coupled with Alexa-594 and/or Alexa-488 (A-11012, A-11001, Life technologies) were used at 1/500 for 1 hr. Nuclei were counterstained with DAPI (Sigma-Aldrich). For the pulse-chase experiments, the cells were incubated for 10 min with 100 ng/ml of EGF-alexa647 or 40 ng/ml of HGF-Alexa647 with at 4°C and chased with fresh media for 0, 5, 10, 30, 60, 120, 180, and 240 min at 37°C (Collinet *et al.*, 2010). Then, the cells were washed, fixed, and immunolabeled as described above. Images were obtained in a randomized fashion using an LSM510 confocal microscope (Zeiss) and a Nikon A1R confocal. At least 20 images per condition were analysed using the unbiased multiparametrics MotionTracking software, as previously described (generous gift from Dr Y. Kalaidzidis, Marino Zerial's lab) (Gilleron *et al.*, 2013; Zeigerer *et al.*, 2012).

## Electron microscopy

For ultrastructural analysis, cells were fixed in 1.6% glutaraldehyde in 0.1 M phosphate buffer, rinsed in 0.1 M cacodylate buffer, post-fixed for 1 hr in 1% osmium tetroxide and 1% potassium ferrocyanide in 0.1 M cacodylate buffer to enhance the staining of membranes. Cells were rinsed in distilled water, dehydrated in alcohols and lastly embedded in epoxy resin. Contrasted ultrathin sections (70 nm) were analysed under a JEOL 1400 transmission electron microscope mounted with a Morada Olympus CCD camera. For quantification, at least 200 structures were counted from at least 20 images per condition acquired randomly.

## Proximity Ligation Assay

The proximity ligation assay (PLA) kit was purchased from Sigma-Aldrich, and the assay was performed according to the manufacturer's protocol. Cells were fixed in 4% PFA for 10 min at room temperature, quenched in 50 mM NH<sub>4</sub>Cl for 10 min, permeabilised with 0.2% Triton X-100 (w/v) for 10 min and blocked in PBS/BSA. Cells were incubated with primary antibodies for 45 min in PBS/BSA. Coverslips were mounted in Fluoromount with DAPI to stain nuclei. PLA signals were visible as fluorescent dots and imaged using an inverted epifluorescence Leica DM 6000B microscope equipped with an HCX PL Apo 63x NA 1.32 oil immersion objective and an EMCCD camera (Photometrics CoolSNAP HQ). Fluorescent dots were quantified using ImageJ. Cells and nuclei were delineated to create masks. After a Max Entropy threshold, the PLA dots were quantified in both masks with the ImageJ Analyze Particles plugin. All counts were divided by the number of cells.

## Flow cytometric analysis

After 48 hr of siRNA transfection, expression of cell surface EGFR was monitored by flow cytometry on living cells without permeabilization. After washing in ice-cold PBS, cells were immunolabeled on ice for 10 min with Alexa Fluor 647 EGF complex (Molecular Probes, Invitrogen, E35351) in PBS containing 2% BSA. After two further washes in ice-cold PBS containing 2% BSA and one wash in ice-cold PBS, cells were suspended in PBS and analysed by flow cytometry on a FACS (MACSQuant VYB, Miltenyi Biotec); data were analysed using the Cell Quest software. Measurements were compared to the isotopic control (APC-conjugated anti-mouse IgG1, Biolegend clone MOPC-21 #BLE400122, 1/100, Ozyme) to determine background and positivity thresholds. Each experiment was repeated at least three times.

## Western blot assays

Cells were lysed in RIPA buffer (Pierce) or directly in Laemmli's buffer. After denaturation, protein lysates were resolved by SDS-PAGE and transferred onto PVDF membranes (Millipore). Membranes were blocked with 2% BSA in TBS tween20 0.1% and incubated in the presence of the primary and then secondary antibodies. After washing, immunoreactive bands were visualized with ECL (Millipore) and analysed on Pxi (Syngene).

## Ubiquitylation assays

HEK293 cells ( $5 \times 10^6$ ) were transfected with 10  $\mu$ g of His-tagged ubiquitin WT expression vectors together with p62, ASAH1, EGFR or MET and siRNA targeting UBTD1. Ubiquitylated proteins were recovered by His-tag affinity purification on cobalt resin in urea denaturing conditions, as described (Torrino *et al.*, 2011).

## Immunoprecipitation

For endogenous immunoprecipitation, cells were harvested and lysed in NP-40 buffer containing a protease inhibitor cocktail (Thermo Fisher). The lysates (13,200 rpm, 10 min, 4°C) were incubated for 2 hr with the indicated antibody (IP) at 4°C. Then, 10  $\mu$ l Dynabeads protein A (Invitrogen) was added to each aliquot for 45 min at 4°C. Beads were washed 3–5 times with NP-40 and eluted by boiling in 2x sample buffer at 95°C for 10 min. The eluted fractions were analysed by western blot.

## RNA isolation and RT-PCR from cell lines

Total RNA was extracted by TRIzol reagent according to the manufacturer's instructions (Invitrogen). RNA quantity and quality were determined using NanoDrop One Spectrophotometer (Thermo Scientific). One microgram of total RNA was reverse transcribed into cDNA (A3500, Promega). Real-time quantitative PCR was performed using Fast SYBR Green master mix (Applied Biosystems) on a StepOnePlus System (Applied Biosystems). The gene-specific primer sets were used at a final concentration of 1  $\mu$ M in a 10  $\mu$ l final volume. RPLP0 mRNA levels were used as an endogenous control to normalise relative expression values of each target gene. The relative expression was calculated by the comparative Ct method. All real-time RT-PCR assays were performed in triplicate with three independent experiments. Primers are provided below. Primers were published in <http://pga.mgh.harvard.edu/primerbank/>. EGFR (Forward: AGGCACGAGTAACAAGCTCAC; Reverse: ATGAGGACA TAACCAGCCACC); BCL2 (Forward: CGCCCTGTGGATGACT; Reverse: GGGCCGTACAGTTCCA); MMP2 (Forward: TGAGCTATGGACCTTGGGAGAA; Reverse: CCATCGGCGTTCCCATAC); MMP9 (Forward: GAACCAATCTCACCGACAGG; Reverse: GCCACCCGAGTGTAACCATA); HIF2 (Forward: TTGCTCTGAAAACGAGTCCGA; Reverse: GGTACCACGGCAATGAAAC); UBTD1 (Forward: GCGGTGACAGGCAGTAGAT; Reverse: CGGAGCAAACGGGATGAGTT). For mRNA expression of Epigen (Hs02385424), Betacellulin (Hs01101201), Epiregulin (Hs00914313), TGF- $\alpha$  (Hs00608187), Amphiregulin (Hs00950669), HB-EGF (Hs00181813), MET (Hs01565584), IL2R (Hs00174759), Transferin Receptor (Hs00951083), TGFR-II (Hs00234253), and UBTD1 (Hs00227913), Taqman probes have been used, and experiments were performed as recommended by the provider (Applied Biosystems).

## Enzyme-linked immunosorbent assay

The levels of Epigen (CSB-EL007719HU, Clinisciences), Betacellulin (ab189575, Abcam), Amphiregulin (ab222504, Abcam), Epiregulin (BGK14944, Peprotech), TGF- $\alpha$  (BGK 01135, Peprotech), and HB-EGF (BGK 99075, Peprotech) were measured according to the provider protocol. Values are normalized to the total amount of protein.

## In-gel digestion

Protein spots were manually excised from the gel and destained by adding 100  $\mu$ L of H<sub>2</sub>O/ACN (1/1). After 10 min incubation with vortexing the liquid was discarded. This procedure was repeated two times. Gel pieces were then rinsed (15 min) with acetonitrile and dried under vacuum. Each excised spot was reduced with 50  $\mu$ L of 10 mM dithiothreitol and incubated for 30 min at 56°C. Alkylation was performed with 15  $\mu$ L of 55 mM iodoacetamide for 15 min at room temperature in the dark. Gel pieces were washed by adding successively (i) 100  $\mu$ L of H<sub>2</sub>O/ACN (1/1), repeated two times and (ii) 100  $\mu$ L of acetonitrile. Next, gel pieces were reswelled in 60  $\mu$ L of 50 mM NH<sub>4</sub>HCO<sub>3</sub> buffer containing 10 ng/ $\mu$ L of trypsin (modified porcine trypsin sequence grade, Promega) incubated for one hour at 4°C. Then the solution was removed and replaced by 60  $\mu$ L of 50 mM NH<sub>4</sub>HCO<sub>3</sub> buffer (without trypsin) and incubated overnight at 37°C. Tryptic peptides were isolated by extraction with (i) 60  $\mu$ L of 1% AF (acid formic) in water (10 min at RT) and (ii) 60  $\mu$ L acetonitrile (10 min at RT). Peptide extracts were pooled, concentrated under vacuum and solubilised in 15  $\mu$ L of aqueous 0.1% formic acid and then injected.

## NanoHPLC-Q-exactive plus analysis

Peptide separation was carried out using a nanoHPLC (ultimate 3000, Thermo Fisher Scientific). 5  $\mu$ L of peptides solution was injected and concentrated on a  $\mu$ -Precolumn Cartridge Acclaim PepMap 100 C<sub>18</sub> (i.d. 5 mm, 5  $\mu$ m, 100 Å, Thermo Fisher Scientific) at a flow rate of 10  $\mu$ L/min and using solvent containing H<sub>2</sub>O/ACN/FA 98%/2%/0.1%. Next peptide separation was performed on a 75  $\mu$ m i.d. x 500 mm (3  $\mu$ m, 100 Å) Acclaim PepMap 100 C<sub>18</sub> column (Thermo Fisher Scientific) at a flow rate of 200 nL/min. Solvent systems were: (A) 100% water, 0.1%FA, (B) 100% acetonitrile, 0.08% FA. The following gradient was used t = 0 min 4% B; t = 3 min 4%B; t = 170 min, 35% B; t = 172 min, 90% B; t = 180 min 90% B (temperature was regulated at 35°C). The nanoHPLC was coupled via a nanoelectrospray ionization source to the Hybrid Quadrupole-Orbitrap High Resolution Mass Spectrometer (Thermo Fisher Scientific). MS spectra were acquired at a resolution of 70 000 (200 m/z) in a mass range of 150–1800 m/z with an AGC target 5e5 value of and a maximum injection time of 50 ms. The 10 most intense precursor ions were selected and isolated with a window of 2 m/z and fragmented by HCD (Higher energy C-Trap Dissociation) with a normalised collision energy (NCE) of 27. MS/MS spectra were acquired in the ion trap with an AGC target 2e5 value, the resolution was set at 17,500 at 200 m/z combined with an injection time of 100 ms. Data were reprocessed using Proteome Discoverer 2.2 equipped with Sequest HT. Files were searched against the Swissprot *Homo sapiens* FASTA database update on September 2018. A mass accuracy of  $\pm$  10 ppm was used for precursor ions and 0.02 Da for product ions. Enzyme specificity was fixed to trypsin with two missed cleavages allowed. Because of previous chemical modification, carbamidomethylation of cysteines was set as a fixed modification and only oxidation of methionine was considered as dynamic modification. Reverses decoy databases were included for all searches to estimate false discovery rates and filtered using the Percolator algorithm with a 1% FDR.

A Protein-Protein Interactions Network (PPI-Net) was created using stringApp in Cytoscape (Szklarczyk *et al.*, 2011), and proteins have been clustered using the Markov Cluster Algorithm (clusterMaker2, Cytoscape).

## Lipid extraction and analysis

Extraction was performed using 1.5 mL solvent-resistant plastic Eppendorf tubes and 5 mL glass hemolyse tubes to avoid contamination. Methanol, chloroform and water were each cooled down on wet ice before the lipid extraction. Lipids were extracted according to a modified Bligh and Dyer protocol. The cell pellet was collected in a 1.5 mL Eppendorf tube and 200  $\mu$ L of water was added. After vortexing (30 s), the sample was transferred to a glass tube containing 500  $\mu$ L of methanol and 250  $\mu$ L of chloroform. The mixture was vortexed for 30 s and centrifuged (2500 rpm, 4°C, 10 min).

After centrifugation, 300  $\mu$ L of the organic phase was collected in a new glass tube and dried under a stream of nitrogen. The dried extract was resuspended in 60  $\mu$ L of methanol/chloroform 1:1 (v/v) and transferred in an injection vial before liquid chromatography and mass spectrometry analysis. Lipid extraction from the membrane purification was carried out with the same protocol in which the solvent volumes used were divided by two. Reverse phase liquid chromatography was selected for separation with a UPLC system (Ultimate 3000, ThermoFisher). Lipid extracts from cells were separated on an Accucore C18 150  $\times$  2.1, 2.5  $\mu$ m column (ThermoFisher) operated at 400  $\mu$ L/min flow rate. The injection volume was 3  $\mu$ L of diluted lipid extract. Eluent solutions were ACN/H<sub>2</sub>O 50/50 (V/V) containing 10 mM ammonium formate and 0.1% formic acid (solvent A) and IPA/ACN/H<sub>2</sub>O 88/10/2 (V/V) containing 2 mM ammonium formate and 0.02% formic acid (solvent B). The step gradient used for elution was: 0 min 35% B, 0.0–4.0 min 35% to 60% B, 4.0–8.0 min 60% to 70% B, 8.0–16.0 min 70% to 85% B, 16.0–25 min 85% to 97% B, 25–25.1 min 97% to 100% B, 25.1–31 min 100% B and finally the column was reconditioned at 35% B for 4 min. The UPLC system was coupled to a Q-exactive orbitrap mass spectrometer (ThermoFisher, CA); equipped with a heated electrospray ionization (HESI) probe. This spectrometer was controlled by the Xcalibur software and was operated in electrospray positive mode. MS spectra were acquired at a resolution of 70,000 (200 m/z) in a mass range of 250–1200 m/z. The 15 most intense precursor ions were selected and isolated with a window of 1 m/z and fragmented by HCD (higher energy C-trap dissociation) with normalized collision energy (NCE) of 25 and 30 eV. MS/MS spectra were acquired with the resolution set at 35 000 at 200 m/z. Data were reprocessed using Lipid Search 4.1.16 (ThermoFisher). In this study, the product search mode was used, and the identification was based on the accurate mass of precursor ions and the MS<sub>2</sub> spectral pattern. Mass tolerance for precursors and fragments was set to 5 ppm and eight ppm respectively. The m-score threshold was selected at five and the ID quality filter was fixed at grades A, B, and C. [M + H]<sup>+</sup>, [M + Na]<sup>+</sup>, and [M + NH<sub>4</sub>]<sup>+</sup> adducts were searched.

### Mass spectrometric analysis for ganglioside

Ganglioside extraction was performed as described with minor modifications (Lee et al., 2011). The aqueous upper layers from two extractions (with a mixture of water–methanol–chloroform, W:M:C = 2:2:1) were collected. Two volumes of water were added to precipitate polyglycoceramides. The dried pellet was resuspended with methanol/water (M:W = 1:1) and analysed in reflector-positive and -negative modes on MALDI-TOF/TOF mass spectrometer Ultraflex III (Bruker Daltonics, Bremen, Germany) from 700 to 2500 Da. External calibration was performed by spotting peptide calibration standard II (BrukerDaltonics). Each sample was spotted in triplicate and mixed with DHB matrix on a steel target plate. All mass spectra were generated by summing 1000 laser shots for reflectron ion mode, and 1000 laser shots for the parent mass. Laser power was adjusted between 15% and 30% of its maximal intensity, using a 200 Hz smartbeam laser. MS spectra were acquired in the reflectron ion mode within a mass range from 500 to 2500 Da. Reflectron ion mode was chosen to obtain high detection sensitivity and resolution. FlexAnalysis version 3.0 and updated 3.4 provided by the manufacturer were applied for data processing. The Human Metabolome Database or HMDB 4.0 (<https://hmdb.ca/>) was used for peak identifications. Heat map and differential intensity analysis with Limma were done using Phantasus (<https://artyomovlab.wustl.edu/phantasus/>).

### Statistical analysis

All analyses were performed using Prism 6.0 software (GraphPad Inc). A two-tailed t-test was used if comparing only two conditions. For comparing more than two conditions, one-way ANOVA was used with: Bonferroni's multiple comparison test or Dunnett's multiple comparison test (if comparing all conditions to the control condition). Significance of mean comparison is marked on the graphs by asterisks. Error bars denote SEM.

### Acknowledgements

This work was supported by INSERM, the Côte d'Azur University, and by grants from the French National Research Agency (ANR) through the Investments for the program UCA JEDI to SC (ANR-15-IDEX-01), the Young Investigator Program to JG (ANR18-CE14-0035-01-GILLERON) and the ITMO, Plan Cancer. ST was supported by the 'Fondation de France' and TB by the French National Research Agency (ANR-18-CE14-0025). We thank the GIS-IBISA multi-sites platform 'Microscopie

Imagerie Côte d'Azur' (MICA), funded by the 'Conseil Départemental 06' support from ITMO Cancer Aviesan (National Alliance for Life Science and Health) within the framework of Cancer Plan. FB is a CNRS investigator. We would like to thank Marino Zerial's lab for giving us access to the MotionTraffic platform for image quantification.

---

## Additional information

### Funding

Funder	Grant reference number	Author
Agence Nationale de la Recherche	ANR-15-IDEX-01	Stephan Clavel
Agence Nationale de la Recherche	ANR18-CE14-0035-01-GILLERON	Jerome Gilleron
Fondation de France		Stéphanie Torrino
Agence Nationale de la Recherche	ANR-18-CE14-0025	Thomas Bertero

The funders had no role in study design, data collection and interpretation, or the decision to submit the work for publication.

### Author contributions

Stéphanie Torrino, Conceptualization, Formal analysis, Supervision, Validation, Investigation, Visualization, Methodology, Writing - original draft, Writing - review and editing; Victor Tiroille, Maeva Dufies, Charlotte Hinault, Sonia Dagnino, Lucile Fleuriot, Delphine Debayle, Formal analysis; Bastien Dolfi, Anne-sophie Gay, Data curation, Formal analysis; Laurent Bonesso, Data curation; Jennifer Uhler, Writing - review and editing; Marie Irondelle, Software; Sandra Lacas-Gervais, Formal analysis, Visualization; Mireille Cormont, Thomas Bertero, Resources, Writing - review and editing; Frederic Bost, Jerome Gilleron, Supervision, Conceptualization, Resources, Data curation, Software, Formal analysis, Funding acquisition, Investigation, Writing - original draft, Writing - review and editing; Stephan Clavel, Conceptualization, Resources, Data curation, Software, Formal analysis, Supervision, Funding acquisition, Validation, Investigation, Visualization, Methodology, Writing - original draft, Project administration, Writing - review and editing; , Conceptualization, Resources, Data curation, Software, Formal analysis, Funding acquisition, Investigation, Writing - original draft, Writing - review and editing

### Author ORCIDs

Stéphanie Torrino  <https://orcid.org/0000-0002-8280-5907>

Maeva Dufies  <http://orcid.org/0000-0003-1732-0388>

Sonia Dagnino  <https://orcid.org/0000-0001-6846-7190>

Delphine Debayle  <http://orcid.org/0000-0003-2807-9198>

Frederic Bost  <https://orcid.org/0000-0003-4509-4701>

Jerome Gilleron  <https://orcid.org/0000-0002-6389-8685>

### Decision letter and Author response

Decision letter <https://doi.org/10.7554/eLife.68348.sa1>

Author response <https://doi.org/10.7554/eLife.68348.sa2>

---

## Additional files

### Supplementary files

- Supplementary file 1. Proteins identified by LC-MS/MS following UBTD1 immunoprecipitation in DU145 cell line.
- Supplementary file 2. Subcellular localization score of UBTD1 interactants in DU145 cell line.

- Transparent reporting form

### Data availability

All data generated or analysed during this study are included in the manuscript and supporting files. Source data files have been provided.

## References

- Albagli-Curiel O**, Lécluse Y, Pognonec P, Boulukos KE, Martin P. 2007. A new generation of pPRIG-based retroviral vectors. *BMC Biotechnology* **7**:85. DOI: <https://doi.org/10.1186/1472-6750-7-85>, PMID: 18053131
- Avraham R**, Yarden Y. 2011. Feedback regulation of EGFR signalling: decision making by early and delayed loops. *Nature Reviews Molecular Cell Biology* **12**:104–117. DOI: <https://doi.org/10.1038/nrm3048>, PMID: 21252999
- Bakker J**, Spits M, Neefjes J, Berlin I. 2017. The EGFR odyssey - from activation to destruction in space and time. *Journal of Cell Science* **130**:4087–4096. DOI: <https://doi.org/10.1242/jcs.209197>, PMID: 29180516
- Brannigan JA**, Dodson G, Duggleby HJ, Moody PC, Smith JL, Tomchick DR, Murzin AG. 1995. A protein catalytic framework with an N-terminal nucleophile is capable of self-activation. *Nature* **378**:416–419. DOI: <https://doi.org/10.1038/378416a0>, PMID: 7477383
- Bremer EG**, Schlessinger J, Hakomori S. 1986. Ganglioside-mediated modulation of cell growth specific effects of GM3 on tyrosine phosphorylation of the epidermal growth factor receptor. *Journal of Biological Chemistry* **261**:2434–2440. DOI: [https://doi.org/10.1016/S0021-9258\(17\)35954-9](https://doi.org/10.1016/S0021-9258(17)35954-9), PMID: 2418024
- Caldieri G**, Malabarba MG, Di Fiore PP, Sigismund S. 2018. EGFR Trafficking in Physiology and Cancer. *Progress in molecular and subcellular biology* **57**:235–272. DOI: [https://doi.org/10.1007/978-3-319-96704-2\\_9](https://doi.org/10.1007/978-3-319-96704-2_9), PMID: 30097778
- Chen YG**. 2009. Endocytic regulation of TGF-beta signaling. *Cell Research* **19**:58–70. DOI: <https://doi.org/10.1038/cr.2008.315>, PMID: 19050695
- Collinet C**, Stöter M, Bradshaw CR, Samusik N, Rink JC, Kenski D, Habermann B, Buchholz F, Henschel R, Mueller MS, Nagel WE, Fava E, Kalaidzidis Y, Zerial M. 2010. Systems survey of endocytosis by multiparametric image analysis. *Nature* **464**:243–249. DOI: <https://doi.org/10.1038/nature08779>, PMID: 20190736
- Coskun Ü**, Grzybek M, Drechsel D, Simons K. 2011. Regulation of human EGF receptor by lipids. *PNAS* **108**:9044–9048. DOI: <https://doi.org/10.1073/pnas.1105666108>, PMID: 21571640
- Eden ER**, Huang F, Sorkin A, Futter CE. 2012. The role of EGF receptor ubiquitination in regulating its intracellular traffic. *Traffic* **13**:329–337. DOI: <https://doi.org/10.1111/j.1600-0854.2011.01305.x>, PMID: 22017370
- Ferguson KM**, Berger MB, Mendrola JM, Cho HS, Leahy DJ, Lemmon MA. 2003. EGF activates its receptor by removing interactions that autoinhibit ectodomain dimerization. *Molecular Cell* **11**:507–517. DOI: [https://doi.org/10.1016/S1097-2765\(03\)00047-9](https://doi.org/10.1016/S1097-2765(03)00047-9), PMID: 12620237
- Futter CE**, Pearse A, Hewlett LJ, Hopkins CR. 1996. Multivesicular endosomes containing internalized EGF-EGF receptor complexes mature and then fuse directly with lysosomes. *Journal of Cell Biology* **132**:1011–1023. DOI: <https://doi.org/10.1083/jcb.132.6.1011>, PMID: 8601581
- Galligan JT**, Martinez-Noël G, Arndt V, Hayes S, Chittenden TW, Harper JW, Howley PM. 2015. Proteomic analysis and identification of cellular interactors of the giant ubiquitin ligase HERC2. *Journal of Proteome Research* **14**:953–966. DOI: <https://doi.org/10.1021/pr501005v>, PMID: 25476789
- Gebai A**, Gorelik A, Li Z, Illes K, Nagar B. 2018. Structural basis for the activation of acid ceramidase. *Nature Communications* **9**:1621. DOI: <https://doi.org/10.1038/s41467-018-03844-2>, PMID: 29692406
- Gillieron J**, Querbes W, Zeigerer A, Borodovsky A, Marsico G, Schubert U, Manygoats K, Seifert S, Andree C, Stöter M, Epstein-Barash H, Zhang L, Koteliansky V, Fitzgerald K, Fava E, Bickle M, Kalaidzidis Y, Akinc A, Maier M, Zerial M. 2013. Image-based analysis of lipid nanoparticle-mediated siRNA delivery, intracellular trafficking and endosomal escape. *Nature Biotechnology* **31**:638–646. DOI: <https://doi.org/10.1038/nbt.2612>, PMID: 23792630
- Good MC**, Zalatan JG, Lim WA. 2011. Scaffold proteins: hubs for controlling the flow of cellular information. *Science* **332**:680–686. DOI: <https://doi.org/10.1126/science.1198701>, PMID: 21551057
- Grant S**, Qiao L, Dent P. 2002. Roles of ERBB family receptor tyrosine kinases, and downstream signaling pathways, in the control of cell growth and survival. *Frontiers in Bioscience* **7**:d376–d389. DOI: <https://doi.org/10.2741/grant>, PMID: 11815285
- Haglund K**, Dikic I. 2005. Ubiquitylation and cell signaling. *The EMBO Journal* **24**:3353–3359. DOI: <https://doi.org/10.1038/sj.emboj.7600808>, PMID: 16148945
- Hanafusa H**, Ishikawa K, Kedashiro S, Saigo T, Iemura S, Natsume T, Komada M, Shibuya H, Nara A, Matsumoto K. 2011. Leucine-rich repeat kinase LRRK1 regulates endosomal trafficking of the EGF receptor. *Nature Communications* **2**:158. DOI: <https://doi.org/10.1038/ncomms1161>, PMID: 21245839
- Jongsma ML**, Berlin I, Wijdeven RH, Janssen L, Janssen GM, Garstka MA, Janssen H, Mensink M, van Veelen PA, Spaepen RM, Neefjes J. 2016. An ER-Associated Pathway Defines Endosomal Architecture for Controlled Cargo Transport. *Cell* **166**:152–166. DOI: <https://doi.org/10.1016/j.cell.2016.05.078>, PMID: 27368102

- Kerscher O**, Felberbaum R, Hochstrasser M. 2006. Modification of proteins by ubiquitin and ubiquitin-like proteins. *Annual Review of Cell and Developmental Biology* **22**:159–180. DOI: <https://doi.org/10.1146/annurev.cellbio.22.010605.093503>, PMID: 16753028
- Komander D**, Rape M. 2012. The ubiquitin code. *Annual Review of Biochemistry* **81**:203–229. DOI: <https://doi.org/10.1146/annurev-biochem-060310-170328>, PMID: 22524316
- Lambert S**, Vind-Kezunovic D, Karvinen S, Gniadecki R. 2006. Ligand-independent activation of the EGFR by lipid raft disruption. *Journal of Investigative Dermatology* **126**:954–962. DOI: <https://doi.org/10.1038/sj.jid.5700168>, PMID: 16456534
- Lee H**, An HJ, Lerno LA, German JB, Lebrilla CB. 2011. Rapid Profiling of Bovine and Human Milk Gangliosides by Matrix-Assisted Laser Desorption/Ionization Fourier Transform Ion Cyclotron Resonance Mass Spectrometry. *International Journal of Mass Spectrometry* **305**:138–150. DOI: <https://doi.org/10.1016/j.ijms.2010.10.020>, PMID: 21860602
- Lemmon MA**, Schlessinger J. 2010. Cell signaling by receptor tyrosine kinases. *Cell* **141**:1117–1134. DOI: <https://doi.org/10.1016/j.cell.2010.06.011>, PMID: 20602996
- Marwaha R**, Sharma M. 2017. DQ-Red BSA trafficking assay in cultured cells to assess cargo delivery to lysosomes. *Bio-Protocol* **7**:e2571. DOI: <https://doi.org/10.21769/BioProtoc.2571>, PMID: 29082291
- Meuillet EJ**, Mania-Farnell B, George D, Inokuchi JI, Bremer EG. 2000. Modulation of EGF receptor activity by changes in the GM3 content in a human epidermoid carcinoma cell line, A431. *Experimental Cell Research* **256**:74–82. DOI: <https://doi.org/10.1006/excr.1999.4509>, PMID: 10739654
- Mizutani N**, Inoue M, Omori Y, Ito H, Tamiya-Koizumi K, Takagi A, Kojima T, Nakamura M, Iwaki S, Nakatochi M, Suzuki M, Nozawa Y, Murate T. 2015. Increased acid ceramidase expression depends on upregulation of androgen-dependent deubiquitinases, USP2, in a human prostate cancer cell line, LNCaP. *Journal of Biochemistry* **158**:309–319. DOI: <https://doi.org/10.1093/jb/mvv039>, PMID: 25888580
- Park KC**, Richardson DR. 2020. The c-MET oncoprotein: Function, mechanisms of degradation and its targeting by novel anti-cancer agents. *Biochimica et Biophysica Acta (BBA) - General Subjects* **1864**:129650. DOI: <https://doi.org/10.1016/j.bbagen.2020.129650>, PMID: 32522525
- Pu J**, Guardia CM, Keren-Kaplan T, Bonifacino JS. 2016. Mechanisms and functions of lysosome positioning. *Journal of Cell Science* **129**:4329–4339. DOI: <https://doi.org/10.1242/jcs.196287>, PMID: 27799357
- Rape M**. 2018. Ubiquitylation at the crossroads of development and disease. *Nature Reviews Molecular Cell Biology* **19**:59–70. DOI: <https://doi.org/10.1038/nrm.2017.83>, PMID: 28928488
- Schuchman EH**. 2016. Acid ceramidase and the treatment of ceramide diseases: The expanding role of enzyme replacement therapy. *Biochimica et Biophysica Acta (BBA) - Molecular Basis of Disease* **1862**:1459–1471. DOI: <https://doi.org/10.1016/j.bbadis.2016.05.001>, PMID: 27155573
- Schulman BA**, Harper JW. 2009. Ubiquitin-like protein activation by E1 enzymes: the apex for downstream signalling pathways. *Nature Reviews Molecular Cell Biology* **10**:319–331. DOI: <https://doi.org/10.1038/nrm2673>, PMID: 19352404
- Scott JD**, Pawson T. 2009. Cell signaling in space and time: where proteins come together and when they're apart. *Science* **326**:1220–1224. DOI: <https://doi.org/10.1126/science.1175668>, PMID: 19965465
- Sigismund S**, Avanzato D, Lanzetti L. 2018. Emerging functions of the EGFR in cancer. *Molecular Oncology* **12**:3–20. DOI: <https://doi.org/10.1002/1878-0261.12155>, PMID: 29124875
- Szklarczyk D**, Franceschini A, Kuhn M, Simonovic M, Roth A, Minguez P, Doerks T, Stark M, Muller J, Bork P, Jensen LJ, von Mering C. 2011. The STRING database in 2011: functional interaction networks of proteins, globally integrated and scored. *Nucleic Acids Research* **39**:D561–D568. DOI: <https://doi.org/10.1093/nar/gkq973>, PMID: 21045058
- Todeschini AR**, Dos Santos JN, Handa K, Hakomori SI. 2008. Ganglioside GM2/GM3 complex affixed on silica nanospheres strongly inhibits cell motility through CD82/cMet-mediated pathway. *PNAS* **105**:1925–1930. DOI: <https://doi.org/10.1073/pnas.0709619104>, PMID: 18272501
- Tokunaga F**, Sakata S, Saeki Y, Satomi Y, Kirisako T, Kamei K, Nakagawa T, Kato M, Murata S, Yamaoka S, Yamamoto M, Akira S, Takao T, Tanaka K, Iwai K. 2009. Involvement of linear polyubiquitylation of NEMO in NF- $\kappa$ B activation. *Nature Cell Biology* **11**:123–132. DOI: <https://doi.org/10.1038/ncb1821>, PMID: 19136968
- Torrino S**, Visvikis O, Doye A, Boyer L, Stefani C, Munro P, Bertoglio J, Gacon G, Mettouchi A, Lemichez E. 2011. The E3 ubiquitin-ligase HACE1 catalyzes the ubiquitylation of active Rac1. *Developmental Cell* **21**:959–965. DOI: <https://doi.org/10.1016/j.devcel.2011.08.015>, PMID: 22036506
- Torrino S**, Roustan FR, Kaminski L, Bertero T, Pisano S, Ambrosetti D, Dufies M, Uhler JP, Lemichez E, Mettouchi A, Gesson M, Laurent K, Gaggioli C, Michiels JF, Lamaze C, Bost F, Clavel S. 2019. UBTD1 is a mechano-regulator controlling Cancer aggressiveness. *EMBO Reports* **20**:e46570. DOI: <https://doi.org/10.15252/embr.201846570>, PMID: 30804013
- Uhler JP**, Spåhr H, Farge G, Clavel S, Larsson NG, Falkenberg M, Samuelsson T, Gustafsson CM. 2014. The Ubl protein UBTD1 stably interacts with the UBE2D family of E2 ubiquitin conjugating enzymes. *Biochemical and Biophysical Research Communications* **443**:7–12. DOI: <https://doi.org/10.1016/j.bbrc.2013.10.137>, PMID: 24211586
- Wells A**. 1999. EGF receptor. *The International Journal of Biochemistry & Cell Biology* **31**:637–643. DOI: [https://doi.org/10.1016/S1357-2725\(99\)00015-1](https://doi.org/10.1016/S1357-2725(99)00015-1), PMID: 10404636
- Yang N**, Chen T, Wang L, Liu R, Niu Y, Sun L, Yao B, Wang Y, Yang W, Liu Q, Tu K, Liu Z. 2020. CXCR4 mediates matrix stiffness-induced downregulation of UBTD1 driving hepatocellular carcinoma progression via YAP signaling pathway. *Theranostics* **10**:5790–5801. DOI: <https://doi.org/10.7150/thno.44789>, PMID: 32483419

- Yarden Y**, Pines G. 2012. The ERBB network: at last, cancer therapy meets systems biology. *Nature Reviews Cancer* **12**:553–563. DOI: <https://doi.org/10.1038/nrc3309>, PMID: 22785351
- Yau R**, Rape M. 2016. The increasing complexity of the ubiquitin code. *Nature Cell Biology* **18**:579–586. DOI: <https://doi.org/10.1038/ncb3358>, PMID: 27230526
- Ye Y**, Rape M. 2009. Building ubiquitin chains: E2 enzymes at work. *Nature Reviews Molecular Cell Biology* **10**: 755–764. DOI: <https://doi.org/10.1038/nrm2780>, PMID: 19851334
- Zeigerer A**, Gilleron J, Bogorad RL, Marsico G, Nonaka H, Seifert S, Epstein-Barash H, Kuchimanchi S, Peng CG, Ruda VM, Del Conte-Zerial P, Hengstler JG, Kalaidzidis Y, Kotliansky V, Zerial M. 2012. Rab5 is necessary for the biogenesis of the endolysosomal system in vivo. *Nature* **485**:465–470. DOI: <https://doi.org/10.1038/nature11133>, PMID: 22622570
- Zhang XW**, Wang XF, Ni SJ, Qin W, Zhao LQ, Hua RX, Lu YW, Li J, Dimri GP, Guo WJ. 2015. UBTD1 induces cellular senescence through an UBTD1-Mdm2/p53 positive feedback loop. *The Journal of Pathology* **235**:656–667. DOI: <https://doi.org/10.1002/path.4478>, PMID: 25382750

## **ARTICLE 2**





# The Adipose Tissue at the Crosstalk Between EDCs and Cancer Development

Emma Bokobza<sup>1</sup>, Charlotte Hinault<sup>1,2</sup>, Victor Tiroille<sup>1</sup>, Stéphan Clavel<sup>1</sup>, Frédéric Bost<sup>1</sup> and Nicolas Chevalier<sup>1,2\*</sup>

<sup>1</sup> Université Côte d'Azur, INSERM U1065, C3M, Nice, France, <sup>2</sup> Université Côte d'Azur, CHU, INSERM U1065, C3M, Nice, France

## OPEN ACCESS

### Edited by:

Elena Grasselli,  
University of Genoa, Italy

### Reviewed by:

Ma. Cecilia Opazo,  
Andres Bello University, Chile  
Vanessa Souza-Mello,  
Rio de Janeiro State University, Brazil

### \*Correspondence:

Nicolas Chevalier  
chevalie@unice.fr;  
chevalier.n@chu-nice.fr

### Specialty section:

This article was submitted to  
Translational Endocrinology,  
a section of the journal  
Frontiers in Endocrinology

**Received:** 06 April 2021

**Accepted:** 30 June 2021

**Published:** 20 July 2021

### Citation:

Bokobza E, Hinault C, Tiroille V,  
Clavel S, Bost F and Chevalier N  
(2021) The Adipose Tissue at the  
Crosstalk Between EDCs  
and Cancer Development.  
*Front. Endocrinol.* 12:691658.  
doi: 10.3389/fendo.2021.691658

Obesity is a major public health concern at the origin of many pathologies, including cancers. Among them, the incidence of gastro-intestinal tract cancers is significantly increased, as well as the one of hormone-dependent cancers. The metabolic changes caused by overweight mainly with the development of adipose tissue (AT), insulin resistance and chronic inflammation induce hormonal and/or growth factor imbalances, which impact cell proliferation and differentiation. AT is now considered as the main internal source of endocrine disrupting chemicals (EDCs) representing a low level systemic chronic exposure. Some EDCs are non-metabolizable and can accumulate in AT for a long time. We are chronically exposed to low doses of EDCs able to interfere with the endocrine metabolism of the body. Importantly, several EDCs have been involved in the genesis of obesity affecting profoundly the physiology of AT. In parallel, EDCs have been implicated in the development of cancers, in particular hormone-dependent cancers (prostate, testis, breast, endometrium, thyroid). While it is now well established that AT secretes adipocytokines that promote tumor progression, it is less clear whether they can initiate cancer. Therefore, it is important to better understand the effects of EDCs, and to investigate the buffering effect of AT in the context of progression but also initiation of cancer cells using adequate models recommended to uncover and validate these mechanisms for humans. We will review and argument here the potential role of AT as a crosstalk between EDCs and hormone-dependent cancer development, and how to assess it.

**Keywords:** adipose tissue, endocrine disruptor (EDC), cancer, secretome, model, endocrine disrupting chemicals

## INTRODUCTION

Obesity, defined as an abnormal or excessive fat accumulation in the body, is a major public health concern with more than 650 million obese adults in 2016 (from World Health Organization). Obesity is at the root of many pathologies, whether functional (orthopedic, esthetic, psychological complications, benign (diabetes, endometriosis) or malignant (gastro-intestinal tract and hormone-dependent cancers). Numerous studies demonstrated the relationship between obesity and an

increased risk of cancer (1–4). For example, obesity increases the risk of breast cancer after menopause by 8% and is responsible for 34.1% of endometrial cancers. Globally, 15–20% of total cancer-related mortality in adults aged 30 and over are attributable to obesity or overweight. Obesity provokes metabolic changes related to adipose tissue (AT) development such as insulin resistance and chronic inflammation. These changes induce hormonal and/or growth factor imbalances, which impact cell proliferation and differentiation and can also explain the increased risk of obesity-related cancers.

Climate transition which has begun several years ago is associated with the use of many pollutants. Some of these pollutants are chemicals that accumulate during the food chain in different tissues but mainly in adipose tissue (AT) due to their lipophilic nature. Some of these persistent organic pollutants (POPs) have already been regulated and/or withdrawn from the market due to their carcinogenic properties. They are still found in many products from the chemical industry, such as pesticides, some plastics or cleaning products, or even in building materials. They are usually classified into five categories (5): dioxins, polychlorinated biphenyls (PCBs), organochlorine pesticides (OCs), polybrominated flame retardants (PBDE) and perfluorinated compounds (like PFOS and PFOA) found especially in non-stick coatings (6, 7).

Because of their long half-life and their ability to store in AT, populations remain exposed, from fetal life, and therefore at risk of developing pathologies even when they are exposed to low doses of these pollutants. It has been shown that some of these POPs could interfere with hormonal signaling and/or regulation pathways, thus giving them endocrine disrupting (ED) activity (5). Early and/or chronic exposure to POPs with ED properties can modify the incidence of certain diseases, in particular obesity (8) or hormone-sensitive cancers (thyroid, prostate, testis, breast, ovary) (9, 10).

Hence, there are credible to convincing evidence for the link between obesity and cancer in one hand, and on the other hand, as we will discuss below, between ED chemicals (EDCs) and obesity or EDCs and cancer. However, the link between EDCs, obesity and cancer have not been yet demonstrated. This link could be the adipose secretome perturbed by EDCs, which modify the balance between proliferation and differentiation cell processes.

## EDCs AND HORMONE SENSITIVE CANCERS

The development of some cancers is stimulated by hormones, which naturally circulate in the body and bind to membrane and/or nuclear receptors of cancer cells favoring their growth and multiplication. Among these hormone-dependent cancers, prostate cancer (PCa) and endometrial cancer (ECa) are the most common cancers of the male and female reproductive systems, respectively, in addition to breast cancer (BCa) which is the most common cancer in women worldwide (2). Steroid hormones (estrogens, androgens) play an important role in the

etiology, progression and treatment of hormone-dependent cancers (11–13). It is therefore obvious that exposure to EDCs can influence the incidence and development of those cancers (9).

EDCs have been firstly identified as risk factor with the dramatic story of diethylstilbestrol (DES) (14). This synthetic diphenol with potent estrogenic properties was widely prescribed to pregnant women until 1970s to reduce the risk of abortion; however, several studies have reported an increased risk of rare cancers in women progenies (14, 15). Importantly, deleterious effects of prenatal DES exposure have been shown to persist in second-generation paving the way of the concepts of epigenetic transgenerational inheritance (16). Since then, several epidemiological studies supported by *in vivo* and *in vitro* experiments have confirmed this association between EDCs (notably PCBs, dioxins, DDE and bisphenol A [BPA]) and an increased risk of hormone-dependent cancers in both sexes (7, 17–19). Regarding testicular cancer, we and others have shown that BPA was able to stimulate the proliferation of seminoma cells involving GPR30/GPER pathway (20–22). Concerning PCa, Prins et al. have shown that exposure to BPA makes prostate stem cells more sensitive to estrogen in adulthood and therefore more likely to develop PCa (23, 24). Regarding persistent EDCs, although discussed, exposure to chlordecone constitutes a demonstrative example with a significant increase in the risk of PCa (25) and of recurrence after radical prostatectomy (26). Observational and experimental studies have suggested a role of PCB-153, an industrial organochlorine product, in the development of high-grade PCa (27). However, a previous study observed an inverse correlation between plasma concentrations of PCB-153 and PCa (28). Likewise, studies differ about a positive association (29) or not (30) between elevated serum levels of PFOA and PCa onset and/or progression. Thus, despite this extensive work on the role of certain EDCs in the incidence of hormone-sensitive cancers, diverse investigations for their action modes, their effects on tumor growth and on the formation of metastases especially in human are still poorly understood (7, 31).

## EDCs AND ADIPOSE TISSUE

AT is a major player in toxicological responses to exposure to EDCs, especially to POPs with predominantly halogenated structure which makes them non-metabolizable and very lipophilic (32). By storing POPs, AT may appear to have a protective role, but it is rather considered to be the main internal source of chronic low-level systemic exposure to EDCs since they will be released progressively or massively when lipolysis will occur. Therefore, AT represents a dynamic storage compartment for EDCs within the body with a continuous flow between storage and release in post-exposure periods. Various *in vitro* and *in vivo* studies have focused on this dynamic mobilization of EDCs by AT, for instance a murine cell model mimicking lipolysis has been developed and tested for PCBs (33). Using a xenografted fat model, others have shown that TCDD stored in

AT of xenograft can be released into the recipient mice and modify gene expression providing a direct evidence of the potential deleterious effects of TCDD (34). Recently, we have shown in a large prospective study that massive weight loss during the first year following bariatric surgery is associated with a prolonged release of POPs from AT, mainly PCB-153, DDE and hexachlorobenzene (35). The fat depot specific differences in EDC bioaccumulation have also been investigated but to date divergent results were obtained even though there is an agreement concerning the abundance of certain EDCs and the correlation with AT macrophage infiltration, adipocyte size or with metabolic parameters (36, 37).

In addition to its storage role, AT functions as a full-fledged endocrine organ producing and responding to hormones and adipokines (38–40). Several EDCs have been described *in vitro* and/or *in vivo* to profoundly affect AT physiology: adipocyte differentiation, adipocytokine secretion, oxidative stress and inflammation (8, 41, 42). Numerous publications have demonstrated a possible role for EDCs in the genesis of obesity, they have been called obesogen based on the hypothesis of Blumberg and Grun (8, 38, 41, 43, 44). Indeed, in case of chronic high caloric intake, AT undergoes into morphological changes: hyperplasia (increase of adipocytes number) and hypertrophy (lipid accumulation in the adipocytes resulting in the increase of adipocyte size) (38, 45). Hyperplasia takes place in healthy AT expansion. However, hypertrophy leads to dysfunctional adipocytes development, secreting adipokines as leptin, adiponectin or resistin for the main ones in addition to pro-inflammatory adipocytokines such as MCP-1, TNF- $\alpha$ , IL-6, IL-8. Hypertrophy also increase hypoxia, decreasing vascular supply resulting in adipocyte death by a rupture of the membrane, leading to a release of cellular content into the microenvironment. All of this results in the infiltration of inflammatory immune cells including lymphocytes, granulocytes type 1 macrophages leading to a change in AT microenvironment characterized by a chronic inflammation, the development of crown-like structures (dead adipocytes surrounded by macrophages within AT). Those structures generate reactive oxygen species (ROS) that are likely to induce DNA damages. This low-grade chronic inflammation affects local metabolism, but also systemic energy homeostasis. EDCs can act on hyperplasia and/or hypertrophy of the AT but also on adipose secretion (32, 46). For example, because PPAR is a key molecule in the regulation of adipogenesis, any EDC acting as an agonist on this receptor will be likely to cause an expansion of adipocytes, and therefore a modification of the secretome and act as an obesogenic EDC. It is the case of tributyltin (TBT) (44) and PFOA (29, 47–50). Indeed, TBT has been shown to promote inflammatory infiltration into adipocytes but also in reproductive tract in addition to increase fat mass (51–53). In addition to binding to PPAR, some EDCs promote adipogenesis by other mechanisms, such as *via* estrogen, glucocorticoid receptors or others. It has also been shown that some EDCs, such as dioxins, were able to induce a pro-inflammatory action on murine (54) and human (55) adipocyte cells, as well as TCDD in mouse AT through AhR

pathway (55). In parallel to *in vitro* and *in vivo* studies, several epidemiological studies support the association of pre/postnatal exposure to EDCs and increased BMI with the concept of transgenerational effects on progeny (7, 8, 41, 44). Therefore, EDCs that disrupt the coordinated regulation of adipocyte development, metabolism and endocrine function may result in disturbances in local and systemic energy metabolism and inflammatory response (56). The impact of EDCs on adipocyte endocrine function have been investigated but mainly in the context of obesity and/or cardiometabolic disorders. Further studies are required to fully examine their role alone or in cocktail at different doses and exposure notably in the context of cancer.

## CANCER AND ADIPOCYTE SECRETOME

Despite recent advances in understanding the biological basis of cancer, the mechanisms underlying its metastatic spread are not clearly established. In this process, the tumor environment plays an essential role. Indeed, a dialogue between cancer cells, the immune system and neighboring tissue cells such as AT is established and modulates the growth and migration of cancer (57, 58). This tumor microenvironment can also transform some adipocytes in so-called cancer-associated adipocytes (CAA) (59). It is also now well established that AT is a key player in the tumor microenvironment, by secreting factors that promote tumor progression and/or by providing metabolite substrates to cancer cells (38, 60–62). An excessive development of AT, as observed in obesity, associated with the existence of a metabolic syndrome, has been correlated with a marked increase in the aggressiveness of cancers (38, 63–65). Adipocytes and AT cells secretome is composed of lipids, adipokines, inflammatory cytokines, peptide hormones as well as extracellular vesicles working both in paracrine and endocrine, extracellular matrix components (38, 60–62).

Among paracrine and endocrine effects, the best characterized adipocytokines are the leptin and the adiponectin (66, 67). *In vitro* studies have demonstrated that leptin was able to activate ERK1/2 and c-Jun NH2-terminal Kinase (JNK) pathway and so promote cancer cell proliferation (68). However, no strong evidence showed the *in vivo* implication of leptin in tumorigenesis, although leptin levels or leptin signaling dysregulation have been observed in BCa, PCa and ECa (69). Concerning adiponectin, which circulating levels is inversely correlated to obesity, *in vitro* studies have shown its inhibitor role in proliferation and apoptosis in cancer cell line such as liver, breast, endometrium and stomach through the activation of AMPK and the inhibition of PI3K/Akt, ERK1/2 pathway, NF- $\kappa$ B, Wnt- $\beta$ -catenin pathway (70). Similarly, *in vivo* experiments demonstrated that adiponectin reduced tumorigenesis of cancer cells and that adiponectin-deficient mice developed more tumors (71). Clinical studies indicated a positive correlation between leptin:adiponectin ratio and increased risks for some cancers like ECa in post-menopausal women (72), BCa (73) and PCa (74). However, a metaanalysis

has then discussed leptin:adiponectin ratio and demonstrated no strong prognosis value for PCa (75).

In addition to adipokines, other factors secreted by adipocytes are involved in tumor progression processes more particularly through a paracrine action. In case of PCa, adipocytes from periprostatic AT (PPAT) secrete CC-chemokine ligand 7 (CCL7) which can diffuse through prostatic capsule to reach the tumor. Interaction between CCL7 and its ligand CC-chemokine receptor 3 (CCR3) will allow tumor migration outside of prostatic gland and initiate metastatic process (61, 76). More recently, creatine has been identified as metabolic substrate in BCa cells (77), which accelerates tumor progression due to a transformation into phosphocreatine to fuel tumor growth, especially in the context of obesity (77). In mammary human tumor, it has been shown that adipocytes in contact with the tumor presented phenotypic modification such as delipidation, dedifferentiation, with an overexpression of pro-inflammatory cytokines such as IL-6 (78).

The bidirectional communication between tumors and adipocytes have also been shown. After invading AT, tumors induce adipocyte lipolysis and thereby released fatty acids, stimulate ROS production favoring tumor invasion (79). Moreover, some AT cells called adipose stromal cells (ASC, multipotent mesenchymal progenitors) can be recruited from AT tumor through chemokine gradient (62) and then enhance PCa progression (80). Besides, FABP4, an abundant adipocyte protein, has been shown to be secreted by adipocytes but also by PCa and stromal cells. This put FABP4 at the heart of a communication between adipocytes and tumor stimulating MMPs and cytokine production in the PCa stromal microenvironment to favor tumor progression (81). More examples of transmitting signals between tumor cells and adipocytes including the potential implication of extravesicles/exosomes have been reviewed elsewhere (39, 57).

Overall, obesity represents a high-risk factor for several cancers because it promotes AT remodeling which can favor tumorigenesis and tumor progression through a crosstalk between tumor cells and adipocytes. Adipocyte secretome has been so far rather implicated in aggressiveness than in initiation of tumorigenesis. These deleterious effects of AT on cancer cells could be induced or exacerbated by the POPs stored there, which could therefore play an important role in the initiation, progression and/or metastasis of hormone-sensitive cancers which develop later in life (Figure 1A).

## MODELS TO ASSESS EDCs EFFECT ON ADIPOSE SECRETOME AND CANCER DEVELOPMENT

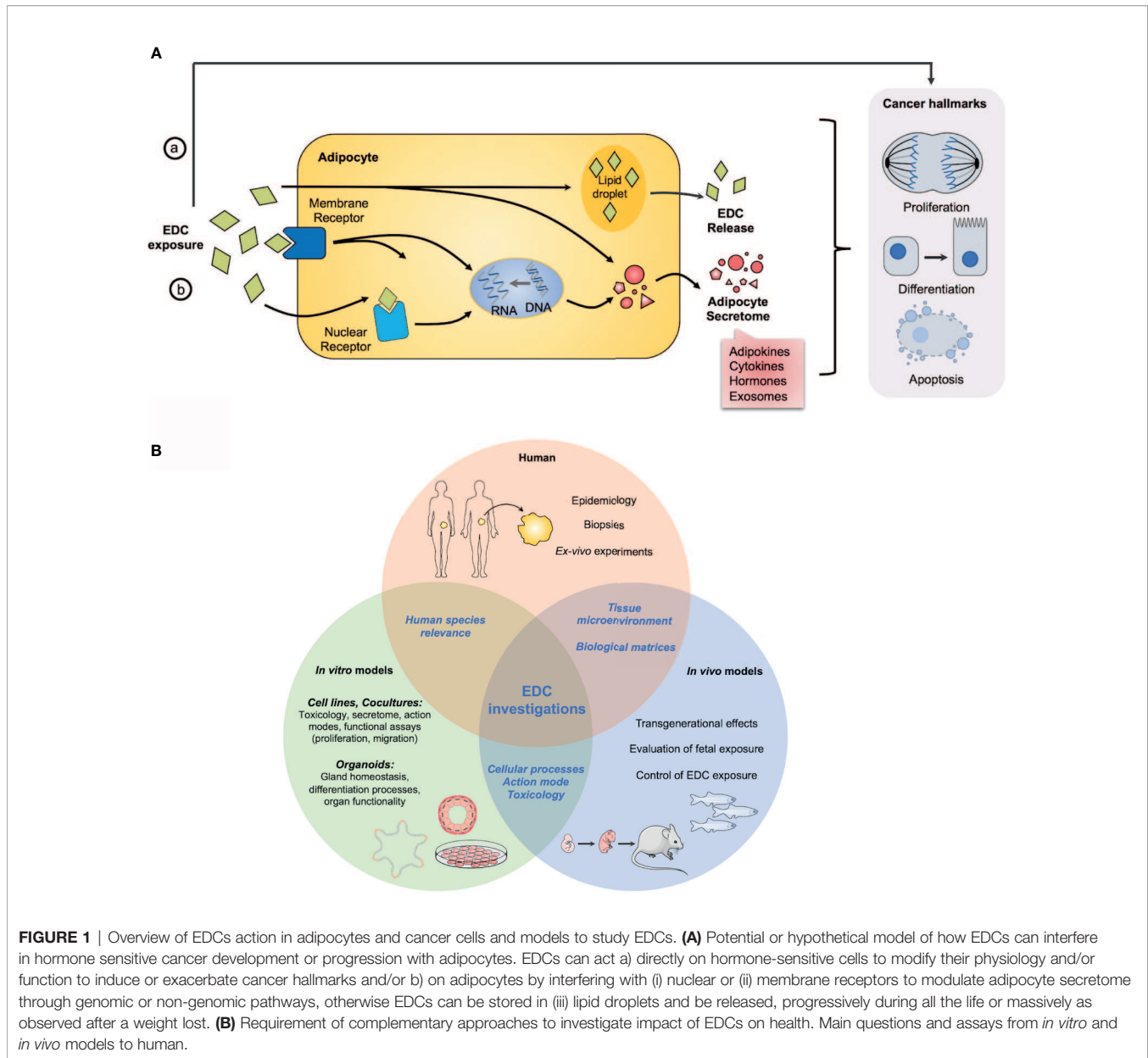
Data from epidemiological studies are essential for the detection of potential adverse effects of EDCs but usually provide only suggestive data (41). However, regulators need strong proofs of the interferences of EDCs with the hormonal system. Thus, *in vitro* assays are required to decipher EDCs molecular mechanisms. To validate *in vitro* experiments and implement

them with physiological and transgenerational data, *in vivo* or at least *ex-vivo* models are needed. Thus, it is important to develop alternative systems making it possible to screen these molecules, upstream, to demonstrate in a reliable, reproducible and robust manner, their safety or their potential toxicity (Table 1). Multiple alternative systems have been developed with frog embryos as developmental toxicity test or zebrafish xenograft assay (5).

Regarding adipose models, 3T3-L1 mouse cells is the most used cell line with the subclone 3T3-F442A. They have allowed to decipher adipogenesis molecular mechanisms and regulations and to screen multiple drugs before starting clinical trials (82). EDCs have been extensively studied in these cells notably to examine their obesogenic capacity (8, 41, 43, 44). To understand the impact of adipocyte secretome, coculture have been developed. Initially, indirect cocultures were performed by incubating cells with adipocyte conditioned medium. This approach has been conducted with different cell types such as melanoma (83), glioma (84) or PCa cells (76). 3T3L-1 as well as *ex-vivo* AT conditioned medium were able to increase overall survival of cancer cell lines both by increasing proliferation and decreasing apoptosis (83, 84) and to promote migration of tumor cells (76). Based on these approaches and to understand the potential role of EDCs on tumorigenesis or tumor progression through the modification of AT secretome, normal or tumoral cell lines/primary cells of an organ could be incubated with conditioned media of adipocytes prior exposed to EDCs. Another way to study adipocyte secretome is to perform “direct” coculture assay based on Boyden chambers with an insert. For instance, cocultures of BCa and 3T3-F442A cells were used to study the bidirectional communication between these cells (78, 79).

The results obtained from toxicity and toxicokinetic studies conducted on animals are usually difficult to transpose to humans (41). Over the past years, human multipotent cell models have been developed, notably hMADS cells (human multipotent adipose-derived stem cells) (85) and hASCs (human primary adipose-derived stromal/stem cells) (86), which allow to well-characterize the different events of lineage commitment (82). TCDD has been shown to increase inflammatory gene expression in hMADS cells but more strongly in undifferentiated than in differentiated adipocytes (55). Bisphenol S has been shown to deregulates adipokine secretion in a fat depot-specific manner in omental *versus* subcutaneous derived adipocytes from hASCs (87). More recently, Koual et al. have shown that coculture of human BCa cells with hMADS cells, although not differentiated into mature adipocytes, treated with TCDD leads to an increased MCF7 cell growth (19).

While 2D cultures of ASCs are easy to isolate and to differentiate into mature adipocytes, they present numerous limitations, including immortalization and lack of neighboring cells. ASCs have been shown to contribute to AT microenvironment given the opportunity to develop *in vitro* tissue-engineered adipose models such as 3D culture and/or cocultures with other cell types (i.e. endothelial cells or macrophages) (88–92). Recently, self-assembled adipose constructs into 3D spheroids using primary human SVF cells and a human blood product-derived biological scaffold have been validated (91). 3D adipocyte cultures bring new insight to study connective tissue interactions and crosstalk with



other cells such as cancer cells. Using adipocytes in a 3D collagen gel matrix, proliferation rate of human bone-metastatic PCa cell line PC3 increased as well as the expression of VEGF and PDGF (93), as it was previously observed with LNCaP or DU145 cells (94).

The other main limitation of classical cell culture is the use of only one cell type while an organ is composed of several cell types that communicate together. This issue can be resolved using a cutting-edge technology developed this past decade: *organoids* (95, 96). Organoids allow the study of cell-cell communication but also organ functionality. Organoids have been developed for hormone sensitive organ (thyroid, prostate, testis, endometrium, ovarian); their potential applications and limitations have been recently reviewed (97–100). Furthermore, organoid treated with special drugs presents phenotypic and morphological

specificities and this allows an easy and relatively cheap drug-screening platform (101), including the field of precision medicine (102) but also the identification of adverse effects of EDCs as discussed for thyroid gland (98). Therefore, organoids can be a good model to screen EDCs impact on the balance of cell differentiation/proliferation through modification of adipocyte secretome. However, because of medium incompatibility, cocultures using organoids and adipose cells, or direct incubation with adipocyte-conditioned medium cannot be performed, even with immune (103), stromal or vascular components (104). This demonstrates the necessity to developed adapted technology such as microfluidic system as already described in BCa cells (105) or to identify specific molecules present in AT secretome by omics approaches.

**TABLE 1** | Overview of in vivo and in vitro models available to study the adverse effect of EDCs.

	Epidemiology	EDC Storage/ Release	EDC Signaling	Cell Death	Cell Proliferation	Cell Differentiation	Inter/Transgenerational effects
<b>In vivo</b>	<b>Human samples</b>	+++	++	-	-	-	+
	<b>Animal models</b>						
	Rodent						
	Xenopus	-	+++	+	+	++	+++
	Zebrafish						
<b>In vitro</b>	<b>Organoid models</b>						
	Thyroid						
	Breast						
	Prostate	-	-	++	+++	+++	-
	Endometrium						
	<b>Cancer cell lines</b>	-	-	+++	+++	-	-
	<b>Pre/Adipocyte cultures</b>	-	+++	+++	-	+++	-

-/+/: low to high relevant models to assess the effects of EDCs on adipose secretome and cancer development.

Therefore, multiple models have been developed to study EDCs impact on the physiology of diverse tissue/organ, more precisely EDCs storage and release from AT and EDCs effects on proliferation and differentiation of hormone-sensitive cells which are summarized in **Figure 1B**.

## CONCLUSION

To study the impact of EDCs on tumor initiation/progression, it is important to be able to provide relevant tools allowing predictive analysis, upstream of the health risk, and in particular carcinogenic, of these molecules. There are inherent biases in epidemiological studies considering EDCs, which prevent definitive data on their role in carcinogenesis/metastatic spread. It is currently recognized that chronic exposure to EDCs may be responsible for an over-incidence of hormone-dependent cancers in humans and that EDCs impact on AT functioning. However, the links between EDCs, AT and cancer remain largely unknown. Therefore, alterations in AT secretome by EDCs could allow to identify specific markers, predictive factors of tumor progression, usable for various

stakeholders in the field (clinicians, manufacturers, decision-making bodies and regulatory health agencies). A better understanding of the functional alterations in AT by EDCs could therefore provide explanatory avenues to elucidate the complex links between obesity and some types of cancer.

## AUTHOR CONTRIBUTIONS

EB, CH, and NC wrote the manuscript. VT, SC, and FB contributed to discussions and manuscript. All authors contributed to the article and approved the submitted version.

## FUNDING

The team was supported by the Institut National de la Santé Et de la Recherche Médicale (INSERM), by the Agence Nationale de Sécurité Sanitaire de l'alimentation, de l'environnement et du travail (ANSES) (PNREST 2017 - IncuPE to Nicolas Chevalier) and the IDEX-UCA<sup>JEDI</sup> program (AAP3 2018 - ProstAdiPE and 2021- OrgaPEPro to Charlotte Hinault).

## REFERENCES

- Global BMIMC, Di Angelantonio E, Bhupathiraju Sh N, Wormser D, Gao P, Kaptoge S, et al. Body-Mass Index and All-Cause Mortality: Individual-Participant-Data Meta-Analysis of 239 Prospective Studies in Four Continents. *Lancet* (2016) 388(10046):776–86. doi: 10.1016/S0140-6736(16)30175-1
- Lauby-Secretan B, Scoccianti C, Loomis D, Grosse Y, Bianchini F, Straif K, et al. Body Fatness and Cancer—Viewpoint of the IARC Working Group. *N Engl J Med* (2016) 375(8):794–8. doi: 10.1056/NEJMs1606602
- Ligibel JA, Barry WT, Alfano C, Hershman DL, Irwin M, Neuhouser M, et al. Randomized Phase III Trial Evaluating the Role of Weight Loss in Adjuvant Treatment of Overweight and Obese Women With Early Breast Cancer (Alliance A011401): Study Design. *NPJ Breast Cancer* (2017) 3:37. doi: 10.1038/s41523-017-0040-8
- Cao Z, Zheng X, Yang H, Li S, Xu F, Yang X, et al. Association of Obesity Status and Metabolic Syndrome With Site-Specific Cancers: A Population-Based Cohort Study. *Br J Cancer* (2020) 123(8):1336–44. doi: 10.1038/s41416-020-1012-6
- Yilmaz B, Terekeci H, Sandal S, Kelestimur F. Endocrine Disrupting Chemicals: Exposure, Effects on Human Health, Mechanism of Action, Models for Testing and Strategies for Prevention. *Rev Endocrine Metab Disord* (2020) 21(1):127–47. doi: 10.1007/s11154-019-09521-z
- Diamanti-Kandarakis E, Bourguignon JP, Giudice LC, Hauser R, Prins GS, Soto AM, et al. Endocrine-Disrupting Chemicals: An Endocrine Society Scientific Statement. *Endocrine Rev* (2009) 30(4):293–342. doi: 10.1210/er.2009-0002
- Gore AC, Chappell VA, Fenton SE, Flaws JA, Nadal A, Prins GS, et al. EDC-2: The Endocrine Society's Second Scientific Statement on Endocrine-Disrupting Chemicals. *Endocrine Rev* (2015) 36(6):E1–150. doi: 10.1210/er.2015-1010
- Heindel JJ, Blumberg B, Cave M, Machtinger R, Mantovani A, Mendez MA, et al. Metabolism Disrupting Chemicals and Metabolic Disorders. *Reprod Toxicol* (2017) 68:3–33. doi: 10.1016/j.reprotox.2016.10.001

9. Soto AM, Sonnenschein C. Environmental Causes of Cancer: Endocrine Disruptors as Carcinogens. *Nat Rev Endocrinol* (2010) 6(7):363–70. doi: 10.1038/nrendo.2010.87
10. Vandenberg LN, Colborn T, Hayes TB, Heindel JJ, Jacobs DR Jr, Lee DH, et al. Hormones and Endocrine-Disrupting Chemicals: Low-Dose Effects and Nonmonotonic Dose Responses. *Endocrine Rev* (2012) 33(3):378–455. doi: 10.1210/er.2011-1050
11. Bosland MC. The Role of Estrogens in Prostate Carcinogenesis: A Rationale for Chemoprevention. *Rev Urol* (2005) 7(Suppl 3):S4–S10. doi: 10.1007/s40495-015-0031-0
12. Green SM, Mostaghel EA, Nelson PS. Androgen Action and Metabolism in Prostate Cancer. *Mol Cell Endocrinol* (2012) 360(1-2):3–13. doi: 10.1016/j.mce.2011.09.046
13. Liang J, Shang Y. Estrogen and Cancer. *Annu Rev Physiol* (2013) 75:225–40. doi: 10.1146/annurev-physiol-030212-183708
14. Palmer JR, Wise LA, Hatch EE, Troisi R, Titus-Ernstoff L, Strohsnitter W, et al. Prenatal Diethylstilbestrol Exposure and Risk of Breast Cancer. *Cancer Epidemiol Biomarkers Prev* (2006) 15(8):1509–14. doi: 10.1158/1055-9965.EPI-06-0109
15. Hoover RN, Hyer M, Pfeiffer RM, Adam E, Bond B, Cheville AL, et al. Adverse Health Outcomes in Women Exposed In Utero to Diethylstilbestrol. *N Engl J Med* (2011) 365(14):1304–14. doi: 10.1056/NEJMoa1013961
16. Fenichel P, Brucker-Davis F, Chevalier N. The History of Distilbene(R) (Diethylstilbestrol) Told to Grandchildren—The Transgenerational Effect. *Annales d'endocrinologie* (2015) 76(3):253–9. doi: 10.1016/j.ando.2015.03.008
17. Rachon D. Endocrine Disrupting Chemicals (EDCs) and Female Cancer: Informing the Patients. *Rev Endocrine Metab Disord* (2015) 16(4):359–64. doi: 10.1007/s11154-016-9332-9
18. Mallozzi M, Leone C, Manurita F, Bellati F, Caserta D. Endocrine Disrupting Chemicals and Endometrial Cancer: An Overview of Recent Laboratory Evidence and Epidemiological Studies. *Int J Environ Res Public Health* (2017) 14(3):334. doi: 10.3390/ijerph14030334
19. Koual M, Cano-Sancho G, Bats AS, Tomkiewicz C, Kaddouch-Amar Y, Douay-Hauser N, et al. Associations Between Persistent Organic Pollutants and Risk of Breast Cancer Metastasis. *Environ Int* (2019) 132:105028. doi: 10.1016/j.envint.2019.105028
20. Bouskine A, Nebout M, Mograbi B, Brucker-Davis F, Roger C, Fenichel P. Estrogens Promote Human Testicular Germ Cell Cancer Through a Membrane-Mediated Activation of Extracellular Regulated Kinase and Protein Kinase a. *Endocrinology* (2008) 149(2):565–73. doi: 10.1210/en.2007-1318
21. Chevalier N, Bouskine A, Fenichel P. Bisphenol A Promotes Testicular Seminoma Cell Proliferation Through GPER/GPR30. *Int J Cancer* (2012) 130(1):241–2. doi: 10.1002/ijc.25972
22. Chevalier N, Hinault C, Clavel S, Paul-Bellon R, Fenichel P. GPER and Testicular Germ Cell Cancer. *Front Endocrinol* (2020) 11:600404. doi: 10.3389/fendo.2020.600404
23. Lobaccaro JM, Trousson A. Environmental Estrogen Exposure During Fetal Life: A Time Bomb for Prostate Cancer. *Endocrinology* (2014) 155(3):656–8. doi: 10.1210/en.2014-1057
24. Prins GS, Hu WY, Shi GB, Hu DP, Majumdar S, Li G, et al. Bisphenol A Promotes Human Prostate Stem-Progenitor Cell Self-Renewal and Increases *In Vivo* Carcinogenesis in Human Prostate Epithelium. *Endocrinology* (2014) 155(3):805–17. doi: 10.1210/en.2013-1955
25. Multigner L, Ndong JR, Giusti A, Romana M, Delacroix-Maillard H, Cordier S, et al. Chlordecone Exposure and Risk of Prostate Cancer. *J Clin Oncol* (2010) 28(21):3457–62. doi: 10.1200/JCO.2009.27.2153
26. Bureau L, Emeville E, Helissey C, Thome JP, Multigner L, Blanchet P. Endocrine Disrupting-Chemicals and Biochemical Recurrence of Prostate Cancer After Prostatectomy: A Cohort Study in Guadeloupe (French West Indies). *Int J Cancer* (2019) 146(3):657–63. doi: 10.1002/ijc.32287
27. Ali I, Julin B, Glynn A, Hogberg J, Berglund M, Johansson JE, et al. Exposure to Polychlorinated Biphenyls and Prostate Cancer: Population-Based Prospective Cohort and Experimental Studies. *Carcinogenesis* (2016) 37(12):1144–51. doi: 10.1093/carcin/bgw105
28. Emeville E, Giusti A, Coumoul X, Thome JP, Blanchet P, Multigner L. Associations of Plasma Concentrations of Dichlorodiphenyldichloroethylene and Polychlorinated Biphenyls With Prostate Cancer: A Case-Control Study in Guadeloupe (French West Indies). *Environ Health Perspect* (2015) 123(4):317–23. doi: 10.1289/ehp.1408407
29. Vieira VM, Hoffman K, Shin HM, Weinberg JM, Webster TF, Fletcher T. Perfluorooctanoic Acid Exposure and Cancer Outcomes in a Contaminated Community: A Geographic Analysis. *Environ Health Perspect* (2013) 121(3):318–23. doi: 10.1289/ehp.1205829
30. Chang ET, Adami HO, Boffetta P, Cole P, Starr TB, Mandel JS. A Critical Review of Perfluorooctanoate and Perfluorooctanesulfonate Exposure and Cancer Risk in Humans. *Crit Rev Toxicol* (2014) 44(Suppl 1):1–81. doi: 10.3109/10408444.2014.905767
31. Di Donato M, Cerneria G, Giovannelli P, Galasso G, Bilancio A, Migliaccio A, et al. Recent Advances on Bisphenol-A and Endocrine Disruptor Effects on Human Prostate Cancer. *Mol Cell Endocrinol* (2017) 457:35–42. doi: 10.1016/j.mce.2017.02.045
32. La Merrill M, Emond C, Kim MJ, Antignac JP, Le Bizet B, Clement K, et al. Toxicological Function of Adipose Tissue: Focus on Persistent Organic Pollutants. *Environ Health Perspect* (2013) 121(2):162–9. doi: 10.1289/ehp.1205485
33. Louis C, Tinan G, Mignolet E, Thome JP, Debier C. PCB-153 Shows Different Dynamics of Mobilisation From Differentiated Rat Adipocytes During Lipolysis in Comparison With PCB-28 and PCB-118. *PLoS One* (2014) 9(9):e106495. doi: 10.1371/journal.pone.0106495
34. Joffin N, Noirez P, Antignac JP, Kim MJ, Marchand P, Falabregue M, et al. Release and Toxicity of Adipose Tissue-Stored TCDD: Direct Evidence from a Xenografted Fat Model. *Environ Int* (2018) 121(Pt 2):1113–20. doi: 10.1016/j.envint.2018.10.027
35. Fenichel P, Coquillard P, Brucker-Davis F, Marchand P, Cano-Sancho G, Boda M, et al. Sustained Bloodstream Release of Persistent Organic Pollutants Induced by Extensive Weight Loss After Bariatric Surgery: Implications for Women of Childbearing Age. *Environ Int* (2021) 151:106400. doi: 10.1016/j.envint.2021.106400
36. Pestana D, Faria G, Sa C, Fernandes VC, Teixeira D, Norberto S, et al. Persistent Organic Pollutant Levels in Human Visceral and Subcutaneous Adipose Tissue in Obese Individuals—Depot Differences and Dysmetabolism Implications. *Environ Res* (2014) 133:170–7. doi: 10.1016/j.envres.2014.05.026
37. Rolle-Kampczyk U, Gebauer S, Haange SB, Schubert K, Kern M, Moulla Y, et al. Accumulation of Distinct Persistent Organic Pollutants is Associated With Adipose Tissue Inflammation. *Sci Total Environ* (2020) 748:142458. doi: 10.1016/j.scitotenv.2020.142458
38. Lee MW, Lee M, Oh KJ. Adipose Tissue-Derived Signatures for Obesity and Type 2 Diabetes: Adipokines, Batokines and MicroRNAs. *J Clin Med* (2019) 8(6):854. doi: 10.3390/jcm8060854
39. Richard AJ, White U, Elks CM, Stephens JM. Adipose Tissue: Physiology to Metabolic Dysfunction. In: Feingold KR, Anawalt B, Boyce A, Chrousos G, de Herder WW, Dungan K, et al. editors. South Dartmouth, MA: Endotext (2000).
40. Scheja L, Heeren J. The Endocrine Function of Adipose Tissues in Health and Cardiometabolic Disease. *Nat Rev Endocrinol* (2019) 15(9):507–24. doi: 10.1038/s41574-019-0230-6
41. Papalou O, Kandaraki EA, Papadakis G, Diamanti-Kandaraki E. Endocrine Disrupting Chemicals: An Occult Mediator of Metabolic Disease. *Front Endocrinol* (2019) 10:112. doi: 10.3389/fendo.2019.00112
42. Kahn LG, Philippat C, Nakayama SF, Slama R, Trasande L. Endocrine-Disrupting Chemicals: Implications for Human Health. *Lancet Diabetes Endocrinol* (2020) 8(8):703–18. doi: 10.1016/S2213-8587(20)30129-7
43. Bateman ME, Strong AL, McLachlan JA, Burrow ME, Bunnell BA. The Effects of Endocrine Disruptors on Adipogenesis and Osteogenesis in Mesenchymal Stem Cells: A Review. *Front Endocrinol* (2016) 7:171. doi: 10.3389/fendo.2016.00171
44. Heindel JJ, Blumberg B. Environmental Obesogens: Mechanisms and Controversies. *Annu Rev Pharmacol Toxicol* (2019) 59:89–106. doi: 10.1146/annurev-pharmtox-010818-021304
45. Longo M, Zatterale F, Naderi J, Parrillo L, Formisano P, Raciti GA, et al. Adipose Tissue Dysfunction as Determinant of Obesity-Associated Metabolic Complications. *Int J Mol Sci* (2019) 20(9):2358. doi: 10.3390/ijms20092358
46. Griffin MD, Pereira SR, DeBari MK, Abbott RD. Mechanisms of Action, Chemical Characteristics, and Model Systems of Obesogens. *BMC BioMed Eng* (2020) 2:6. doi: 10.1186/s42490-020-00040-6

47. Yamamoto J, Yamane T, Oishi Y, Kobayashi-Hattori K. Perfluorooctanoic Acid Binds to Peroxisome Proliferator-Activated Receptor Gamma and Promotes Adipocyte Differentiation in 3T3-L1 Adipocytes. *Biosci Biotechnol Biochem* (2015) 79(4):636–9. doi: 10.1080/09168451.2014.991683
48. Ma Y, Yang J, Wan Y, Peng Y, Ding S, Li Y, et al. Low-Level Perfluorooctanoic Acid Enhances 3 T3-L1 Preadipocyte Differentiation via Altering Peroxisome Proliferator Activated Receptor Gamma Expression and Its Promoter DNA Methylation. *J Appl Toxicol* (2018) 38(3):398–407. doi: 10.1002/jat.3549
49. Li CH, Ren XM, Guo LH. Adipogenic Activity of Oligomeric Hexafluoropropylene Oxide (Perfluorooctanoic Acid Alternative) Through Peroxisome Proliferator-Activated Receptor Gamma Pathway. *Environ Sci Technol* (2019) 53(6):3287–95. doi: 10.1021/acs.est.8b06978
50. Liu S, Yang R, Yin N, Wang YL, Faiola F. Environmental and Human Relevant PFOS and PFOA Doses Alter Human Mesenchymal Stem Cell Self-Renewal, Adipogenesis and Osteogenesis. *Ecotoxicol Environ Saf* (2019) 169:564–72. doi: 10.1016/j.ecoenv.2018.11.064
51. Ceotto Freitas-Lima L, Merlo E, Campos Zicker M, Navia-Pelaez JM, de Oliveira M, Dos Santos Aggum Capettini L, et al. Tributyltin Impacts in Metabolic Syndrome Development Through Disruption of Angiotensin II Receptor Signaling Pathways in White Adipose Tissue from Adult Female Rats. *Toxicol Lett* (2018) 299:21–31. doi: 10.1016/j.toxlet.2018.08.018
52. da Costa CS, Miranda-Alves L, La Merrill MA, Silva IV, Graceli JB. The tributyltin Leads to Obesogenic Mammary Gland Abnormalities in Adult Female Rats. *Toxicol Lett* (2019) 307:59–71. doi: 10.1016/j.toxlet.2019.02.016
53. Zanol JF, Nino OMS, da Costa CS, Freitas-Lima LC, Miranda-Alves L, Graceli JB. Tributyltin and High-Refined Carbohydrate Diet Lead to Metabolic and Reproductive Abnormalities, Exacerbating Premature Ovary Failure Features in the Female Rats. *Reprod Toxicol* (2021) 103:108–23. doi: 10.1016/j.reprotox.2021.06.004
54. Arsenescu V, Arsenescu RI, King V, Swanson H, Cassis LA. Polychlorinated Biphenyl-77 Induces Adipocyte Differentiation and Proinflammatory Adipokines and Promotes Obesity and Atherosclerosis. *Environ Health Perspect* (2008) 116(6):761–8. doi: 10.1289/ehp.10554
55. Kim MJ, Pelloux V, Guyot E, Tordjman J, Bui LC, Chevallier A, et al. Inflammatory Pathway Genes Belong to Major Targets of Persistent Organic Pollutants in Adipose Cells. *Environ Health Perspect* (2012) 120(4):508–14. doi: 10.1289/ehp.1104282
56. Regnier SM, Sargis RM. Adipocytes Under Assault: Environmental Disruption of Adipose Physiology. *Biochim Biophys Acta* (2014) 1842(3):520–33. doi: 10.1016/j.bbadis.2013.05.028
57. Quail DF, Dannenberg AJ. The Obese Adipose Tissue Microenvironment in Cancer Development and Progression. *Nat Rev Endocrinol* (2019) 15(3):139–54. doi: 10.1038/s41574-018-0126-x
58. Santoni M, Piva F, Scarpelli M, Cheng L, Lopez-Beltran A, Massari F, et al. The Origin of Prostate Metastases: Emerging Insights. *Cancer Metastasis Rev* (2015) 34(4):765–73. doi: 10.1007/s10555-015-9597-6
59. Dirat BA, Bochet L, Escourrou G, Valet P, Muller C. Unraveling the Obesity and Breast Cancer Links: A Role for Cancer-Associated Adipocytes? *Endocr Dev* (2010) 19:45–52. doi: 10.1159/000316896
60. Sun K, Kusminski CM, Scherer PE. Adipose Tissue Remodeling and Obesity. *J Clin Invest* (2011) 121(6):2094–101. doi: 10.1172/JCI45887
61. Duong MN, Geneste A, Fallone F, Li X, Dumontet C, Muller C. The Fat and the Bad: Mature Adipocytes, Key Actors in Tumor Progression and Resistance. *Oncotarget* (2017) 8(34):57622–41. doi: 10.18632/oncotarget.18038
62. Cozzo AJ, Fuller AM, Makowski L. Contribution of Adipose Tissue to Development of Cancer. *Compr Physiol* (2017) 8(1):237–82. doi: 10.1002/cphy.c170008
63. Himbert C, Ose J, Delphan M, Ulrich CM. A Systematic Review of the Interrelation Between Diet- and Surgery-Induced Weight Loss and Vitamin D Status. *Nutr Res* (2017) 38:13–26. doi: 10.1016/j.nutres.2016.12.004
64. Quagliariello V, Rossetti S, Cavaliere C, Di Palo R, Lamantia E, Castaldo L, et al. Metabolic Syndrome, Endocrine Disruptors and Prostate Cancer Associations: Biochemical and Pathophysiological Evidences. *Oncotarget* (2017) 8(18):30606–16. doi: 10.18632/oncotarget.16725
65. Moreira DM, Anderson T, Gerber L, Thomas JA, Banez LL, McKeever MG, et al. The Association of Diabetes Mellitus and High-Grade Prostate Cancer in a Multiethnic Biopsy Series. *Cancer Causes Control: CCC* (2011) 22(7):977–83. doi: 10.1007/s10552-011-9770-3
66. Park J, Euhus DM, Scherer PE. Paracrine and Endocrine Effects of Adipose Tissue on Cancer Development and Progression. *Endocrine Rev* (2011) 32(4):550–70. doi: 10.1210/er.2010-0030
67. Booth A, Magnuson A, Fouts J, Foster MT. Adipose Tissue: An Endocrine Organ Playing a Role in Metabolic Regulation. *Horm Mol Biol Clin Investig* (2016) 26(1):25–42. doi: 10.1515/hmbci-2015-0073
68. Ghasemi A, Hashemy SI, Aghaei M, Panjehpour M. Leptin Induces Matrix Metalloproteinase 7 Expression to Promote Ovarian Cancer Cell Invasion by Activating ERK and JNK Pathways. *J Cell Biochem* (2018) 119(2):2333–44. doi: 10.1002/jcb.26396
69. Garofalo C, Surmacz E. Leptin and Cancer. *J Cell Physiol* (2006) 207(1):12–22. doi: 10.1002/jcp.20472
70. Katira A, Tan PH. Evolving Role of Adiponectin in Cancer-Controversies and Update. *Cancer Biol Med* (2016) 13(1):101–19. doi: 10.20892/j.issn.2095-3941.2015.0092
71. Nishihara T, Baba M, Matsuda M, Inoue M, Nishizawa Y, Fukuhara A, et al. Adiponectin Deficiency Enhances Colorectal Carcinogenesis and Liver Tumor Formation Induced by Azoxy methane in Mice. *World J Gastroenterol* (2008) 14(42):6473–80. doi: 10.3748/wjg.14.6473
72. Ashizawa N, Yahata T, Quan J, Adachi S, Yoshihara K, Tanaka K. Serum Leptin-Adiponectin Ratio and Endometrial Cancer Risk in Postmenopausal Female Subjects. *Gynecol Oncol* (2010) 119(1):65–9. doi: 10.1016/j.ygyno.2010.07.007
73. Chen DC, Chung YF, Yeh YT, Chaung HC, Kuo FC, Fu OY, et al. Serum Adiponectin and Leptin Levels in Taiwanese Breast Cancer Patients. *Cancer Lett* (2006) 237(1):109–14. doi: 10.1016/j.canlet.2005.05.047
74. Philip LK, Rockstroh A, Lehman M, Sadowski MC, Bartonicek N, Wade JD, et al. Adiponectin Receptor Activation Inhibits Prostate Cancer Xenograft Growth. *Endocr Relat Cancer* (2020) 27(12):711–29. doi: 10.1530/ERC-20-0297
75. Burton AJ, Gilbert R, Tilling K, Langdon R, Donovan JL, Holly JMP, et al. Circulating Adiponectin and Leptin and Risk of Overall and Aggressive Prostate Cancer: A Systematic Review and Meta-Analysis. *Sci Rep* (2021) 11(1):320. doi: 10.1038/s41598-020-79345-4
76. Laurent V, Guerard A, Mazerolles C, Le Gonidec S, Toulet A, Nieto L, et al. Periprostatic Adipocytes Act as a Driving Force for Prostate Cancer Progression in Obesity. *Nat Commun* (2016) 7:10230. doi: 10.1038/ncomms10230
77. Maguire OA, Ackerman SE, Szwed SK, Maganti AV, Marchildon F, Huang X, et al. Creatine-Mediated Crosstalk Between Adipocytes and Cancer Cells Regulates Obesity-Driven Breast Cancer. *Cell Metab* (2021) 33(3):499–512 e6. doi: 10.1016/j.cmet.2021.01.018
78. Wang YY, Attane C, Milhas D, Dirat B, Dauvillier S, Guerard A, et al. Mammary Adipocytes Stimulate Breast Cancer Invasion Through Metabolic Remodeling of Tumor Cells. *JCI Insight* (2017) 2(4):e87489. doi: 10.1172/jci.insight.87489
79. Laurent V, Toulet A, Attane C, Milhas D, Dauvillier S, Zaidi F, et al. Periprostatic Adipose Tissue Favors Prostate Cancer Cell Invasion in an Obesity-Dependent Manner: Role of Oxidative Stress. *Mol Cancer Res* (2019) 17(3):821–35. doi: 10.1158/1541-7786.MCR-18-0748
80. Zhang T, Tseng C, Zhang Y, Sirin O, Corn PG, Li-Ning-Tapia EM, et al. CXCL1 Mediates Obesity-Associated Adipose Stromal Cell Trafficking and Function in the Tumour Microenvironment. *Nat Commun* (2016) 7:11674. doi: 10.1038/ncomms11674
81. Huang M, Narita S, Inoue T, Koizumi A, Saito M, Tsuruta H, et al. Fatty Acid Binding Protein 4 Enhances Prostate Cancer Progression by Upregulating Matrix Metalloproteinases and Stromal Cell Cytokine Production. *Oncotarget* (2017) 8(67):111780–94. doi: 10.18632/oncotarget.22908
82. Sadie-Van Gijzen H. Adipocyte Biology: It is Time to Upgrade to a New Model. *J Cell Physiol* (2019) 234(3):2399–425. doi: 10.1002/jcp.27266
83. Coelho P, Almeida J, Prudencio C, Fernandes R, Soares R. Effect of Adipocyte Secretome in Melanoma Progression and Vasculogenic Mimicry. *J Cell Biochem* (2016) 117(7):1697–706. doi: 10.1002/jcb.25463
84. Almeida J, Costa J, Coelho P, Cea V, Galesio M, Noronha JP, et al. Adipocyte Proteome and Secretome Influence Inflammatory and Hormone Pathways in Glioma. *Metab Brain Dis* (2019) 34(1):141–52. doi: 10.1007/s11011-018-0327-y
85. Rodriguez AM, Elabd C, Delteil F, Astier J, Vernochet C, Saint-Marc P, et al. Adipocyte Differentiation of Multipotent Cells Established From Human Adipose Tissue. *Biochem Biophys Res Commun* (2004) 315(2):255–63. doi: 10.1016/j.bbrc.2004.01.053
86. Hauner H, Entenmann G, Wabitsch M, Gaillard D, Ailhaud G, Negrel R, et al. Promoting Effect of Glucocorticoids on the Differentiation of Human

- Adipocyte Precursor Cells Cultured in a Chemically Defined Medium. *J Clin Invest* (1989) 84(5):1663–70. doi: 10.1172/JCI114345
87. Peshdary V, Styles G, Gagne R, Yauk CL, Sorisky A, Atlas E. Depot-Specific Analysis of Human Adipose Cells and Their Responses to Bisphenol s. *Endocrinology* (2020) 161(6):bqaa044. doi: 10.1210/endo/bqaa044
  88. Murphy CS, Liaw L, Reagan MR. In Vitro Tissue-Engineered Adipose Constructs for Modeling Disease. *BMC BioMed Eng* (2019) 1:27. doi: 10.1186/s42490-019-0027-7
  89. Freemerman AJ, Zhao L, Pingjili AK, Teng B, Cozzo AJ, Fuller AM, et al. Myeloid Slc2a1-Deficient Murine Model Revealed Macrophage Activation and Metabolic Phenotype Are Fueled by GLUT1. *J Immunol* (2019) 202(4):1265–86. doi: 10.4049/jimmunol.1800002
  90. Huttala O, Sarkanen JR, Mannerstrom M, Toimela T, Heinonen T, Ylikomi T. Development of Novel Human *In Vitro* Vascularized Adipose Tissue Model With Functional Macrophages. *Cytotechnology* (2020) 72(5):665–83. doi: 10.1007/s10616-020-00407-6
  91. De Francesco F, Matta C, Riccio M, Sbarbati A, Mobasheri A. Reevolution of Tissue Regeneration: From Recent Advances in Adipose Stem Cells to Novel Therapeutic Approaches. *Stem Cells Int* (2021) 2021:2179429. doi: 10.1155/2021/2179429
  92. Muller S, Ader I, Creff J, Lemenager H, Achard P, Casteilla L, et al. Human Adipose Stromal-Vascular Fraction Self-Organizes to Form Vascularized Adipose Tissue in 3D Cultures. *Sci Rep* (2019) 9(1):7250. doi: 10.1038/s41598-019-43624-6
  93. Tokuda Y, Satoh Y, Fujiyama C, Toda S, Sugihara H, Masaki Z. Prostate Cancer Cell Growth Is Modulated by Adipocyte-Cancer Cell Interaction. *BJU Int* (2003) 91(7):716–20. doi: 10.1046/j.1464-410X.2003.04218.x
  94. Kaneko A, Satoh Y, Tokuda Y, Fujiyama C, Udo K, Uozumi J. Effects of Adipocytes on the Proliferation and Differentiation of Prostate Cancer Cells in a 3-D Culture Model. *Int J Urol* (2010) 17(4):369–76. doi: 10.1111/j.1442-2042.2010.02472.x
  95. Clevers H. Modeling Development and Disease With Organoids. *Cell* (2016) 165(7):1586–97. doi: 10.1016/j.cell.2016.05.082
  96. Drost J, Karthaus WR, Gao D, Driehuis E, Sawyers CL, Chen Y, et al. Organoid Culture Systems for Prostate Epithelial and Cancer Tissue. *Nat Protoc* (2016) 11(2):347–58. doi: 10.1038/nprot.2016.006
  97. Alves-Lopes JP, Soder O, Stukenborg JB. Testicular Organoid Generation by a Novel *In Vitro* Three-Layer Gradient System. *Biomaterials* (2017) 130:76–89. doi: 10.1016/j.biomaterials.2017.03.025
  98. Moroni L, Barbaro F, Caiment F, Coleman O, Costagliola S, Conza GD, et al. SCREENED: A Multistage Model of Thyroid Gland Function for Screening Endocrine-Disrupting Chemicals in a Biologically Sex-Specific Manner. *Int J Mol Sci* (2020) 21(10):3648. doi: 10.3390/ijms21103648
  99. Gleave AM, Ci X, Lin D, Wang Y. A Synopsis of Prostate Organoid Methodologies, Applications, and Limitations. *Prostate* (2020) 80(6):518–26. doi: 10.1002/pros.23966
  100. Alzamil L, Nikolakopoulou K, Turco MY. Organoid Systems to Study the Human Female Reproductive Tract and Pregnancy. *Cell Death Differ* (2021) 28(1):35–51. doi: 10.1038/s41418-020-0565-5
  101. Lukonin I, Serra D, Challet Meylan L, Volkman K, Baaten J, Zhao R, et al. Phenotypic Landscape of Intestinal Organoid Regeneration. *Nature* (2020) 586(7828):275–80. doi: 10.1038/s41586-020-2776-9
  102. Driehuis E, Kretzschmar K, Clevers H. Establishment of Patient-Derived Cancer Organoids for Drug-Screening Applications. *Nat Protoc* (2020) 15(10):3380–409. doi: 10.1038/s41596-020-0379-4
  103. Cattaneo CM, Dijkstra KK, Fanchi LF, Kelderman S, Kaing S, van Rooij N, et al. Tumor Organoid-T-Cell Coculture Systems. *Nat Protoc* (2020) 15(1):15–39. doi: 10.1038/s41596-019-0232-9
  104. Zahmatkesh E, Khoshdel-Rad N, Mirzaei H, Shpichka A, Timashev P, Mahmoudi T, et al. Evolution of Organoid Technology: Lessons Learnt in Co-Culture Systems From Developmental Biology. *Dev Biol* (2021) 475:37–53. doi: 10.1016/j.ydbio.2021.03.001
  105. Yang Y, Yang X, Zou J, Jia C, Hu Y, Du H, et al. Evaluation of Photodynamic Therapy Efficiency Using an *In Vitro* Three-Dimensional Microfluidic Breast Cancer Tissue Model. *Lab Chip* (2015) 15(3):735–44. doi: 10.1039/C4LC01065E

**Conflict of Interest:** The authors declare that the research was conducted in the absence of any commercial or financial relationships that could be construed as a potential conflict of interest.

Copyright © 2021 Bokobza, Hinault, Tiroille, Clavel, Bost and Chevalier. This is an open-access article distributed under the terms of the Creative Commons Attribution License (CC BY). The use, distribution or reproduction in other forums is permitted, provided the original author(s) and the copyright owner(s) are credited and that the original publication in this journal is cited, in accordance with accepted academic practice. No use, distribution or reproduction is permitted which does not comply with these terms.



## **CURRICULUM VITAE**



# CURRICULUM VITAE



## Mr. Victor TIROILLE

### PROFIL

**Nationalité** : Français  
**N° étudiant** : 21811485  
**Né le** 01/05/1995  
**Tel** : +33 6 76 50 20 27  
**e-mail**: victor.tiroille@gmail.com

**Date de soutenance** : 17/12/2021  
**Heure** : 14h  
**Lieu** :  
Amphithéâtre Rampal – Archimed  
151 Route de St Antoine de  
Ginestière  
06200 NICE  
FRANCE

**Directeur de thèse** :  
Dr Frédéric Bost (DR2-CNRS,  
HDR)

**Laboratoire de thèse** :  
INSERM U1065, C3M  
151 Route de St Antoine de  
Ginestière  
BP 2 3194  
06200 NICE CEDEX 3,  
France

### EDUCATION

- 2018-2021** Doctorant, Centre Méditerranéen de Médecine Moléculaire  
Inserm U1065 / Université Côte d'Azur, Nice, France  
**Directeur** : Dr Frédéric Bost  
Co-supervisor : Dr Stéphan Clavel
- 2016-2018** Master Recherche, Biologie Santé, Physiopathologies  
Université François Rabelais, Tours, France
- 2013-2016** Licence de Biologie  
Université François Rabelais, Tours, France

### INTERNSHIP & TRAINING

- 2021** Single-cell RNA-seq & network analysis using Galaxy and Cytoscape  
Virtual course, EMBL-EBI Training
- 2019** Organoid culture training, Hans Clevers lab: Adult stem cell-based organoids  
Hubrecht Institute, Utrecht, Netherlands  
*Cancéropôle PACA mobility grant*
- 2018** Master 2 internship, Centre d'Étude des Pathologies Respiratoires  
Inserm UMR 1100, Tours, France
- 2017** Master 1 internship, Nutrition, Croissance et Cancer, Inserm UMR 1069, Tours, France

### STUDENT SUPERVISION

- 2021** PhD Student, Université Côte d'Azur (~6 months)
- 2020** PhD Student, Université Côte d'Azur (organoid training, two weeks)
- 2020** Master 2 student, Université Côte d'Azur (six months)
- 2019** Post-doc (organoid training, two weeks)
- 2019** Master 1 Erasmus student, Uppsala University (six months)
- 2018** Master 1 student, Université de Tours (six weeks)

### AWARD

- 2021** Oral communication Award  
Société Française de Thérapie Cellulaire et Génique, Lyon, France
- 2019** Young Researcher Award (Oral Communication)  
European Organoids Symposium, Milan, Italy

## SELECTED ORAL COMMUNICATIONS IN SCIENTIFIC MEETINGS

- 2021 Invited Speaker, Webinar, Société Française de Thérapie Cellulaire et Génique  
2020 Canceropole PACA, Saint-Raphaël, France  
*“A new toolbox to study human physiology: genome editing and « painting » in synthetic organs”*
- 2020 Société Française de Thérapie Cellulaire et Génique, Lyon, France  
*« UBTD1 is a mechano-regulator controlling cancer aggressiveness : deciphering its role in prostate cancer using organoid »*
- 2019 Symposium Translationnel Oncologie Prostate, Nice, France  
*« Prostate cancer and organoid »*
- 2019 European Organoids Symposium, Milan, Italy  
*« UBTD1 is a mechano-regulator controlling cancer aggressiveness : deciphering its role in prostate cancer using organoid »*
- 2018 Lungstorming, Marseille, France  
*« L'inhibition du complexe Actin related protein Arp2/3 inhibe la différenciation des fibroblastes pulmonaires humains induite par le TGF-β1 in vitro »*

## SELECTED POSTERS

- 2021 EMBO | EMBL: Life at the Periphery: Mechanobiology of the Cell Surface  
2020 EMBO | EMBL: Organoids: Modelling Organ Development and Disease in 3D Culture  
2020 Canceropole PACA, Saint-Raphaël, France  
2019 Canceropole PACA, Saint-Raphaël, France

## SCIENCE DISSEMINATION

- 2020 Immersion Labos Les mini-organes, YouTube video, Université Cote d'Azur  
[https://www.youtube.com/watch?v=uT9jyl\\_pNf0&t=243s](https://www.youtube.com/watch?v=uT9jyl_pNf0&t=243s)
- 2020 Creation of a website to share scientific ideas  
[www.thecollectivelab.org](http://www.thecollectivelab.org)
- 2020 Collaboration with a YouTube channel, Scilabus, 'How to grow organs'  
<https://www.youtube.com/watch?v=lvitxX-06qY&t=14s>
- 2020 3 Minute Thesis, Université Cote d'Azur, France  
<https://www.youtube.com/watch?v=d78X-8IH6F0&t=16s>
- 2019 Intervention in a middle school to present the organoid model, Nice, France

## LIST OF PUBLICATIONS

V. Tiroille, A. Krug, E. Bokobza, A. Gutierrez-Guerrero, L. Medaer, P. Mangeot, F. Bost and E. Verhoeyen. Nanoblades allow high-level genome editing in organoids. **(Submitted in Frontiers)**, 2021

E. Bokobza, C. Hinault, V. Tiroille, S. Clavel, F. Bost, N. Chevalier. The Adipose Tissue at the Crosstalk Between EDCs and Cancer Development. **(Frontiers in Endocrinology)**, 2021

E. Bokobza, V. Tiroille, C. Karamaoun, M. Argentina, B. Mauroy, C. Hinault, F. Bost, S. Clavel, N. Chevalier. Organoids as a model to study the impact of EDCs on the prostate gland. **(European Society of Endocrinology, Conference Paper)**, 2021

S.Torrino, V.Tiroille, B.Dolfi, M.Dufies, C.Hinault, L.Bonesso, S.Dagnino, J.Uhler, M.Irondelle, A.Gay, L.Fleuriot, D.Debayle, S.Lacas-Gervais, M.Cormont, T.Bertero, F.Bost, J.Gilleron, S.Clavel. UBTD1 regulates ceramide balance and endolysosomal positioning to coordinate EGFR signaling. **(eLife)**, 2021

C.Mergault, F.Lisée, V.Tiroille, N.Heuzé-Vourc'h, C.Parent, D.Sizaret, S.Marchand-adam, L.Plantier. Inhibition of the Arp2/3 complex represses human lung myofibroblast differentiation and attenuates bleomycin-induced pulmonary fibrosis. **(master project, British Journal of Pharmacology)**, 2021

C.Mergault, F.Lisée, V.Tiroille, N.Heuzé-Vourc'h, C.Parent, D.Sizaret, S.Marchand-adam, L.Plantier. Inhibition of the Arp2/3 complex inhibits lung myofibroblast differentiation in vitro and attenuates bleomycin-induced pulmonary fibrosis in mice. **European Respiratory Journal** (master project, Conference Paper), 2019, doi: 10.1183/13993003.congress-2019.PA594

## **LIST OF PUBLICATIONS**



## LIST OF PUBLICATIONS

**V. Tiroille**, A. Krug, E. Bokobza, A. Gutierrez-Guerrero, L. Medaer, P. Mangeot, F. Bost and E. Verhoeyen. Nanoblades allow high-level genome editing in organoids. (**Submitted in Frontiers**), 2021

E. Bokobza, C. Hinault, **V. Tiroille**, S. Clavel, F. Bost, N. Chevalier. The Adipose Tissue at the Crosstalk Between EDCs and Cancer Development. (**Frontiers in Endocrinology**), 2021

E. Bokobza, **V. Tiroille**, C. Karamaoun, M. Argentina, B. Mauroy, C. Hinault, F. Bost, S. Clavel, N. Chevalier. Organoids as a model to study the impact of EDCs on the prostate gland. (**European Society of Endocrinology, Conference Paper**), 2021

S.Torrino, **V.Tiroille**, B.Dolfi, M.Dufies, C.Hinault, L.Bonesso, S.Dagnino, J.Uhler, M.Irondelle, A.Gay, L.Fleuriot, D.Debayle, S.Lacas-Gervais, M.Cormont, T.Bertero, F.Bost, J.Gilleron, S.Clavel. UBTD1 regulates ceramide balance and endolysosomal positioning to coordinate EGFR signaling. (**eLife**), 2021

C.Mergault, F.Lisée, **V.Tiroille**, N.Heuzé-Vourc'h, C.Parent, D.Sizaret, S.Marchand-adam, L.Plantier. Inhibition of the Arp2/3 complex represses human lung myofibroblast differentiation and attenuates bleomycin-induced pulmonary fibrosis. (**master project, British Journal of Pharmacology**), 2021

C.Mergault, F.Lisée, **V.Tiroille**, N.Heuzé-Vourc'h, C.Parent, D.Sizaret, S.Marchand-adam, L.Plantier. Inhibition of the Arp2/3 complex inhibits lung myofibroblast differentiation in vitro and attenuates bleomycin-induced pulmonary fibrosis in mice. **European Respiratory Journal** (master project, Conference Paper), 2019, doi: 10.1183/13993003.congress-2019.PA594



## **RÉSUMÉ**



## English

During my thesis, I worked on the 3D organoid model following two main objectives: i) developing genetic tools to modify the genome of organoids and ii) deciphering the role of ubiquitin domain-containing protein 1 (UBTD1) in the development of prostate organoids .

Genome engineering has become in the last few years more accessible thanks to the RNA programmable endonucleases such as the CRISPR-Cas9 system. However, using this editing technology in synthetic organs called ‘organoids’ is still very inefficient. This is mainly due to the delivery methods used for the CRISPR-Cas9 machinery, which are predominantly performed by electroporation of RNPs containing the CAS9-gRNA complex, a procedure toxic for the organoids. Here we describe the use of the ‘Nanoblade’ technology to accomplish genome editing in organoids. Nanoblades outperformed by far knockout (KO) levels achieved with other techniques used to date for delivery of the gene editing machinery. We reached up to 80% of gene knockout in organoids after treatment with nanoblades. We achieved high-level nanoblade-mediated KO for the androgen receptor (AR) encoding gene and the cystic fibrosis transmembrane conductance regulator (CFTR) gene with single gRNA or dual gRNA containing nanoblades. Most importantly, in contrast to other gene editing methods, this was obtained without toxicity for the organoids. Moreover, it requires only four weeks to obtain stable lines KO for a gene in organoids and no obvious unwanted INDELS in off-target site in the genome were detected. In conclusion, nanoblades simplify and allow rapid genome editing in organoids with little to no side-effects.

Morphogenesis and tissue remodeling are finely regulated processes governed by cell-cell adhesions. However, the spatial and temporal control of adhesion molecules remains partially unexplored. Here we studied the role of UBTD1 as a modulator of the strength of adherens in the prostate epithelium. We showed that down-regulation of UBTD1 disrupted the self-organization of cells in three dimensions. Conversely, we demonstrated that overexpression of UBTD1 induced more regular epithelial monolayers and increased cell surface tension. Transcriptomic analyses revealed a gene expression profile of proteins involved in cell junctions affected by UBTD1 modulation. Using the prostate organoid model, we showed that UBTD1 expression in luminal cells disrupted cyst formation in mouse prostate organoids. Finally using a co-immunoprecipitation approach coupled to mass spectrometry, we showed that UBTD1 interacts with partners involved in cell-cell junctions and that these interactants have their expression modulated by UBTD1 deregulation. Our results show that a protein involved in protein degradation processes regulates the strength of adherens junctions.

## Français

Au cours de ma thèse, j'ai travaillé sur le modèle d'organoïde 3D en suivant deux objectifs principaux : i) développer des outils génétiques pour modifier le génome des organoïdes et ii) déchiffrer le rôle de la ubiquitin domain-containing protein 1 (UBTD1) dans le développement des organoïdes de la prostate.

L'ingénierie du génome est devenue ces dernières années plus accessible grâce aux endonucléases programmables par ARN telles que le système CRISPR-Cas9. Cependant, l'utilisation de cette technologie d'édition dans des organes synthétiques appelés "organoïdes" reste très inefficace. Ceci est principalement dû aux méthodes de livraison utilisées pour la machinerie CRISPR-Cas9, qui sont principalement réalisées par électroporation de RNP contenant le complexe CAS9-gRNA, une procédure toxique pour les organoïdes. Nous décrivons ici l'utilisation de la technologie "Nanoblade" pour réaliser l'édition du génome dans les organoïdes. Les nanoblades ont dépassé de loin les niveaux de knock-out (KO) obtenus avec d'autres techniques utilisées jusqu'à présent pour la livraison de la machinerie d'édition de gènes. Nous avons atteint jusqu'à 80 % de knockout génétique dans les organoïdes après traitement avec les nanoblades. Nous avons atteint un niveau élevé de KO médié par les nanoblades pour le gène codant le récepteur des androgènes (AR) et le gène du cystic fibrosis transmembrane conductance regulator (CFTR) avec des nanoblades contenant un seul ARNg ou un double ARNg. Plus important encore, contrairement à d'autres méthodes d'édition de gènes, ce résultat a été obtenu sans toxicité pour les organoïdes. En outre, il ne faut que quatre semaines pour obtenir des lignées stables KO pour un gène dans les organoïdes et aucun INDELS indésirable évident dans un site hors cible du génome n'a été détecté. En conclusion, les nanoblades simplifient et permettent une édition rapide du génome dans les organoïdes avec peu ou pas d'effets secondaires.

La morphogénèse et le remodelage des tissus sont des processus finement régulés, régis par les adhésions entre cellules. Cependant, le contrôle spatial et temporel des molécules d'adhésion reste partiellement inexploré. Nous avons étudié ici le rôle d'UBTD1 comme modulateur de la force des adhésions dans l'épithélium de la prostate. Nous avons montré que la régulation négative d'UBTD1 perturbe l'auto-organisation des cellules en trois dimensions. Inversement, nous avons démontré que la surexpression d'UBTD1 induit des monocouches épithéliales plus régulières et augmente la tension de la surface cellulaire. Les analyses transcriptomiques ont révélé un profil d'expression génique des protéines impliquées dans les jonctions cellulaires affectées par la modulation d'UBTD1. En utilisant le modèle d'organoïde de prostate, nous avons montré que l'expression d'UBTD1 dans les cellules luminales perturbait la formation de lumen dans les organoïdes de prostate de souris. Enfin, en utilisant une approche de co-immunoprécipitation couplée à la spectrométrie de masse, nous avons montré que UBTD1 interagit avec des partenaires impliqués dans les jonctions cellule-cellule et que ces interactants voient leur expression modulée par la dérégulation de UBTD1. Nos résultats montrent qu'une protéine impliquée dans les processus de dégradation des protéines régule la force des jonctions d'adhérence.